Paleoenvironmental interpretations of the Late Triassic marine realm across the Canadian Cordillera: Slow burn of the end-Triassic mass extinction

by

Jerry Zhen Xiao Lei
B.Sc. (Hons), University of British Columbia, 2018

A Dissertation Submitted in Partial Fulfillment of the
Requirements for the Degree of
DOCTOR OF PHILOSOPHY
in the School of Earth and Ocean Sciences

University of Victoria

Paleoenvironmental interpretations of the Late Triassic marine realm across the Canadian Cordillera: Slow burn of the end-Triassic mass extinction

by

Jerry Zhen Xiao Lei
B.Sc. (Hons), University of British Columbia, 2018

Supervisory Committee

Dr. Jon Husson, Supervisor
School of Earth and Ocean Sciences

Dr. Martyn Golding, Outside Member
Geological Survey of Canada

Dr. Vera Pospelova, Departmental Member
School of Earth and Ocean Sciences / University of Minnesota

Dr. Blake Dyer, Departmental Member
School of Earth and Ocean Sciences

Dr. Terri Lacourse, Outside Member
Department of Biology

Abstract

Despite representing some of the most pivotal intervals in evolutionary history, the timing and tempo of mass extinction events have remained contentious. Many studies have contributed evidence suggesting that ecosystem disturbance associated with the end-Triassic mass extinction (ETME) began prior to the Triassic/Jurassic boundary (TJB), but the extent and duration of this leadup phase is not well established. This uncertainty is exacerbated by a comparative lack of studies investigating the ETME within the context of long-term Late Triassic trends, as well as by the dominance of Tethyan datasets in paleoenvironmental interpretations of the epoch. The research presented in this dissertation consists of a multi-faceted investigation of Panthalassan paleoenvironmental conditions spanning from the Norian/Rhaetian boundary (NRB) to across the TJB, as recorded in western Canadian marine strata.

An instance of coral reef collapse on Mount Sinwa, British Columbia, is associated with the paleoenvironmental disturbance around the NRB via conodont and Re–Os isochron age constraints. Ratios of $^{87}Sr/^{86}Sr$ are observed to gradually increase across the late Norian, as opposed to the sudden drop previously observed in Tethyan datasets, indicating the NRB disturbance was not triggered by mantle-derived volcanism on a global scale. A 3 – 4‰ negative excursion in $\delta^{13}C$ values is captured in the latest Norian on Mount Sinwa, consistent with the global carbon cycling disruption proposed to occur around the NRB by prior studies.

The conodont species *Mockina carinata* and *Mockina englandi* are especially abundant in the Norian and Rhaetian strata of Panthalassa. Morphometric analyses on these two conodont species demonstrate a gradual reduction of platform width across the NRB. These intraspecific trends are likely a more conservative parallel to concurrent intergeneric morphology shifts observed in Tethyan conodonts, together potentially implying a global shift in conodont diet away from mineralized food sources during this time. This may suggest that the biomineralization pressure typically associated with the ETME began at a lesser severity around the NRB, and that conodont biodiversity underwent only limited recovery between the substantive turnover at the NRB and complete extinction of the class around the ETME. Specimens of both these species that have a mid-platform length to breadth ratio greater than 3:1 are observed exclusively in the Rhaetian, a clear sign of morphotype origination or subspeciation, with implications for improved biostratigraphic utility.

The compilation of $\delta^{13}C$ values across stratigraphic sections from Williston Lake, Holberg Inlet, and Kyuquot Sound in the Canadian Cordillera develops a comprehensive Panthalassan record spanning from the Norian through into the Hettangian, with representation from a variety of depositional settings across a wide paleogeographic area. Three distinct negative excursions are observed, with one proximal to the NRB, one within the Rhaetian, and another across the TJB. The somewhat variable positions of these excursions suggest that the earliest “precursor” excursion associated with the Rhaetian leadup to the ETME may be indistinguishable from an excursion associated with the NRB. Some of the observed excursions are too

large in magnitude to reflect shifts in global ocean water chemistry, necessitating a local-scale amplification mechanism, such as disturbance-triggered organic carbon respiration in a water column with restricted circulation. Nevertheless, this evidence for repeated carbon cycling instability indicates the ecological distress that initiated around the NRB persisted across the Rhaetian, escalating into the TJB.

Drawing from a combination of lithological, paleontological, and geochemical evidence from across the Canadian Cordillera, this dissertation supports the hypothesis of a protracted ETME that initiated as early as the NRB. With implications of elevated extinction pressure persisting for millions of years before the climax at the TJB, this research challenges preconceptions of the timescale in which mass extinction events ought to be envisioned.

Table of Contents

List of Figures

List of Tables

Acknowledgements

To Mom and Dad, for everything. I owe a great deal to my academic advisors, Martyn Golding and Jon Husson, for taking a chance on a clueless undergrad, and all the subsequent years of guidance. Everyone at the University of Victoria Earth History group and all of my collaborators made research feel more like a cooperative effort. Scientific pursuit can often be daunting, but I've had the fortune of supportive colleagues to share the burden.

I would like to thank Stuart Sutherland (University of British Columbia) for advising the Honours thesis investigating the Sinwa East section which led into this wider project; Janet Gabites (Pacific Centre for Isotopic and Geochemical Research, University of British Columbia) for conducting the $\delta^{13}C_{carb}$ analysis of Sinwa East and the $\delta^{13}C_{org}$ analysis of both sections; Dave Daquioag (Pacific Centre for Isotopic and Geochemical Research, University of British Columbia) for conducting the $^{87}Sr/^{86}Sr$ analysis; Alan Rooney (Yale University) for conducting the Re–Os dating; Jody Spence (University of Victoria) for conducting the major, minor, and trace element analysis; Discovery Helicopters in Atlin, British Columbia for providing transport to Mount Sinwa. I would also like to thank the editor Shuzhong Shen, reviewer Manuel Rigo, and an anonymous reviewer for constructive reviews that greatly improved the Mount Sinwa manuscript.

I would like to thank Nicholas Hogancamp (Hess Corporation) for providing absolutely instrumental guidance on conodont morphometric techniques; Terri Lacourse

(University of Victoria) for providing comprehensive feedback on an earlier draft of the morphometrics manuscript; Andy Fraass (University of Victoria) for providing feedback regarding general utilization of morphometric techniques; Mike Orchard (Geological Survey of Canada) for providing Canadian Cordillera conodont expertise and for collecting much of the specimen pool utilized; Hillary Taylor (Geological Survey of Canada) for conducting the conodont preparation work and curation. I would also like to thank the editor C. Kevin Boyce, reviewer Mike Orchard, and an anonymous reviewer for constructive reviews that greatly improved the morphometrics manuscript.

I would like to thank John-Paul Zonneveld (University of Alberta) for providing guidance and expertise on Williston Lake stratigraphy; Morgan Weatherbie (University of Victoria) for providing assistance both in the field and in the lab for the Williston Lake and Holberg Inlet research; Olivia Wren and Shannon Murtonen (University of Victoria) for providing assistance in the field for the Kyuquot Sound research; Travis Mayer and Alex Dyck (Williston Lake Outfitters) for providing transport and other logistical support for the Williston Lake research; Luke Osenenko (Outer Edge Adventures) for providing transport and other logistical support for the Kyuquot Sound research.

This research was funded by the Geological Survey of Canada Geo-Mapping for Energy and Minerals (GEM-2 and GEM-GeoNorth) program, and by a Natural Sciences and Engineering Research Council of Canada (NSERC) Discovery Grant to Jon Husson (RGPIN-2017-03887).

Chapter 1

Introduction

1.1. Late Triassic overview

The paleoenvironmental conditions of deep time are preserved in the sedimentary rock record, providing a glimpse of distant worlds separated from ours not spatially, but instead temporally. The Late Triassic Epoch was an especially pivotal time in Earth history, when all the world's larger landmasses were pushed together into the Pangea supercontinent (Figure 1.1; e.g. Veevers, 1994). This continental arrangement was beginning to rift apart, eventually forming the Atlantic Ocean between America and Afro-Eurasia (e.g. Marzoli et al., 1999; 2004). The associated tectonic activity caused periods of enhanced volcanism, which greatly impacted both marine and terrestrial ecosystems (e.g. Marzoli et al., 1999; 2004; Blackburn et al., 2013; Zaffani et al., 2017).

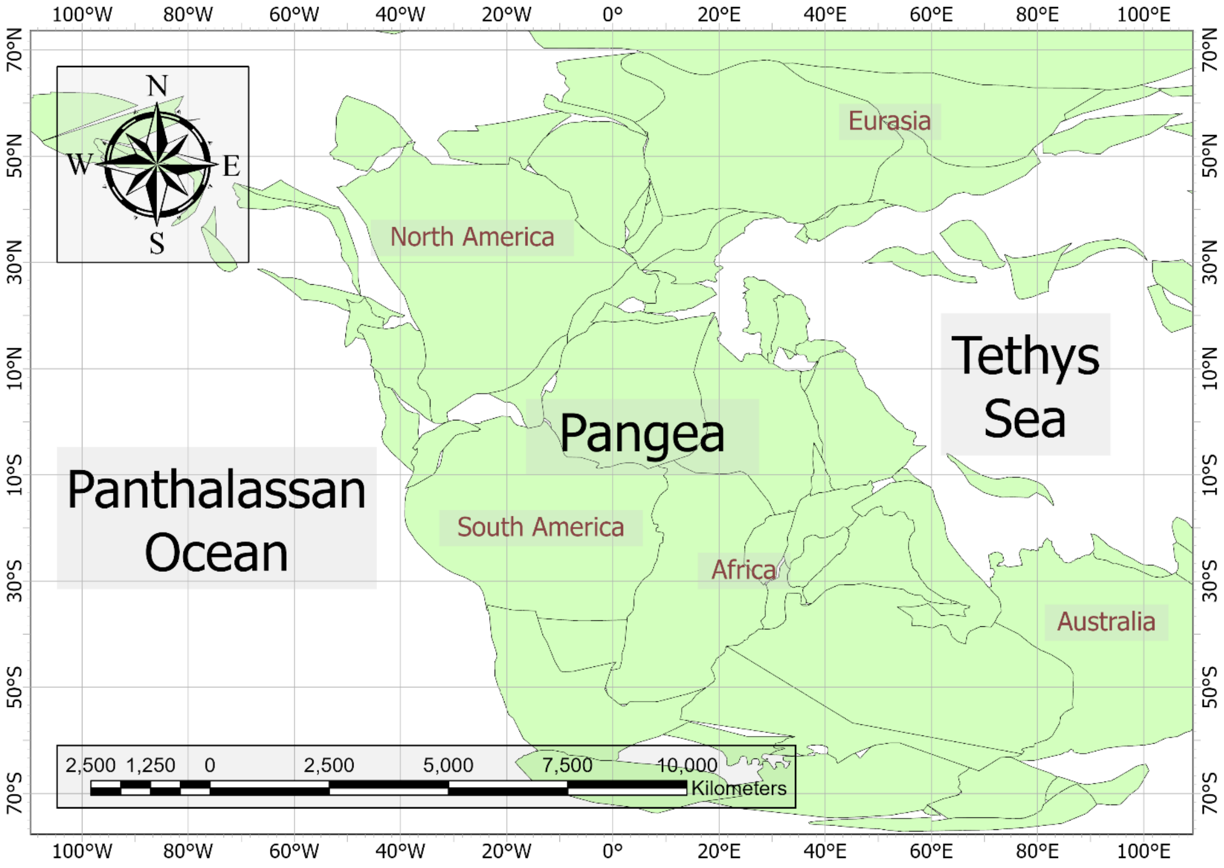

Figure 1.1: Paleotectonic reconstruction of the world during the Late Triassic Epoch (208Ma). Rotational model from Wright et al. (2013), accessed via the Macrostrat application programming interface (Peters et al., 2018).

Prior to the Triassic, the faunal assemblages of the Earth were fundamentally and irrevocably altered by the Permian/Triassic mass extinction, considered to be the most significant amongst the “Big Five” mass extinctions (e.g. Sepkoski, 1981; Raup & Sepkoski, 1982). Following a lengthy recovery period, many important biotic groups first found widespread success in the Middle to Late Triassic, such as mammals, bivalves, and scleractinian corals (e.g. Sepkoski, 1981; Raup & Sepkoski, 1982; Stanley, 2003;

Tanner et al., 2004; Benton et al., 2018; Dal Corso et al., 2020; Rigo et al., 2020). Some of these groups went on to dominate within the global biosphere, even to the present day (e.g. Sepkoski, 1981; Raup & Sepkoski, 1982). A post-extinction arms race manifested in the marine realm through a considerable intensification of grazing and predation, with the higher metabolism Modern evolutionary fauna superseding the comparatively sedentary filter feeders that dominated the Paleozoic evolutionary fauna (e.g. Sepkoski, 1981; Raup & Sepkoski, 1982; Wagner et al., 2006). Initially termed the Mesozoic Marine Revolution, primarily based on a continual increase in gastropod shell robustness across the Jurassic and Cretaceous (Vermeij, 1977), subsequent evidence from a large variety of other faunal groups around the world suggest this ecological overhaul actually began in the Middle Triassic (e.g. McRoberts, 2001; Baumiller et al., 2010; Hu et al., 2011). The newly established biodiversity in the Triassic Period proved to be short-lived however, as another mass extinction occurred around the Triassic/Jurassic boundary (e.g. Sepkoski, 1981; Raup & Sepkoski, 1982). The end-Triassic mass extinction (EMTE) was triggered by volcanism associated with a large igneous province (LIP) termed the Central Atlantic Magmatic Province (CAMP), portions of which are identified on either side of the modern Atlantic Ocean (e.g. Marzoli et al., 1999; 2004; Blackburn et al., 2013; Zaffani et al., 2017).

1.2. Outstanding questions

Since their conceptualization, mass extinction events have largely been considered geologically instantaneous, with the Mesozoic mass extinctions marking the boundary between geologic periods or eras. Some have argued that when placed in the context of their preceding and succeeding trends, these Mesozoic mass extinctions appear more prolonged and multi-phased (e.g. Keller, 2001; Hallam, 2002; Clapham et al., 2009). There is both fossil and geochemical evidence that the paleoenvironmental disturbances associated with the ETME initiated well before the Triassic/Jurassic boundary (TJB), and perhaps as early as the Norian/Rhaetian boundary (NRB) (e.g. Hallam, 2002; Tanner et al., 2004; Rigo et al., 2018, 2020). With the Late Triassic Epoch subdivided into the Carnian, Norian, and Rhaetian stages chronologically, this would mean the ETME spanned ~5 million years across the Rhaetian Stage before culminating in a climax at the TJB (Figure 1.2).

Ma		Stage/Substage		Conodont Zone/Subzone Tethys/Western Pacific		North America
201 to 201.5	UPPER TRIASSIC	RHAETIAN	Upper Rhaetian	Misikella ultima		Norigondolella sp.
				Misikella posthernsteini	Misikella koessenensis	Misikella posthernsteini
						Orchardella mosheri
			Lower Rhaetian		Misikella hernsteini-Misikella posthernsteini	
206		NORIAN	Sevatian	M. hernsteini-P. andrusovi		Mockina bidentata
				Mockina bidentata	Subzone 2	
					Subzone 1	Mockina ? serrulata
			Alaunian	Mockina postera		Mockina postera
						Orchardella elongata
				Mockina ? spiculata		Mockina ? spiculata
				M. medionorica		Orchardella multidentata
			Lacian	Epigondolella triangularis-Norigondolella hallstattensis		Epigondolella triangularis
				Epigondolella rigoi		
225 ± 3				Epigondolella quadrata		Epigondolella quadrata

Figure 1.2: Late Triassic time scale and conodont biozonation, correlating between the Tethyan and Panthalassan realms. Modified from Rigo et al. (2018).

The present dissertation will attempt to elucidate the paleoenvironmental conditions surrounding the ETME by investigating stratigraphic sections across western Canada. Late Triassic strata in the Canadian Cordillera represent marine deposition along the northwestern margin of Pangea, as well as along the margins of outboard tectonostratigraphic terranes situated in the Panthalassan Ocean (Figure 1.1), which have subsequently accreted to western North America (e.g. Colpron & Nelson, 2009, 2011). The stratigraphic sections investigated in this dissertation therefore reflect a large paleogeographic coverage representative of the Late Triassic Panthalassan realm as a whole, which has received comparatively less study than the Tethyan realm (Figure 1.1). These sections were selected for sedimentary continuity across time intervals of interest, with preference for carbonate-rich and fossiliferous lithologies. Fieldwork involved recording notes detailing the strata, while regularly taking rock samples for a variety of paleontological and geochemical analyses. The two main investigative tools utilized in the present dissertation are conodont microfossils due to their high biostratigraphic utility in the Late Triassic, and the $\delta^{13}C$ isotope system because these measurements efficiently capture instances of disruption to the carbon cycle. These tools facilitate the gathering of evidence which may support the hypothesis of a prolonged and multi-phased ETME.

1.3. Conodont microfossils

Conodonts were a class of marine vertebrates that originated in the Late Cambrian, having been amongst the first animals to evolve mineralized dentition (e.g. Briggs et al., 1983). These teeth-like structures composed of bioapatite are typically the only part of the conodont animal that are preserved in the fossil record, and they have very high biostratigraphic utility (e.g. Briggs et al., 1983). Pectiniform conodont elements in particular, a category of conodont element with a platform perpendicular to the central row of denticles called the carina (Figure 1.3), are frequently utilized to finely constrain the age of marine sedimentary strata. Conodonts persisted across almost the entire Paleozoic, and finally went extinct in the earliest Jurassic, widely considered an emblematic casualty of the ETME (e.g. Clark, 1983).

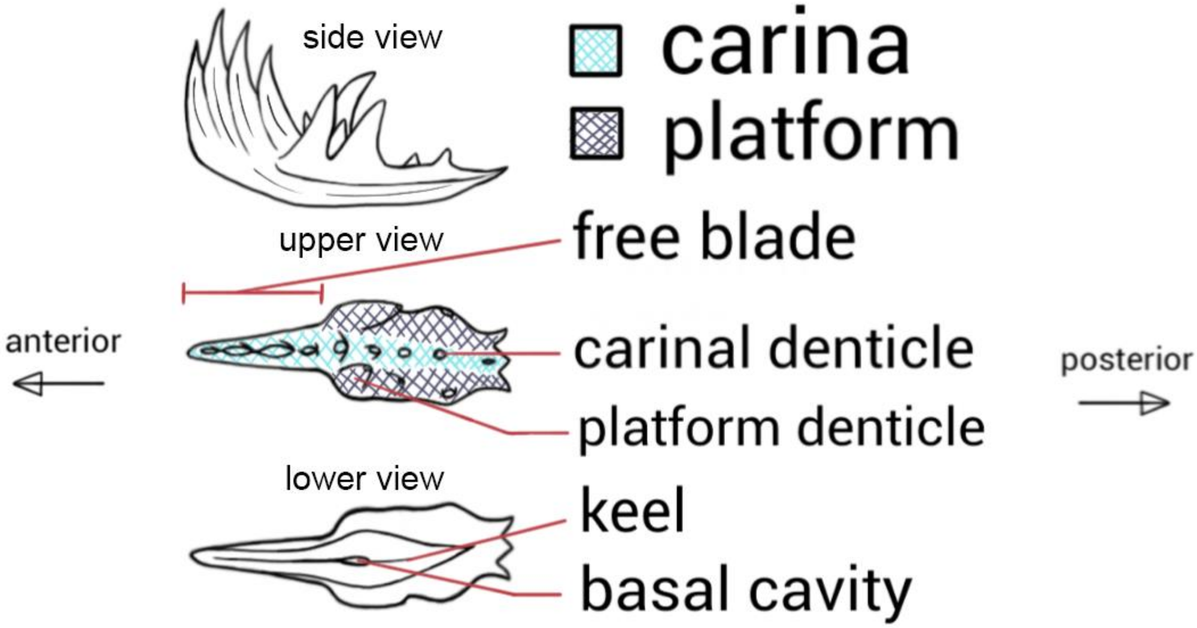

Figure 1.3: Conodont pectiniform element morphology diagram, with general terminology as applied to Late Triassic elements belonging to the genus *Mockina*.

Throughout the Late Triassic, although conodonts exhibited pulses of extinction and origination, an overall trend of diversity decline is observed throughout the epoch (Martínez-Pérez et al., 2014a; Rigo et al., 2018). The latest Norian represents the last local peak of conodont standing diversity, before precipitous decline towards complete extinction across the Rhaetian (Martínez-Pérez et al., 2014a; Rigo et al., 2018). Additionally, the typically cosmopolitan conodonts display some degree of uncharacteristic endemism in the Late Triassic, resulting in biozonations differing between the Panthalassan and Tethyan realms (Figure 1.2; e.g. Rigo et al., 2018).

1.4. Carbon isotope system

Life on Earth is greatly facilitated by the global carbon cycle. As carbon is transferred into, out of, and across the ocean-atmosphere system, it not only provides organisms with organic building blocks to form tissue, but also fosters hospitable climate via atmospheric carbon dioxide. The primary influx of carbon into the ocean-atmosphere system on geological timescales is volcanic outgassing, with the primary outflux being deposition of carbonate rocks and organic matter on the seafloor, which eventually results in much of the carbon being returned to the mantle via subduction (e.g. Kump & Arthur, 1999; Ripperdan, 2001). Also on long timescales, this system is regulated by the silicate weathering feedback mechanism (e.g. Walker et al., 1981). For example, if an initial perturbation of enhanced volcanism results in higher concentrations of atmospheric carbon dioxide, the warmer climate produced accelerates the rate of chemical weathering, a process which consumes carbon dioxide (e.g. Walker et al., 1981). With the chemical weathering of continental silicates, carbon is transported as aqueous bicarbonate ions into the ocean via riverine systems (e.g. Walker et al., 1981). This flux increases the concentration of dissolved inorganic carbon (DIC) in the ocean, which prompts more precipitation of carbonate minerals on the seafloor (e.g. Walker et al., 1981).

Unlike fossils, concentrations of atmospheric carbon dioxide or oceanic DIC do not preserve visually in the rock record. However, instances of disturbance to this carbon cycling system can be recorded in the geochemistry of carbonate rocks. The relative abundance of ^{13}C to ^{12}C in material is commonly expressed as its $\delta^{13}C$ value, which is measured in per mille, comparing the sample's isotopic ratio to an established standard:

$$\delta^{13}\mathrm{C}_{sample} = \left(\frac{{}^{13}\mathrm{C}/\,{}^{12}\mathrm{C}_{sample}}{{}^{13}\mathrm{C}/\,{}^{12}\mathrm{C}_{standard}} - 1\right) \times 1000.$$

All $\delta^{13}C$ values presented throughout the dissertation are expressed relative to Vienna Pee Dee Belemnite (VPDB). The $\delta^{13}C$ value of carbon released from the mantle averages -5‰ (Figure 1.4; e.g. Kump & Arthur, 1999; Ripperdan, 2001). As biological carbon fixation favours the lighter ^{12}C isotope, this biotic fractionation causes the $\delta^{13}C$ value of marine organic matter to be negatively offset from that of oceanic DIC by an average of 25‰ (Figure 1.4; e.g. Kump & Arthur, 1999; Ripperdan, 2001). The $\delta^{13}C$ value of well-preserved limestone reflect that of the marine DIC in which they formed (Keith & Weber, 1964). Across the Phanerozoic, the $\delta^{13}C$ value of carbonates hover around 0‰, which would imply global carbon burial is approximately 80% carbonate and 20% organic (Figure 1.4; e.g. Kump & Arthur, 1999; Ripperdan, 2001). When environmental disturbances impact biotic communities such that the values or proportions of these fluxes are changed, the $\delta^{13}C$ value of global DIC can typically shift around 3‰ in either direction, before returning to the ~0‰ baseline upon ecological recovery (e.g. Kump & Arthur, 1999; Ripperdan, 2001). These shifts in $\delta^{13}C$ values are termed “excursions”.

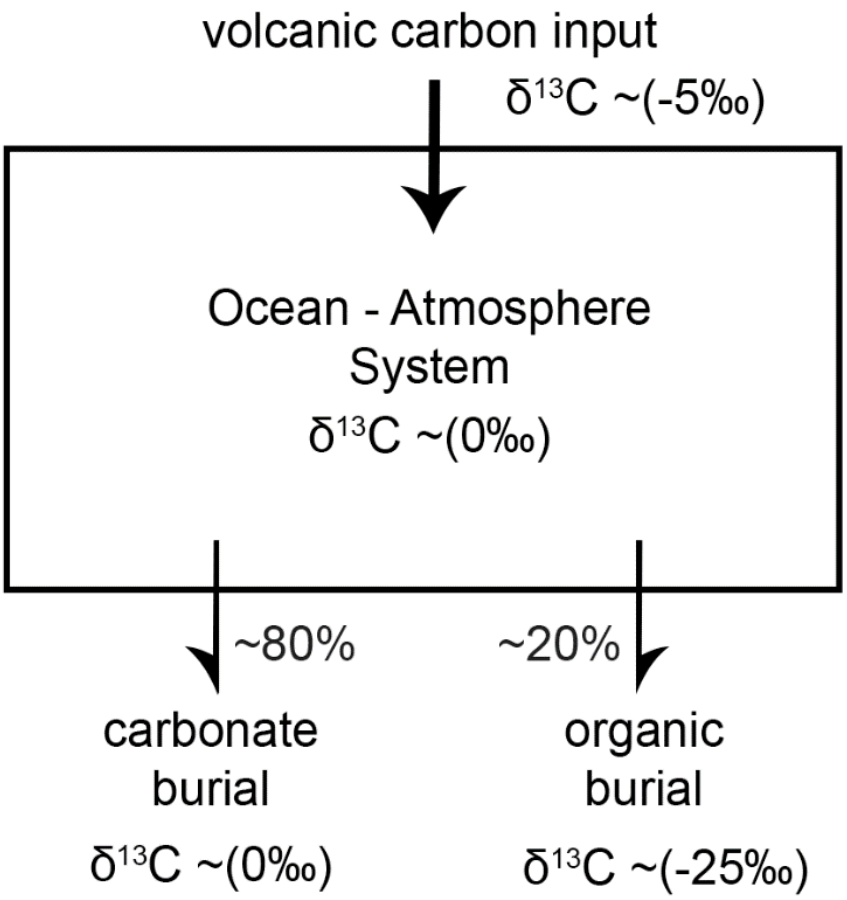

Figure 1.4: Carbon fluxes in the global carbon cycle with isotopic values. Simplified from Kump and Arthur (1999) and Ripperdan (2001).

A multitude of processes can result in the $\delta^{13}C$ value of limestone not reflecting open-ocean values, meaning the paleoenvironmental utility of the isotope system is highly contingent on the identification of whether or not these influences are present. Shallow marine carbonates dominate in the marine rock record, but this depositional setting is liable to developing pockets of restricted sea water circulation, where evaporation and continental freshwater discharge can shift the local carbon isotope signal away from global values (e.g. Patterson & Walter, 1994; Knauth & Kennedy, 2009). Even after the deposition of carbonate sediments, a variety of processes can change the properties of these sediments prior to lithification, collectively termed diagenesis. In particular, diagenetic processes involving significant interaction with CO_2-rich fluid can influence the $\delta^{13}C$ value of the eventually lithified carbonate rock. These mechanisms include sub-aerial exposure to meteoric fluids (e.g. Allan & Matthews, 1982), interaction with pore fluids just below the water-sediment interface (e.g. Banner & Hanson, 1990), and fluid-rock reaction at higher temperatures during burial (e.g. Derry, 2010).

Lithological indicators of diagenesis include the presence of sub-aerial exposure surfaces within stratigraphic sections, a facies dependence of $\delta^{13}C$ values since different lithologies will be variably susceptible to diagenesis, and signs of low-grade metamorphism such as coarse calcite recrystallization (e.g. Marshall, 1992). Diagenesis impacts the geochemistry of carbonates beyond just carbon isotopes, so a variety of geochemical indicators can also be used to recognize diagenesis. For example, a strong correlation between $\delta^{13}C$ and $\delta^{18}O$ values is a commonly used indicator of diagenetic influence on $\delta^{13}C$ values, since the $\delta^{18}O$ system is significantly more susceptible to alteration than $\delta^{13}C$ (e.g. Marshall, 1992). High Mn/Sr ratios are another proxy which signals diagenesis, as fluid interactions during carbonate alteration typically increase Mn abundance while decreasing Sr abundance (e.g. Jacobsen & Kaufman, 1999; Fölling & Frimmel, 2002). These lithological and geochemical indicators can suggest for or against diagenetic influence, but it is important to note that they cannot do so absolutely.

1.5. Research approaches

Despite the prominent faunal turnover associated with the NRB, convincing determinations regarding the paleoenvironmental conditions surrounding this event have thus far proven elusive. Decreasing $^{87}Sr/^{86}Sr$ ratios observed across the NRB in the Tethyan realm suggests volcanism to be the trigger (Korte et al., 2003; Callegaro et al., 2012), but CAMP volcanism did not occur until significantly after the NRB (Marzoli et al., 1999, 2004; Blackburn et al., 2013; Zaffani et al., 2017), and no LIP has been precisely dated to coincide with the age of the boundary. If the NRB does mark the first of several extinction events that together constitute the ETME, it is problematic that the NRB lacks a well-defined trigger mechanism. Investigation of the NRB in western Canada using a variety of geochemical proxies could support or refute previous paleoenvironmental interpretations, which have largely been based on Tethyan data, and assumed to represent global trends.

The final extinction of conodonts is considered one of the more conspicuous consequences of the ETME, but long-term diversity trends suggest the latest Norian actually represented their last peak in standing diversity (Martínez-Pérez et al., 2014a; Rigo et al., 2018). While it is evident that the NRB had a significant impact on conodont communities, the intergeneric shift observed in Tethyan conodonts is not as clear in Panthalassa, exacerbated by the differences in biozonation between the two realms (e.g. Orchard et al., 2007; Rigo et al., 2018). Investigation of intrageneric and intraspecific conodont morphology across the NRB in Panthalassa could greatly contribute to interpretations of how prolific marine fauna responded to the NRB disturbance. If no signs of recovery can be observed in the Rhaetian, that would suggest the stress of extinction pressure persisted continually into the climax of the ETME at the TJB.

Supporting the concept of a drawn-out ETME, this event is associated with a global series of three negative excursions in δ^{13}C values leading up to and across the TJB, termed “precursor”, “initial”, and “main” chronologically (e.g. Hesselbo et al., 2002; Ward et al., 2004; Ruhl et al., 2009; Ruhl & Kürschner, 2011; Fujisaki et al., 2018; Zaffani et al., 2018; Du et al., 2020b; de Graaff et al., 2022). While the “precursor” and “initial” excursions are understood to occur in the Rhaetian, their exact positions are ambiguous due to the limitations of their relevant stratigraphic age constraints. A negative excursion in δ^{13}C values is also associated with the NRB (e.g. Maron et al., 2015; Rigo et al., 2016; Zaffani et al., 2017), but a connection between this excursion and the later ETME excursions has largely not been pursued. Systematic measurements of δ^{13}C values along continuous stratigraphic sections spanning the NRB, entire Rhaetian Stage, and TJB, could refine the timing of carbon cycling disruptions across this time interval. In particular, this could demonstrate whether or not carbon isotope instability was pervasive throughout the entirety of the Rhaetian.

1.6. Dissertation outline

This dissertation is organized into five chapters. The first introductory chapter provides overarching background and context for the dissertation, as well as a broad overview of the major research tools utilized. The second, third, and fourth chapters each represent a standalone scientific paper in which I am the first author. Chapter two has been published in the journal *Palaeogeography, Palaeoclimatology, Palaeoecology* (Lei et al., 2022), chapter three has been published in the journal *Paleobiology* (Lei et al., 2024), and chapter four is being prepared for publication. The final fifth chapter concludes the dissertation with a brief summary of the research and highlights potential avenues for future research.

Chapter two encompasses the paleoenvironmental interpretation of two parallel sections on Mount Sinwa, in the far northwest of British Columbia. These sections span the middle to latest Norian, as confirmed by the conodonts documented in this chapter, and features a prominent coral reef that is overlain by shale near the top of the sections. This lithological shift from coral boundstone to shale occurs near the NRB, as identified by conodont occurrences of *Mockina mosheri* B and corroborated by Re–Os isochron ages. A negative excursion of ~3‰ magnitude is observed in the $\delta^{13}C_{carb}$ values just below the shale transition, potentially correlative with carbon cycle instability that has been associated with the NRB around the world (e.g. Ward et al., 2001, 2004; Sephton et al., 2002; Korte et al., 2005; Wignall et al., 2007; Muttoni et al., 2014; Maron et al., 2015; Rigo et al., 2016, 2020; Zaffani et al., 2017). Measurements of $^{87}Sr/^{86}Sr$ ratios at the Mount Sinwa sections contribute long term trends across the middle to latest Norian, which were previously unestablished for the Panthalassan record. The compilation of Panthalassan $^{87}Sr/^{86}Sr$ ratios surrounding the NRB does not convincingly replicate the decrease observed in the Tethyan realm (Korte et al., 2003; Callegaro et al., 2012;

Tackett et al., 2014). This suggests the trigger mechanism of the NRB disturbance was not mantle derived volcanism, at least not at a scale that would influence global ocean water chemistry.

Chapter three involves the morphometric analyses of the two conodont species *Mockina carinata* and *Mo. englandi*, with specimens from both new and archival collections spanning the Canadian Cordillera. Canonical variate analyses reveal that platform width overwhelmingly accounts for the morphological variation that differentiates specimens by age. Elements of *Mo. carinata* display a sequential platform width reduction from the middle Norian to late Norian to Rhaetian, whereas elements of *Mo. englandi* only display platform width reduction from the late Norian to Rhaetian. Specimens of both species with a mid-platform length to breadth ratio greater than 3:1 are found exclusively in the Rhaetian Stage. At Kennecott Point on Haida Gwaii, this conodont platform width reduction occurs stratigraphically above the NRB. In terms of biomechanics, the change in conodont morphology may reflect a dietary shift from mineralized to more soft-bodied prey, perhaps indicating mineralization pressure around the NRB. A disruption of carbonate sedimentation is associated with the ETME near the TJB (e.g. Hautmann, 2004), but extending this phenomena to the NRB suggests prolonged disturbance to the marine realm.

Chapter four investigates eight stratigraphic sections from disparate tectonostratigraphic terranes across the Canadian Cordillera, in order to compile a Panthalassan record of

δ^{13}C values, which collectively span the Norian through Hettangian stages. Generally, three distinct negative excursions are observed: one proximal to the NRB, one in the Rhaetian, and one coinciding with the TJB. These excursions may correlate to the three negative excursions previous studies have attributed to the ETME (e.g. Hesselbo et al., 2002; Ward et al., 2004; Ruhl et al., 2009; Ruhl & Kürschner, 2011; Fujisaki et al., 2018; Zaffani et al., 2018; Du et al., 2020b; de Graaff et al., 2022), but suggest there may be no clear distinction between a Rhaetian "precursor" excursion and one associated with the NRB. Furthermore, while a wide variety of proxies are utilized across the western Canadian sections to constrain age boundaries, diachroneity is evident for at least some of the excursions, even amongst nearby sections that use a common proxy. This asynchroneity would not be expected from excursions representing global scale perturbations to the carbon cycle (e.g. Kump & Arthur, 1999; Ripperdan, 2001). Additionally, the negative excursions observed are often too large in magnitude to plausibly reflect global ocean δ^{13}C values, indicating the presence of some local mechanism capable of amplifying or even inducing these signals. One potential explanation would be if the episodes of biotic disturbance triggered greatly increased organic carbon respiration, forcing local DIC to very negative δ^{13}C values. However, a restricted circulation environment would be needed for this process to record extreme values in carbonates, suggesting such environments were common across many different depositional settings across Panthalassa. Overall, repeated carbon isotope excursions spanning the interval from the Norian through to the Hettangian is interpreted as representing persistent ecological instability.

All three main content chapters investigate instances of paleoenvironmental disturbance during the Late Triassic, with focus on the NRB and leading into the ETME, but with a variety of approaches. Chapter two focuses specifically on the NRB and utilizes a multitude of geochemical tools, including carbon and strontium isotopes, in an attempt to discern specific paleoenvironmental qualities of the event. Chapter three shifts focus to paleontological evidence for ecological distress, interpreting conodont morphology changes across the middle Norian through Rhaetian stages. Chapter four focuses specifically on carbon isotopes, but expands the temporal range of the investigation to encompass the NRB, the entire Rhaetian Stage, and the TJB. All three chapters provide evidence for paleoenvironmental disturbance preceding the TJB in Panthalassa, supporting the concept of a drawn-out mass extinction around the end of the Triassic Period.

Chapter 2

Paleoenvironmental interpretation of the Late Triassic Norian/Rhaetian boundary interval in the Whitehorse Trough (Stikine Terrane, northern Canadian Cordillera)[1]

2.1. Abstract

The Norian/Rhaetian boundary (NRB) is associated with significant faunal turnover in a wide variety of groups. Following the relative stability of the Norian Stage, this boundary potentially marks the beginning of a protracted and continuous episode of elevated extinction rates, which culminated with the ETME. Despite the importance of the NRB to paleontological trends in the Late Triassic, much about this event remains enigmatic, including potential causal mechanisms as well as the characteristics of the resulting paleoenvironmental changes. Fossiliferous limestone of the Sinwa Formation occurs in extensive outcrops throughout northwestern British Columbia and provides an exceptional record of Upper Triassic stratigraphy that represents a paleogeographic region largely uninvestigated prior. The present study integrates lithostratigraphic, paleontological, and geochemical data to reconstruct the shallow marine paleoenvironments recorded by the Sinwa Formation in two sections on Mount Sinwa, south of Atlin, within the Stikine Terrane. The progression of lithological facies observed

---

[1] This chapter is published as: Lei, J.Z.X., Golding, M.L., and Husson, J.M. (2022). Paleoenvironmental interpretation of the Late Triassic Norian – Rhaetian boundary interval in the Whitehorse Trough (Stikine Terrane, northern Canadian Cordillera). Palaeogeography, Palaeoclimatology, Palaeoecology, v. 608(111306), p. 1–17.

in these sections suggests a gradual base level rise throughout the late Norian. Following this steady facies progression is a prominent shift from coral reef boundstone to shale near the top of both sections. This facies change approximately coincides with the NRB interval as evidenced by the first occurrence of the latest Norian – Rhaetian conodont species *Mockina mosheri* morphotype B, as well as by Re–Os isochron ages of organic-rich limestone. Although the base level rise observed at the NRB interval could be due to regional tectonics, it could also potentially be recording eustatic sea level rise given the lack of consensus around sea level change at the NRB. Measurements of late Norian $^{87}Sr/^{86}Sr$ ratios on Mount Sinwa are consistent with those recorded in Tethyan studies, but the Panthalassan record overall does not replicate the same drop across the NRB observed in the Tethys. The lithological facies shift is also immediately preceded by a negative excursion in the $\delta^{13}C$ values of carbonate, indicating that the NRB interval on Mount Sinwa is associated with coral reef collapse as well as the globally observed disruption of carbon cycling.

2.2. Introduction

The Late Triassic was a turbulent time of substantial climatic change and extensive faunal turnover, punctuated by multiple extinction and origination pulses which ultimately culminated in the end-Triassic mass extinction (ETME) (e.g. Simms & Ruffell, 1989; Hallam, 2002; Tanner et al., 2004; Rigo et al., 2020). The Pangea supercontinent began to rift apart during this interval, associated with episodes of volcanism which altered atmospheric composition and resulted in major paleoenvironmental disturbances (e.g. Marzoli et al., 1999, 2004; Blackburn et al., 2013). The present study focuses on the Norian/Rhaetian boundary (NRB) interval, which followed the relative stability of the Norian Stage (e.g. Hallam, 2002; Sephton et al., 2002; Tanner et al., 2004) with significant faunal turnover in a wide variety of groups including conodonts, bivalves, radiolarians, and ammonoids (e.g. Carter & Orchard, 2007; Tanner et al., 2004; Rigo et al., 2020). This biotic disturbance has not been convincingly tied to any eustatic sea level change, which remains uncertain with Haq et al. (1988) suggesting sea level fall at the NRB and Embry (1988) suggesting sea level rise. Currently, no official Global Boundary Stratotype Section and Point (GSSP) has been selected for the base of the Rhaetian Stage, although candidates have been proposed in Austria (Krystyn et al., 2007a, b) and Italy (Rigo et al., 2016). The base of the Rhaetian Stage is commonly defined by the First Appearance Datum (FAD) of the conodont species *Misikella posthernsteini* (Krystyn, 2010; Rigo et al., 2016). This genus is rare in North America, but several more readily utilized latest Norian proxies have been established that indicate close proximity to the base of the Rhaetian, including the FAD of the conodont *Mockina mosheri* (Carter & Orchard, 2007; Orchard et al., 2007), and the Last Appearance Datum (LAD) of the bivalve *Monotis* (Ward et al., 2001, 2004). It is crucial to note, however, that temporal offset does exist between some if not all of these proxies, the extent of which remains somewhat uncertain (e.g. Carter & Orchard, 2007; Krystyn, 2010; Orchard et al., 2007; Rigo & Campbell, 2021; Taylor et al., 2021).

The causal mechanism of the paleoenvironmental disturbance at the NRB remains largely unknown, despite potentially being a significant turning point for global ocean water chemistry. In the Tethyan records, $^{87}Sr/^{86}Sr$ ratios have been observed to increase across the Norian, attributed to the uplift and erosion of the Cimmerian Mountains (Korte et al., 2003; Onoue et al., 2018). In contrast, the NRB has been associated with decreasing $^{87}Sr/^{86}Sr$ values (Korte et al., 2003; Callegaro et al., 2012; Tackett et al., 2014). Korte et al. (2003) attributed this shift to enhanced hydrothermal activity at mid-ocean ridges as well as to increased weathering of arc volcanic material associated with the opening of the Vardar Ocean. Callegaro et al. (2012) interpreted the cause of this decline as the beginning of large igneous province (LIP) weathering input from Central Atlantic Magmatic Province (CAMP) volcanism. However, radiometric dating of the CAMP places the onset of eruptive volcanism at ~201.5 Ma (Blackburn et al., 2013), which is much younger than estimates for the age of the NRB, postulated to be either ~209 Ma (e.g. Caruthers et al., 2022) or ~205 Ma (e.g. Wotzlaw et al., 2014). The CAMP volcanism coincides instead with the later end-Triassic mass extinction (Marzoli et al., 1999, 2004; Blackburn et al., 2013; Zaffani et al., 2017). It has been proposed that outgassing from intrusive CAMP magmatism contributed to climatic disturbance which precedes the end-Triassic (Davies et al., 2017), but no CAMP intrusions have been dated at ~209 Ma, nor would such intrusions influence ocean $^{87}Sr/^{86}Sr$ values via weathering input. Volcanism associated with the lesser known Angayucham Province located further north in Alaska has been proposed as an alternative cause for the paleoenvironmental disturbance at the NRB (Zaffani et al., 2017; Rigo et al., 2020). This claim also requires further testing, as current radiometric age constraints on this LIP are very imprecise, with uncertainties of ±7 million years (Ernst & Buchan, 2001).

The record of $\delta^{13}C$ values is a widely utilized proxy for interpreting paleoenvironmental disturbance events, recording the isotopic values of dissolved inorganic carbon (DIC) in global seawater into the geologic past (Kump & Arthur, 1999). Major biotic turnover events are typically associated with excursions in $\delta^{13}C$ values (e.g. Pálfy et al., 2001, 2007; Ward et al., 2001, 2004; Hesselbo et al., 2002). Disturbance to the $\delta^{13}C$ values of global ocean DIC would be expected to produce parallel excursions in both the carbonate $\delta^{13}C$ ($\delta^{13}C_{carb}$) and the organic $\delta^{13}C$ ($\delta^{13}C_{org}$) records, the assumption being the organic material largely formed from the same DIC pool (e.g. Kump & Arthur, 1999; Johnston et al., 2012; Meyer et al., 2013). A negative excursion in values of $\delta^{13}C_{org}$ is associated with the NRB in several localities within the Lagonegro Basin in southern Italy (Rigo et al., 2016; Zaffani et al., 2017). This negative excursion is also observed in the values of $\delta^{13}C_{org}$ at Wombat Basin, Australia, and in the $\delta^{13}C$ values of biomarkers fluoranthene and benzofluoranthene at the North Rankin - 5 well, North West Shelf, Australia (Rigo et al., 2020). Tethyan $\delta^{13}C_{carb}$ records compiled from sections across Europe (Korte et al., 2005; Muttoni et al., 2014), and Panthalassan organic and carbonate $\delta^{13}C$ records from Haida Gwaii, Canada (Ward et al., 2001, 2004; Whiteside & Ward, 2011) do not present as clear of an excursion at this boundary but do seem to indicate an increase in point-to-point stratigraphic variability compared to samples taken from strata before and after the boundary. This trend of increased scatter is also observed in the values of $\delta^{13}C_{org}$ at Kiritehere, New Zealand, as well as in the values of $\delta^{13}C_{org}$ at Kastelli, Greece, and in the values of organic and kerogen $\delta^{13}C$ at the Delambre - 1 well North West Shelf, Australia (Rigo et al., 2020; Rigo & Campbell, 2021). Whiteside and Ward (2011) termed instances of these rapid oscillations during the early Mesozoic as “Chaotic Carbon Intervals”, wherein prolonged periods of low biodiversity following disturbance events create unstable ecosystems more prone to positive feedback loops. Thriving biotic realms have long been proposed to have a stabilizing effect on global climate (e.g. Charleson et al., 1987), the absence of which would more easily allow runaway amplification of an initial disturbance, and continuous carbon cycle instability persisting until biodiversity recovers beyond a certain threshold (Whiteside & Ward, 2011). These authors, however, do not specifically identify the NRB as an example of a “Chaotic Carbon Interval.” Rapidly oscillating values are also observed in the $\delta^{13}C_{org}$ record of the NRB boundary interval at Williston Lake, Canada, and are alternatively interpreted as a positive excursion resulting from widespread ocean stagnation and anoxia (Sephton et al., 2002; Wignall et al., 2007).

The present study aims to characterize the NRB interval in North America via lithological, paleontological, and geochemical analyses. Investigations were conducted on continuous stratigraphic sections of carbonate located on Mount Sinwa in northwestern British Columbia, Canada. This study aims to compare records of the paleoenvironmental disturbance at the NRB interval between the Panthalassan realm and the better established Tethyan perspective, in order to achieve a global synthesis of this event.

2.3. Geological setting

Stretching from the Canadian Rockies to the Pacific coast, the Canadian Cordillera is an expansive zone of deformation resulting from the amalgamation of crustal terranes with varying stratigraphic and tectonic histories that accreted to the western margin of the North American Craton (Monger & Ross, 1971; Monger, 1997). These terranes have been interpreted as fragments of continental crust, oceanic crust, and volcanic island arcs (e.g. Colpron & Nelson, 2009, 2011). Based on evidence from faunal distributions, paleomagnetism, detrital zircon geochronology, and crustal geochemistry, these terranes display evidence for considerable latitudinal and longitudinal displacement prior to accretion (e.g. Monger & Ross, 1971; Jones et al., 1977; Mihalynuk et al., 1994; Belasky et al., 2002; Johnston, 2008; Kent & Irving, 2010; Beranek & Mortensen, 2011). However, the relationships between these terranes, and their relative positionings throughout the late Paleozoic and Mesozoic prior to accretion remain poorly constrained and contentious.

As the Stikine Terrane approached ancestral North America in the Late Triassic, a sedimentary basin developed to the east of the terrane termed the Whitehorse Trough (English & Johnston, 2005; Colpron et al., 2015; George et al., 2021). Basaltic volcanics were deposited on top of the Stikine Assemblage basement in the Carnian, alongside associated sedimentary deposition, and formed the Stuhini Group in British Columbia, as well as the coeval Lewes River Group in Yukon (Tempelman-Kluit, 1979; Hart, 1997; English & Johnston, 2005; Colpron et al., 2015; George et al., 2021). Arc construction and subsequent erosion produced volcaniclastic material that was delivered into a shallow marine shelf on the western margin of the basin (Tempelman-Kluit, 1979; Hart, 1997). The carbonate Sinwa Formation in British Columbia caps the volcano-sedimentary rocks of the Stuhini Group and is interpreted as Norian to Rhaetian deposition in the nascent Whitehorse Trough (Figure 2.1; e.g. Souther, 1971; Gabrielse, 1998; English et al., 2005; Mihalynuk et al., 2017). The dominantly limestone Hancock Member of the Aksala Formation in Yukon is considered to be correlative with the Sinwa Formation based on similarities in age and lithology (Figure 2.1; e.g. Hart, 1997; Mihalynuk, 1999; Lowey et al., 2009). The TJB is typically represented by a disconformity in the Whitehorse Trough, with overlying Early Jurassic siliciclastic deposition having formed the Inklin Formation in British Columbia, and the Tanglefoot Formation or the Richthofen Formation in Yukon (Figure 2.1; e.g. Hart, 1997; Lowey et al., 2009).

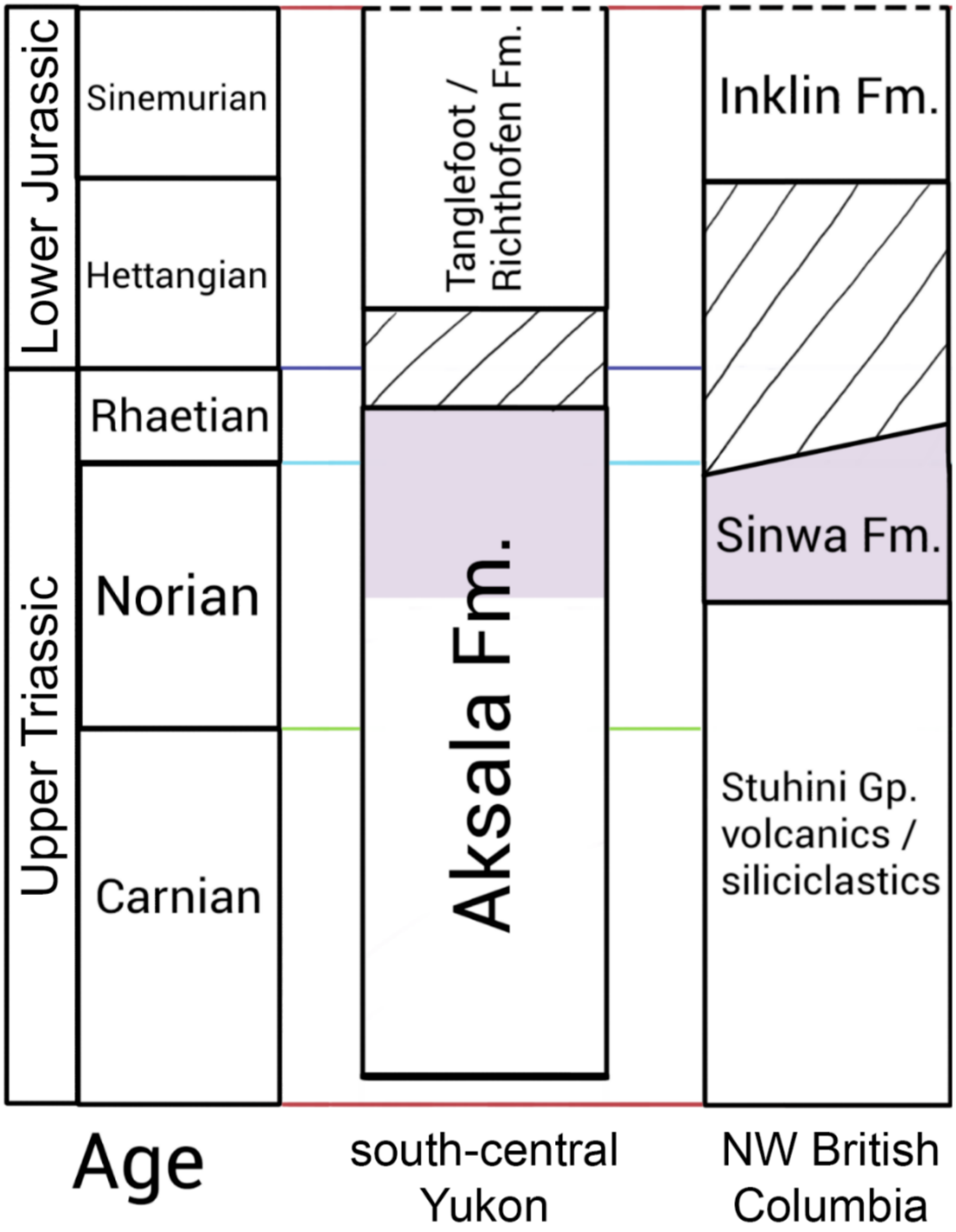

Figure 2.1: Chronostratigraphy across the Whitehorse Trough with stratigraphy of interest shaded in purple. Compiled from Lowey et al. (2009) for south-central Yukon and English et al. (2005) for northwestern British Columbia.

Gabrielse (1998) describes the Sinwa Formation around the Dease Lake area as limestone that is generally massive and non-fossiliferous, commonly exhibiting recrystallization and 20 – 75 m thick. Further northwest, Mihalynuk et al. (2017) describes the Sinwa Formation south of Atlin Lake similarly but at least 2 km thick, and host to zones of nodular chert. Mihalynuk et al. (2017) interprets the Sinwa Formation as being formed in two major depositional cycles, with the first cycle progressively grading from fine-grained siliciclastics into fossiliferous limestone up-section, capped by a distinct and traceable horizon of colonial coral packstone identified as *Retiophyllia* sp. The second cycle begins with this limestone being abruptly overlain by dark grey siliciclastics (Mihalynuk et al., 2017).

Two stratigraphic sections through the Sinwa Formation on Mount Sinwa were investigated for the present study, located approximately 3.5 km apart along strike (Figures 2.2A, B). Mount Sinwa is located approximately 80 km south-southwest of Atlin, British Columbia (Figure 2.2A), a region of Stikine Terrane affinity, with the Sinwa Formation therein representing Panthalassan marine deposition to the west of Pangea (Figure 2.2C). The base of the Sinwa East section is at 58°51’48.604” N, 133°18’54.593” W, and the base of the Sinwa West section is at 58°52’40.503” N, 133°22’13.539” W (Figures 2.2A, B). The Sinwa Formation on Mount Sinwa has previously been broadly described by Mihalynuk et al. (2017), but the present study marks the first detailed paleontological investigation conducted on Mount Sinwa, and the first detailed geochemical investigation of the Sinwa Formation at any locality.

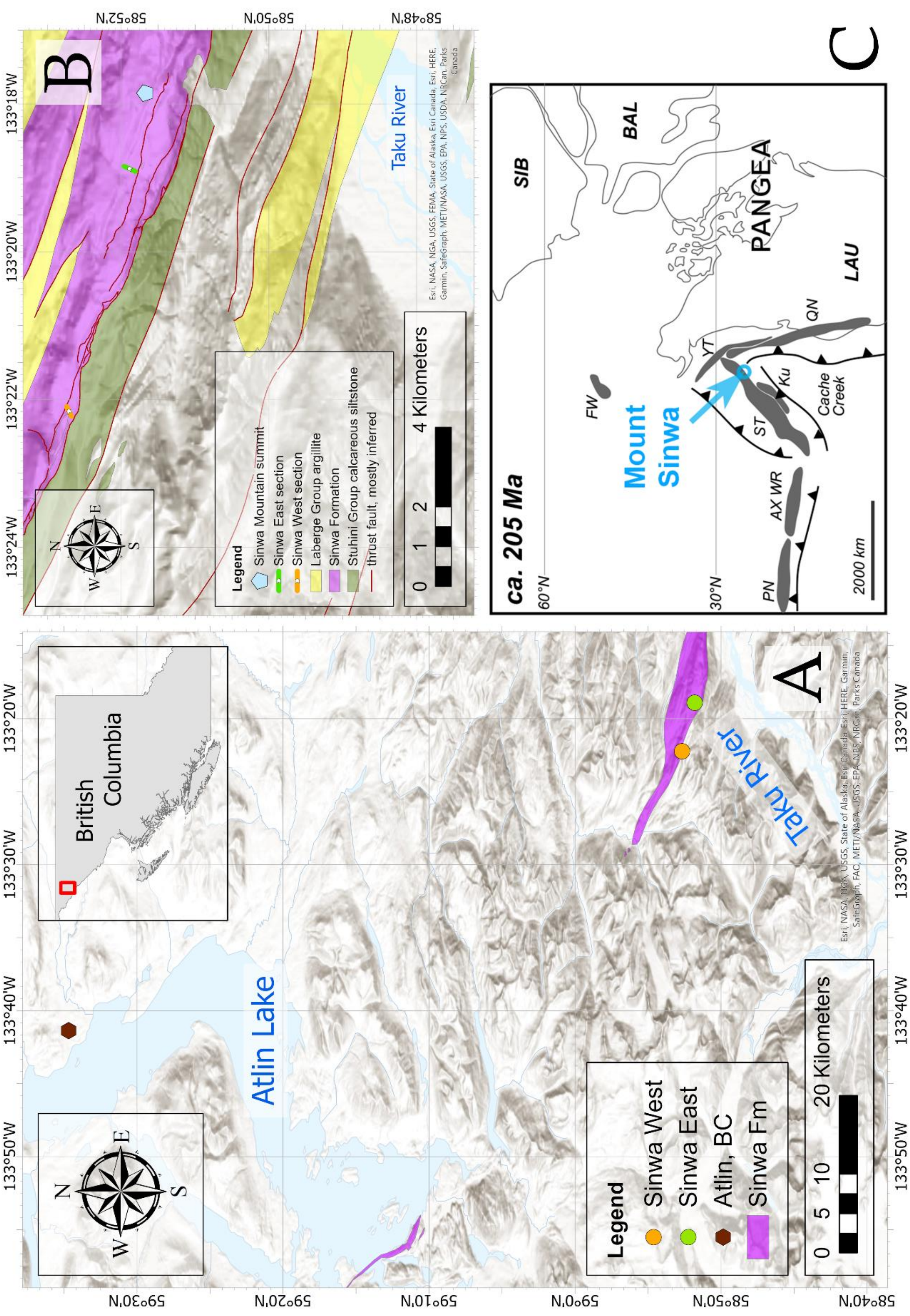
A
Atlin Lake
Taku River
British Columbia
Legend
Sinwa West
Sinwa East
Atlin, BC
Sinwa Fm
0 5 10 20 Kilometers
133°50'W
133°40'W
133°30'W
133°20'W
59°30'N
59°20'N
59°10'N
59°0'N
58°50'N
58°40'N
Esri, NASA, NGA, USGS, State of Alaska, Esri Canada, Esri, HERE, Garmin, SafeGraph, FAO, METI/NASA, USGS, EPA, NPS, NRCan, Parks Canada
B
Taku River
Legend
Sinwa Mountain summit
Sinwa East section
Sinwa West section
Laberge Group argillite
Sinwa Formation
Stuhini Group calcareous siltstone
thrust fault, mostly inferred
0 1 2 4 Kilometers
133°24'W
133°22'W
133°20'W
133°18'W
58°52'N
58°50'N
58°48'N
Esri, NASA, NGA, USGS, FEMA, State of Alaska, Esri Canada, Esri, HERE, Garmin, SafeGraph, METI/NASA, USGS, EPA, NPS, USDA, NRCan, Parks Canada
N
E
S
W
C
ca. 205 Ma
60°N
30°N
SIB
BAL
PANGEA
LAU
FW
YT
QN
Ku
ST
Cache Creek
Mount Sinwa
AX WR
PN
2000 km

Figure 2.2: A: Locations of the Sinwa East and Sinwa West sections on Mount Sinwa in northwestern British Columbia. B: Sinwa East and Sinwa West on geological map of Mount Sinwa from Mihalynuk et al. (2017), with arrows pointing up section. C: Paleogeographic reconstruction of the Rhaetian with a focus on the allochthonous terranes of the North American Cordillera from George et al. (2021). The approximate paleogeographic position of Mount Sinwa in the northern Stikine Terrane is circled in blue.

2.4. Materials and methods

2.4.1. Fieldwork

Across both stratigraphic sections, 4 – 5 cm diameter samples for stable isotope, major element, minor element, and trace element analyses were taken every meter as outcrop allowed, avoiding veins, silicification, coarsely recrystallized zones, and bioclasts where possible. Approximately 2 kg samples for conodonts were taken as well, concentrating on fossiliferous beds and at lithological shifts, with sampling every ~10 m across the rest of the two sections. Samples for Re–Os dating were taken near the top of each section, where limestone tended to be the most organic-rich, avoiding heavily veined and fissile beds. For Sinwa East, 10 Re–Os samples of 100 g each were taken across 1.17 m along strike and within a 0.48 m interval of stratigraphic height. For Sinwa West, 12 samples of 100 g each were taken across 2.90 m along strike and within a 0.36 m interval of stratigraphic height.

2.4.2. Thin section preparation

A total of 14 samples across the two sections were prepared into 30-microns-thick standard thin sections for petrographic analysis, representing the full range of lithofacies observed. Thin section preparation was conducted by Vancouver Petrographics Ltd. in Langley, British Columbia.

2.4.3. Conodont separation

Samples for conodonts were processed at the Geological Survey of Canada - Pacific in Vancouver, British Columbia. Individual samples were crushed into approximately 3 cm fragments before being dissolved in acetic acid for 10 – 14 days (Stone, 1987). Per 1 kg of sample, a solution of 6 L of water, 3.2 L of 10 – 15% acetic acid (to create a buffer), and 0.8 – 1 L of 99.5% glacial acetic acid was used (Stone, 1987). The residues that remained after treatment were then sieved to collect the 90 – 850 μm fraction (Stone, 1987). The isolated fraction was then rinsed, dried, and put through heavy liquid separation using sodium polytungstate (specific gravity of 2.85 kg/L) with the heavy fraction collected (Stone, 1987). Conodont images were taken with a Hitachi TM3000 scanning electron microscope at the Geological Survey of Canada, Pacific Division, in Vancouver.

2.4.4. Re–Os dating

Re–Os samples were polished, dried, and crushed into a 30 μm powder in a metal-free process to avoid contamination. The powders were then digested in a CrO_3-H_2SO_4

solution, which preferentially incorporates hydrogenous Re and Os (sourced from seawater), resulting in less scatter and more robust isochrons (Selby and Creaser, 2003; Rooney et al., 2011). Re and Os were purified from the acid solution with $CHCl_3$ solvent extraction, micro-distillation, and anion chromatography. Re and Os were then loaded onto Ni and Pt filaments, respectively. Isotopic measurements were made at the Yale University Geochemistry and Geochronology Center on a Thermo Scientific Triton-Plus multi-collector thermal ionization mass spectrometer. Static Faraday collection was used for Re, and ion counting using a secondary electron multiplier in peak-hopping mode was used for Os. Uncertainty calculation follows prior studies (Rooney at al., 2011, 2014). Re–Os isochron plots are included in the supplementary figures.

2.4.5. Major, minor, and trace element analysis

For multi-element analysis, samples were cut into 1.2 cm thick slabs, perpendicular to bedding when visible. The slabs were microdrilled using a carbide burr to extract approximately 60 mg of powder per sample, preferentially from fine grained matrix and avoiding veins, bioclasts, and weathered surfaces. These powders were acidified with acetic acid buffered with ammonium hydroxide to a pH of 5 at a 1:1 acid to sample ratio, using 6 – 8 mg of powder per sample. The samples were agitated for 4 hours in an ultrasonicator, then centrifuged at 2500 rpm for 30 minutes. Acid solution for analysis was extracted without remobilizing the insoluble residues, and diluted with 2% nitric acid to a dilution factor of 1:40 000 (solid sample to final solution). Calibration standards were diluted to matrix-match the typical elemental concentrations of natural samples. Multi-element analysis for a broad suite of major, minor, and trace element abundances was conducted at the University of Victoria on an Agilent 8800 inductively coupled plasma mass spectrometer in single quadrupole, no gas mode. Elements Rh, In, and Re were added on-line during analysis as internal standard elements. External calibration was conducted by serial dilutions of mixed element standards prepared in-house from single element stock solutions. As sample preparation involved partial dissolution to avoid leaching from non-carbonate components, minor and trace element abundances were normalized to both Ca and Mg concentrations for mixed dolostone-limestone samples (Sinwa East: 8, 13, 29.6, 34 m from base) and Ca concentrations for limestone samples (all other samples) in order to calculate elemental abundances of just the dissolved calcite and dolomite portions. Precision of repeated measurements of drift solutions prepared from a mixture of natural samples in each individual run is calculated to be between 1.6 – 2.2% (1σ) for Sr/Ca and between 1.4 – 4.0% (1σ) for Mn/Ca. Accuracy and precision was assessed by repeated analysis of National Research Council of Canada (NRCC) reference material SLRS-5. Measurements for Sr/Ca of SLRS-5 were calculated to be 0.00535 ± 0.0002 (1σ), compared to the NRCC certified value of 0.00510 ± 0.0002 (1σ). Measurements for Mn/Ca of SLRS-5 were calculated to be 0.000401 ± 0.00002 (1σ), compared to the NRCC certified value of 0.000412 ± 0.00002 (1σ).

2.4.6. $^{87}Sr/^{86}Sr$ analysis

Powder microdrilling for $^{87}Sr/^{86}Sr$ analysis was conducted in the same manner as for multi-element analysis, but in larger quantities of approximately 250 mg per sample. Powders of 100 – 250 mg per sample were acidified in concentrated HF-HNO_3-$HClO_4$ at

190°C in high-pressure polytetrafluoroethylene bombs (Fourny et al., 2016). Following digestion, Sr isolation was conducted by passing the samples in solution twice through a resin column of Sr.Spec extraction chromatographic material (Deniel & Pin, 2001). Measurements for $^{87}Sr/^{86}Sr$ was conducted at the University of British Columbia Pacific Centre for Isotopic and Geochemical Research on a Nu thermal ionization mass spectrometer. Measurements were normalized internally to a ratio of 0.1194 using an exponential correction. Measurements were also normalized with repeated analysis of National Institute of Standards and Technology (NIST) standard SRM 987. Measurements for $^{87}Sr/^{86}Sr$ of SRM 987 were calculated to be 0.710266 ± 0.000010 (1σ), compared to the NIST certified value of 0.71034 ± 0.00013 (1σ).

2.4.7. Carbonate $\delta^{13}C$ and $\delta^{18}O$ analysis

For the measurement of $\delta^{13}C$ and $\delta^{18}O$ values of carbonate, powder microdrilling was conducted in the same manner as for mutli-element analysis. The drilled powders were then weighed into glass vials (approximately 0.5 mg per sample) and heated at 90°C for 12 hours to remove any moisture, then acidified with 100% phosphoric acid under a helium flushed headspace. Values of $\delta^{13}C$ and $\delta^{18}O$ from Sinwa East carbonates were measured at the University of British Columbia Pacific Centre for Isotopic and Geochemical Research on a Delta PlusXL mass spectrometer with a Finnigan Gas Bench front end. Measurements were corrected with repeated analysis of internal standards BN 13, BN 83-2, and H6M, which have been calibrated against International Atomic Energy Agency (IAEA) standards IAEA-NBS 18 and IAEA-NBS 19. A total of 47 natural samples were measured twice on the Delta PlusXL, with the difference between measurements being within 0.26‰ or better for $\delta^{13}C$ excluding three outliers (difference of 0.36, 0.48, 0.54‰), and within 0.79‰ or better for $\delta^{18}O$ excluding three outliers (difference of 0.96, 1.06, 1.47‰). Values of $\delta^{13}C$ and $\delta^{18}O$ from Sinwa West carbonates were measured at the University of Victoria on a Sercon 20-22 gas-source continuous-flow isotope ratio mass spectrometer with a GasBox II front end. Measurements were corrected with repeated analysis of IAEA standards IAEA-CO-8 and IAEA-603, with internal standard VTS used as a monitoring standard. Precision of repeated measurements of VTS on the Sercon 20-22 is calculated to be within 0.09‰ (1σ) for $\delta^{13}C$, and within 0.29‰ (1σ) for $\delta^{18}O$. Precision of repeated measurements of IAEA-CO-8 on the Sercon 20-22 is calculated to be -5.70 ± 0.09‰ (1σ) for $\delta^{13}C$, and -22.68 ± 0.34‰ (1σ) for $\delta^{18}O$, compared to the IAEA certified value of -5.764 ± 0.032‰ (1σ) for $\delta^{13}C$, and -22.7 ± 0.2‰ (1σ) for $\delta^{18}O$.

2.4.8. Organic $\delta^{13}C$ analysis

Samples for $\delta^{13}C_{org}$ analysis were ground to powder with a vibrating cup pulverizer. Organic separation was conducted by acidifying approximately 1 g of powder per sample with 10 mL of 6 M hydrochloric acid and centrifuged at 2500 rpm for 4 minutes before decanting the supernatant. This acid rinse was repeated until no more carbonate dissolution was visible (typically three cycles), then the remaining insoluble residue was cleaned with deionized water. Organic $\delta^{13}C$ measurements were conducted at the University of British Columbia Pacific Centre for Isotopic and Geochemical Research on a Delta PlusXL mass spectrometer in continuous flow mode with a thermal combustion elemental analyzer front end. Measurements were corrected for instrument fractionation with repeated analysis of internal standards Mess-1, BCSS-1, and acetanelide, which have been calibrated against IAEA standards IAEA-NBS 18 and IAEA-NBS 19. A total of 18 natural samples were measured twice, with the difference between measurements being within 0.35‰ or better, excluding two outliers (difference of 0.55, 0.88‰).

2.5. Results

2.5.1. Lithology

The limestone classification scheme of Dunham (1962), modified by Embry and Klovan (1971), is used for all field lithological descriptions, while the classification scheme of Folk (1959) is used for all thin section lithological descriptions.

Facies 1

Facies 1 consists of grey weathering, massive to bedded mudstone, wackestone, and floatstone. Bivalve wackestone and floatstone are common, with intact shells being typically 20 – 30 mm across. Many mudstone portions lack bioclasts entirely, and bioclasts tend to be only variably present even within an individual fossiliferous bed. A single 3.6 m thick horizon of coral floatstone is observed in Sinwa East, with the coral fragments being 1 – 10 mm in diameter. This facies in Sinwa West differs from Sinwa East in exhibiting silicification (dark grey silicified protrusions, possibly being shelly and tubular bioclasts) and recrystallization, both of which generally increase in prevalence up-section. Thin section analysis indicates Facies 1 consists of a mix of micrite, intrabiomicrite, and intrapelbiomicrite, with bivalve and bryozoan bioclasts common (Figure 2.4A–B).

Facies 2

Facies 2 consists of massive to bedded mudstone, wackestone, and floatstone with carbonate mud chip rip-up clasts which are typically 1 – 3 mm across but can be larger, angular to sub-angular, and paler in colour than the grey limestone matrix (Figure 2.3A). Several horizons of interbedded limestone and dolostone can be observed but are not extensive and largely restricted to the lower portions of the Sinwa East section. Alternations between dolostone-limestone units occur every 1 – 3 m, with bedding 10 – 20 cm thick. Only minor dolostone horizons occur higher in the stratigraphy, varying between 20 – 75 mm thick. Laminations are common, 1 – 2 mm thick in the bedded units and can be locally convoluted (Figure 2.3B). The localized nature of these structures indicates they were formed by soft sediment deformation, likely sediment loading or dewatering. It is also possible that some of these structures could be microbial. Like Facies 1, bivalve wackestone is common, with many mudstone portions lacking bioclasts entirely. Facies 2 is only observed in Sinwa East. Thin section analysis indicates Facies 2 consists of a mix of micrite and intrabiomicrite petrographically, with bivalve bioclasts common (Figure 2.4C–D).

Facies 3

Facies 3 consists of grey bivalve coral wackestone, floatstone, and packstone, distinguished from Facies 1 and 2 by its higher bioclastic content. Bedding is present, but not as clearly as in Facies 1 and 2. Between 163.8 m to 165.5 m above the base of Sinwa East, minor interbedded limestone/dolostone is observed. Beds in this horizon are 20 – 40 mm thick. The bivalve and solitary coral bioclast content progressively increases up-section. Intact bivalves are typically 20 – 30 mm across. Coral fragments are highly variable in size but rarely exceed 10 mm. Facies 3 also exhibits silicification, the degree of which increases up-section, observed as protruding dark brown/grey weathering bioclasts, chert layers 60 – 220 mm thick, and round chert nodules 140 mm to 0.5 m in diameter (Figure 2.3C–D). This facies in Sinwa West differs from Sinwa East by featuring brown weathering, clearer bedding and laminations (as fine as mm scale), smaller fragmented pale white shelly bioclasts aligned with bedding (up to 1 cm across), and by lacking coral bioclasts. Thin section analysis indicates Facies 3 consists of biomicrite (pelbiomicrite in Sinwa West), with a wide variety of bioclasts present that include bryozoans, corals, gastropods, bivalves, and crinoids (Figure 2.4E–F). The matrix of Facies 3 is considerably darker than other facies, including other biomicrite, likely indicating higher organic content (Figure 2.4E–F).

Facies 4

Facies 4 consists of in-situ colonial coral boundstone in Sinwa East (Figure 2.3E), and dark grey, bedded, coral floatstone with discontinuous patches of coral boundstone 5 –

30 cm across in Sinwa West. Coral bioclasts are uncommonly silicified, and coarse recrystallization is not observed. Thin section analysis of inter-coral areas indicates those portions of Facies 4 consists of biomicrite (mix of micrite and biointramicrite in Sinwa West), with a wide variety of bioclasts present including bryozoans, corals, gastropods, bivalves, and crinoids.

Facies 5

Facies 5 consists of recessive, dark, finely laminated, fissile shale. High organic content is indicated by both the dark colour and fetid smell. There is a sharp transition from Facies 4 to Facies 5 in Sinwa East, while the shift is more gradational in Sinwa West, expressed as 0.5-meter interbeds of Facies 4 wackestone and Facies 5 shale (Figure 2.3F).

Facies 6

Facies 6 consists of massive to weakly bedded mudstone. No clear bioclasts are observed macroscopically. This facies weathers pale beige-grey, possibly as a result of pervasive recrystallization. Weak silicification expressing as dark grey veins and minor tubular protrusions (possibly bioclasts) becomes more common up-section. Facies 6 is only observed in Sinwa West.

Sinwa East lithological facies

The 231.3 m thick Sinwa East section can be subdivided into 5 distinct lithological facies (Figure 2.6). The first 105 m of the section alternates between Facies 1 and Facies 2. The span from 105 m to 210 m is dominated by Facies 3. Between 163.8 m and 165.5 m above the base, minor interbedded limestone/dolostone is observed. Beds in this horizon are 20 – 40 mm thick. The upper portion of Facies 3 progressively grades into Facies 4 which dominates the interval from 221.1 m to 231.3 m above the base of the section. Above 231.3 m Facies 5 occurs, and continues to the top of the section.

Sinwa West lithological facies

The 163.5 m thick Sinwa West section can be subdivided into 5 distinct lithological facies (Figure 2.7). The first 54 m of the section is dominated by Facies 6, alongside significant portions of Facies 1; a single 75 cm thick bed of Facies 3 is observed at 40 m from the base. The span from 54 m to 143.75 m is almost entirely Facies 1, with 136.75 m to 143.75 m representing a transitional interval into Facies 4, exhibiting strong silicification, lack of visible recrystallization, and patches of dark grey, fetid limestone. The span from 146 m to 163 m consists of Facies 4 with interbeds of Facies 5. The uppermost portion of the section at 163 m to 163.5 m consists of Facies 3.

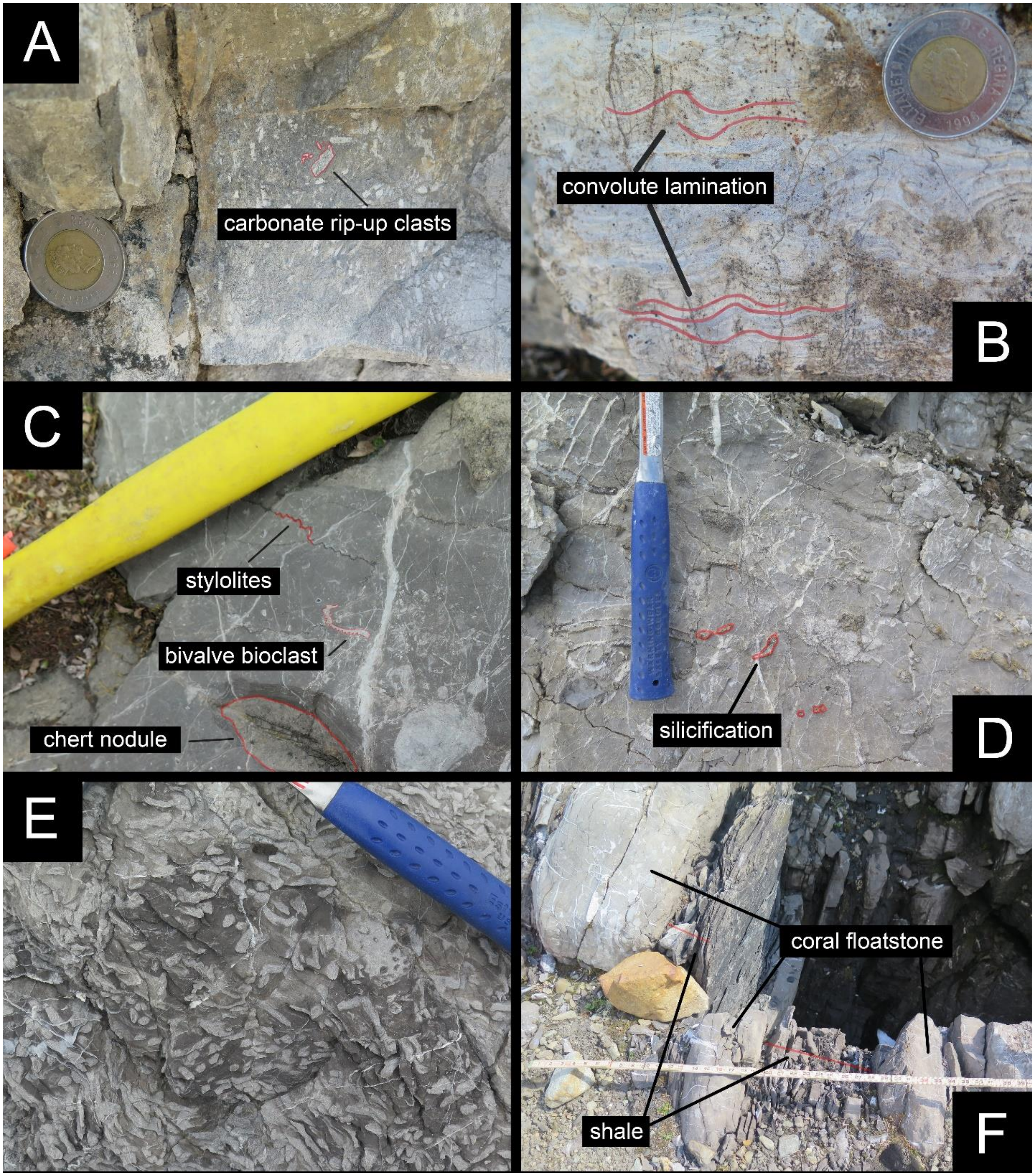

Figure 2.3: Diagnostic features across the lithological facies observed in the Sinwa East and Sinwa West stratigraphic sections. A: Facies 2, 30 m from base of Sinwa East. Pale grey carbonate mud chip rip-up clasts 3 – 10 mm across (particularly large), in a

darker grey micrite matrix. B: Facies 2, 34 m from base of Sinwa East. Convolute lamination. C: Facies 3, 118 m from base of Sinwa East. Bivalve floatstone with calcite veins and a chert nodule. D: Facies 3, 141 m from base of Sinwa West. Dark silicified clasts of various shape weathering out from the matrix. E: Facies 4, 226 m from base of Sinwa East. Coral boundstone. F: Facies 4 and 5, 153 m from base of Sinwa West. Interbedded coral floatstone and fissile shale.

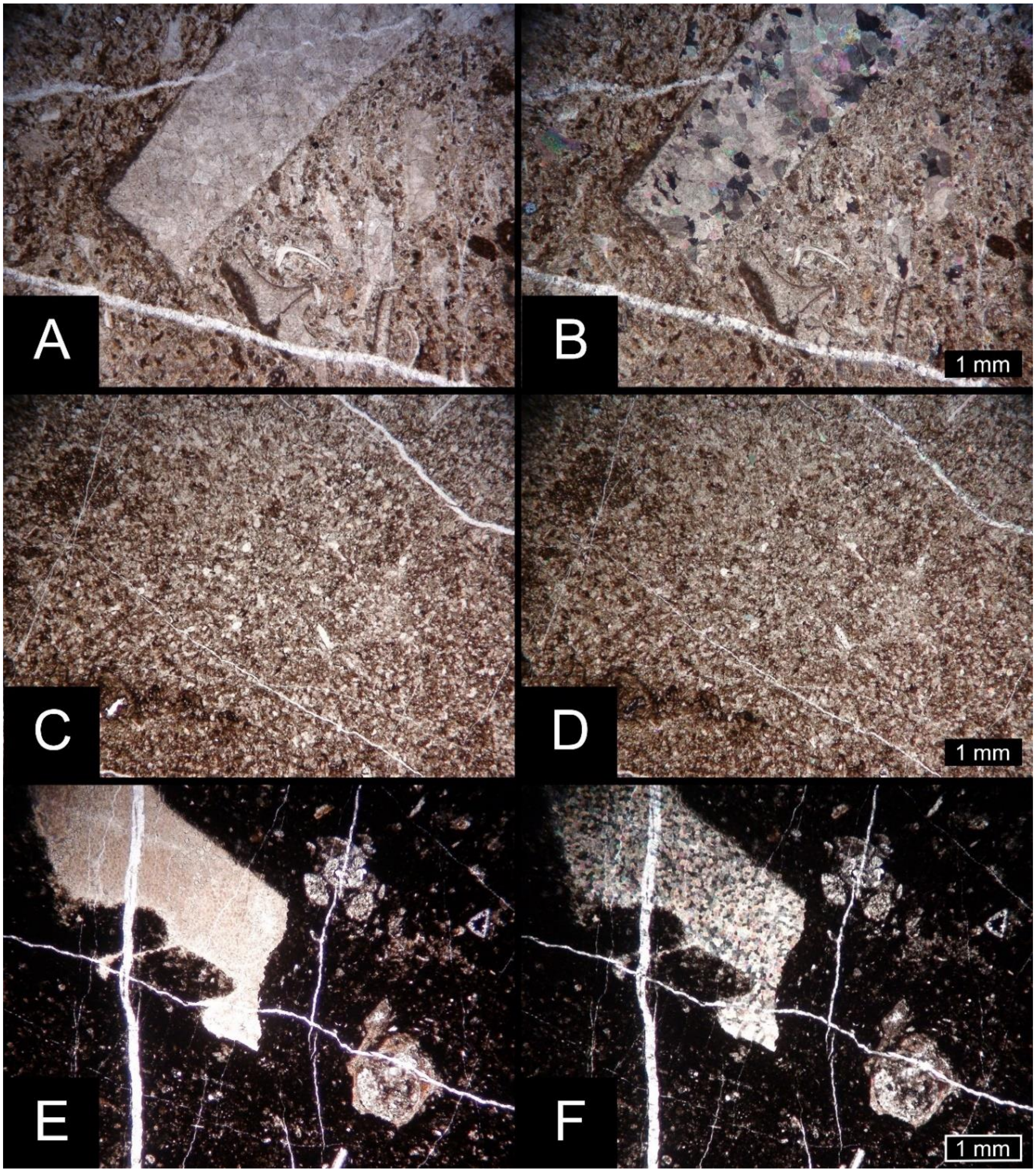

Figure 2.4: Thin sections representing the range of petrographic micro-characteristics observed across the Mount Sinwa sections. A–B: Intrapelbiomicrite in PPL and XPL, Facies 1, 0 m from base of Sinwa East. C–D: Micrite in PPL and XPL, Facies 2, 72 m from base of Sinwa East. E–F: Biomicrite in PPL and XPL, Facies 3, 118 m from base of Sinwa East.

2.5.2. Paleontology

Conodonts belonging to eight different species of the genus *Mockina* were recovered from the Sinwa Formation on Mount Sinwa (Figure 2.5). *Mockina* cf. *englandi* (Orchard, 1991a) is found spanning the entire range of productive samples from Sinwa East, 5–231 m above the base of the section. In the lower 100 m or so of Sinwa East, *Mo.* cf. *englandi* is joined by *Mockina postera* (Kozur & Mostler, 1971) at 42 m from the base of the section, the only occurrence of that species in both sections. Both *Mockina carinata* (Orchard, 1991a) and *Mockina* cf. *spiculata* (Orchard, 1991a) begin to occur at 106 m from the base of Sinwa East, and persist to the top of the section at 231 m. Next, *Mo. englandi* (Orchard, 1991a) has been recovered from 112–231 m above the base of Sinwa East, whereas *Mockina bidentata* (Mosher, 1968) occurs from 114–231 m above the base of the section. *Mockina spinosa* (Orchard, 2018) is found in Sinwa East ranging 164–211 m from the base of the section. Restricted to the upper portion of Sinwa East, *Mockina mosheri* (Kozur & Mostler, 1976) morphotype B has been recovered at 211–231 m from the base of the section. The lowest productive sample from the Sinwa West section at 138 m from the base marks the only occurrence of *Mo*. cf. *spiculata* in the section, as well as the lowest occurrence of *Mo*. cf. *englandi* which persists to the uppermost portion of the section at 163 m. In Sinwa West, both *Mo. carinata* and *Mo*. *mosheri* morphotype B are only recovered at 146 m from the base of the section. *Mo. spinosa* is found at Sinwa West 163 m from the base of the section.

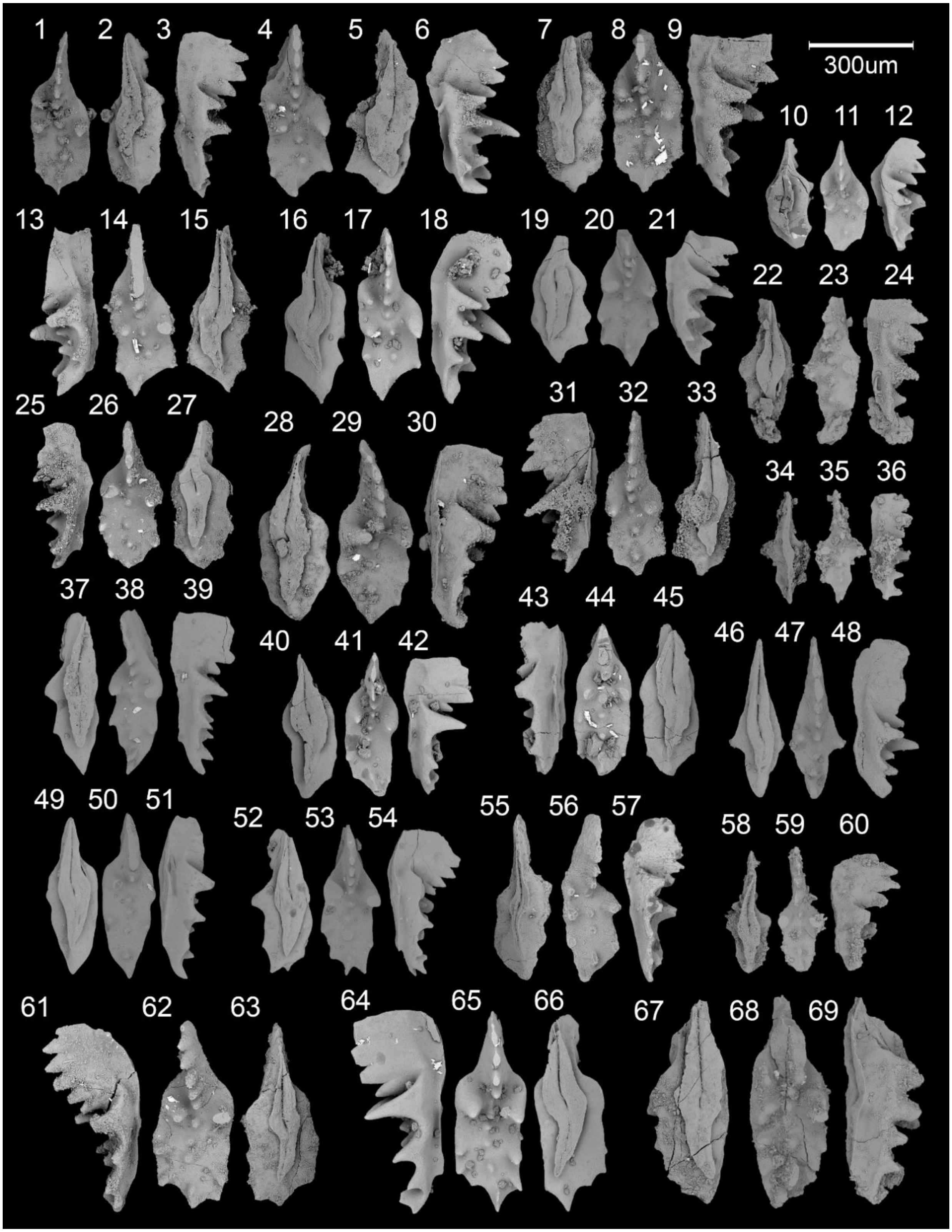
1
2
3
4
5
6
7
8
9
300um
10
11
12
13
14
15
16
17
18
19
20
21
22
23
24
25
26
27
28
29
30
31
32
33
34
35
36
37
38
39
40
41
42
43
44
45
46
47
48
49
50
51
52
53
54
55
56
57
58
59
60
61
62
63
64
65
66
67
68
69

Figure 2.5: Conodont specimens recovered from the Sinwa Formation on Mount Sinwa.

1–18: *Mockina carinata* (Orchard, 1991a). 1–6: GSC 139647, from sample GSC Cur. No. V-003826, 114 m from base of Sinwa East, late Norian. 7–9: GSC 139648, from sample GSC Cur. No. V-003829, 127 m from base of Sinwa East, late Norian. 10–12: GSC 139649, from sample GSC Cur. No. V-003833, 188 m from base of Sinwa East, late Norian. 13–15: GSC 139650, from sample GSC Cur. No. V-003830, 164 m from base of Sinwa East, late Norian. 16–18: GSC 139651, from sample GSC Cur. No. V-003834, 231 m from base of Sinwa East, late Norian.

19–21, 31–33: *Mockina* cf. *englandi* (Orchard, 1991a). 19–21: GSC 139652, from sample GSC Cur. No. V-012698, 138 m from base of Sinwa West, late Norian. 31–33: GSC 139653, from sample GSC Cur. No. V-003825, 112 m from base of Sinwa East, late Norian.

22–24, 34–36, 46–48, 58–60: *Mockina bidentata* (Mosher, 1968). 22–24: GSC 139654, from sample GSC Cur. No. V-003826 sample, 114 m from base of Sinwa East, late Norian. 34–36: GSC 139655, from sample GSC Cur. No. V-012683, 205 m from base of Sinwa East, late Norian. 46–48: GSC 139656, from sample GSC Cur. No. V-003834, 231 m from base of Sinwa East, late Norian. 58–60: GSC 139657, from sample GSC Cur. No. V-012679, 231 m from base of Sinwa East, late Norian.

25–30: *Mockina englandi* (Orchard, 1991a). 25–27: GSC 139658, from sample GSC Cur. No. V-003825, 112 m from base of Sinwa West, late Norian. 28–30: GSC 139659, from sample GSC Cur. No. V-003828, 120 m from base of Sinwa East, late Norian.

37–45, 49–51: *Mockina mosheri* (Kozur & Mostler, 1976) morphotype B sensu (Carter & Orchard, 2007). 37–39: GSC 139660, from sample GSC Cur. No. V-012681, 211 m from base of Sinwa East, late Norian. 40–45: GSC 139661, from sample GSC Cur. No. V-003834, 231 m from base of Sinwa East, late Norian. 49–51: GSC 139662, from sample GSC Cur. No. V-012699, 146 m from base of Sinwa West, late Norian.

52–54, 61–66: *Mockina* cf. *spiculata* (Orchard, 1991a). 52–54: GSC 139663, from sample GSC Cur. No. V-012698, 138 m from base of Sinwa West, late Norian. 61–63: GSC 139664, from sample GSC Cur. No. V-003824, 106 m from base of Sinwa East, late Norian. 64–66: GSC 139665, from sample GSC Cur. No. V-003824, 231 m from base of Sinwa East, late Norian.

55–57: *Mockina postera* (Kozur & Mostler, 1971). GSC 139666, from sample GSC Cur. No. V-003820, 42 m from base of Sinwa East, middle Norian.

67–69: *Mockina spinosa* (Orchard, 2018). GSC 139667, from sample GSC Cur. No. V-003830, 164 m from base of Sinwa East, late Norian.

2.5.3. Geochemistry

2.5.3.1. Sinwa East geochemical data

In Sinwa East, Re–Os radiometric dating of Facies 4 coral boundstone at 231 m above the base of the section results in 208.3 ± 3.8 Ma (2σ) proximal to the lowermost occurrence of Facies 5 shale (Figure 2.6).

Sr abundances across Sinwa East are notably high for limestone with an average of 2557 ppm and 98% of the 58 total samples above 950 ppm (Figure 2.6). Sr concentrations are particularly high in the uppermost portion of Sinwa East, averaging 4388 ppm across 171–231 m from the base of the section (Figure 2.6). Mn concentrations are generally low Sinwa East, predominantly lower than 60 ppm (81% of 58 total samples) with an average of 48 ppm (Figure 2.6). Together these results demonstrate low Mn/Sr ratios, with an average of 0.063 mol/mol and 90% of 58 total samples lower than 0.05 mol/mol (Figure 2.6). Higher Mn/Sr ratios are observed in the four dolomitic samples from the lower portion of the section (8, 13, 29.6, 34 m), with an average of 0.26 mol/mol (Figure 2.6). With a total of 12 samples, a gradual increase is observed in the $^{87}Sr/^{86}Sr$ ratios across Sinwa East from 0.7077 at the base of the section to 0.7079 at 229 m from the base (Figure 2.6). Three data points deviate from this trend (91, 171, 231 m) by exhibiting lower ratios than expected given the trend (Figure 2.6).

Values of $\delta^{13}C_{carb}$ at Sinwa East predominantly range between 0.5 and 2.5‰ (90% of 193 total data points excluding excursion intervals), with 3 prominent negative excursions of approximately 3‰ magnitude where measurements reach around -1‰ (Figure 2.6). The lowermost excursion is observed at 32–39 m from the base of the section, the next at 60–64 m, and the uppermost at 230–231 m (Figure 2.6). Values of $\delta^{13}C_{org}$ at Sinwa East predominantly range between -28 to -23‰ (90% of 31 total data points) with no clear stratigraphic trends (Figure 2.6).

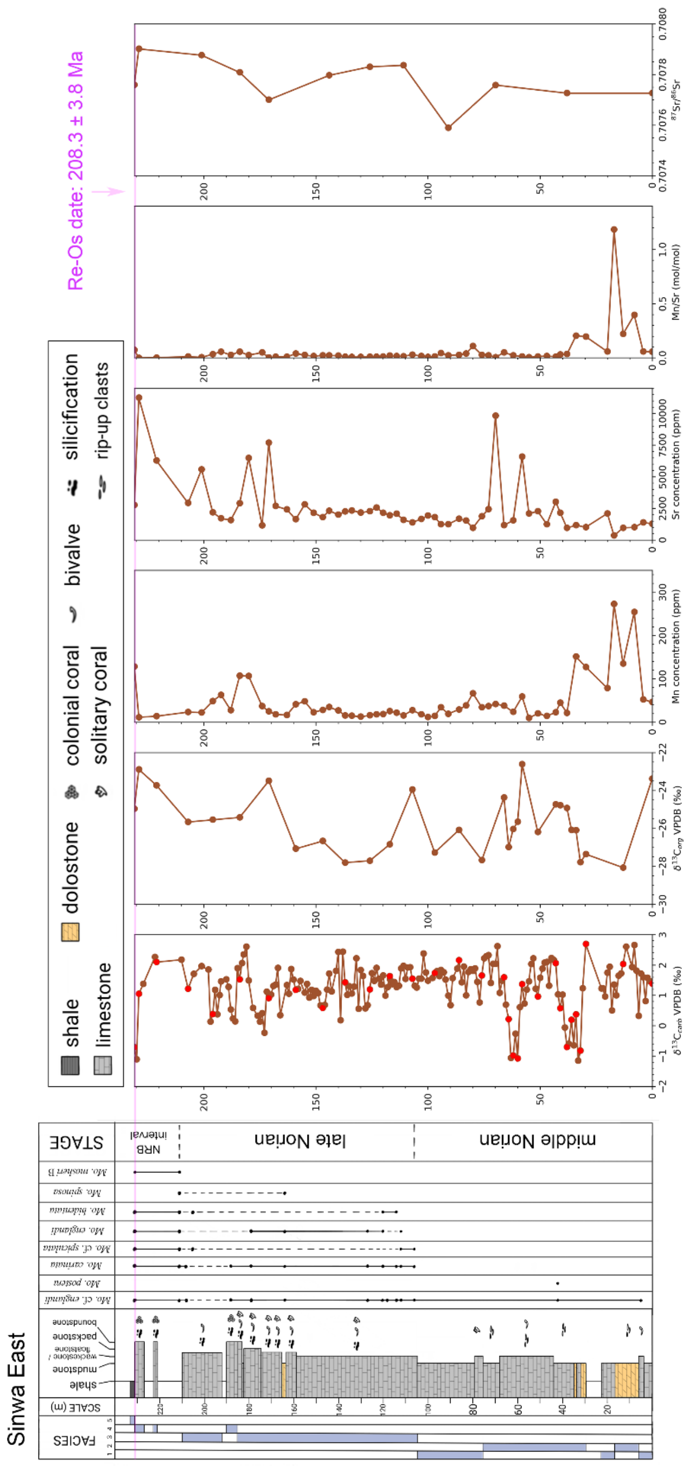

Figure 2.6: Compiled lithostratigraphic, biostratigraphic, geochemical results from the Sinwa East section. Carbonate δ^{13}C measurements which have corresponding organic δ^{13}C measurements conducted on the same sample are highlighted in red.

2.5.3.2. Sinwa West geochemical data

In Sinwa West, Re–Os radiometric dating of Facies 4 coral wackestone at 151 m above the base of the section results in 209.9 ± 5.3 Ma (2σ) proximal to the lowermost occurrence of Facies 5 shale (Figure 2.7).

Sr abundances across Sinwa West are notably high for limestone, with an average of 1492 ppm and 96% of 45 total samples above 600 ppm (Figure 2.7). Sr concentrations are particularly high in the uppermost portions of the section with Sinwa West averaging 3335 ppm across 139–163 m (Figure 2.7). Mn concentrations are generally low across Sinwa West, predominantly lower than 90 ppm (80% of 45 total samples) with an average of 78 ppm (Figure 2.7). Together these results demonstrate low Mn/Sr ratios in the section, with an average of 0.12 mol/mol and 89% of 45 total samples lower than 0.1 mol/mol (Figure 2.7). With a total of 12 samples, the $^{87}Sr/^{86}Sr$ ratios of Sinwa West decrease across the lower portion of the section, from 0.7077 at 4 m from the base of the section to 0.7075 at 40 m (Figure 2.7). Ratios of $^{87}Sr/^{86}Sr$ then remain constant at around 0.7075 across much of Sinwa West, before an increase is observed in the upper portion of the section from 0.7075 at 126 m from the base of the section to 0.7078 at 163 m (Figure 2.7).

Values of $\delta^{13}C_{carb}$ at Sinwa West predominantly range between 1.5 and 3‰ (96% of 147 total data points excluding the base and excursion intervals), with more negative values observed at the base and in 3 prominent negative excursions of approximately

4‰ magnitude (Figure 2.7). The bottom 16 m of the section ranges between around -1.5 and -3‰ (Figure 2.7). The lowermost excursion observed at 45.5–62 m from the base of the section also reaches approximately -2‰ (Figure 2.7). The next excursion is observed at 91–92 m, and the uppermost at 136.75–149 m, both reaching approximately -3‰ (Figure 2.7). Values of the $\delta^{13}C_{org}$ record at Sinwa West predominantly range between -28 to -21‰ (84% of 37 total data points), weakly following excursions in the values of the $\delta^{13}C_{carb}$ record, with $R^2 = 0.199$ between the paired measurements (Figure 2.7).

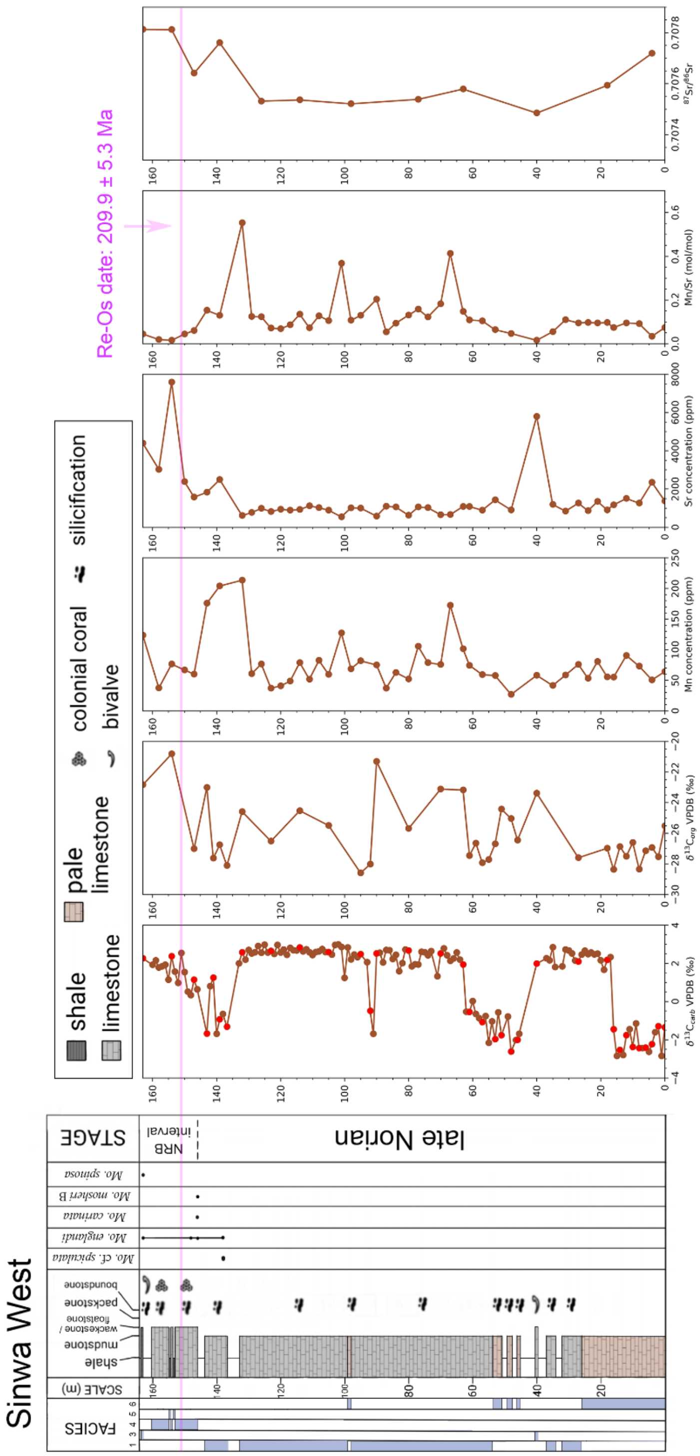

Figure 2.7: Compiled lithostratigraphic, biostratigraphic, geochemical results from the Sinwa West section. Carbonate $\delta^{13}C$ measurements which have corresponding organic $\delta^{13}C$ measurements conducted on the same sample are highlighted in red.

2.6. Discussion

2.6.1. Interpreting paleoenvironmental shifts from lithofacies

The lithofacies preserved on Mount Sinwa are interpreted to represent a range of reefal depositional settings in the Whitehorse Trough forearc basin, consistent with and expanding upon past interpretations of the Sinwa Formation in a multitude of localities (e.g. Tempelman-Kluit, 1979; Hart, 1997; Gabrielse, 1998; Mihalynuk, 1999; Mihalynuk et al., 2017). Due to the prevalence of coarse recrystallization characteristic of Facies 6 in the lower portions of Sinwa West, the lithological trends observed in the Sinwa East section will be the focus of paleoenvironmental interpretations. The progression through the facies of Sinwa East represents depositional environments arranged from landward to basinward (Figure 2.8).

Carbonate rip-up clasts are observed in abundance in the lower portion of Sinwa East, designated Facies 2. These mud chips likely represent semi-consolidated substrate being eroded and redeposited by storm events, which would indicate a depositional environment above storm wave base (e.g. Sepkoski, 1982; Wignall & Twitchett, 1999; Pruss et al., 2005; Woods, 2009). Also, the presence of such features in shallow marine Upper Triassic limestone reflects a conspicuous lack of bioturbation (e.g. Sepkoski, 1982; Wignall & Twitchett, 1999; Pruss et al., 2005; Woods, 2009). A restricted back reef setting would represent an environment with sufficiently shallow water depth for storm events to churn up the substrate while maintaining high enough environmental stress to minimize bioturbation (e.g. Wilson, 1975; Tucker & Wright, 1990). Carbonate deposition in such a restricted setting would be prone to dolomitization via brine reflux (e.g. Adams & Rhodes, 1960; Wilson, 1975; Warren, 2000), which would explain why dolostones are largely limited to the lower portion of Sinwa East.

Fossiliferous wackestone and floatstone of Facies 3 dominate the middle and upper-middle portions of Sinwa East. The presence of intact bioclasts within a micrite matrix observed in this facies is typical of the gentle gradient and high productivity of open circulation back reef settings (e.g. Wilson, 1975). The absence of any grainstones, conglomerates, or breccias argues against a comparatively steeper forereef slope setting, where gravity flow deposits would be expected to dominate (e.g. Wilson, 1975; Tucker & Wright, 1990). This fossiliferous wackestone and floatstone facies grades into patches of coral boundstone towards the upper portion of both Mount Sinwa sections, indicating increasing proximity to the reef crest. The reef crest itself is likely represented by Facies 4, where extensive boundstone would dominate with greater biotic homogeneity (e.g. Wilson, 1975; Tucker & Wright, 1990). Therefore, the progression from Facies 1 through to Facies 4 at Sinwa East is interpreted as representing a gradual marine transgression (Figure 2.8).

The coral boundstone of Facies 4 is overlain by the shale of Facies 5 at the top of both Mount Sinwa sections, reflecting a dramatic change from reef to deeper marine deposition (Figure 2.8; e.g. Wilson, 1975). Carbonate reefs generally have the ability to keep pace with base level changes driven by slow geological processes, such that any apparent reef drowning would require either exceptionally rapid base level rise, or the elevation of environmental stress by other means (e.g. Schlager, 1981). Haq et al. (1988) interpret eustatic sea level to be steady in the late Norian and falling across the NRB, whereas Embry (1988) interprets eustatic sea level to be falling in the late Norian and rising across the NRB. The apparent base level shift preserved in the Sinwa Formation is thus potentially consistent with the eustatic sea level rise at the NRB suggested by Embry (1988) but does not fully corroborate either past study. Regional effects such as basin subsidence, sediment loading, and faulting could also have been the cause of the rapid base level rise observed in the Sinwa Formation. However, no such effects have been recorded elsewhere in the Whitehorse Trough, with Hart (1997) suggesting widespread shallow marine carbonate deposition in the late Norian, followed by the deposition of supratidal and lagoonal siliciclastics in the Rhaetian.

Rather than being a response to base level change, the cessation of reef production across the NRB at Mount Sinwa could have more to do with the elevated environmental stress associated with this boundary (e.g. Hallam, 2002; Sephton et al., 2002; Tanner et al., 2004). Sephton et al. (2002) suggests widespread anoxia at the NRB based on investigation of the Black Bear Ridge section in the Western Canada Sedimentary Basin, which could provide a plausible explanation for both the reef collapse and the subsequent shale deposition on Mount Sinwa, all without necessitating base level changes. It is possible this reef collapse in the Whitehorse Trough could also be related to the suppression of carbonate precipitation more universally characteristic of the following end-Triassic mass extinction interval, which disproportionately impacted aragonite biomineralizing organisms such as the scleractinian corals that had just risen to prominence as framework builders in the Late Triassic (e.g. Stanley, 1988; Hautmann, 2004). However, this carbonate suppression is typically attributed to enhanced volcanic outgassing as a consequence of CAMP emplacement at the end of the Triassic and is therefore difficult to evoke for the NRB (Marzoli et al., 1999, 2004; Blackburn et al., 2013). Although the impact of the end-Triassic mass extinction on reef communities is overwhelmingly interpreted to overshadow that of the NRB, Rhaetian reefs are observed to be considerably smaller, less complex, and less widely distributed than their Norian counterparts (e.g. Flügel & Kiessling, 2002; Rigo et al., 2020). If further investigation into the effects of the disturbance at the NRB on reef communities at a global scale reveals a degree of biomineralization pressure initiated well prior to the end-Triassic, then this phenomenon would require a causal mechanism outside of CAMP emplacement.

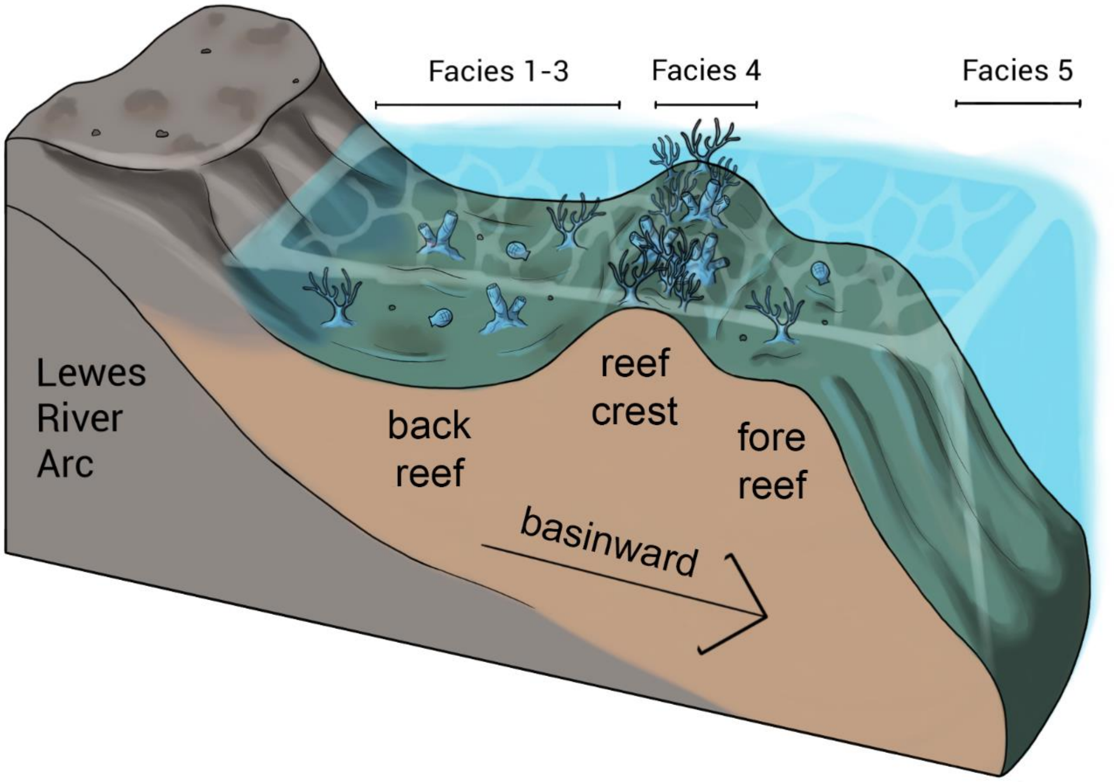

Figure 2.8: Reef zonation representing the depositional settings of Facies 1 through 5 of the Sinwa East stratigraphic section in the context of the Whitehorse Trough forearc basin.

2.6.2. Identifying the Norian/Rhaetian boundary via conodont biostratigraphy

Tethyan conodont pectiniform morphology sees an overall shift near the NRB from the prominent platform denticulation typical of *Mockina* to smaller elements with reduced or absent platforms exemplified by *Misikella* and *Parvigondolella* (e.g. Rigo et al., 2018; Giordano et al., 2010; Karádi et al., 2020). In the Tethys, NRB is defined by the base of the *Misikella posthernsteini* Zone (Krystyn et al., 2007a, b; Krystyn, 2010; Bertinelli et al., 2016; Rigo et al., 2016; Karádi et al., 2020). The morphological trend of platform reduction is also observed in Panthalassa (e.g. Carter & Orchard, 2007; Orchard et al., 2007), but the few rare occurrences of *Mi. posthernsteini* only appear higher in the Rhaetian, occurring together with the Rhaetian ammonite *Choristoceras* (Tipper et al., 1994; Tozer, 1994; Umhoefer & Tipper, 1998). Alternative biomarkers are thus necessary for recognition of the NRB in Panthalassa. One such proposed proxy is the conodont species *Mockina mosheri*, considered to be typically Rhaetian, with the occurrence of the B morphotype being unique in extending slightly older into the latest Norian (Carter & Orchard, 2007; Orchard et al., 2007). This conclusion was reached from the co-occurrence of *Mo. mosheri* with radiolaria of the *Proparvicingula moniliformis* Zone in many localities across western North America (e.g. Carter & Orchard, 2007; Orchard et al., 2007). In southern Italy, the base of the *Pr. moniliformis* Zone is situated between the first occurrences of *Misikella hernsteini* and *Mi. posthernsteini* (Bazzucchi et al., 2005). With radiolarians being more cosmopolitan than conodonts in the Norian and Rhaetian, an indirect correlation between Tethyan and Panthalassan conodont biozonation can therefore be made from radiolarian intercalibration (e.g. Carter & Orchard, 2007; Orchard et al., 2007; Rigo et al., 2018). Specimens of *Mo. mosheri* morphotype B have been recovered from both Sinwa East and Sinwa West. This species is found 20.3 m below the transition to shale facies in Sinwa East (Figure 2.6), and exactly at the transition to shale facies in Sinwa West (Figure 2.7). The First Occurrence (FO) of *Mo. mosheri* morphotype B in the latest Norian is used as a proxy approximating the NRB in both Mount Sinwa sections.

2.6.3. Age of the Norian/Rhaetian boundary and new Re–Os dates

The age of the TJB has been well established at 201.36 ± 0.17 Ma by U–Pb radiometric dating of zircon from tuffs bracketing the boundary in Peru (Wotzlaw et al., 2014), but the same degree of consensus has not been reached for the age of the NRB. Two conflicting interpretations have emerged from efforts to precisely define and date the NRB, with the "long Rhaetian" spanning approximately 8 Myr which places the boundary at around 209 Ma (e.g. Caruthers et al., 2022), and the "short Rhaetian" spanning approximately 4 Myr which places the boundary at around 205 Ma (e.g. Wotzlaw et al., 2014).

The "long Rhaetian" interpretation defines the NRB by the FAD of *Mi. posthernsteini* sensu lato (Krystyn et al., 2007a, b). Supporting this interpretation, magnetostratigraphy of the Steinbergkogel section in Austria dates the NRB as defined by the FAD of *Mi. posthernsteini* sensu lato to be around 209.8 Ma by correlation to the astronomically calibrated Newark Supergroup in eastern North America (Hüsing et al., 2011). Astronomical-magnetostratigraphic calibration of compiled sections in Austria suggests that the NRB is older than 208.05 Ma, as identified by the FAD of *Mi. posthernsteini* sensu lato (Galbrun et al., 2020). High precision U–Pb radiometric dating straddling the NRB as marked by the FO of *Vandaites suttonensis* at the Grotto Creek section in Alaska also supports a boundary age of approximately 209 Ma (Caruthers et al., 2022).

The “short Rhaetian” interpretation defines the NRB by the FAD of *Mi. posthernsteini* sensu stricto (Rigo et al., 2016). High precision U–Pb radiometric dating of volcanic ash beds in the Aramachay Formation in Peru dates the NRB as approximated by the Last Occurrence (LO) of *Monotis subcircularis* to be 205.50 ± 0.35 Ma (Wotzlaw et al., 2014). A sedimentation age model of the Pignola-Abriola section in Italy agrees with this by proposing a NRB age of 205.7 Ma, as defined by the FAD of *Mi. posthernsteini* sensu stricto (Maron et al., 2015, 2019). At the Black Bear Ridge section in Canada, U–Pb radiometric dating of first-cycle detrital zircons dates Rhaetian strata above the FO of *Mo. mosheri* to be younger than 205.2 ± 0.9 Ma (Golding et al., 2016). Astronomical-magnetostratigraphic calibration of the Newark Supergroup in eastern North America suggests a NRB age of 205.5 Ma, when correlated to the negative excursion in $\delta^{13}C$ positioned 50 cm below the FAD of *Mi. posthernsteini* sensu stricto at the Pignola-Abriola section in Italy (Kent et al., 2017). The Newark Supergroup astronomical-magnetostratigraphic calibration is corroborated by a similar investigation of the Xujiahe Formation in southern China (Li et al., 2017).

The new Re–Os dates of 208.3 ± 3.8 Ma for Sinwa East and 209.9 ± 5.3 Ma for Sinwa West come from samples taken near the transition to shale facies in both sections, stratigraphically above the FO of *Mo. mosheri* B and therefore within the NRB interval. These dates are much closer to the “long Rhaetian” interpretation, but ultimately support either interpretation, as both ages of the NRB fall within the uncertainty of the two Re–Os dates.

2.6.4. Global correlation of strontium isotopes

It is notable that $^{87}Sr/^{86}Sr$ ratios tend to be higher in Sinwa East than Sinwa West throughout the *Mockina bidentata* Zone (Figure 2.9). Mn/Sr ratios are a commonly used diagenetic proxy. As carbonate rocks undergo alteration, fluid interactions typically increase Mn abundance while decreasing Sr abundance (e.g. Jacobsen & Kaufman, 1999; Fölling & Frimmel, 2002). The average Mn/Sr ratio of 0.063 mol/mol at Sinwa East is considerably lower than 0.12 mol/mol at Sinwa West, potentially suggesting Sinwa East better captures primary seawater ratios (e.g. Jacobsen & Kaufman, 1999; Fölling & Frimmel, 2002). While the Mn/Sr ratios at Sinwa West are also not large enough to suggest diagenetic influence (e.g. Jacobsen & Kaufman, 1999; Fölling & Frimmel, 2002), the comparatively higher ratios paired with observations of recrystallization throughout the lower portions of the section ultimately does still point to the $^{87}Sr/^{86}Sr$ ratios of Sinwa East being more reliable.

Current understanding of trends in $^{87}Sr/^{86}Sr$ ratios leading up to and across the NRB is largely based on studies from the Tethyan realm, which observe a gradual increase throughout the Norian and then a drop across the boundary (Korte et al., 2003; Callegaro et al., 2012; Onoue et al., 2018). Tackett et al. (2014) identify a decreasing shift in $^{87}Sr/^{86}Sr$ ratios at the NRB at New York Canyon, Nevada, located on the eastern margin of Panthalassa during the Late Triassic. However, this interpretation is predicated on the assumption that the same decreasing shift observed in the Tethys is captured and uses this geochemical marker to identify the NRB in a manner that supersedes the established biozonations. From the perspective of both conodont and ammonoid biostratigraphy, the portion of the New York Canyon section sampled by Tackett et al. (2014) is either entirely late Norian in age (Figure 2.9; option A) if the FO of *Mo. mosheri* A is older than the FAD of *Mi. posthernsteini* (Krystyn et al., 2007b; Rigo & Campbell, 2021), or entirely Rhaetian in age (Figure 2.9; option B) if the FO of *Mo. mosheri* A coincides with the FAD of *Mi. posthernsteini* (Carter & Orchard, 2007; Orchard et al., 2007; Taylor et al., 2021). This correlation uncertainty arises from how Krystyn et al. (2007b) recorded the FO of *Mo. mosheri* A below the FO of *Mi. posthernsteini* at Steinbergkogel (Austria), whereas Carter & Orchard (2007) observed the FO of *Mo. mosheri* A to be younger than the FO of *Pr. moniliformis* at Kennecott Point (Canada). This discrepancy may be due to the rarity of *Mo. mosheri* A in Tethys (Krystyn et al., 2007a, b) causing asynchroneity in the FO of this morphotype between hemispheres, similar to how the few rare occurrences of *Mi. posthernsteini* in Panthalassa seem to occur at a later point than in Tethys (Tipper et al., 1994; Tozer, 1994; Umhoefer & Tipper, 1998). Also, given how *Mo. mosheri* A occurs right from the base of the New York Canyon $^{87}Sr/^{86}Sr$ data, with no older biozones stratigraphically below to provide context (Orchard et al., 2007; Tackett et al., 2014), the occurrence of this morphotype in New York Canyon may not represent the FO, instead recording younger portions of *Mo. mosheri* A's range. Regardless, based on the distributions of *Mo. Mosheri*, both options A and B place the New York Canyon data from Tackett et al. (2014) stratigraphically above the Mount Sinwa sections (Figure 2.9; Carter & Orchard, 2007; Orchard et al., 2007). Compiling the middle to late Norian $^{87}Sr/^{86}Sr$ ratios from Mount Sinwa with the early Norian measurements from Berlin Ichthyosaur State Park and the late Norian or Rhaetian measurements from New York Canyon (Tackett et al., 2014), the NRB interval of Panthalassa is better characterized by a continuation of the increasing trend in $^{87}Sr/^{86}Sr$ ratios observed throughout the Norian (Figure 2.9).

Therefore, the Panthalassan $^{87}Sr/^{86}Sr$ ratios across the late Norian agree with the gradual increase from approximately 0.7077 to 0.7080 observed in the Tethys by Onoue et al. (2018). The Panthalassan measurements around the NRB interval are also consistent with late Norian measurements from Onoue et al. (2018) and Rhaetian measurements from Callegaro et al. (2012). However, the comparatively high late Norian $^{87}Sr/^{86}Sr$ ratios of Korte et al. (2003), that largely creates the drop across the NRB, are not observed in Panthalassa (Figure 2.9). This discrepancy suggests that the late Norian interval from Korte et al. (2003) is either above the top of the New York Canyon section (Figure 2.9; option A) or is missing in the gap between the top of the Mount Sinwa sections and the base of the New York Canyon section (Figure 2.9; option B). This option B gap ought to be very short however, spanning just the difference in FO between *Mo. mosheri* A and B at the most (Carter & Orchard, 2007; Orchard, 2007). Alternatively, the drop in $^{87}Sr/^{86}Sr$ values across the boundary of Korte et al. (2003) is not representative of global ocean trends, evidenced by the lack of convincing replicability by other studies in both Tethys and Panthalassa. The absence of a global decrease in $^{87}Sr/^{86}Sr$ ratios across the NRB would suggest the biotic turnover associated with this stage boundary does not coincide with a substantial increase in mantle-derived volcanism and LIP emplacement, as suggested by Callegaro et al. (2012).

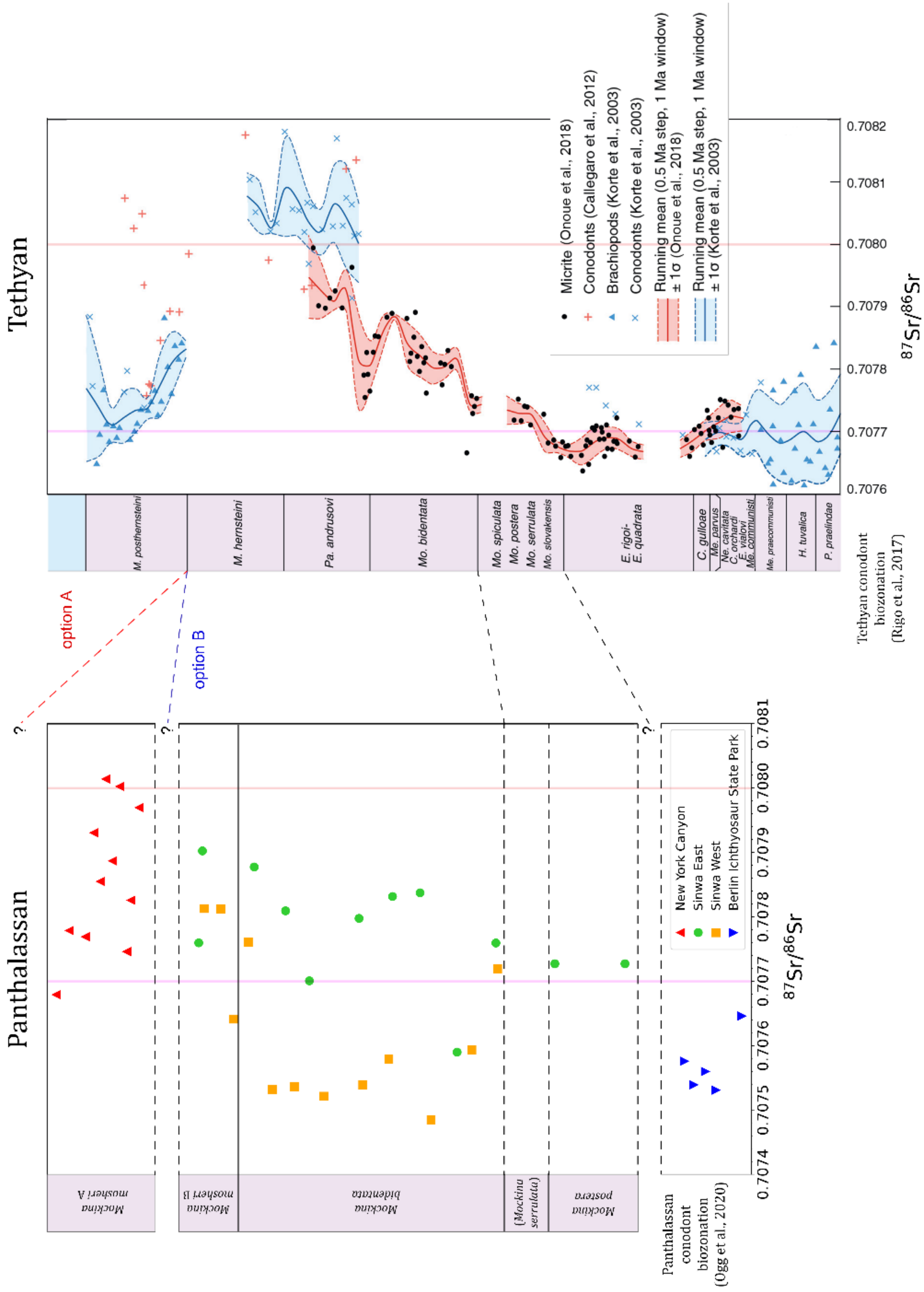
Panthalassan
Tethyan
option A
option B
?
Mockina mosheri A
Mockina mosheri B
Mockina bidentata
[Mockina serrulata]
Mockina postera
Panthalassan conodont biozonation (Ogg et al., 2020)
New York Canyon
Sinwa East
Sinwa West
Berlin Ichthyosaur State Park
0.7074
0.7075
0.7076
0.7077
0.7078
0.7079
0.7080
0.7081
$^{87}Sr/^{86}Sr$
M. posthernsteini
M. hernsteini
Pa. andrusovi
Mo. bidentata
Mo. spiculata
Mo. postera
Mo. serrulata
Mo. slovakensis
E. rigoi-
E. quadrata
C. gulloae
Ne. parvus
Ne. cavitata
C. orchardi
E. vialovi
Me. communisti
Me. praecommunisti
H. tuvalica
P. praelindae
Tethyan conodont biozonation (Rigo et al., 2017)
Micrite (Onoue et al., 2018)
Conodonts (Callegaro et al., 2012)
Brachiopods (Korte et al., 2003)
Conodonts (Korte et al., 2003)
Running mean (0.5 Ma step, 1 Ma window) ± 1σ (Onoue et al., 2018)
Running mean (0.5 Ma step, 1 Ma window) ± 1σ (Korte et al., 2003)
0.7076
0.7077
0.7078
0.7079
0.7080
0.7081
0.7082
$^{87}Sr/^{86}Sr$

Figure 2.9: Correlation of $^{87}Sr/^{86}Sr$ value trends between Panthalassa and Tethys. New York Canyon and Berlin Ichthyosaur State Park data is from Tackett et al. (2014). The Panthalassan conodont biozonation used is from Ogg et al. (2020). Tethyan data is compiled from Korte et al. (2003), Callegaro et al. (2012), and Onoue et al. (2018). The Tethyan conodont biozonation used is from Rigo et al. (2018). The correlation line from the base of *Misikella posthernsteini* is split into option A and option B. Option A represents the FO of *Mockina mosheri* A being older than the FAD of *Mi. posthernsteini* and therefore late Norian in age (Krystyn et al., 2007b; Rigo & Campbell, 2021), whereas option B represents the FO *Mo. mosheri* A being equivalent to the FAD of *Mi. posthernsteini* and therefore coincident with the base of the Rhaetian Stage (Carter & Orchard, 2007; Orchard et al., 2007; Taylor et al., 2021). Values of 0.7077 and 0.7080 $^{87}Sr/^{86}Sr$ are highlighted in purple and red respectively across both Panthalassan and Tethyan compilations for ease of comparison.

2.6.5. Global correlation of carbon isotopes

The transition from Facies 4 boundstone to Facies 5 shale immediately overlies the beginning of a negative excursion in $\delta^{13}C_{carb}$ values at Sinwa East (Figure 2.6), and this same lithological shift occurs just above the end of a negative excursion at Sinwa West (Figure 2.7). Although additional lower excursions are observed in both sections, correlating them would be questionable given the present data, both between the Mount Sinwa sections and globally. The lower excursions at Sinwa East fall within the *Mockina postera* Zone which is older than the late Norian excursions described by Zaffani et al. (2017), while the lower excursions at Sinwa West are not well constrained by biostratigraphy. Since the δ^{18}O record is significantly more susceptible to alteration than δ^{13}C, a strong correlation between δ^{13}C and δ^{18}O is a commonly used indicator of diagenetic influence on δ^{13}C (Marshall, 1992). Correlation between δ^{13}C$_{carb}$ and δ^{18}O$_{carb}$ is low for both Sinwa Formation sections (Figure 2.10), with $R^2 = 0.0625$ for Sinwa East, and $R^2 = 0.0221$ for Sinwa West. The very low Mn/Sr ratios consistent across both Sinwa East and Sinwa West also indicate a lack of significant diagenesis (Figures 2.6, 2.7).

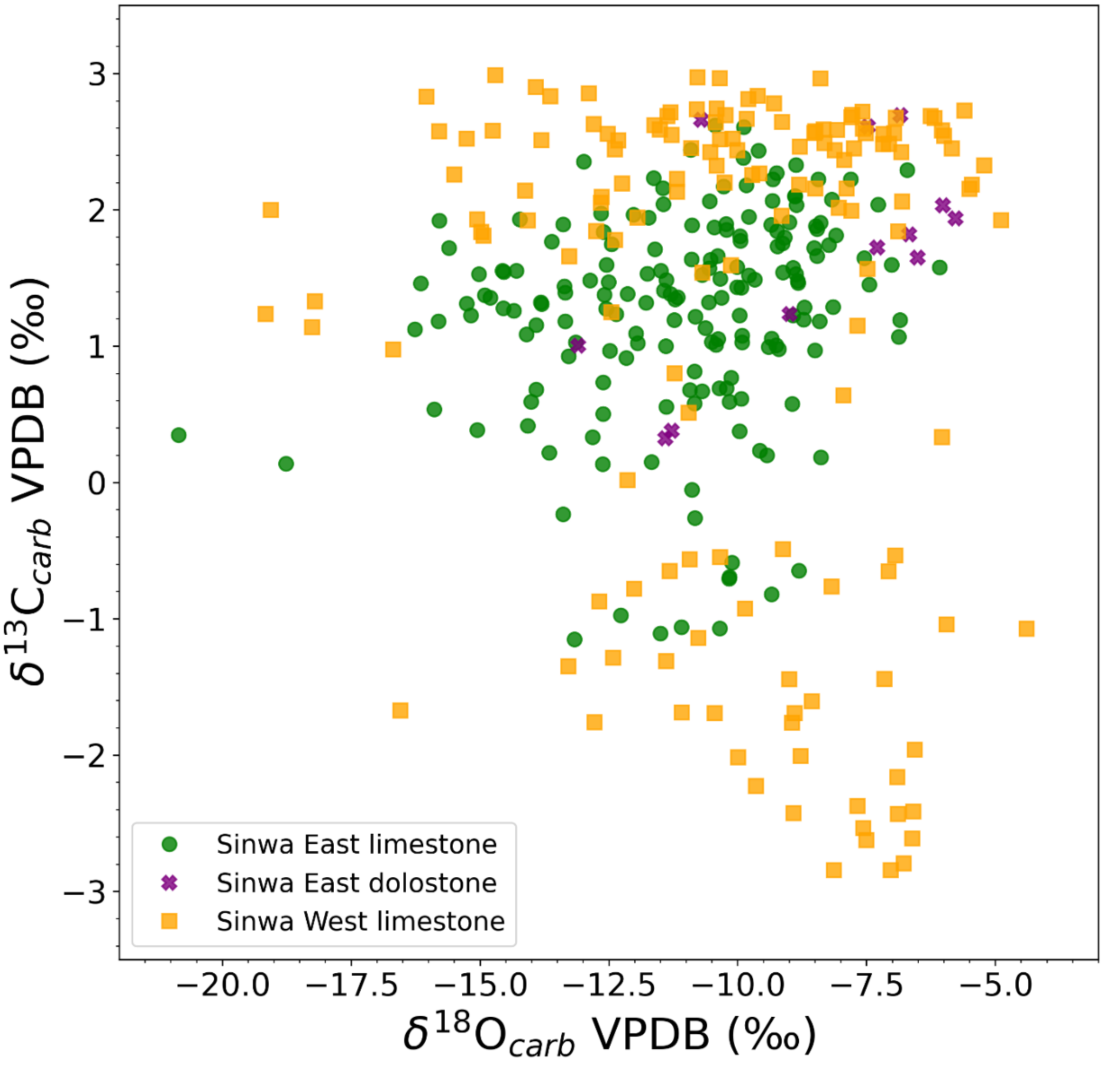

Figure 2.10: Comparison of δ^{13}C$_{carb}$ vs δ^{18}O$_{carb}$ for Sinwa East and Sinwa West.

The organic $\delta^{13}C$ values across both Sinwa East and Sinwa West do not clearly present the negative excursions observed in the carbonate $\delta^{13}C$ values (Figures 2.6, 2.7). Each organic $\delta^{13}C$ measurement does not correlate well with its respective carbonate $\delta^{13}C$ measurement of the same sample, with $R^2 = 3.74e-6$ for Sinwa East, and $R^2 = 0.199$ for Sinwa West. Decoupling of carbonate and organic $\delta^{13}C$ values is often an indicator of diagenesis, but given the evidence for well-preserved carbonate geochemistry at both Mount Sinwa sections, this interpretation is unlikely. Organic $\delta^{13}C$ values can be contaminated by detrital organic material, obscuring primary organic $\delta^{13}C$ trends with no impact on the validity of carbonate $\delta^{13}C$ value preservation (Johnston et al., 2012). Samples with low total organic content would be particularly susceptible to this type of contamination (Johnston et al., 2012). With the majority of both the Sinwa East and Sinwa West sections representing deposition in a backreef setting, significant terrestrial organic influence is plausible. Furthermore, the organic content of the Sinwa Formation limestone on Mount Sinwa is generally quite low, with weight percent carbonate averaging 98.7% in Sinwa East, and 97.1% in Sinwa West.

Maron et al. (2015) and Rigo et al. (2016) propose a negative excursion in $\delta^{13}C$ to be a globally correlatable marker for the NRB. While many sections around the world exhibit instability in $\delta^{13}C$ values at the NRB interval (Ward et al., 2001, 2004; Sephton et al., 2002; Korte et al., 2005; Wignall et al., 2007; Whiteside & Ward, 2011; Muttoni et al., 2014; Rigo et al., 2016, 2020; Zaffani et al., 2017), the trends are often more chaotic than the relatively clear negative excursion observed in the $\delta^{13}C_{carb}$ values of the Sinwa Formation (Figure 2.11). Also, these intervals of instability often do not seem to precisely begin or end at biostratigraphic boundaries, instead occurring proximal to the NRB (Figure 2.11). Du et al. (2020b) observes a similar decoupling between the final extinction of conodonts and the main negative carbon isotope excursion at the end-Triassic, with conodonts in the Tethys and eastern Panthalassa disappearing earlier than open ocean conodonts. Since CAMP volcanism is widely accepted as the primary driver of the end-Triassic mass extinction (Marzoli et al., 1999, 2004), it would be feasible for continental margin biotic communities to be impacted measurably earlier than their open ocean counterparts, owing to closer proximity to the volcanism occurring in central Pangea, while any associated shift in the $\delta^{13}C$ value of global ocean DIC would be geologically instantaneous (Du et al., 2020b). The asynchroneity between conodont biostratigraphy and carbon isotope chemostratigraphy in the Whitehorse Trough, as well as for the NRB as a whole, could potentially also be explained by such a decoupling between biotic community disturbance and global ocean DIC impact. However, unlike the end-Triassic mass extinction, it is unclear whether the faunal turnover and carbon cycle disturbance at the NRB even had a centralized trigger, precluding attempts to identify the paleogeographic position of such a trigger or speculate regarding the ensuing mechanisms of Earth system response.

Abundant evidence exists for some manner of global disturbance to the carbon cycle at the NRB, demonstrated by instability in $\delta^{13}C$ values, and connected to faunal turnover in a wide variety of biota across stratigraphic sections around the world (Figure 2.11). However, the record of $\delta^{13}C$ values appears to be inconsistent in both shift pattern and biostratigraphic position (Figure 2.11); as well, separate similar intervals of disturbance tend to be observed both older into the late Norian (e.g. Zaffani et al., 2017) and younger into the Rhaetian (e.g. Ruhl & Kürschner, 2011). Therefore, the use of an excursion in $\delta^{13}C$ values as a marker for the NRB is exceedingly tenuous without strong corroboration with other proxies.

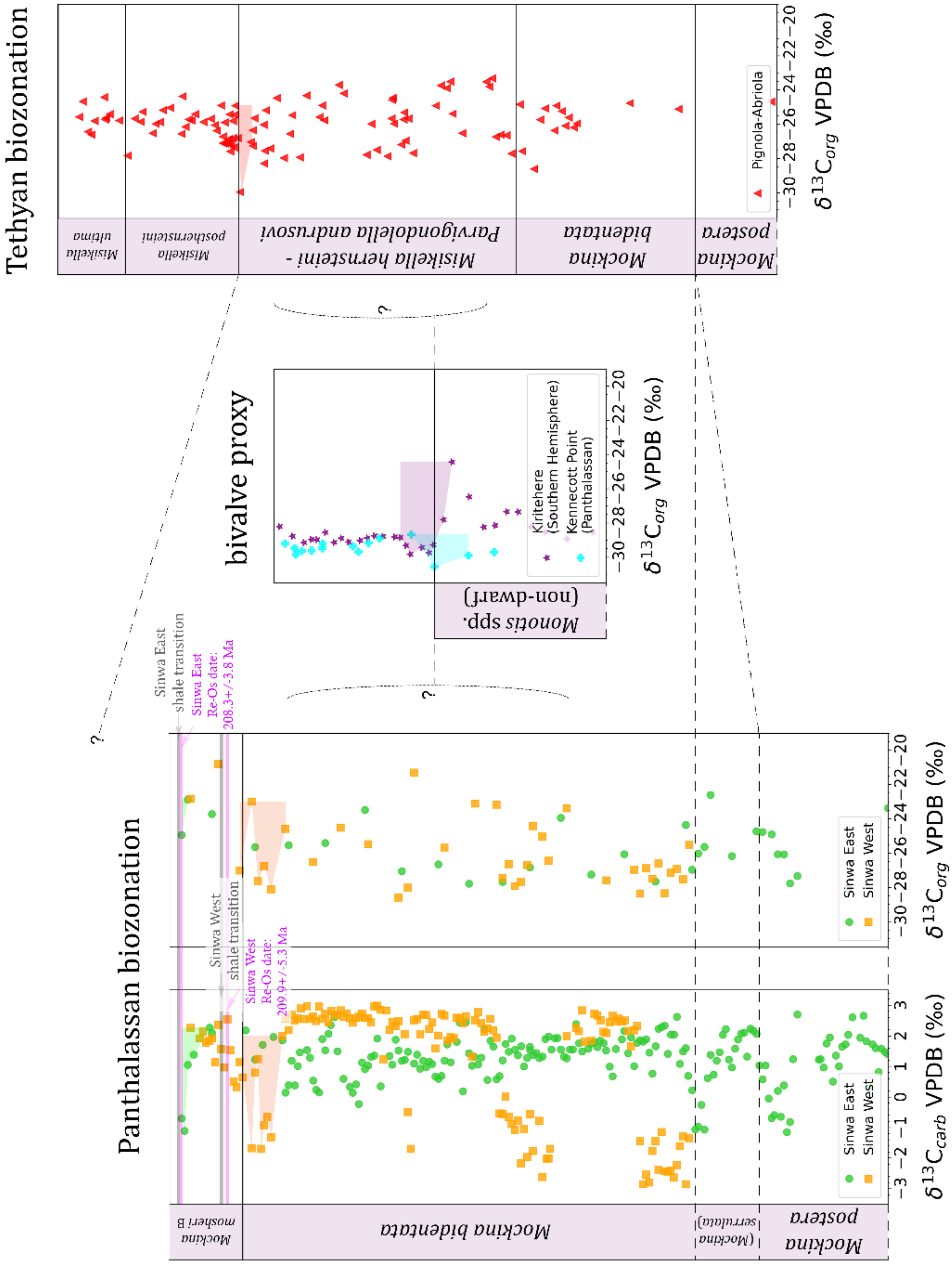
Tethyan biozonation
Misikella ultima
Misikella posthernsteini
Misikella hernsteini - Parvigondolella andrusovi
Mockina bidentata
Mockina postera
Pignola-Abriola
−30 −28 −26 −24 −22 −20
$\delta^{13}C_{org}$ VPDB (‰)
?
bivalve proxy
Monotis spp. (non-dwarf)
Kiritehere (Southern Hemisphere)
Kennecott Point (Panthalassan)
−30 −28 −26 −24 −22 −20
$\delta^{13}C_{org}$ VPDB (‰)
?
?
Panthalassan biozonation
Sinwa East shale transition
Sinwa East Re-Os date: 208.3+/-3.8 Ma
Sinwa West shale transition
Sinwa West Re-Os date: 209.9+/-5.3 Ma
Mockina mosheri B
Mockina bidentata
(Mockina serrulata)
Mockina postera
Sinwa East
Sinwa West
−3 −2 −1 0 1 2 3
$\delta^{13}C_{carb}$ VPDB (‰)
Sinwa East
Sinwa West
−30 −28 −26 −24 −22 −20
$\delta^{13}C_{org}$ VPDB (‰)

Figure 2.11: Selection of sections with δ^{13}C values exhibiting excursions proposed to be related to disturbance at the NRB interval aligned by various biostratigraphic proxies. The relative positions of Panthalassan conodont biozonation, Tethyan conodont biozonations, and *Monotis* bivalves are based on Orchard (1991), Krystyn et al. (2007a, b), and Rigo and Campbell (2021). The Mount Sinwa data includes the positions of Re–Os dating marked in magenta as well as the positions of the lithofacies transition from Facies 4 boundstone to Facies 5 shale marked in grey. Pignola-Abriola data is from Rigo et al. (2016, 2020) and Zaffani et al. (2017). Kiritehere data from is Rigo et al. (2020). Kennecott Point data is from Ward et al. (2001, 2004). Proposed excursion intervals are highlighted in the same colours as the datapoint markers of each section.

2.7. Conclusions

The Sinwa Formation on Mount Sinwa preserves a record of the middle Norian – latest Norian paleoenvironmental progression of the Whitehorse Trough. Observed lithofacies shifts suggest a gradual marine transgression in a coral reef environment throughout the late Norian. This reef system ceased production near the NRB, and is overlain by black shale, potentially due to rapid base level rise and/or the onset of widespread environmental pressure. The latest Norian through Rhaetian conodont species *Mockina mosheri* morphotype B occurs at both Mount Sinwa sections, with the FO just below the transition from carbonate boundstone to shale facies, suggesting close proximity of this facies shift to the NRB. Re–Os isochron ages just below the transition from boundstone to shale facies are 208.3 ± 3.8 Ma for Sinwa East, and 209.9 ± 5.3 Ma for Sinwa West, both of which are consistent with previous age estimates of the NRB. Through the integration of measurements between Mount Sinwa and New York Canyon, $^{87}Sr/^{86}Sr$ ratios are observed to follow a gradually increasing trend across the late Norian in the Panthalassan realm, consistent with that observed in the Tethyan realm. However, the $^{87}Sr/^{86}Sr$ ratio drop across the NRB proposed in the Tethys is not replicated in Panthalassa. The lack of a global decreasing shift in $^{87}Sr/^{86}Sr$ values would suggest that the disturbance at the NRB was not triggered by a substantial increase in mantle-derived volcanism. A negative excursion of 3 – 4‰ is observed in the $\delta^{13}C_{carb}$ record values of both Mount Sinwa sections stratigraphically proximal to the transition from boundstone to shale facies. This excursion is interpreted to potentially represent a global carbon cycle disruption related to the NRB.

Chapter 3

Morphological trends across the Norian/Rhaetian boundary within Late Triassic conodonts in western Canada: Implications for protracted paleoenvironmental disturbance preceding the end-Triassic mass extinction[2]

3.1. Abstract

The Late Triassic conodont species *Mockina* ex gr. *carinata* and *Mockina.* ex gr. *englandi* were exceptionally prevalent amongst the marine fauna of the Panthalassan realm from the middle Norian through to the Rhaetian. Leading into the complete extinction of conodonts near the Triassic/Jurassic boundary, a significant turnover event occurred in conodont fauna across the Norian/Rhaetian boundary (NRB), with the pectiniform elements of common Rhaetian genera from Tethys exhibiting minimal or absent platforms. This intergeneric trend of platform reduction is not as evident in Panthalassa where these genera are very rare, but morphometric analyses of *Mo.* ex gr. *carinata* and *Mo.* ex gr. *englandi* specimens from across the Canadian Cordillera demonstrate that comparable shifts in morphology occurred intraspecifically in Panthalassa across the NRB, confirming the global extent of these trends. Pectiniform elements of *Mo.* ex gr. *carinata* display a sequential reduction of platform width from

---

[2] This chapter is published as: Lei, J.Z.X., Golding, M.L., and Husson, J.M. (2024). Morphological trends across the Norian/Rhaetian boundary within Late Triassic conodonts in western Canada: Implications for protracted paleoenvironmental disturbance preceding the end-Triassic mass extinction. Paleobiology, v. 50(1), p. 85–95.

middle Norian to late Norian to Rhaetian, whereas pectiniform elements of *Mo.* ex gr. *englandi* display a reduction of platform width only from late Norian to Rhaetian. Specimens of both species that have a mid-platform length to breadth ratio greater than 3:1 are restricted to the Rhaetian. Specimens from the Kennecott Point section on Haida Gwaii, British Columbia, demonstrate that this morphological shift occurred somewhat later than other biostratigraphic proxies for the NRB. The global trend of platform width reduction in many conodont pectiniform elements may reflect a change in primary diet away from hard food sources, perhaps suggesting some degree of carbonate biomineralization suppression beginning around the NRB. This interpretation would support CO_2 outgassing as the causal mechanism of the environmental disturbance at the NRB, and identify the NRB as a significant turning point for Late Triassic ecosystems, marking the beginning of a protracted, multiphase end-Triassic mass extinction.

3.2. Introduction

The Middle to Late Triassic was a unique time in geologic history in which “modern fauna” was first able to extensively radiate and thrive following the drawn-out aftermath of the Permian/Triassic mass extinction (e.g. Sepkoski, 1981; Raup & Sepkoski, 1982). During this interval, the global biosphere experienced a short-lived diversity peak in the Late Triassic, before being devastated by the subsequent end-Triassic mass extinction (ETME) (e.g. Sepkoski, 1981; Raup & Sepkoski, 1982). Much emphasis has been placed on investigating both of these mass extinctions, but research on the broader paleobiologic trends across the Late Triassic has been much less common. Mass extinction events are traditionally thought of as geologically instantaneous, but there is considerable evidence that the paleoenvironmental disturbance and biotic distress associated with the ETME began prior to the actual Triassic/Jurassic boundary (e.g. Hesselbo et al., 2002; Ward et al., 2004; Ruhl & Kürschner, 2011; Schoepfer et al., 2016; Davies et al., 2017; Yager et al., 2017; Larina et al., 2019). Some have even argued that the ETME may be better characterized as the aggregation of multiple temporally disparate biotic turnover events throughout the latest Triassic, beginning as early as the Norian/Rhaetian boundary (NRB) (e.g. Hallam, 2002; Tanner et al., 2004; Lucas, 2018; Rigo et al., 2018, 2020). Many faunal groups experienced significant turnover at the NRB including bivalves, conodonts, radiolarians, and ammonoids (e.g. Ward et al., 2001, 2004; Tanner et al., 2004; Carter & Orchard, 2007; Lucas, 2018; Rigo et al., 2018, 2020). Recovery within these faunal groups was limited during the Rhaetian, potentially suggesting a prolonged interval of elevated environmental stress persisting after the NRB, which in turn contributed to the severity of the ETME since a fragile biosphere would be more vulnerable to extinction pressures (e.g. Hallam, 2002; Tanner et al., 2004; Lucas, 2018; Rigo et al., 2018, 2020). For example, although coral reefs are present in Rhaetian strata, they are considerably smaller in size and less widespread compared to their Norian counterparts, with the latter representing peak diversity in the Triassic (e.g. Flügel & Kiessling, 2002; Stanley, 2003; Rigo et al., 2020). It was these relatively less robust Rhaetian communities that were then subsequently devastated during the ETME (e.g. Flügel & Kiessling, 2002; Stanley, 2003; Rigo et al., 2020).

While the primary trigger of the ETME has been broadly accepted as enhanced volcanic outgassing associated with the Central Atlantic Magmatic Province (CAMP) (Marzoli et al., 1999, 2004; Blackburn et al., 2013), the causal mechanism for disturbance at the NRB has remained elusive. A potential mechanism is volcanism preceding CAMP emplacement (e.g. Zaffani et al., 2017; Rigo et al., 2020). This hypothesis is supported indirectly by decreasing $^{87}Sr/^{86}Sr$ ratios in seawater across the NRB, interpreted as an increase in weathering input of mantle-derived volcanics (Korte et al., 2003; Callegaro et al., 2012; Tackett et al., 2014). However, this signal from the Tethyan realm (marine environment on the eastern margin of Pangea) has not been convincingly documented in the Panthalassan realm (marine environment on the western margin of Pangea), arguably undermining its supposed global extent (Lei et al., 2022). Emplacement of the Angayucham Province in Alaska has been proposed as the source of this hypothetical volcanism at the NRB (Zaffani et al., 2017; Rigo et al., 2020), but the poor precision of current age constraints (Ernst & Buchan, 2001) makes this link tenuous. The true driver of the NRB disturbance and faunal turnover therefore remains uncertain.

The ETME has long been held to mark the total extinction of the long-ranging class Conodonta (e.g. Clark, 1983), with perhaps just a handful of examples globally where rare conodont specimens are found in the earliest Hettangian (Pálfy et al., 2007; Du et al., 2020b, 2023; Caruthers et al., 2022). A general trend of declining conodont diversity is observed throughout the Late Triassic, indicating that the final extinction of the class may be better interpreted as the culmination of a multi-million-year process of deterioration rather than solely as the result of a sudden cataclysmic event (Martínez-

Pérez et al., 2014a; Rigo et al., 2018). The latest Norian represents the last significant peak of conodont standing diversity, which then dropped precipitously across the Rhaetian Stage (Martínez-Pérez et al., 2014a; Rigo et al., 2018). This diversity trend points towards the NRB as being a crucially important interval in conodont evolutionary history, the study of which could lead to a better understanding of the ETME and paleoenvironmental conditions preceding it. This in turn may help in determining why the class went extinct during the ETME, after having survived the more severe Permian/Triassic mass extinction (e.g. Sepkoski, 1981; Raup & Sepkoski, 1982).

Conodont pectiniform element morphology displays a general trend of simplification across the NRB, with the forms of genera like *Misikella* and *Parvigondolella*, which dominate Rhaetian fauna, having minimal platforms or none at all (e.g. Orchard et al., 2007; Giordano et al., 2010; Mazza et al., 2012; Rigo et al., 2018; Karádi et al., 2020; Du et al., 2021, 2023). This is in contrast to the forms that dominate Norian fauna, such as the genera *Epigondolella* and *Mockina*, both of which commonly display prominent platforms hosting sharp and discrete platform denticles; another Norian example is the genus *Norigondolella*, which display forms with prominent and anteriorly extended platforms, typically resulting in the absence of any free blade (e.g. Orchard, 1991a, 1991b, 2018; Mazza et al., 2012; Rigo et al., 2018; Du et al., 2021). The genus *Misikella* is commonly found in the Rhaetian of Tethys, but is extremely rare in the Rhaetian of Panthalassa, such that it has limited biostratigraphic utility in the latter region (Carter & Orchard, 2007; Orchard et al., 2007). Comparable trends of platform reduction within pectiniform elements across the NRB interval can potentially still be observed in the morphologies of genera and species that are more abundant in Panthalassa, such as within *Mockina mosheri*. Morphotype B of this species ranges from the latest Norian through Rhaetian, in contrast with morphotypes A and C which are exclusively Rhaetian (Orchard, 1994; Carter & Orchard, 2007; Orchard et al., 2007). Morphotype B is unique in possessing accessory platform denticles, resulting in wider platforms overall compared to the exclusively Rhaetian forms (Orchard, 1994; Carter & Orchard, 2007; Orchard et al., 2007). However, any platform reduction exhibited by *Mo. mosheri* is considerably less clear than the intergeneric Tethyan trends, since the stratigraphic ranges of all three morphotypes are nearly identical, with morphotype B only differing from the others by extending slightly older into the latest Norian. Also, *Mo. mosheri* may not be the most representative species of Panthalassan fauna since none of the morphotypes are particularly common in either the Norian or the Rhaetian.

The present study aims to investigate morphological shifts displayed by *Mockina* ex gr. *carinata* and *Mockina* ex gr. *englandi* as these conodont species cross the NRB. Pectiniform elements of these two conodont species have been recovered in exceptionally high abundance from North American strata (Panthalassan realm) ranging from middle Norian through Rhaetian. Therefore, they make excellent candidates for the application of morphometric analysis to investigate trends in Panthalassan conodont pectiniform morphology across the NRB interval. No prior morphometric studies have been conducted on these two conodont species, nor any conodont species crossing the NRB. If the intergeneric trends of pectiniform platform reduction largely observed in Tethys can also be recognized intraspecifically in species that dominate Panthalassa, this would greatly reinforce the hypothesis that these morphological shifts occurred in response to global-scale stressors.

3.3. Materials and methods

The present study utilizes new and archival collections of *Mockina* ex gr. *carinata* and *Mockina* ex gr. *englandi* from across the Canadian Cordillera (Figure 3.1). Limestone samples were processed for conodonts at the Geological Survey of Canada Pacific Division in Vancouver, British Columbia, using standard techniques as outlined by Stone (1987). Individual samples were crushed into ~3 cm fragments before being dissolved in acetic acid for 10–14 days. Per ~1 kg of sample, a solution of 6.0 L of water, 3.2 L of 10–15% acetic acid (to create a buffer), and 0.8–1.0 L of 99.5% glacial acetic acid was used. The residues that remained after treatment were then sieved to collect the 90–850 μm fraction. The isolated fraction was rinsed, dried, and put through heavy liquid separation using sodium polytungstate (specific gravity of 2.85 kg/L) with the heavy fraction collected.

Table 3.1. Specimen counts of *Mockina* ex gr. *carinata* and *Mockina* ex gr. *englandi* grouped by terrane affinity and age.

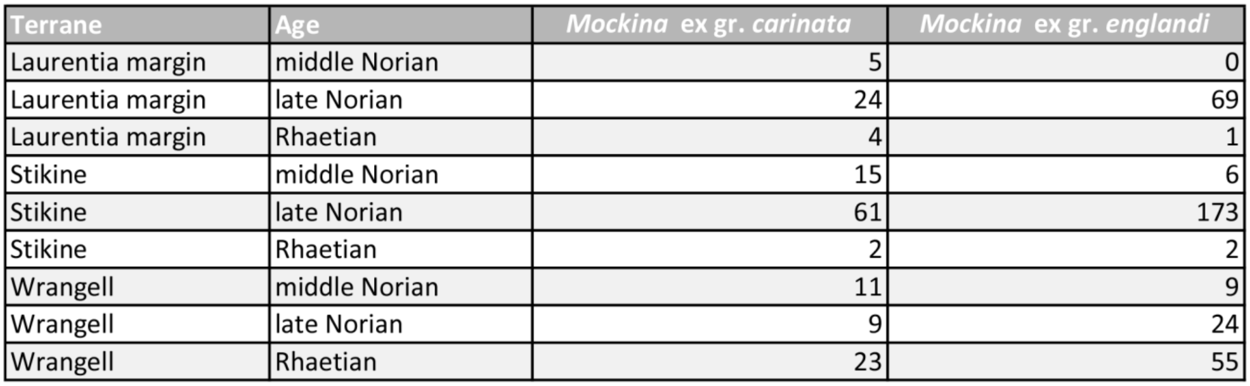

Terrane	Age	*Mockina* ex gr. *carinata*	*Mockina* ex gr. *englandi*
Laurentia margin	middle Norian	5	0
Laurentia margin	late Norian	24	69
Laurentia margin	Rhaetian	4	1
Stikine	middle Norian	15	6
Stikine	late Norian	61	173
Stikine	Rhaetian	2	2
Wrangell	middle Norian	11	9
Wrangell	late Norian	9	24
Wrangell	Rhaetian	23	55

As the Canadian Cordillera is comprised of a multitude of allochthonous terranes (e.g. Monger & Ross, 1971; Jones et al., 1977; Mihalynuk et al., 1994; Belasky et al., 2002; Johnston & Borel, 2007; Johnston, 2008; Colpron & Nelson, 2009, 2011; Kent & Irving, 2010; Beranek & Mortensen, 2011), this sampling of specimens represents a wide paleogeographic distribution stretching from the western margin of Laurentia to the open Panthalassic Ocean during the Late Triassic (Figure 3.1). Specimen counts classified by terrane affinity and age are summarized in Table 3.1, and a detailed list of samples can be found in Appendix B. Particularly productive localities include the Black Bear Ridge section at Williston Lake representing the Laurentia margin, the Sinwa East section on Mount Sinwa representing the Stikine Terrane imminently converging with Laurentia, and the Kennecott Point section on Haida Gwaii representing the Wrangell Terrane in open ocean (e.g. Colpron & Nelson, 2009, 2011; Figure 3.1).

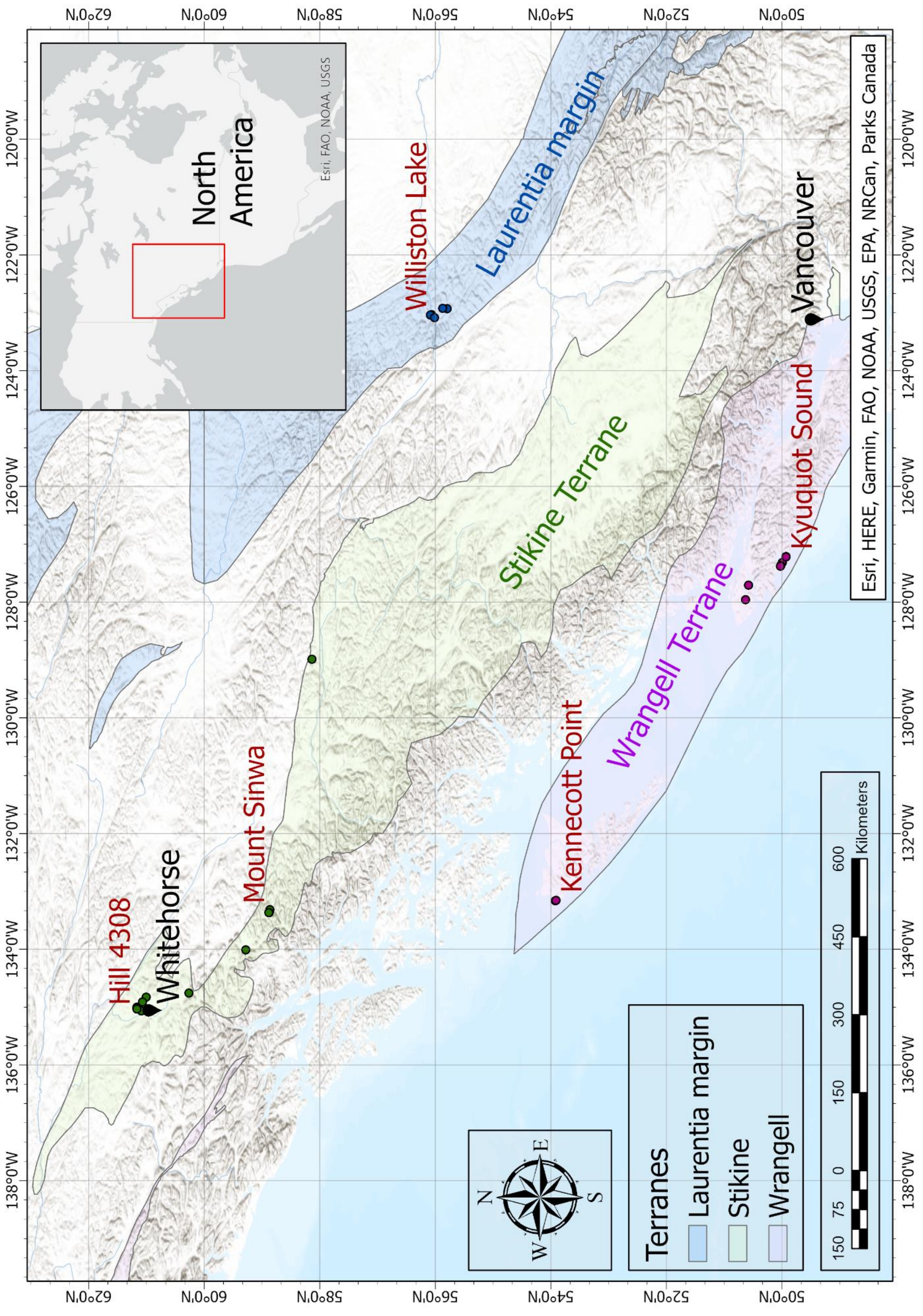
North America
Esri, FAO, NOAA, USGS
Williston Lake
Laurentia margin
Stikine Terrane
Vancouver
Kyuquot Sound
Wrangell Terrane
Kennecott Point
Mount Sinwa
Hill 4308
Whitehorse
Terranes
Laurentia margin
Stikine
Wrangell
N
E
S
W
150 75 0 150 300 450 600
Kilometers
Esri, HERE, Garmin, FAO, NOAA, USGS, EPA, NRCan, Parks Canada
62°0'N
60°0'N
58°0'N
56°0'N
54°0'N
52°0'N
50°0'N
120°0'W
122°0'W
124°0'W
126°0'W
128°0'W
130°0'W
132°0'W
134°0'W
136°0'W
138°0'W

Figure 3.1: Locations of all samples across western Canada from which specimens in the present study were recovered, colour-coded by their terrane affinity. Select localities containing particularly productive sections are labelled by name. The western margin of Laurentia is in blue, including Williston Lake sections. The Stikine Terrane is in green, including the Mount Sinwa and Hill 4308 sections. The Wrangell Terrane is in purple, including the Kyuquot Sound and Kennecott Point sections. The displayed extent of each terrane is from Colpron and Nelson (2011).

Both *Mo.* ex gr. *carinata* and *Mo.* ex gr. *englandi* have previously been included in the genus *Epigondolella*, under a more expansive interpretation of that genus diagnosed by tall and discrete anterior platform denticles (e.g. Orchard, 1991a; Carter & Orchard, 2007; Orchard et al., 2007). More recent studies have generally reinterpreted these two species as belonging to the genus *Mockina* (e.g. Mazza et al., 2012; Orchard, 2018; Du et al., 2020a; Caruthers et al., 2022; Lei et al., 2022). *Mockina* was initially proposed as a derivative of *Epigondolella* in which the bifurcated keel was lost entirely, resulting in a keel that terminates posteriorly in a single point (Kozur, 1989a, b). Current differentiation between these two genera also emphasizes the less ornamented platforms of *Mockina* relative to that of *Epigondolella* (e.g. Mazza et al., 2012; Orchard, 2018; Du et al., 2020a). Orchard (1991a) initially defined *Mo. carinata* as a short species of *Epigondolella* with two large denticles on one anterior platform margin and one large denticle on the other (Figure 3.2A). Additional smaller platform denticles continue posteriorly of the large main set (Orchard, 1991a). Orchard (1991a) defined the species *Mo. englandi* similarly, primarily differentiated from *Mo. carinata* by possessing only a single pair of large anterior platform denticles (one on each side of the element), typically resulting in a comparatively more bilaterally symmetric platform outline (Figure 3.2B). Although *Mo. englandi* was originally defined by specimens displaying an ovoid platform, an abundance of specimens have since been recovered across western Canada that exhibit the strong anterior platform denticle pair, but with a wide variety of platform shapes. These varieties that deviate from the original diagnosis have been referred to as *Mo.* cf. *englandi* (Lei et al., 2022). Initially, *Mo. englandi* was proposed to have developed from *Mo. carinata* in the late Norian via the loss of one anterior platform denticle (Orchard, 1991a), but significant numbers of *Mo.* cf. *englandi* have subsequently been recovered from middle Norian strata. The present study does not differentiate *Mo.* cf. *englandi* from *Mo. englandi* for the purposes of analysis, resulting in *Mo.* ex gr. *englandi* being present in the middle Norian, late Norian, and Rhaetian. Similarly, the present study considers all specimens with the anterior platform denticle arrangement consistent with *Mo. carinata* as *Mo.* ex gr. *carinata*.

Morphometric techniques have been widely utilized in both biology and paleontology to investigate the geometric form of specimens (e.g. Bookstein, 1991). The platform landmark analysis methodology employed by the present study follows that utilized by prior morphometric analyses of Late Pennsylvanian conodont pectiniform elements (Hogancamp et al., 2016; Hogancamp & Barrick, 2018; Hogancamp, 2020). This landmarking methodology emphasizes the positions of distinct anatomical features, in contrast to morphometric studies of conodont pectiniform elements that focus more on the traced outline of elements (Klapper & Foster, 1986, 1993; Renaud & Girard, 1999;

Girard et al., 2007; Zimmerman et al., 2018; Guenser et al., 2019). The outline-focused methodology has the advantage of not requiring identification of many common point features, resulting in analysis specimen pools that accommodate a greater degree of morphological variability, potentially even including multiple genera. This methodology also produces a more precise representation of an element's outline shape, but can overlook crucial variation that does not affect the outline, which the feature-focused method would better capture. Both methods have been shown to be equally effective in detecting the pectiniform morphological variation that distinguishes species of the Late Devonian *Palmatolepis winchelli* group when employed on the same specimen pool (Hogancamp & Manship, 2016). Given the universally prominent denticulation observed in both *Mo.* ex gr. *carinata* and *Mo.* ex gr. *englandi*, the feature-focused methodology is more appropriate for the present study.

Two similar geometric landmark models are utilized for the two species in the present study, comprised predominantly of Type 1 landmarks as defined by Bookstein (1991). Type 1 landmarks are points readily identifiable as homologous between specimens by being defined by a discrete junction of anatomical features; Type 2 landmarks are points of reliable maxima/minima along a boundary, typically with biomechanical implications (Bookstein, 1991). For *Mo.* ex gr. *carinata* (Figure 3.2A), these landmarks are the anterior shoulders where the platform meets the blade (1, 2, Type 1), the positions of the large anterior platform denticles (3–5, Type 1), the points of maximum mid-platform constriction between the main and accessory platform denticles (6, 7, Type 2), smaller accessory platform denticles posterior of the main set (8–11, Type 1), the positions of the carina denticles (12–15, Type 1), and the posterior margin of the carina (16, Type 1). For *Mo.* ex gr. *englandi* (Figure 3.2B), these landmarks are the anterior shoulders where the platform meets the blade (1, 2, Type 1), the positions of the large anterior platform denticles (3, 4, Type 1), the points of maximum mid-platform constriction between the main and accessory platform denticles (5, 6, Type 2), smaller accessory platform denticles posterior of the main set (7–10, Type 1), the positions of the carina denticles (11–14, Type 1), and the posterior margin of the carina (15, Type 1).

In order for the landmark models to accommodate an adequately large specimen pool despite the variability in the number of carina and accessory platform denticles in both species, it is necessary that any “leftover” platform denticle landmarks are overlapped on the posterior-most platform denticle of the same side, and any “leftover” carina denticles are overlapped on the posterior margin of the carina (Figures 3.2A, B). Any loss in the quantity of carina and accessory platform denticles would therefore be expressed in analysis results by the convergence and overlapping of those landmarks in question, and vice-versa for any gain in denticle quantity. This overlapping and de-overlapping of landmark positions would not be easily confused with results reflecting other aspects of morphological variance. Specimens of *Mo.* ex gr. *carinata* where the large anterior platform denticle set are mirrored from the landmark model displayed in Figure 3.2B were flipped horizontally for consistent chirality. All landmarks across both geometric models are based on the positions of various features within each conodont element as seen in upper view (lying on base and denticles pointing up towards camera). Other potentially important morphological features that are only visible in other views, such as denticle height, keel shape, and basal pit location, are therefore not considered in the present study. More complicated geometric models incorporating additional landmarks from lateral and lower views would be impractical for the present study given the large specimen pool size, but could be the focus of more targeted future investigations.

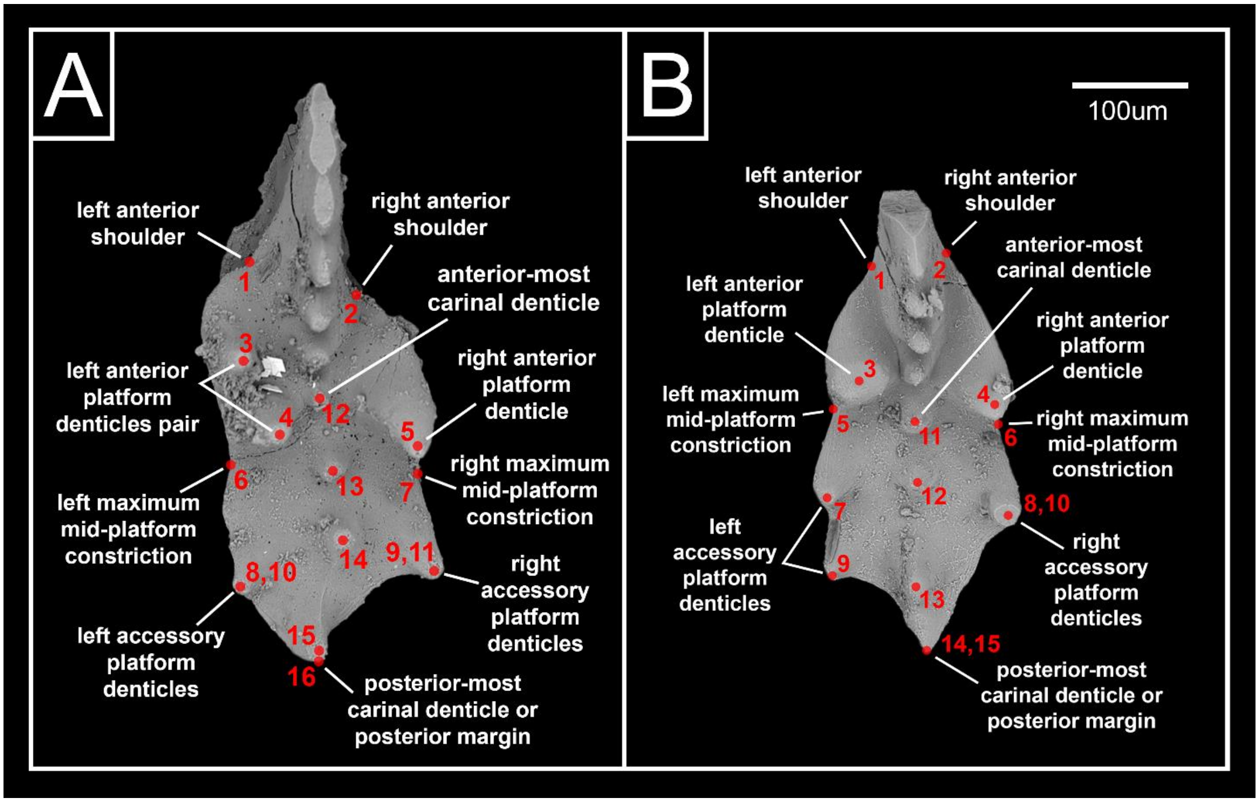

Figure 3.2: Geometric landmark models for (A) *Mockina* ex gr. *carinata* and (B) *Mockina* ex gr. *englandi* displayed on example specimens.

With the geometric landmark models as defined, the number of suitable specimens utilized in the present study totals 154 for *Mo.* ex gr. *carinata* and 339 for *Mo.* ex gr. *englandi* across all localities (Table 3.1, Appendix B). The primary criteria for including specimens in the present study was applicability of the respective geometric landmark models as defined above, as opposed to coherence with any species diagnoses. For example, specimens of both species required at least a single accessory platform denticle on each side to be included in the analyses, but all manner of platform shapes were included regardless of whether such forms are typical for *Mo. carinata*, *Mo. englandi*, or even other similar species within *Mockina*. The requirement for prominent accessory platform denticulation screens out juvenile *Mockina* specimens, as these features generally only develop in adulthood (e.g. Orchard, 1983; Rigo et al., 2018). The juvenile forms of many *Mockina* species can be indistinguishable from one another (e.g. Orchard, 1983; Rigo et al., 2018), so the inclusion of juveniles would have introduced unnecessary taxonomic confusion in the specimen selection process. A more detailed exploration of *Mockina* taxa and phylogeny can be found in a number of past studies (Orchard, 1983, 1991a, 1991b, 1994, 2018; Orchard et al., 2007; Mazza et al., 2012; Rigo et al., 2018). Digital photographs were taken of each specimen using a Nikon SMZ1270 microscope with integrally connected Canon Vixia HF G20 camcorder. All photography was conducted at 120x magnification, and specimens were positioned at a consistent orientation. The JPEG files were converted to TPS files using the software TpsUtil (Rohlf, 2010a), and then the positions of all landmarks were identified per specimen in the software TpsDig (Rohlf, 2010b). Morphometric analyses were conducted using the software MorphoJ (Klingenberg, 2011). First, a generalized Procrustes analysis was conducted on each species dataset, which minimizes all variation in specimen position, size, and rotation, in order to conserve only variation in specimen shape. Then, a wireframe model was created for each species, where landmark points are linked in a consistent manner to better facilitate visualization of form changes.

Lastly, eigen-analyses were conducted. Canonical variate analysis (CVA) is a specific discriminatory eigen-analysis that produces eigenvectors (canonical variates) which represent axes that maximize separation of sets in multivariate space, with the sets externally predefined by classifiers. CVA was utilized in the present study, with the age of each specimen binned into middle Norian, late Norian, or Rhaetian as the predefined classifier. Therefore, the canonical variates (CV1, CV2) represent the factors of morphological variance that most significantly differentiates these age bins, each responsible for a certain proportion of total variance and summing to 100%. Each individual specimen has an eigenscore for each eigenvector, reflecting their morphology relative to the rest of the specimen pool for the given morphological factor. The changes in form along the scaling of these canonical variates are displayed using the wireframe models across the ranges of eigenscores exhibited by the specimens, connecting each eigenvector to tangible qualities in morphology.

3.4. Results

3.4.1. CVA of *Mockina* ex gr. *carinata* with age as the group classifier

Conducting a CVA on the *Mockina* ex gr. *carinata* specimen pool with age as the group classifier (middle Norian, late Norian, Rhaetian) results in CV1 explaining 69% of variance maximizing separation between the three age bins, whereas CV2 explains

31%. More positive eigenscores along the CV1 axis correspond to forms with a broader platform width, additional accessory platform denticles, and a slightly shortened carina (Figure 3.3). More positive eigenscores along the CV2 axis correspond to forms with an elongated carina, additional carina denticles, a constricted mid-platform between the anterior and accessory platform denticles, and posteriorly shifted accessory platform denticles (Figure 3.3). A continuous range of specimens are observed across both CV axes, but generally the most positive CV1 scores are from middle Norian specimens (Figure 3.3). CV1 scores are more negative in late Norian specimens, and most negative in Rhaetian specimens (Figure 3.3). Specimens from the middle Norian have a mean CV1 score of 1.69, with values more positive than that almost exclusively associated with middle Norian specimens (Figure 3.3). Specimens from the late Norian have a mean CV1 score of -0.09 (Figure 3.3). Specimens from the Rhaetian have a mean CV1 score of -1.52, with values more negative than that almost exclusively associated with Rhaetian specimens (Figure 3.3). There is overlap among the three age bins along the CV2 axis, and no considerable separation between middle Norian and Rhaetian ranges, but CV2 scores more negative than -1.12 are exclusively associated with late Norian specimens (Figure 3.3).

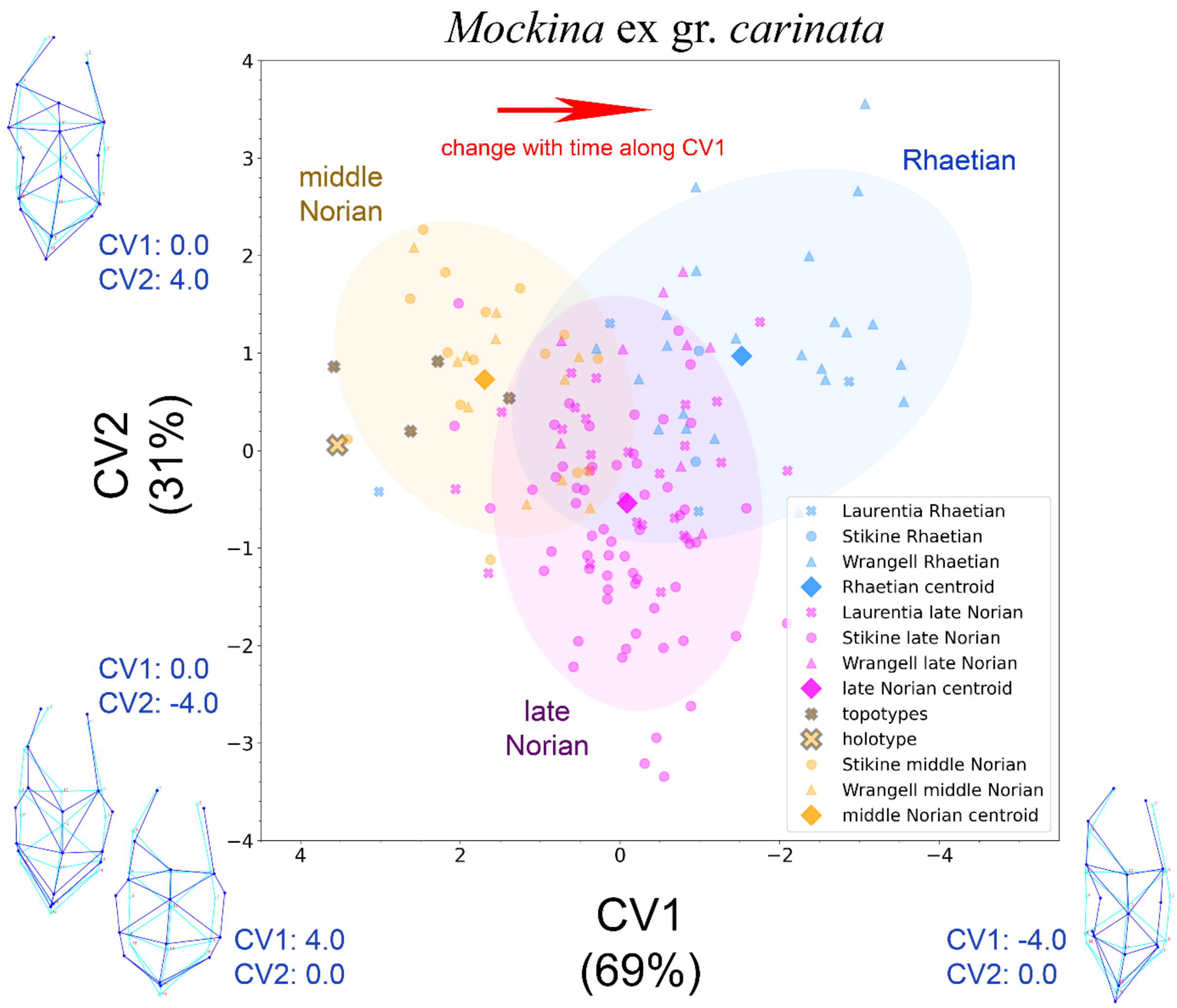

Figure 3.3: CVA biplots for *Mockina* ex gr. *carinata* with age as the group classifier. The percentages along each axis label refers to the proportion of variance explained by each eigenvector. Also plotted for each age bin is a centroid representing the mean values of each age bin along both axes, and ellipses representing 2σ from each centroid. Dark blue wireframe models illustrate the extremes of each CV eigenscore still exhibited by natural specimens, overlaid on light blue wireframe models where all CV eigenscores are zero.

3.4.2. CVA of *Mockina* ex gr. *englandi* with age as the group classifier

Conducting a CVA on the *Mockina* ex gr. *englandi* specimen pool with age as the group classifier (middle Norian, late Norian, Rhaetian) results in CV1 explaining 73% of variance maximizing separation between the three age bins, whereas CV2 explains 27%. More positive eigenscores along the CV1 axis correspond to forms with a narrower platform width, an elongated carina, and additional carina denticles (Figure 3.4). More positive eigenscores along the CV2 axis correspond to forms with a shortened carina, a posterior carina curvature, and posteriorly shifted accessory platform denticles on the concave side of said curvature (Figure 3.4). A continuous range of specimens are observed across both CV axes, but generally the most positive CV1 scores are from Rhaetian specimens, whereas middle Norian and late Norian specimens tend to have more negative scores (Figure 3.4). Specimens from the middle Norian have a mean CV1 score of -0.45, whereas specimens from the late Norian have a mean CV1 score of -0.26, with considerable overlap between the ranges of these two groups (Figure 3.4). Specimens from the Rhaetian have a mean CV1 score of 1.41, with values more positive than that almost exclusively associated with Rhaetian specimens (Figure 3.4). There is overlap among the three age bins along the CV2 axis, and no considerable separation between late Norian and Rhaetian ranges, but middle Norian specimens tend towards more positive values (Figure 3.4). It is notable that overall separation of age bins for *Mo.* ex gr. *englandi* morphologies is less than that observed for *Mo.* ex gr. *carinata* (Figures 3.3, 3.4).

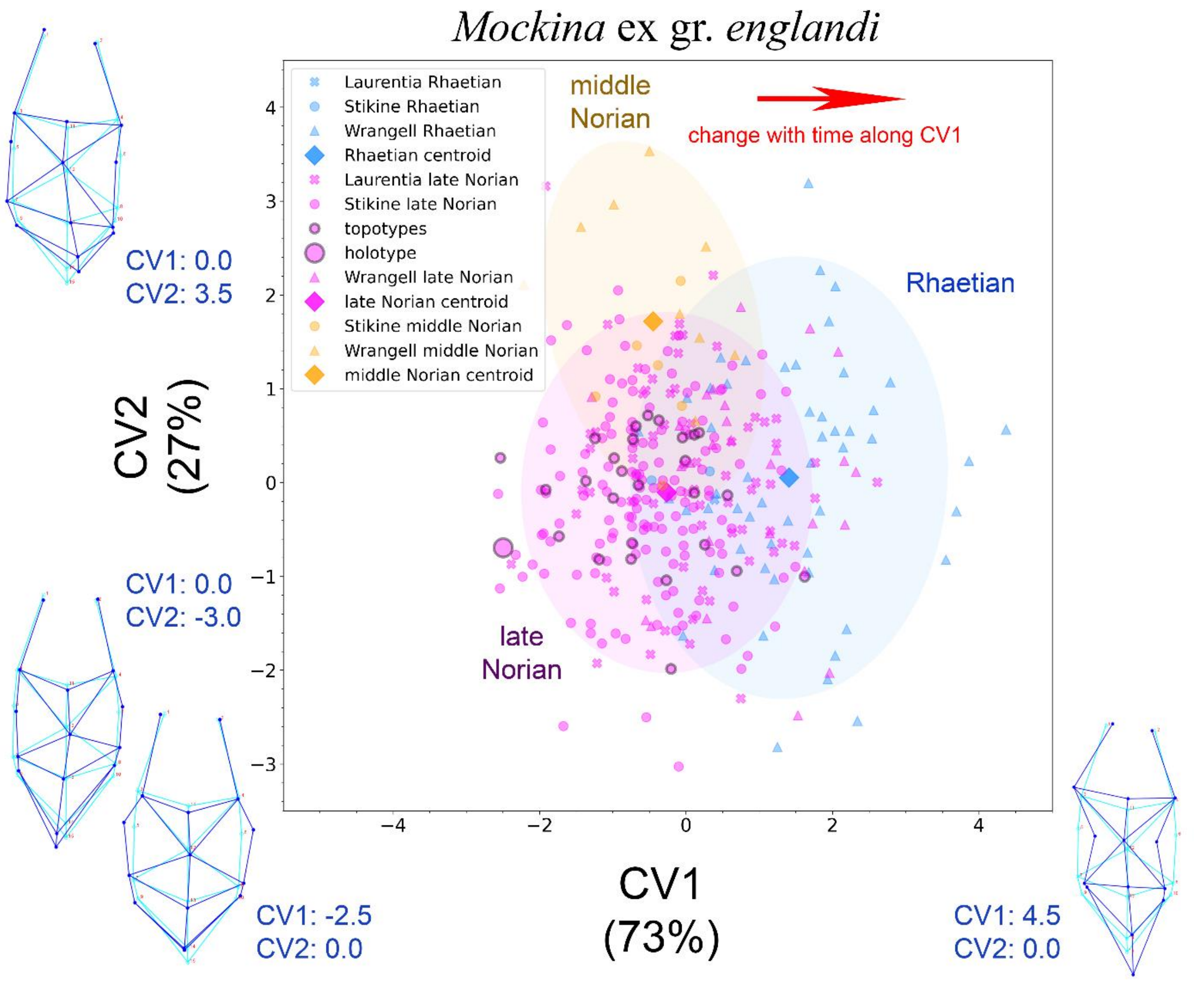

Figure 3.4: CVA biplots for *Mockina* ex gr. *englandi* with age as the group classifier. The percentages along each axis label refers to the proportion of variance explained by each eigenvector. Also plotted for each age bin is a centroid representing the mean values of each age bin along both axes, and ellipses representing 2σ from each centroid. Dark blue wireframe models illustrate the extremes of each CV eigenscore still exhibited by natural specimens, overlaid on light blue wireframe models where all CV eigenscores are zero.

3.5. Discussion

3.5.1. Evidence for morphotype origination or subspeciation

It is notable that for both *Mockina* ex gr. *carinata* and *Mockina* ex gr. *englandi*, the holotype of each species has extreme CV1 eigenscores far from the mean, with both late Norian and Rhaetian forms of *Mo.* ex gr. *carinata* progressing to more negative values than that of the middle Norian holotype, and Rhaetian forms of *Mo.* ex gr. *englandi* progressing to more positive values than that of the late Norian holotype (Figures 3.3, 3.4). Although the holotype of *Mo. englandi* is generally assumed to be late Norian, the lack of independent age constraints for the specimen means it could potentially be Rhaetian instead (Orchard, 1991a). Based on the present study, the broader platform of the *Mo. englandi* holotype indicates that it resembles late Norian forms much more than Rhaetian forms (Figure 3.4). The topotypes of *Mo.* ex gr. *carinata* are largely restricted to more positive CV1 values indicative of the middle Norian forms of that species (Figure 3.3), whereas the topotypes of *Mo.* ex gr. *englandi* span a large portion of the CV1 axis variability but largely do not encroach into the more positive CV1 values indicative of the Rhaetian forms of that species (Figure 3.4). There are multiple potential explanations for the outlier morphologies of both holotypes. It is possible that the holotypes were selected precisely due to their aberrant forms, being distinct within the species. Alternatively, they may have been selected due to their particularly broad platforms, as reflected in their CV1 eigenscores. The arrangement and height of platform denticles are key to the diagnoses of both species, such that a specimen with a broader platform would likely display these features more clearly. Nevertheless, both species are now defined by holotypes that are not representative of the species as a whole in terms of platform width, with CV1 distribution as evidence for morphotype origination or subspeciation away from the holotypes towards reduced platform morphologies across the NRB.

From the CVA results, thresholds of platform width can be determined for both *Mo.* ex gr. *carinata* and *Mo.* ex gr. *englandi*, past which specimens can be reliably identified as Rhaetian in age. For *Mo.* ex gr. *carinata*, the most negative CV1 score for a late Norian specimen is -2.10, with all values more negative than that associated with Rhaetian specimens (Figures 3.3, 3.5A). This CV1 score threshold represents a mid-platform length to breadth ratio of 2.9:1. For *Mo.* ex gr. *englandi*, the most positive CV1 score for a late Norian specimen is 2.61, with all values more positive than that associated with Rhaetian specimens (Figures 3.4, 3.5B). This CV1 score threshold represents a mid-platform length to breadth ratio of 3.1:1. Therefore, specimens of these two species with ratios greater than this threshold ratio of ~3:1 can be reliably identified as Rhaetian in age; however, given the overlap between the Norian and Rhaetian CV1 score ranges of both species, specimens displaying ratios lower than ~3:1 are not exclusively Norian (Figures 3.3, 3.4, 3.5). These determinations will have biostratigraphic utility for future studies involving Norian and Rhaetian conodonts from the Canadian Cordillera, and with wider testing may even prove to have global utility.

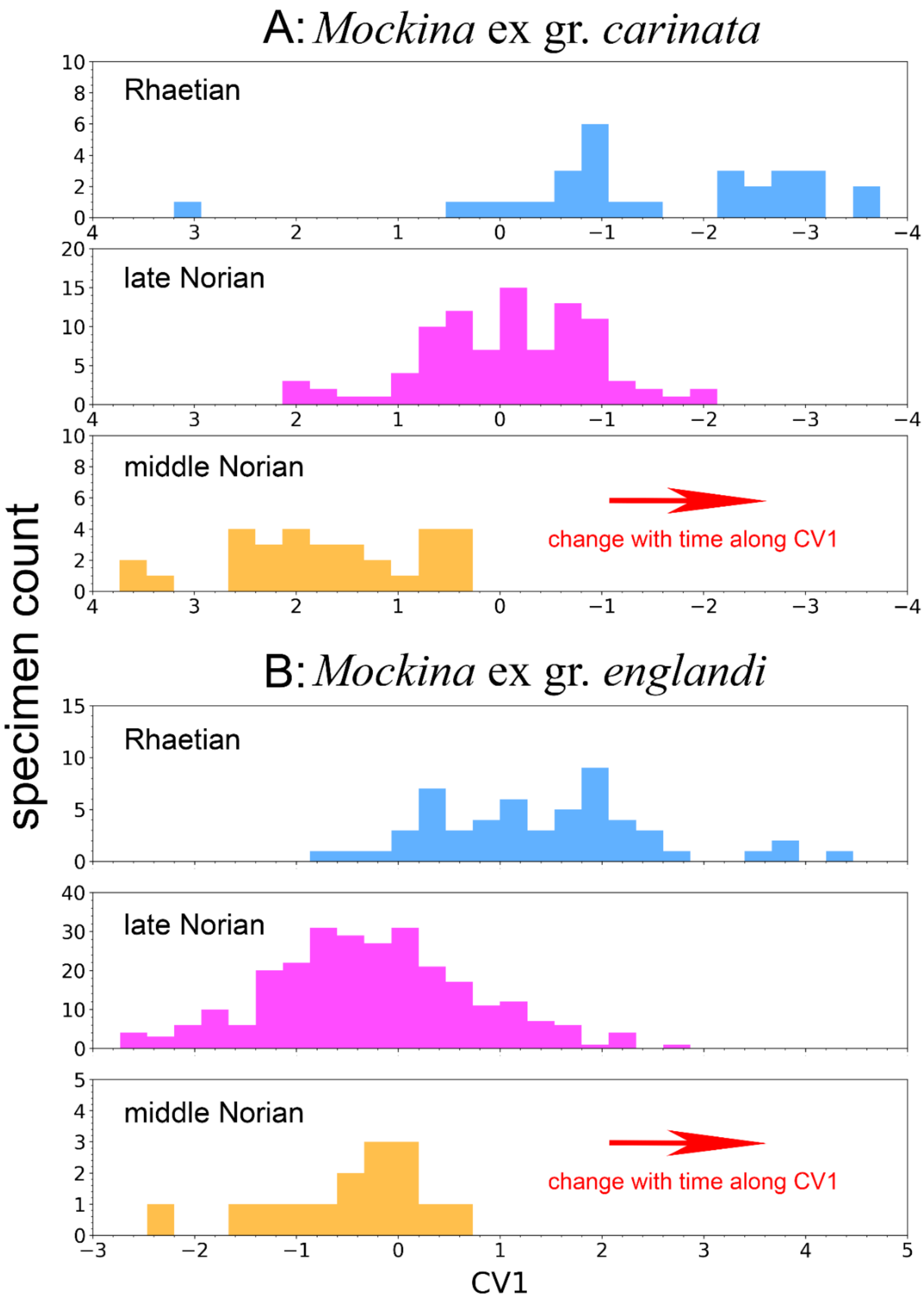

Figure 3.5: CV1 eigenscore distribution from CVA with age as the group classifier of (A) *Mockina* ex gr. *carinata* and (B) *Mockina* ex gr. *englandi* for specimens of each age bin.

3.5.2. Correlation to the NRB at Kennecott Point

The exact position of the NRB remains uncertain and contentious, with a number of different biostratigraphic proxies having been proposed and utilized, despite the asynchroneity between some if not all of these proxies (e.g. Carter & Orchard, 2007; Orchard et al., 2007; Krystyn, 2010; Rigo et al., 2016, 2020; Taylor et al., 2021; Lei et al., 2022; Rigo & Campbell, 2022). As such, understanding the timing of pectiniform platform reduction in *Mo.* ex gr. *carinata* and *Mo.* ex gr. *englandi* requires precise correlation of conodont morphology shifts to these various NRB proxies. Many of the specimens utilized in the present study do not have age constraints more precise than their age bin (middle Norian, late Norian, Rhaetian), but the composite Kennecott Point section on Haida Gwaii compiled by Carter and Orchard (2007) represents an opportunity to extract a subset of the specimen pool, and observe how the forms of both these species change within a continuous stratigraphic section. These specimens can be situated precisely within the Kennecott Point section, spanning a large variety of stratigraphic positions relative to a well constrained NRB primarily defined by the first occurrence of the Rhaetian radiolarian *Proparvicingula moniliformis* at 10.7 m, supported by the slightly higher first occurrence of the Rhaetian conodont *Mockina mosheri* morphotype A at 13.0 m (Figure 3.6; Carter & Orchard, 2007).

Lower in the Kennecott Point section (0.9 m in Figure 3.6), Ward et al. (2001, 2004) previously identified the NRB as defined by the conspicuous disappearance of the bivalve genus *Monotis*, coinciding with a positive excursion in $\delta^{13}C$ values of organic carbon, interpreted together to indicate environmental stress via deoxygenation. The positive excursion of ~1.5‰ is arguably dubious because it is largely defined by a single datapoint. However, the disappearance of *Monotis*, which often dominates amongst Norian fauna, is unambiguous (e.g. Ward et al., 2001, 2004; Wignall et al., 2007; Rigo et al., 2016, 2020). The last occurrence of *Monotis* has been used as a proxy approximating the NRB in many sections globally, despite being understood to be somewhat older than many other proxies (e.g. Ward et al., 2001, 2004; Wignall et al., 2007; Rigo et al., 2016, 2020; Lei et al., 2022). The Kennecott Point section also hosts a rare occurrence of *Misikella posthernsteini* in Panthalassa, at ~77 m extrapolating from Figure 3.6 (Orchard, 1991b; Carter & Orchard, 2007; Orchard et al., 2007). The first occurrence of this conodont species is widely used to mark the NRB in Tethys (e.g. Krystyn, 2010; Rigo et al., 2016, 2018; Karádi et al., 2020), but co-occurrence with the ammonoid *Chorisoceras nobile* at Kennecott Point suggests this occurrence of *Mi. posthernsteini* is well into the Rhaetian Stage (Tipper et al., 1994; Orchard, 1991b; Carter & Orchard, 2007; Orchard et al., 2007).

Deposition at the Kennecott Point section has been interpreted as having occurred in an open ocean slope setting (e.g. Desrochers & Orchard, 1991; Kasprak et al., 2015; Schoepfer et al., 2016). A number of past studies have utilized a wide variety geochemical proxies to investigate the paleoenvironmental conditions spanning the Norian–Hettangian interval of Kennecott Point, and generally propose expanding anoxic conditions and biotic distress at the Triassic/Jurassic boundary, as well as for variable portions of the late Rhaetian, but do not suggest that these disturbances extend back to the NRB (e.g. Ward et al., 2001, 2004; Williford et al., 2007b, 2009; Kasprak et al., 2015; Schoepfer et al., 2016).

The occurrence of reduced platform morphologies in *Mo.* ex gr. *carinata* begins at 16.8 m within the Kennecott Point section, and in *Mo.* ex gr. *englandi* at 18.0 m, both situated higher than the radiolarian-defined NRB at 10.7 m (Figure 3.6). Although these reduced platform morphologies emerge in the Rhaetian, it is notable that the late Norian forms still occur in the highest conodont sample recovered from the section (Figure 3.6). Although limited by the absence of middle Norian specimens at Kennecott Point, the lack of a clear gradual trend towards more negative CV1 values for *Mo.* ex gr. *carinata* may suggest pectiniform platform reduction did not occur continuously from the middle Norian through to the Rhaetian as could be interpreted from the CVA results, but perhaps stepwise instead. Although the emergence of reduced platform morphologies in both conodont species occur somewhat later than other NRB proxies, this shift is likely still associated with the NRB as all these biotic changes are clustered much closer to each other stratigraphically than to the Triassic/Jurassic boundary located significantly higher in the Kennecott Point section (99.9 m, extrapolating from Figure 3.6) (Ward et al., 2001, 2004; Carter & Orchard, 2007; Williford et al., 2007b, 2009; Kasprak et al., 2015; Schoepfer et al., 2016). The apparent asynchroneity of response to the disturbance around the NRB could be interpreted as evidence for different biotic groups having differing degrees of susceptibility to the environmental changes associated with the boundary, as motile organisms such as conodonts (e.g. Briggs et al., 1983; Purnell,

1995) were perhaps able to endure the abiotic stress better than benthic, sessile communities.

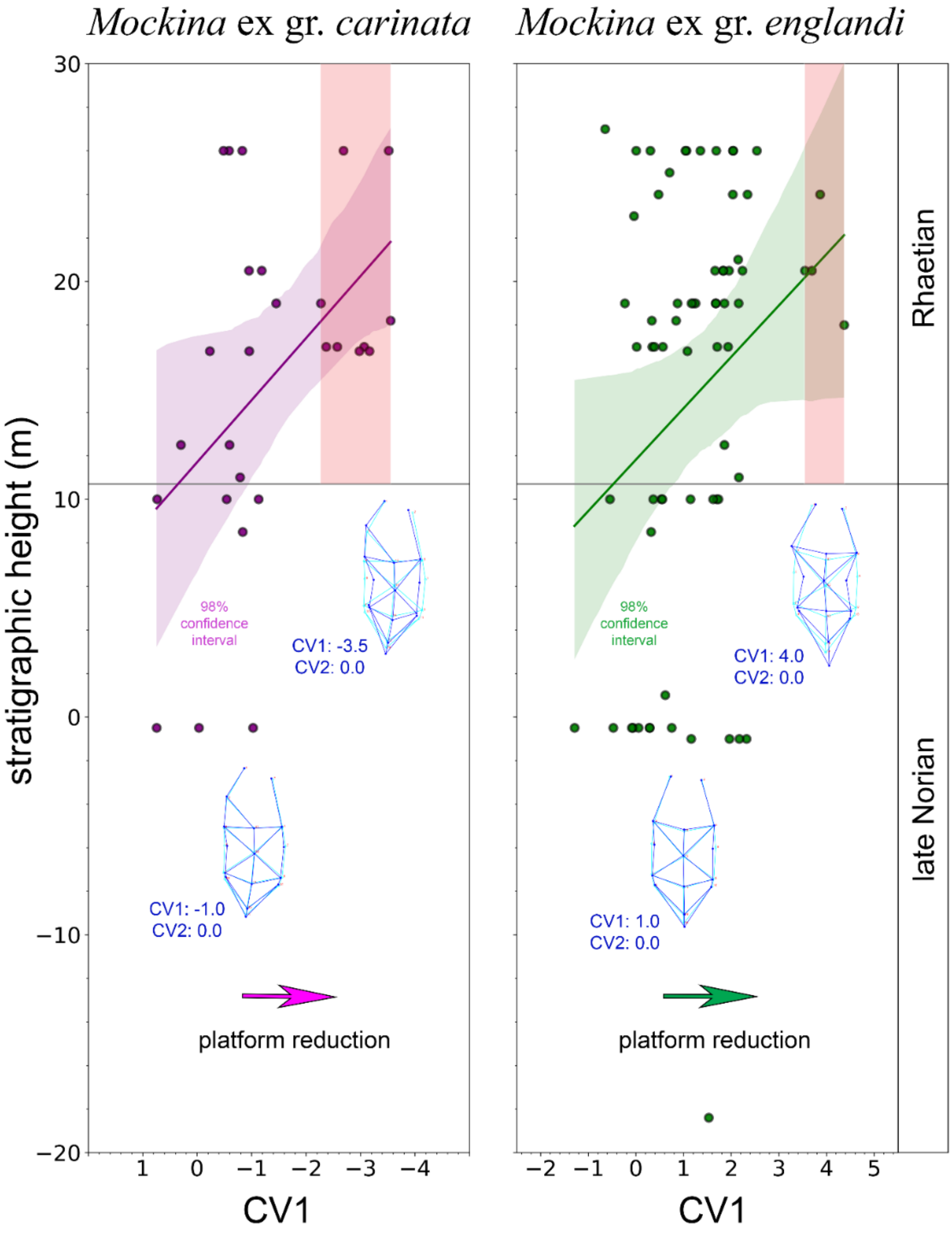

Figure 3.6: CV1 eigenscores from CVA with age as the group classifier of *Mockina* ex gr. *carinata* and *Mockina* ex gr. *englandi* across the Kennecott Point section from Carter and Orchard (2007). The NRB is drawn at the base of the *Proparvicingula moniliformis* Zone. The range of CV1 eigenscores exclusively exhibited by Rhaetian specimens are highlighted in red for each species. A linear line of best fit is displayed in purple for *Mo.* ex gr. *carinata*, and in green for *Mo.* ex gr. *englandi*, with each regression surrounded by their respective 98% confidence interval.

3.5.3. Paleoenvironmental implications

Shifts in conodont element morphology may reflect the changing needs of food resource acquisition, as it has been widely suggested that conodont elements comprised a feeding apparatus that functioned by grasping and masticating food material (e.g. Briggs et al., 1983; Purnell & von Bitter, 1992; Purnell, 1993, 1995; Donoghue & Purnell, 1999; Purnell & Jones, 2012; Martínez-Pérez et al., 2014b, 2016; Kelz et al., 2023). Conodont survivorship across the Permian/Triassic mass extinction was remarkably high, and this may have been due in some degree to adaptations made in response to the extreme environmental pressures of this time interval, such as decreasing pectiniform element size in response to previous food sources becoming compromised (e.g. Clark et al.,1986; Luo et al., 2006; Schaal et al., 2016; Zhang et al., 2017; Lai et al., 2018). The platform reduction observed across the NRB in both *Mo.* ex gr. *carinata* and *Mo.* ex gr. *englandi*, even when controlling for specimen size, may similarly reflect a response to environmental disturbance impacting food availability.

While changes in the overall size or complexity of conodont elements can indicate some manner of disruption to feeding habits, the presence/absence of platforms on pectiniform elements is not wholly dependent on element size, but instead likely reflects diversity in ecological niche (e.g. Ginot & Goudemand, 2019). Therefore, the platform width reduction observed across the NRB may allow for more specific inferences regarding mode of life shifts due to the greater linkage between morphology and function than consideration of element size alone. It has long been proposed that pectiniform conodont elements were somewhat analogous in function to mammal molars, in the sense of being specialized for grinding motions as opposed to grasping or shearing motions, based on multiple lines of evidence including growth allometry, patterns of microwear, and occlusion modelling (e.g. Purnell, 1993, 1995; Donoghue & Purnell, 1999; Purnell & Jones, 2012; Martínez-Pérez et al., 2014b; Kelz et al., 2023). Although food sources for conodonts remain largely speculative, Martínez-Pérez et al. (2016) demonstrate how the gradual evolutionary expansion of a wider platform in the conodont genus *Polygnathus* would work to distribute stress such that greater forces can be endured during element function, opening up the viability of processing harder materials. The platform reduction in pectiniform elements across the NRB, both intraspecifically in Panthalassa and intergenerically in Tethys, may therefore indicate a trend in which some conodonts shifted away from mineralized food sources in the Rhaetian. This response may have been due to a change in availability of different food sources as compared to the Norian.

An alternative driver for the pectiniform platform reduction across the NRB would be elevated bioapatite mineralization pressure, directly inhibiting the growth of robust conodont elements. However, there is no evidence of phosphatic mineralization suppression around the Norian–Rhaetian interval. For example, at Williston Lake in British Columbia, the presence of abiotically precipitated phosphatic pebble conglomerate beds commonly mark the Rhaetian, and are interpreted to indicate spreading anoxic conditions off the western margin of Laurentia in the leadup to the ETME (Larina et al., 2019).

Global carbonate mineralization suppression has long been associated with the ETME, caused by ocean acidification linked to the enhanced volcanic outgassing of CAMP emplacement (e.g. Stanley, 1988; Hautmann, 2004). The decline of faunal groups such as bivalves and corals at the NRB may suggest that this carbonate suppression began to occur much earlier, albeit to a lesser degree (Ward et al., 2001, 2004; Flügel & Kiessling, 2002; Stanley, 2003; Wignall et al., 2007; Rigo et al., 2016, 2020; Lei et al., 2022). If carbonate biomineralization was suppressed in these groups, it is possible that the same pressures were being exerted on potential conodont food sources at the NRB as well. A decrease in the prevalence of mineralized food sources would render robust pectiniform elements unnecessary. This interpretation involving carbonate suppression would support the hypothesis of large-scale CO_2 emission being the causal mechanism of the environmental disturbance at the NRB, as has been previously proposed by a number of studies (e.g. Korte et al., 2003; Callegaro et al., 2012; Tackett et al., 2014; Zaffani et al., 2017; Rigo et al., 2020). However, with the absence of any large igneous province convincingly associated with the NRB, the source of this hypothetical episode of enhanced greenhouse gas emission remains speculative.

3.6. Conclusions

Morphometric analyses conducted on the pectiniform elements of the conodont species *Mockina* ex gr. *carinata* and *Mockina* ex gr. *englandi* spanning the middle Norian through Rhaetian of many localities in western Canada demonstrate that both species exhibit platform width reduction across the NRB. In regard to *Mo.* ex gr. *carinata*, this platform reduction occurs sequentially from middle Norian to late Norian to Rhaetian, whereas in *Mo.* ex gr. *englandi* the shift only occurs across the NRB. Overall, *Mo.* ex gr. *englandi* seems to be more conservative in terms of morphological change than *Mo.* ex gr. *carinata*, as the former's morphologies do not separate the age bin clusters as prominently as the latter's along CV axes. With the reduced platform morphologies of both species arising in the Rhaetian, specimens of *Mo.* ex gr. *carinata* and *Mo.* ex gr. *englandi* from the Canadian Cordillera that have a mid-platform length to breadth ratio greater than 3:1 can be reliably identified as Rhaetian in age. It is notable that many of the Norian forms are still conserved across the NRB, so specimens with a lower ratio can still potentially be Rhaetian. At Kennecott Point specifically, the emergence of the reduced platform morphologies does not occur until somewhat after many other disturbances and biostratigraphic proxies associated with the NRB, such as the disappearance of the bivalve genus *Monotis* (Ward et al., 2001, 2004). This new intraspecific platform reduction observed in Panthalassa is consistent with intergeneric trends largely observed in many conodonts from the Tethys (e.g. Orchard et al., 2007;

Giordano et al., 2010; Mazza et al., 2012; Rigo et al., 2018; Karádi et al., 2020; Du et al., 2021, 2023), suggesting that these morphological trends (as well as their driving mechanisms) are global in extent. A potential explanation for the pectiniform platform reduction is a shift in primary diet away from hard materials, perhaps reflecting elevated carbonate mineralization pressure beginning around the NRB. Biomineralization suppression is typically associated with the ETME (e.g. Stanley, 1988; Hautmann, 2004), but if this pressure began at a lesser severity as far back as the NRB, this would support the concept of a drawn-out multiphase mass extinction leading into the end-Triassic.

Chapter 4

Late Triassic carbon isotope anomalies in the Canadian Cordillera: Paleoenvironmental disturbances associated with the Norian/Rhaetian boundary and end-Triassic mass extinction event

4.1. Abstract

The Late Triassic was a particularly turbulent interval of the geologic past, marked by repeated paleoenvironmental instability culminating in the end-Triassic mass extinction (ETME). These episodes of disturbance are associated with enhanced volcanism, harbinger to the eventual break-up of Pangea. As evidenced by geochemical signals in the marine carbon isotope record, these events were often significant enough to disrupt the global carbon cycle. However, the duration and extent of ETME-associated disturbance leading up to the Triassic/Jurassic boundary (TJB) remains contentious. The present study investigates eight stratigraphic sections from across British Columbia to compile a Panthalassan carbon isotope record spanning the Norian to early Hettangian. A series of three distinct negative excursions are observed: an excursion proximal to the Norian/Rhaetian boundary (NRB), another excursion within the Rhaetian, and a final excursion coinciding with the TJB. This is generally consistent with prior studies, but suggests there may be no clear distinction between the negative excursion associated with the NRB, and the oldest Rhaetian “precursor” excursion proposed to be associated with the TJB. Several of the excursions observed in the

present study are too large in magnitude to plausibly reflect global ocean water chemistry (~10‰ compared to the expected ~3‰), suggesting some local mechanism was amplifying these carbon isotope excursions. A potential explanation is increased organic carbon respiration in restricted marine environments, triggered during episodes of paleoenvironmental disturbance. Regardless, this evidence for repeated carbon isotope excursions supports some prior fossil evidence that the ETME is not just a geologically instantaneous event at the TJB, but is instead the amalgamation of several turnovers beginning as early as the NRB. This work highlights the importance of the NRB within the broader trends of Late Triassic Earth history, motivating further research into this interval.

4.2. Introduction

4.2.1. Timing of Late Triassic paleoenvironmental shifts

As one of the “Big Five” mass extinctions, much emphasis has been placed on investigating the end-Triassic mass extinction (ETME), but efforts have largely focused on the Triassic/Jurassic boundary (TJB) where the event is most striking (e.g. Sepkoski, 1981; Raup & Sepkoski, 1982). Research on the longer term paleoenvironmental trends across the Late Triassic have been much less common, with the comparative lack of data contributing to uncertainty and disagreement regarding the paleoenvironmental conditions leading up to the TJB (e.g. Hesselbo et al., 2002; Ward et al., 2004; Ruhl & Kürschner, 2011; Schoepfer et al., 2016; Davies et al., 2017; Yager et al., 2017; Larina et al., 2019; Wignall & Atkinson, 2020). Some studies have even argued that the ETME may be better characterized as the aggregation of multiple temporally disparate biotic turnover events throughout the latest Triassic, beginning as early as the Norian/Rhaetian boundary (NRB) (Hallam, 2002; Tanner et al., 2004; Rigo et al., 2018, 2020). This potential misattribution of all latest Triassic faunal turnover to the ETME is exacerbated by an apparent global suppression of carbonate sedimentation near the end-Triassic, resulting in very few sections around the world preserving continuous carbonate strata and calcifying organisms across the latest Triassic (e.g. Hautmann, 2004). With the Rhaetian Stage hosting a collection of unique fauna distinct from those of both the preceding Norian and subsequent Hettangian stages, the Rhaetian can be interpreted as an ephemeral phase in evolutionary history that spanned several million years, during which extinction rates were high following the relative stability of the Norian (Hallam, 2002; Tanner et al., 2004; Rigo et al., 2018, 2020).

If Rhaetian ecosystems were to some extent stressed into being more susceptible to collapse than their Norian counterparts, and this state was maintained on geological timescales leading up to the terminal extinction event at the TJB, persistent mechanisms for ecosystem disturbance such as tectonic drivers and volcanism would need to be invoked.

The Pangea supercontinent separating the Panthalassan Ocean (preserved in North American and East Asian strata) and the Tethyan Ocean (preserved in European strata) was beginning to rift apart in the Late Triassic (e.g. Colpron & Nelson, 2009, 2011). This process reached a climax during volcanism that emplaced the Central Atlantic

Magmatic Province (CAMP), a large igneous province (LIP) temporally associated with the ETME, specifically at the TJB (Marzoli et al., 1999, 2004; Blackburn et al., 2013; Zaffani et al., 2017). As episodes of rifting-associated volcanism trigger ecological perturbations that disrupt global marine carbon cycling, they can be preserved as carbon isotope anomalies in the sedimentary rock record (e.g. Ward et al., 2001, 2004, 2007; Korte et al., 2005; Zaffani et al., 2017, 2018). Longer timescale investigation of these carbon isotope anomalies during the Norian through Hettangian interval may better elucidate the nature of the ETME by placing it in the broader context of Late Triassic paleoenvironmental change.

4.2.2. The Norian/Rhaetian boundary

Significant faunal turnover occurred at the NRB that affected many marine groups, including bivalves, conodonts, radiolarians, and ammonoids (e.g. Ward et al., 2001, 2004; Carter & Orchard, 2007; Lucas, 2018; Rigo et al., 2018, 2020). The causal mechanism of the paleoenvironmental disturbance at the NRB has been largely speculative. Callegaro et al. (2012) interpreted decreasing $^{87}Sr/^{86}Sr$ values across the NRB as the beginning of weathering input from CAMP volcanism, but this trend in $^{87}Sr/^{86}Sr$ values was established in Tethyan localities and appears to not be convincingly reproducible in Panthalassan localities (Tackett et al., 2014; Lei et al., 2022). Additionally, all current radiometric dating of the CAMP places the onset of eruptive volcanism at ~201.5 Ma, coinciding with the later TJB (Marzoli et al., 1999, 2004; Blackburn et al., 2013; Zaffani et al., 2017). This is much younger than the NRB at ~209 Ma (e.g. Galbrun et al., 2020; Caruthers et al., 2022). Volcanism associated with the lesser known Angayucham LIP in Alaska has been proposed as an alternative trigger for the paleoenvironmental disturbance at the NRB, supported by a late Norian decrease in $^{187}Os/^{188}Os$ ratios (Zaffani et al., 2017; Rigo et al., 2020; Sato et al., 2023). However, this claim requires further testing, as current radiometric age constraints on this LIP are imprecise, with uncertainties of ±7 million years (Ernst & Buchan, 2001).

4.2.3. The end-Triassic mass extinction

The ETME represents faunal turnover at an extreme severity and scale, impacting a wide variety of both marine and terrestrial groups (e.g. Sepkoski, 1981; Raup & Sepkoski, 1982). However, there is evidence suggesting that many faunal groups experienced significant diversity decline preceding the TJB, even including groups generally considered to have been the most impacted by the ETME, such as conodonts and ammonoids (e.g. Hallam, 2002; Tanner et al., 2004; Rigo et al., 2020; Lei et al., 2024). Some latest Triassic conodonts in the Rhaetian potentially even reflect distress through a shift to less robust morphologies, as compared to their Norian predecessors (Lei et al., 2024). The trajectory that ultimately lead to the final extinction of conodonts, as well as extinctions amongst many other groups commonly attributed to the ETME, was perhaps set well prior to the TJB (e.g. Hallam, 2002; Tanner et al., 2004; Martínez-Pérez et al., 2014a; Rigo et al., 2018; Lei et al., 2024). It is widely accepted that the paleoenvironmental disturbance of the ETME was principally caused by enhanced volcanic outgassing resulting from the emplacement of the CAMP, which ranks amongst the largest known LIPs (Marzoli et al., 1999; 2004; Blackburn et al., 2013). The apparent global suppression of carbonate sedimentation near the end-Triassic (e.g.

Hautmann, 2004), as well as disproportionately high extinction rates for aragonite and high-magnesium calcite biomineralizing organisms (e.g. Hautmann, 2004), suggests that temperature rise and ocean acidification associated with elevated atmospheric CO_2 was the primary driver for extinction (McElwain et al., 1999; Greene et al., 2012). Increased outgassing from non-eruptive volcanism that is nevertheless associated with the CAMP has also been proposed as the cause of paleoenvironmental instability in the late Rhaetian, leading up to the TJB (Ruhl & Kürschner, 2011; Davies et al., 2017).

4.2.4. Carbon isotope anomalies in the Late Triassic

Records of $\delta^{13}C$ values are commonly used proxies in paleoenvironmental studies, recording instances of disruption to the global carbon cycle throughout Earth history (e.g. Baud et al., 1989; Keller & Lindinger, 1989; Ward et al., 2001, 2004, 2007; Korte et al., 2004, 2005; Zaffani et al., 2017, 2018). A negative excursion in $\delta^{13}C_{org}$ values is associated with the NRB in several localities within the Lagonegro Basin in southern Italy (Maron et al., 2015; Rigo et al., 2016; Zaffani et al., 2017). This negative excursion is also observed in the values of $\delta^{13}C_{org}$ at Wombat Basin, Australia, and in the $\delta^{13}C$ values of biomarkers fluoranthene and benzofluoranthene at the North Rankin - 5 well, North West Shelf, Australia (Rigo et al., 2020). In eastern Panthalassa, this negative excursion has been observed in the values of $\delta^{13}C_{carb}$ from the Whitehorse Trough, Canada (Lei et al., 2022). However, other Tethyan $\delta^{13}C_{carb}$ records compiled from sections across Europe (Korte et al., 2005; Muttoni et al., 2014), and Panthalassan organic and carbonate $\delta^{13}C$ records from Haida Gwaii, Canada (Ward et al., 2001, 2004; Whiteside & Ward, 2011) do not present a clear negative excursion at this boundary, but do seem to show an increase in point-to-point stratigraphic variability compared to samples taken from strata before and after the boundary. This trend of increased scatter is also observed in the values of $\delta^{13}C_{org}$ at Kiritehere, New Zealand, as well as in the values of $\delta^{13}C_{org}$ at Kastelli, Greece, and in the values of organic and kerogen $\delta^{13}C$ at the Delambre - 1 well North West Shelf, Australia (Rigo et al., 2020; Rigo & Campbell, 2022). Rapidly oscillating values are observed in the $\delta^{13}C_{org}$ record of the NRB interval at Williston Lake, Canada, and are alternatively interpreted as a positive excursion resulting from widespread ocean stagnation and anoxia (Sephton et al., 2002; Wignall et al., 2007).

Whilst interpreting potentially comparable phenomena around the Early Triassic and TJB, Whiteside and Ward (2011) termed instances of rapid oscillation in $\delta^{13}C$ values as "Chaotic Carbon Intervals", wherein prolonged periods of low biodiversity following disturbance events create unstable ecosystems more prone to positive feedback loops. Thriving biotic realms have long been proposed to have a stabilizing effect on global climate (e.g. Charlson et al., 1987), the absence of which would more easily allow runaway amplification of an initial disturbance, and cause continuous carbon cycle instability persisting until biodiversity recovers beyond a certain threshold (Whiteside & Ward, 2011). These authors, however, do not specifically identify the NRB as an example of a "Chaotic Carbon Interval."

A negative excursion in $\delta^{13}C$ values is associated with the TJB globally, observed in both $\delta^{13}C_{carb}$ and $\delta^{13}C_{org}$ records at Kennecott Point, Canada (Ward et al., 2001, 2004; Williford et al., 2007b), Csővár, Hungary (Pálfy et al., 2001, 2007), the Bergamasc Alps, Italy (Galli et al., 2005), and near Levanto, Peru (Yager et al., 2017). This negative excursion is observed in $\delta^{13}C_{carb}$ profiles from Lorüns, Austria (McRoberts et al., 1997), and the Budva Basin, Montenegro (Črne et al., 2011; de Graaff et al., 2022), as well as in $\delta^{13}C_{org}$ records at St. Audrie's Bay, United Kingdom (Hesselbo et al., 2002), New York Canyon, United States of America (Guex et al., 2004; Ward et al., 2007; Thibodeau et al., 2016), the Northern Calcareous Alps, Austria (Kürschner et al., 2007; Ruhl et al., 2009; Ruhl & Kürschner, 2011), Inuyama, Japan (Kuroda et al., 2010; Fujisaki et al., 2018), Wüstenwelsberg, Germany (Ruhl & Kürschner, 2011), the Lombardy Basin, Italy (Bachan et al., 2012; Zaffani et al., 2018), and the La Spezia Basin, Italy (Du et al., 2020b). Many studies suggest two additional negative excursions distinct from and preceding the "main" excursion coinciding with the TJB, termed "precursor" and "initial" chronologically (e.g. Hesselbo et al., 2002; Ward et al., 2004; Ruhl et al., 2009; Ruhl & Kürschner, 2011; Fujisaki et al., 2018; Zaffani et al., 2018; Du et al., 2020b; de Graaff et al., 2022).

The present study integrates lithostratigraphy, biostratigraphy, and carbon isotope chemostratigraphy to investigate the paleoenvironmental conditions during the Late Triassic, spanning both the NRB and TJB in stratigraphic sections of well-preserved carbonate strata across the Canadian Cordillera. Whereas past studies have typically investigated these Late Triassic events in isolation, the present study examines the

NRB, TJB, and intervening strata in a more unified context. These sections also represent a wide variety of depositional settings, ranging from nearshore ocean island plateau, to deep marine off the Laurentian Craton. This approach has the potential to improve understanding of the ETME in North America by investigating paleoenvironmental shifts throughout the Norian – Rhaetian interval leading up to the TJB.

4.3. Geological setting

Stretching from the Canadian Rockies to the Pacific coast, the Canadian Cordillera is an expansive zone of deformation resulting from the amalgamation of crustal terranes with varying stratigraphic and tectonic histories that accreted to the western margin of the Laurentian Craton (Monger & Ross, 1971; Monger, 1997). These terranes have been interpreted as fragments of continental crust, oceanic crust, and volcanic island arcs (e.g. Colpron & Nelson, 2009, 2011). Based on evidence from faunal distributions, paleomagnetism, detrital zircon geochronology, and crustal geochemistry, these terranes display evidence for considerable latitudinal and longitudinal displacement prior to accretion (e.g. Monger & Ross, 1971; Jones et al., 1977; Mihalynuk et al., 1994; Belasky et al., 2002; Johnston & Borel, 2007; Johnston, 2008; Kent & Irving, 2010; Beranek & Mortensen, 2011). The exact relationships between these terranes, and their relative positionings throughout the late Paleozoic and Mesozoic, remain poorly constrained and contentious. It has been proposed that during the Triassic, the contiguous Stikine and Quesnel terranes were approaching close to ancestral North America, forming a forearc basin to the east of the terranes (e.g. Colpron & Nelson, 2009, 2011). Meanwhile, the contiguous Wrangell and Alexander terranes were likely located further to the west, in the open ocean of Panthalassa (e.g. Colpron & Nelson, 2009, 2011). The present study investigates several localities preserving the NRB and TJB distributed throughout the Canadian Cordillera (Figure 4.1A). Examining sections from a variety of tectonic settings enable local trends to be differentiated from regional trends, facilitating the compilation of a unified Panthalassan record.

Along the eastern branch of Williston Lake in northeastern British Columbia, stratigraphic sections of Laurentian Craton affinity spanning the NRB and TJB are exposed in the predominantly carbonate Pardonet Formation and mixed carbonate/siliciclastic Fernie Formation at Ne Parle Pas Point, Pardonet Creek, and Black Bear Ridge (Figures 4.1B, 4.2; e.g. Orchard et al., 2001; Sephton et al., 2002; Hall & Pitaru, 2004; Orchard, 2007, 2014, 2019; McRoberts, 2007, 2011; Wignall et al., 2007; Williford et al., 2007a; Zonneveld et al., 2010; Greene et al., 2012; Golding et al., 2016; Larina et al., 2019; Lei et al., 2021). These sections represent Late Triassic marine deposition off the western margin of Laurentia, then part of the supercontinent Pangea (e.g. Colpron & Nelson, 2009, 2011), along a carbonate ramp ranging from medial to distal in setting (e.g. Orchard et al., 2001; Wignall et al., 2007; Zonneveld et al., 2010; McRoberts, 2011).

Across northern Vancouver Island, stratigraphic sections of Wrangell Terrane affinity spanning the NRB and TJB are exposed in the mixed carbonate/volcaniclastic Parson

Bay Formation along Holberg Inlet (Figures 4.1C, 4.2; e.g. Nixon & Orr, 2007; Nixon et al., 2011). Sections spanning the NRB are also exposed in the Parson Bay Formation around Kyuquot Sound (Figures 4.1D, 4.2; Jeletzky, 1970; Orchard, unpublished data). These sections represent Late Triassic marine deposition off an ocean island plateau in the open Panthalassan Ocean (e.g. Colpron & Nelson, 2009, 2011), interpreted as a nearshore setting with strong volcanic and terrestrial siliciclastic influence, evidenced by common interbeds of volcaniclastic breccia, sandstone, and conglomerate (e.g. Nixon & Orr, 2007; Nixon et al., 2011).

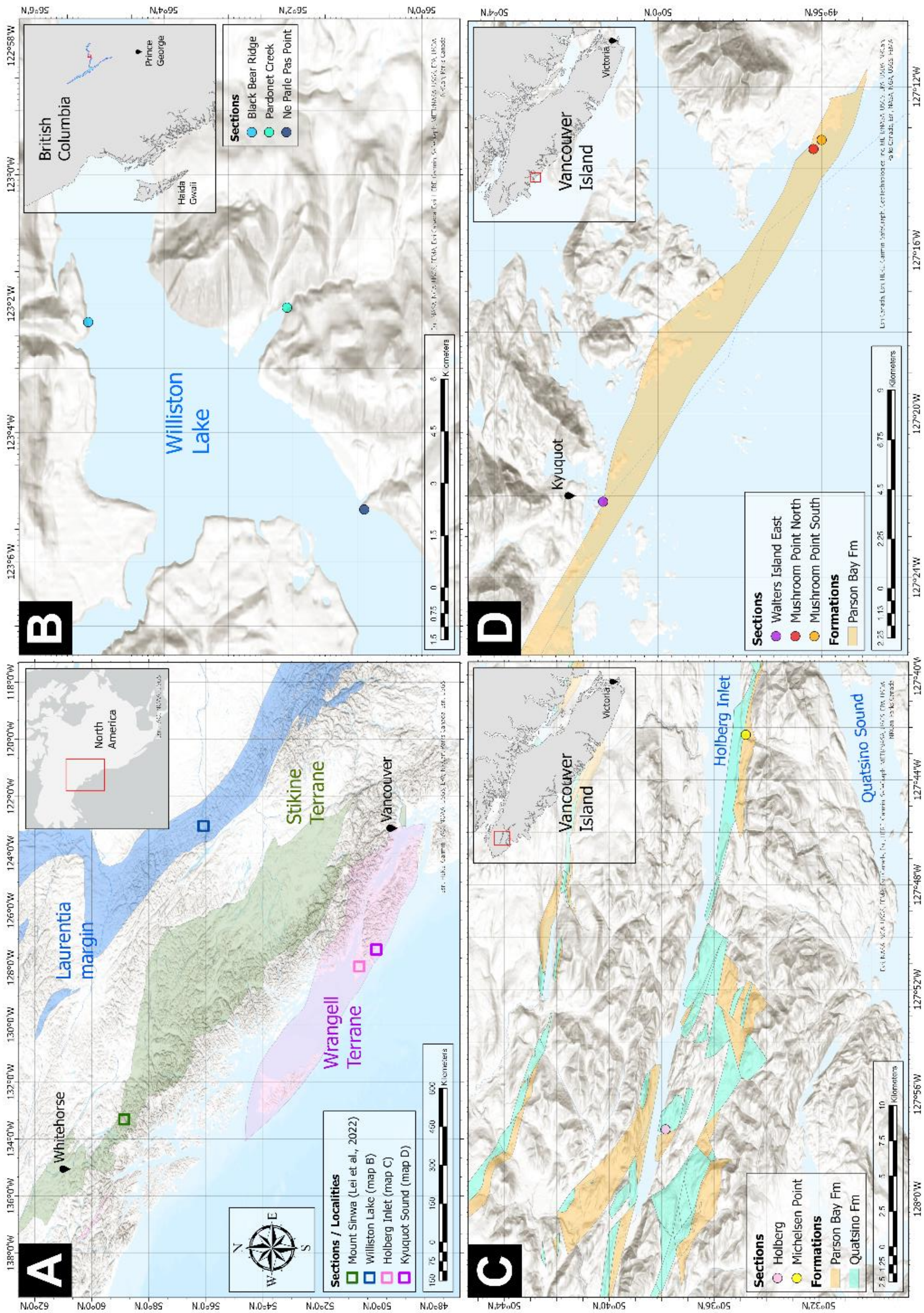
A
Whitehorse
Laurentia margin
Stikine Terrane
Wrangell Terrane
Vancouver
North America
Sections / Localities
Mount Sinwa (Lei et al, 2022)
Williston Lake (map B)
Holberg Inlet (map C)
Kyuquot Sound (map D)
Kilometers
B
Williston Lake
British Columbia
Haida Gwaii
Prince George
Sections
Black Bear Ridge
Pardonet Creek
Ne Parle Pas Point
Kilometers
C
Holberg Inlet
Quatsino Sound
Vancouver Island
Victoria
Sections
Holberg
Michelsen Point
Formations
Parson Bay Fm
Quatsino Fm
Kilometers
D
Kyuquot
Vancouver Island
Victoria
Sections
Walters Island East
Mushroom Point North
Mushroom Point South
Formations
Parson Bay Fm
Kilometers

Figure 4.1: A: Locations of select stratigraphic sections that span the NRB and/or the TJB across the Canada Cordillera. Terrane affinities include the Laurentia margin, the Stikine Terrane, and the Wrangell Terrane (from east to west). Terrane boundaries are from Colpron and Nelson (2011). B: Locations of the Black Bear Ridge, Pardonet Creek, and Ne Parle Pas Point sections along the shoreline of Williston Lake. C: Locations of the Holberg and Michelsen Point sections on a geological map of the Holberg Inlet from Nixon et al. (2011). D: Positions of the Walters Island East, Mushroom Point North, and Mushroom Point South sections on a geological map of Kyuquot Sound from Massey et al. (1994).

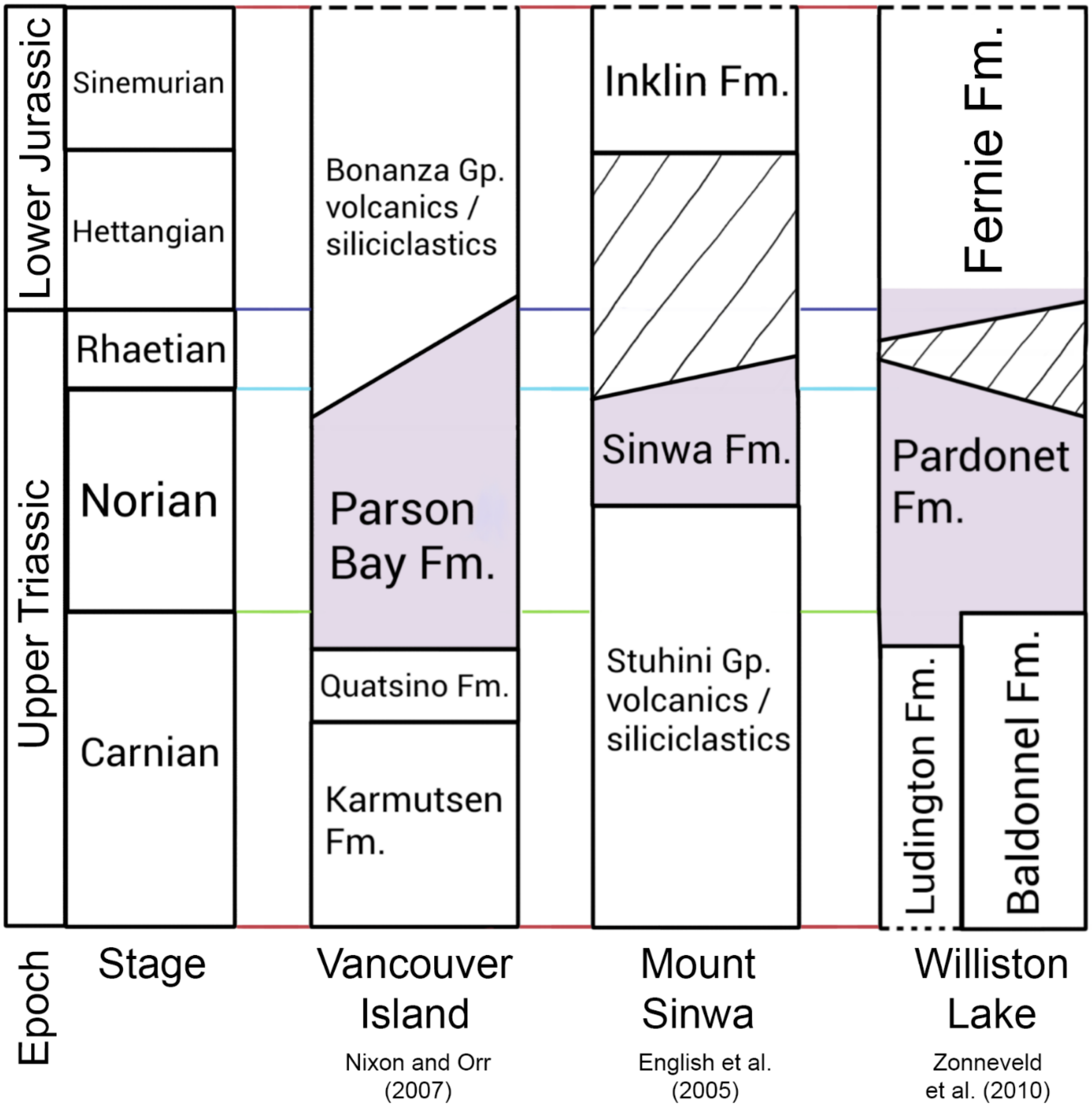

Figure 4.2: Chronostratigraphy across western Canadian localities with relevant stratigraphy (Norian – lower Hettangian limestone) highlighted in purple. Vancouver Island stratigraphy is from Nixon and Orr (2007), and applies to the Holberg, Michelsen Point, Walters Island East, Mushroom Point North, and Mushroom Point South sections. Mount Sinwa stratigraphy is from English et al. (2005), and applies to the Sinwa East

and Sinwa West sections from Lei et al. (2022). Williston Lake stratigraphy is from Zonneveld et al. (2010), and applies to the Black Bear Ridge, Pardonet Creek, and Ne Parle Pas Point sections.

4.4. Materials and methods

4.4.1. Field sampling

Across all stratigraphic sections, 4 – 5 cm diameter samples for geochemical analysis were taken every meter as outcrop allowed, avoiding veins, silicification, coarsely recrystallized zones, and bioclasts where possible. For the Williston Lake sections, sampling intervals for geochemical analysis were tightened to every 10 cm when proximal to suspected age boundaries inferred from prior research. Approximately 2 kg samples for conodonts were taken as well, with sampling every ~10 m across each section and preferentially targeting visibly fossiliferous beds.

4.4.2. Conodont separation

Samples for conodonts were processed at the Geological Survey of Canada Pacific Division in Vancouver, British Columbia using standard techniques as outlined by Stone (1987). Individual samples were crushed into approximately 3 cm fragments before being dissolved in acetic acid for 10 – 14 days. Per 1 kg of sample, a solution of 6 L of water, 3.2 L of 10 – 15% acetic acid (to create a buffer), and 0.8 – 1 L of 99.5% glacial acetic acid was used. The sample residues that remained after dissolution were then sieved to collect the 90 – 850 μm fraction. The isolated fraction was then rinsed, dried, and put through heavy liquid separation using sodium polytungstate (specific gravity of 2.85 kg/L) with the heavy fraction collected. Conodont images were taken with a Hitachi TM3000 scanning electron microscope at the Geological Survey of Canada Pacific Division in Vancouver.

4.4.3. Carbonate $\delta^{13}C$ and $\delta^{18}O$ analysis

For the measurement of $\delta^{13}C$ and $\delta^{18}O$ values of carbonate, samples were cut into 1 – 2 cm thick slabs, perpendicular to bedding when possible. The slabs were microdrilled using a carbide burr to extract approximately 60 mg of powder per sample, preferentially from fine grained matrix and avoiding veins, bioclasts, and weathered zones. The drilled powders were then weighed into glass vials (~0.5 mg per sample) and heated at 90°C for 12 hours to remove any moisture, then acidified with 100% phosphoric acid under a helium flushed headspace. Values of $\delta^{13}C$ and $\delta^{18}O$ from all carbonates were measured at the University of Victoria on a Sercon 20-22 gas-source continuous-flow isotope ratio mass spectrometer with a GasBox II front end. Measurements were corrected with repeated analysis of International Atomic Energy Agency (IAEA) standards IAEA-CO-8 and IAEA-603, or internal standards UVic1 and UVic3 which have been calibrated against IAEA-CO-8 and IAEA-603. Internal standard VTS was used as a monitoring standard. The precision of repeated measurements of standards are ~0.05‰ (1σ) for $\delta^{13}C$ and ~0.20‰ (1σ) for $\delta^{18}O$ (Table 4.1).

Table 4.1: Statistical summary of repeated measurements of standards on a Sercon 20-22 mass spectrometer. All values are expressed in units of per mil (‰ VPDB). Data are only included here if the standard was run as a secondary standard, and thus was not used in the data reduction process.

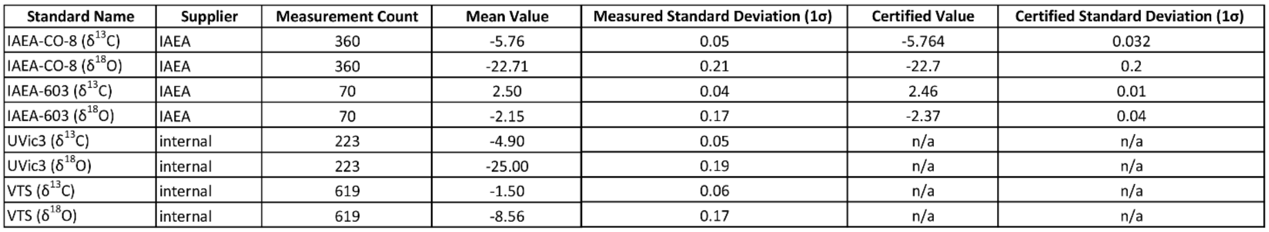

Standard Name	Supplier	Measurement Count	Mean Value	Measured Standard Deviation (1σ)	Certified Value	Certified Standard Deviation (1σ)
IAEA-CO-8 ($\delta^{13}C$)	IAEA	360	-5.76	0.05	-5.764	0.032
IAEA-CO-8 ($\delta^{18}O$)	IAEA	360	-22.71	0.21	-22.7	0.2
IAEA-603 ($\delta^{13}C$)	IAEA	70	2.50	0.04	2.46	0.01
IAEA-603 ($\delta^{18}O$)	IAEA	70	-2.15	0.17	-2.37	0.04
UVic3 ($\delta^{13}C$)	internal	223	-4.90	0.05	n/a	n/a
UVic3 ($\delta^{18}O$)	internal	223	-25.00	0.19	n/a	n/a
VTS ($\delta^{13}C$)	internal	619	-1.50	0.06	n/a	n/a
VTS ($\delta^{18}O$)	internal	619	-8.56	0.17	n/a	n/a

When interpreting these results from the Canadian Cordillera, intervals with anomalous $\delta^{13}C$ values were flagged as to potentially correspond with the negative excursions identified in prior studies. Therefore, focus was especially placed on the intervals where excursions were expected: the NRB, throughout the Rhaetian Stage, and the TJB. Excursion intervals were generally identified when three or more $\delta^{13}C$ values in close stratigraphic proximity deviate from background values by 3‰ or more, with close stratigraphic proximity being within ~2 m for the Williston Lake sections and ~20 m for the Vancouver Island sections, given the differences in sample density and the expanded/condensed nature of each section. Exceptions to this criteria were made when potential excursions were supported by additional stratigraphic context, as will be subsequently described. Based on this definition, excursion intervals in the present study often exhibit high point-to-point stratigraphic variability, presenting as an intermixing of anomalous $\delta^{13}C$ values alongside more background values.

4.5. Results

The limestone classification scheme of Dunham (1962), modified by Embry and Klovan (1971), is used for all lithological descriptions. All reference to meterages and intervals of stratigraphic height are expressed relative to the base of their respective section, unless otherwise specified. A variety of fauna is used for constraining biostratigraphic age across the sections, including bivalves, conodonts, ammonoids, and radiolarians. Comprehensive lists of conodont and ammonoid occurrences can be found in Appendix C, along with all $\delta^{13}C$ and $\delta^{18}O$ values.

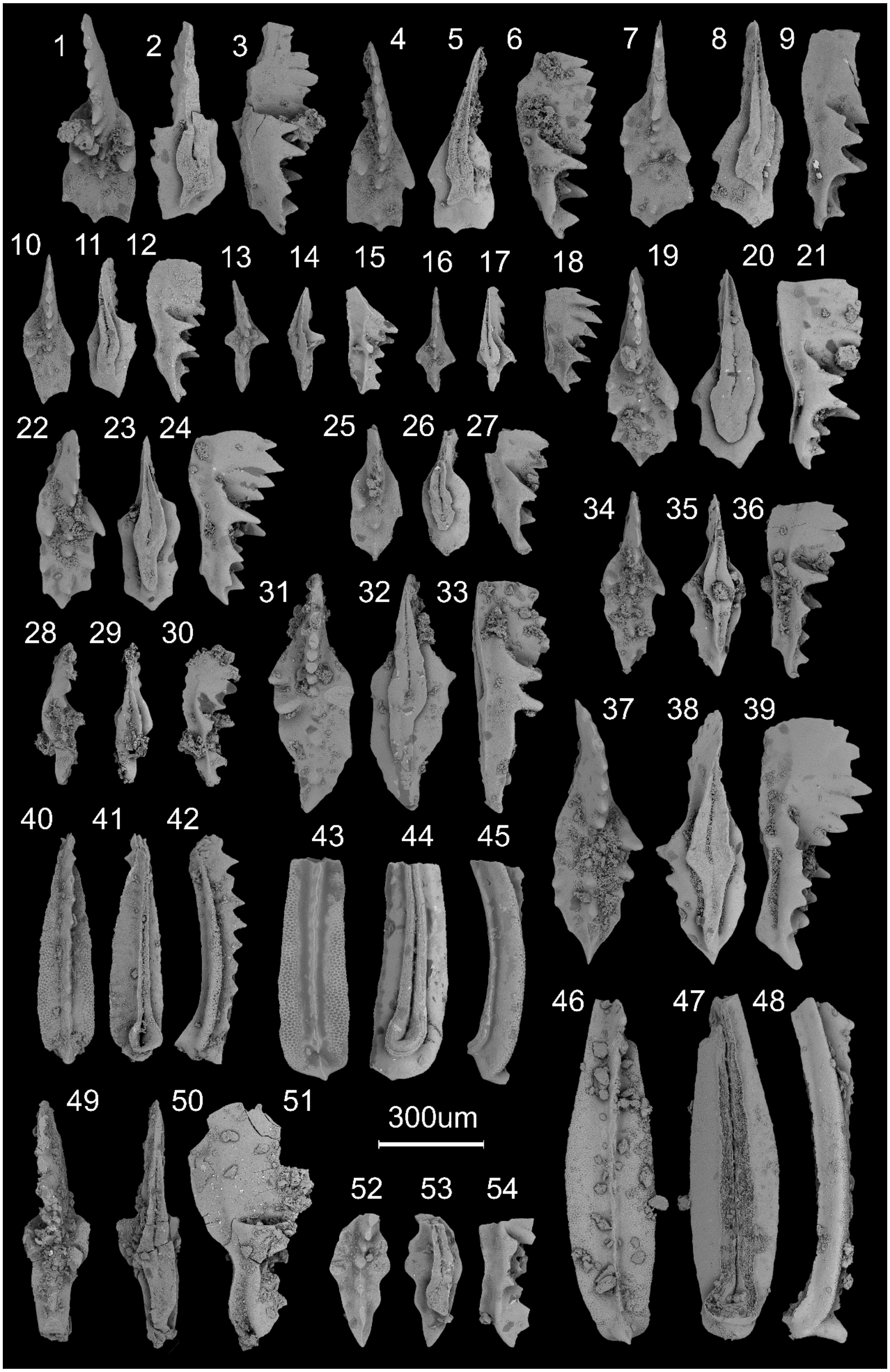
1
2
3
4
5
6
7
8
9
10
11
12
13
14
15
16
17
18
19
20
21
22
23
24
25
26
27
28
29
30
31
32
33
34
35
36
37
38
39
40
41
42
43
44
45
46
47
48
49
50
51
52
53
54
300um

Figure 4.3: Conodont specimens recovered from localities across Williston Lake, Holberg Inlet, and Kyuquot Sound.

1 – 12: *Epigondolella spiculata* Orchard, 1991a. 1 – 3: GSC 139691, from sample GSC Cur. No. C-640943, 25.0 m at Amos Island East (AIE-25), middle Norian. 4 – 6: GSC 139692, from sample GSC Cur. No. C-640943, 25.0 m at Amos Island East (AIE-25), middle Norian. 7 – 9: GSC 139693, from sample GSC Cur. No. C-640941, 1.3 m at Amos Island East (AIE-1.3), middle Norian. 10 – 12: GSC 139694, from sample GSC Cur. No. C-640941, 1.3 m at Amos Island East (AIE-1.3), middle Norian.

13 – 18: *Mockina bidentata* (Mosher, 1968). 13 – 15: GSC 139695, from sample GSC Cur. No. V-016845, 332.8 m at Michelsen Point (MP3-75.3), Norian. 16 – 18: GSC 139696, from sample GSC Cur. No. C-640941, 1.3 m at Amos Island East (AIE-1.3), middle Norian.

19 – 21: *Mockina carinata* (Orchard, 1991a). GSC 139697, from sample GSC Cur. No. V-016679, 187.0 m at Michelsen Point (H2-1), Norian.

22 – 27: *Mockina* cf. *englandi* (Orchard, 1991a). 22 – 24: GSC 139698, from sample GSC Cur. No. V-016998, 176.0 m at Mushroom Point South (MUP2-176), Rhaetian. 25 – 27: GSC 139699, from sample GSC Cur. No. C-640941, 1.3 m at Amos Island East (AIE-1.3), middle Norian.

28 – 30: *Mockina mosheri* (Kozur & Mostler, 1976), morphotype A sensu (Carter & Orchard, 2007). GSC 139700, from sample GSC Cur. No. C-202783, 8.0 m at Walters Island East (92WAI-C4), Rhaetian.

31 – 36: *Mockina mosheri* (Kozur & Mostler, 1976), morphotype B sensu (Carter & Orchard, 2007). 31 – 33: GSC 139701, from sample GSC Cur. No. C-202785, 14.0 m at Walters Island East (92WAI-C6), Rhaetian. 34 – 36: GSC 139702, from sample GSC Cur. No. C-202783, 8.0 m at Walters Island East (92WAI-C4), Rhaetian.

37 – 39: *Mockina*? *spinosa* Orchard, 2018. GSC 139703, from sample GSC Cur. No. V-016998, 176.0 m at Mushroom Point South (MUP2-176), Rhaetian.

40 – 42: *Norigondolella imperfecta* Golding & Orchard, 2021. GSC 139704, from sample GSC Cur. No. C-640942, 12.8 m at Amos Island East (AIE-12.8), middle Norian.

43 – 45: *Norigondolella navicula* (Huckriede, 1958). GSC 139705, from sample GSC Cur. No. V-016678, 78.8 m at Holberg (H1-70.2), early Norian.

46 – 48: *Norigondolella steinbergensis* (Mosher, 1968). GSC 139706, from sample GSC Cur. No. V-016817, 29.7 m at Pardonet Creek (PC-29.7), Rhaetian.

49 – 54: *Orchardella elongata* (Orchard, 1991a). 49 – 51: GSC 139707, from sample GSC Cur. No. V-016824, 124.0 m at Black Bear Ridge (BL-124), middle Norian. 52 – 54: GSC 139708, from sample GSC Cur. No. V-016816, 18.0 m at Pardonet Creek (PC-18), middle Norian.

4.5.1. Williston Lake

4.5.1.1. Williston Lake lithostratigraphy

Wackestone/floatstone and packstone/rudstone containing abundant monotid bivalves dominate the middle to upper Norian strata of all three sections along the shores of

Williston Lake (Figure 4.1B). These prominently bivalve-hosting lithologies are observed from 0.0 – 89.5 m at Ne Parle Pas Point, 0.0 – 29.3 m at Pardonet Creek, and 89.4 – 194.7 m at Black Bear Ridge (Figure 4.4). At the Ne Parle Pas Point and Pardonet Creek sections, shale and lime mudstone dominate above the *Monotis* beds until the top of each section, with distinctive phosphatic lag deposits serving as regional marker beds for Rhaetian strata (Figure 4.4; Larina et al., 2019). These phosphorites are scattered between 101.2 – 105.1 m at Ne Parle Pas Point, and between 38.8 – 41.9 m at Pardonet Creek (Figure 4.4). Larina et al. (2019) interpret these phosphorite deposits as indicative of spreading anoxic conditions in the Rhaetian, and suggest that the uppermost of these deposits approximate the TJB in these sections (Figure 4.4).

At the Black Bear Ridge section, shale and calcareous siltstone dominate above the *Monotis* beds until the top of the section (Figure 4.4). Formerly aragonite fans that have since been recrystallized to calcite are observed between 195.1 – 195.9 m at the section, indicating close proximity to the TJB, as these structures have been suggested to form in response to the loss of biotic carbonate burial during the ETME (Figure 4.4; Greene et al., 2012). Past studies observe early Hettangian ammonoid occurrences beginning just 2.5 m above the top of *Monotis* (197.2 m above the base), presenting a highly condensed Rhaetian interval compared to the other Williston Lake sections (Figure 4.4; Tozer, 1982; Hall & Pitaru, 2004; Wignall et al., 2007; Greene et al., 2012; Golding et al., 2016). The formerly aragonite fans can thus be interpreted as Rhaetian in age (Figure 4.4). More detailed discussion of Williston Lake sedimentary lithofacies can be found in a number of past studies (e.g. Orchard et al., 2001; Hall & Pitaru, 2004;

McRoberts, 2011; Wignall et al., 2007; Zonneveld et al., 2010; Greene et al., 2012; Larina et al., 2019).

4.5.1.2. Williston Lake biostratigraphy

The present study does not differentiate between varieties of monotid, but bivalves proximal to the NRB are assumed to belong to the genus *Monotis*, being by far the most prolific variety in the late Norian (e.g. McRoberts, 2011). Consistent with previous work in the area, the present study utilizes the last occurrence of large *Monotis* specimens to approximate the NRB, although isolated dwarf *Monotis* are still found in the Rhaetian (Figure 4.4; e.g. Sephton et al., 2002; Hall & Pitaru, 2004; Wignall et al., 2007; Zonneveld et al., 2010; McRoberts, 2011; Greene et al., 2012; Golding et al., 2016).

At the Ne Parle Pas Point section, large *Monotis* bivalves are found until 89.5 m, approximating the NRB (Figure 4.4). In terms of ammonoids, *Sagenites minaensis* was recovered between 86.3 – 89.8 m, followed by a single occurrence of *Placites* cf. *polydactylus* at 100.1 m, both species signifying late Norian to Rhaetian age (Figure 4.4).

At the Pardonet Creek section, the highest large *Monotis* is observed at 29.3 m, placing the NRB at this level (Figure 4.4). The conodont *Orchardella elongata* has been recovered from 18.0 m (indicative of middle Norian age), and *Norigondolella* *steinbergensis* occurs at 29.7 m, signifying middle Norian to Rhaetian age (Figures 4.3, 4.4). The ammonoid *Cladiscites tornatus* is found at 32.7 m, reinforcing the Rhaetian age assignment of this stratigraphic height (Figure 4.4).

At the Black Bear Ridge section, the NRB is placed at 194.7 m, where the youngest large *Monotis* are found (Figure 4.4). Ammonoids recovered from the Black Bear Ridge section all indicate early Hettangian age in a rapid succession of *Psiloceras* cf. *tibeticum* at 201.4 m, *Choristoceras* cf. *minutum* at 204.6 m, *Psiloceras* cf. *tilmanni* at 205.6 m, and *Ps. tilmanni* between 205.6 – 206.2 m (Figure 4.4). The conodonts *Mockina carinata*, *Mockina postera*, and *Or. elongata* have been recovered from 124.0 m, with the latter two species specifying middle Norian age, whereas *Mockina bidentata* and *No. steinbergensis* are found at 167.6 m, indicating a middle Norian to Rhaetian age (Figures 4.3, 4.4).

4.5.1.3. Williston Lake chemostratigraphy

Values of $\delta^{13}C_{carb}$ at Ne Parle Pas Point predominantly range between -1.5 – 1.0‰ (92% of 270 data points outside excursion intervals), with two negative excursions of approximately 3‰ magnitude where values reach around -3‰ (Figure 4.4). The lower excursion is observed at 95.9 – 98.7 m, starting 6.4 m above the top of *Monotis*; the upper excursion is observed at 104.0 – 105.9 m, starting 14.5 m above the top of *Monotis* and coinciding with the uppermost phosphorite deposits (Figure 4.4). No significant trends in $\delta^{13}C_{carb}$ values are observed in the datapoints outside of these excursion intervals, with an average of -0.5 ± 0.7‰ (1σ) (Figure 4.4).

Values of $\delta^{13}C_{carb}$ at Pardonet Creek predominantly range between -2.5 – 0.0‰ (92% of 110 data points outside excursion intervals), with three distinct negative excursions observed (Figure 4.4). The lower excursion is approximately 4‰ in magnitude with values reaching around -5‰, observed at 30.1 – 34.2 m, starting 0.8 m above the top of *Monotis* (Figure 4.4). The middle excursion is approximately 2‰ in magnitude with values reaching around -4‰, observed at 41.0 – 41.4 m, starting 11.7 m above the top of *Monotis* and 0.9 m below the uppermost phosphorite deposits (Figure 4.4). This middle excursion is proposed despite the relatively smaller shift magnitude because an additional excursion is expected within the Rhaetian Stage and the substantial covered intervals have likely truncated the signal (Figure 4.4). The upper excursion is approximately 15‰ in magnitude where values reach around -16‰, observed at 45.0 – 53.6 m, starting 15.7 m above the top of *Monotis* and 3.1 m above the uppermost phosphorite deposits (Figure 4.4). There are no significant broader stratigraphic trends in the Norian $\delta^{13}C_{carb}$ values at Pardonet Creek, but it appears that values shift negative across the NRB, and again across the TJB (Figure 4.4). Excluding values within these excursion intervals, the average Norian $\delta^{13}C_{carb}$ value is -0.9 ± 0.7‰ (1σ), the average Rhaetian value is -1.4 ± 0.6‰ (1σ), and the average Hettangian value is -2.9 ± 0.3‰ (1σ) (Figure 4.4).

Values of $\delta^{13}C_{carb}$ from the middle Norian through early Hettangian portion of Black Bear Ridge (between 100.0 m and the section top) predominantly range between -6.0 – -1.0‰ (91% of 152 data points outside excursion intervals), with two negative excursions of approximately 5‰ magnitude where measurements reach around -9‰ (Figure 4.4). The lower excursion is observed at 187.6 – 196.0 m, coinciding with the top of *Monotis*; the upper excursion is observed at 201.3 – 204.6 m, starting 6.6 m above the top of *Monotis* (Figure 4.4). In terms of $\delta^{13}C_{carb}$ value trends across the Norian, Black Bear Ridge has much more scatter than the other Williston Lake sections (Figure 4.4). The average middle Norian $\delta^{13}C_{carb}$ value is -4.4 ± 1.5‰ (1σ). There is then a slight gradual positive shift across the late Norian from approximately -3‰ to -1‰ leading up to the lower excursion interval (Figure 4.4). The average Rhaetian and Hettangian value excluding the upper excursion interval is -3.6 ± 1.3‰ (1σ) (Figure 4.4).

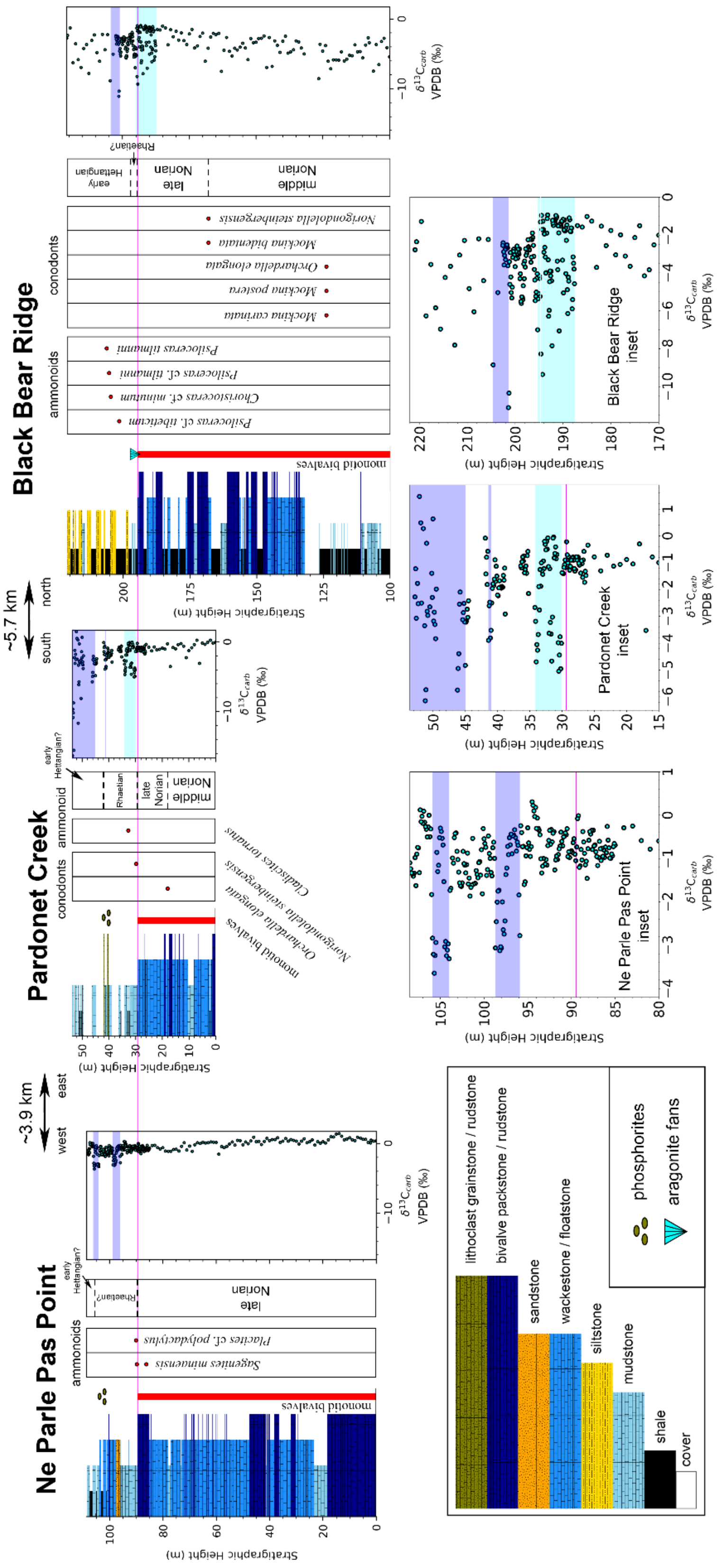
Ne Parle Pas Point
~3.9 km
west
east
Pardonet Creek
~5.7 km
south
north
Black Bear Ridge
Stratigraphic Height (m)
monotid bivalves
ammonoids
Sagenites minaensis
Placites cf. polydactylus
early Hettangian?
Rhaetian?
late Norian
δ13Ccarb VPDB (‰)
conodonts
ammonoid
Monotid bivalves
Orchardella elongata
Norigondolella steinbergensis
Cladiscites tornatus
middle Norian
late Norian
Rhaetian
early Hettangian?
Psiloceras cf. tilmanni
Choristoceras cf. minutum
Psiloceras cf. ibericum
Psiloceras tilmanni
Mockina carinata
Mockina postera
Orchardella elongata
Mockina bidentata
Norigondolella steinbergensis
middle Norian
late Norian
early Hettangian
Rhaetian?
Ne Parle Pas Point inset
Pardonet Creek inset
Black Bear Ridge inset
lithoclast grainstone / rudstone
bivalve packstone / rudstone
sandstone
wackestone / floatstone
siltstone
mudstone
shale
cover
phosphorites
aragonite fans

Figure 4.4: Compiled lithostratigraphic, biostratigraphic, and geochemical results from the Williston Lake sections spanning the upper Pardonet and lower Fernie formations. The sections are correlated using the last occurrence of *Monotis* in each section, marked by a magenta line. The positions of the TJB at both Ne Parle Pas Point and Pardonet Creek are placed at the uppermost phosphorite deposits observed, an approximation consistent with that of Larina et al. (2019). The position of the TJB at Black Bear Ridge is based on ammonoid occurrences from prior studies (Hall & Pitaru, 2004; Wignall et al., 2007; Greene et al., 2012; Golding et al., 2016). All other boundaries are based on new data from the present study, and only new fossil occurrences are plotted. Excursions in $\delta^{13}C$ values associated with the NRB are highlighted in light blue, whereas excursions within the Rhaetian or associated with the TJB are highlighted in dark blue.

4.5.2. Holberg Inlet

4.5.2.1. Holberg Inlet lithostratigraphy

The Holberg section is located along the southern shore of Holberg Inlet (Figure 4.1C), with the lower portion between 0.0 – 290.4 m dominated by shale, bivalve wackestone, and grainstone (Figure 4.5). There are lesser but distinctive beds of basalt and lime mudstone, as well as sizeable stretches of no exposed outcrop due to beaches and coves (Figure 4.5). The middle portion of the section between 290.4 – 467.6 m is entirely silty grainstone, and the upper portion above 467.6 m is predominately calcareous siltstone with lesser silty grainstone (Figure 4.5). Nixon et al. (2011) interpret this shift from silty grainstone to calcareous siltstone as the contact between the Parson

Bay Formation and the Pegattem Creek siltstone, approximating the TJB (Figure 4.5). Therefore, dominant lithologies generally become increasingly siliciclastic-rich progressing up the Holberg section, and decreasingly calcareous (Figure 4.5).

The Michelsen Point section is located along a creek extending south from Holberg Inlet (Figure 4.1C), with the portion between 69.4 – 252.5 m involving extended intervals of no outcrop between exposures of basalt and bivalve rudstone, followed by an interval dominated by bivalve wackestone and sandstone between 252.5 – 362.1 m (Figure 4.5). The upper portion of the section between 362.1 – 402.0 m is entirely shale with interbedded lime mudstone, followed by an interval dominated by wackestone, packstone, and lithoclastic rudstone between 402.0 – 462.3 m (Figure 4.5). The section is uncomformably overlain by hematitic sandstone, likely the Cretaceous Blumberg Formation (Figure 4.5; Nixon et al., 2011). Wackestone/floatstone (and lesser packstone/rudstone) hosting monotid bivalves feature in the Norian strata of both Holberg Inlet sections, observed 201.0 – 277.8 m at Holberg, and 144.4 – 362.1 m at Michelsen Point (Figure 4.5).

4.5.2.2. Holberg Inlet biostratigraphy

As with the Williston Lake sections, the present study utilizes the last occurrence of *Monotis* to approximate the NRB at the Holberg Inlet sections (Figure 4.5). At the Holberg section, large *Monotis* bivalves are found until 277.8 m, approximating the NRB (Figure 4.5). The conodont *Norigondolella* cf. *navicula* begins to occur at 78.8 m and persists until 271.8 m, indicating Norian age for that interval; a single occurrence of *Mo. carinata* is observed at 187.0 m, reinforcing middle Norian to Rhaetian age (Figures 4.3, 4.5). The only ammonoid occurrence at Holberg is *Discamphiceras* aff. *antiquum* at 550.0 m, very high up in the section and indicative of middle Hettangian age (Figure 4.5).

At the Michelsen Point section, the highest large *Monotis* is observed at 362.1 m, placing the NRB (Figure 4.5). The conodont *Mo. carinata* begins to occur at 143.1 m alongside a single occurrence of *Mockina spinosa*, with the former indicating a middle Norian to Rhaetian age and persisting until 332.8 m where it is joined by *Mo. bidentata*, signifying a late Norian to Rhaetian age (Figures 4.3, 4.5).

4.5.2.3. Holberg Inlet chemostratigraphy

Values of $\delta^{13}C_{carb}$ from the Norian through middle Hettangian portion of Holberg investigated by the present study (between 186.0 m and the section top) predominantly range between -2.0 – 2.0‰ (84% of 188 data points outside excursion intervals), with three negative excursions of approximately 8‰ magnitude in which values reach around -8‰ (Figure 4.5). The lower excursion is observed at 280.8 – 301.5 m, starting 3.0 m above the top of *Monotis* (Figure 4.5). Next, the middle excursion is observed at 458.3 – 475.0 m, starting 180.5 m above the top of *Monotis* (Figure 4.5). Lastly, the upper excursion is observed at 490.3 – 545.5 m, starting 212.5 m above the top of *Monotis* (Figure 4.5). There are no significant long-term trends in the Norian or Rhaetian

$\delta^{13}C_{carb}$ values at Holberg, with measurements averaging 0.2 ± 1.4‰ (1σ) excluding excursion intervals (Figure 4.5). The values shift to be more negative across the TJB, such that Hettangian $\delta^{13}C_{carb}$ measurements average -2.8 ± 1.4‰ (1σ) excluding excursion intervals (Figure 4.5).

Values of $\delta^{13}C_{carb}$ from the Norian through Rhaetian portion of Michelsen Point (between 140.7 m and the section top) predominantly range between -3.5 – 1.5‰ (92% of 168 data points outside excursion interval), with three distinct negative excursions (Figure 4.5). The lower negative excursion is approximately 5‰ in magnitude with values reaching around -6.5‰, observed at 350.5 – 372.8 m and coinciding with the top of *Monotis* (Figure 4.5). The next middle excursion is approximately 3‰ in magnitude with values reaching around -4.0‰, observed at 405.8 – 425.8 m, starting 43.7 m above the top of *Monotis* (Figure 4.5). The upper excursion is also approximately 3‰ in magnitude, reaching around -3.0‰ and observed at 455.8 – 462.3 m, starting 93.7 m above the top of *Monotis* (Figure 4.5). Excluding a cluster of anomalously negative $\delta^{13}C_{carb}$ measurements near the base of the Norian between 140.7 – 144.6 m, no significant trends in Norian or Rhaetian $\delta^{13}C_{carb}$ values are observed outside the excursion intervals, with measurements averaging -0.5 ± 1.1‰ (1σ) (Figure 4.5). This anomalous Norian cluster is not identified as a potential excursion interval due to how it is confined to a 4.6 m thick block of strata isolated by long intervals of no exposed outcrop both above and below (Figure 4.5).

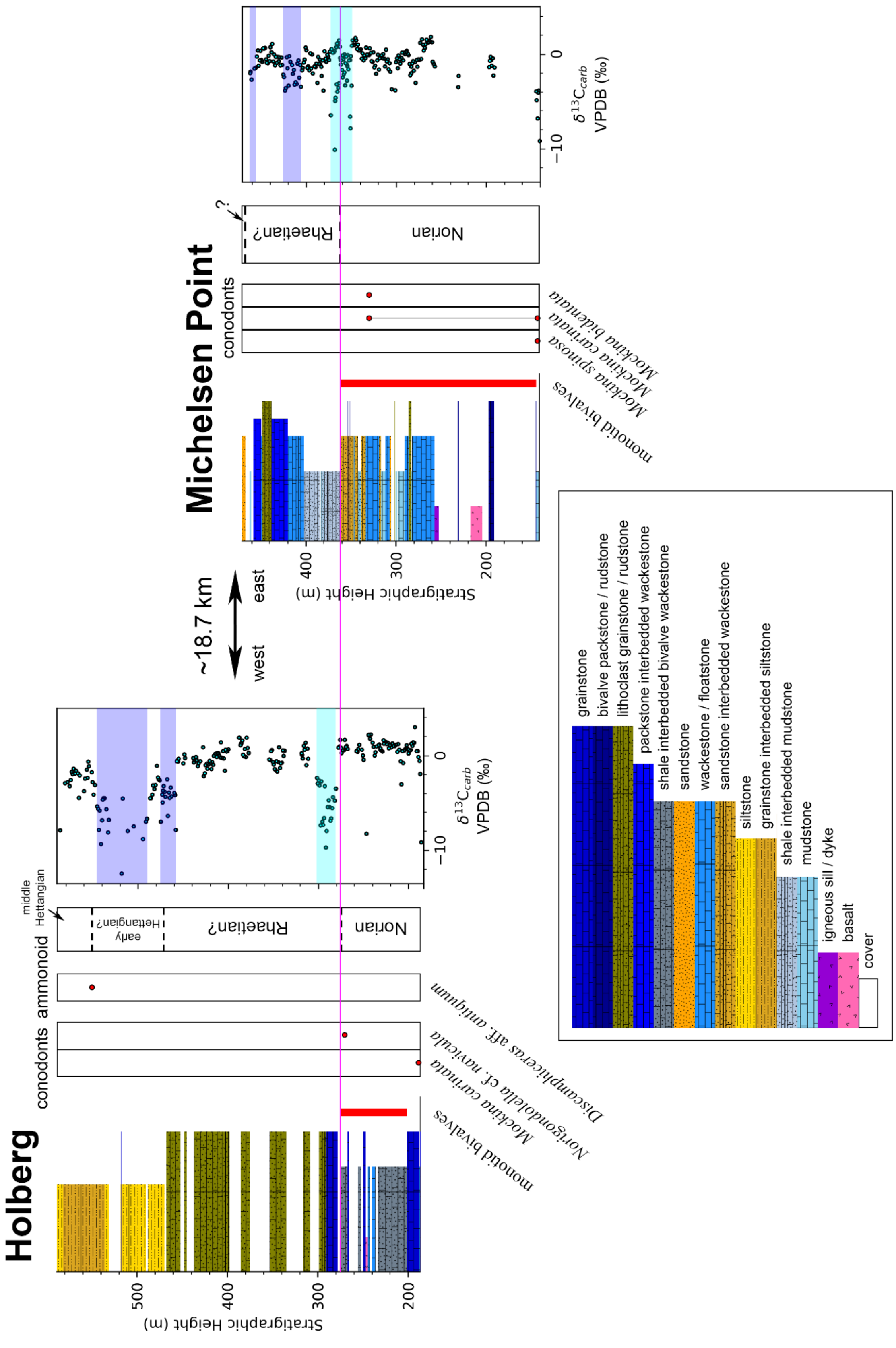
Holberg
Stratigraphic Height (m)
500
400
300
200
monotid bivalves
conodonts
Mockina carinata
Norigondolella cf. navicula
ammonoid
Discamphiceras aff. antiquum
middle Hettangian
early Hettangian?
Rhaetian?
Norian
$\delta^{13}C_{carb}$ VPDB (‰)
−10
0
~18.7 km
west
east
Michelsen Point
Stratigraphic Height (m)
400
300
200
monotid bivalves
conodonts
Mockina spinosa
Mockina carinata
Mockina bidentata
?
Rhaetian?
Norian
$\delta^{13}C_{carb}$ VPDB (‰)
−10
0
grainstone
bivalve packstone / rudstone
lithoclast grainstone / rudstone
packstone interbedded wackestone
shale interbedded bivalve wackestone
sandstone
wackestone / floatstone
sandstone interbedded wackestone
siltstone
grainstone interbedded siltstone
shale interbedded mudstone
mudstone
igneous sill / dyke
basalt
cover
]

Figure 4.5: Compiled lithostratigraphic, biostratigraphic, and geochemical results from the Holberg Inlet sections. The sections are correlated by the last occurrence of *Monotis* in each section, marked by a magenta line. The position of the TJB at Holberg is placed at the lithological shift to calcareous siltstone, consistent with Nixon et al. (2011). Excursions in $\delta^{13}C$ values associated with the NRB are highlighted in light blue, while excursions within the Rhaetian or associated with the TJB are highlighted in dark blue.

4.5.3. Kyuquot Sound

4.5.3.1. Kyuquot Sound lithostratigraphy

The Mushroom Point North and Mushroom Point South sections are located along the coast of Vancouver Island, whereas the Walters Island East section is at the southeastern-most point of Walters Island within Kyuquot Sound (Figure 4.1D). The lower portion of the Mushroom Point North section between 0.0 – 41.2 m is dominated by shale interbedded with lime mudstone, followed by an interval between 41.2 – 276.5 m which is dominated by shale and grainstone, with large intervals of no exposed outcrop due to beaches (Figure 4.6). The upper part of the section above 276.5 m is predominantly siltstone (Figure 4.6). Hummocky cross stratification is observed throughout the lower half of the section, and coral floatstone throughout the whole section, indicating shallow marine deposition above storm wave base.

The lower part of the Mushroom Point South section between 0.0 – 108.8 m is dominated by shale and grainstone, cut by several igneous intrusions (Figure 4.6). The upper portion of the section between 108.8 – 172.8 m is dominated by siltstone and grainstone, followed by coral bivalve floatstone above 172.8 m (Figure 4.6). The entirety of the Walters Island East section is dominated by lime mudstone, with lesser shale, wackestone, and floatstone (Figure 4.6).

4.5.3.2. Kyuquot Sound biostratigraphy

The conodonts *Mo. bidentata* and *Mo.* cf. *englandi* first occur at 161.5 m, with the former persisting until 180.25 m and indicative of late Norian to Rhaetian age for the interval, whereas the latter persists until 177.25 m (Figure 4.6). Occurrences of *Mo. carinata* range between 173.0 – 177.25 m, signifying middle Norian to Rhaetian age (Figure 4.6). The conodonts *Epigondolella* cf. *spiculata*, *Mockina mosheri* A, and *Mo. mosheri* B are all found at 175.25 m, with morphotype A indicating a Rhaetian age, and *Ep.* cf. *spiculata* persisting to 177.25 m (Figure 4.6). The recovery of *Mo. spinosa* at 176.0 m signifies a Norian to Rhaetian age. The radiolarians *Ferresium triquetrum*, *Proparvicingula moniliformis*, *Deflandrecyrtium nobense*, and *Droltus orchardi* have all been found at 169.5 m, collectively representing the *Pr. moniliformis* Zone, and therefore Rhaetian age (Figure 4.6). The latter two radiolarian species further extend to 173.0 m (Figure 4.6).

At Walters Island East, the conodont species *Mo. carinata*, *Mo. mosheri* A, *Mo. mosheri* B, and *Mo.* cf. *englandi* are all found at 8.0 m, with *Mo. mosheri* B extending to 14.0 m and *Mo.* cf. *englandi* extending to 23.0 m (Figure 4.6). The occurrence of *Mo. mosheri* A specifies a Rhaetian age (Figure 4.6). The species *Mo. bidentata* ranges between 12.0 – 23.0 m, supporting the Rhaetian age assignment for that interval (Figure 4.6).

4.5.3.3. Kyuquot Sound chemostratigraphy

Values of $\delta^{13}C_{carb}$ at Mushroom Point North predominantly range between -4.0 – 0.0‰ (90% of 144 data points outside excursion interval), with a negative excursion of approximately 9‰ magnitude where measurements reach around -10‰ (Figure 4.6). The excursion is observed at 279.4 – 280.3 m, identified despite consisting of only two datapoints because this negative shift parallels the clearer shift in Mushroom Point South as described below (Figure 4.6). For long-term trends, $\delta^{13}C_{carb}$ values gradually shift positive from approximately -4‰ to 0‰ between 0.0 – 39.3 m (Figure 4.6). Between 39.3 – 208.0 m, there are no significant trends and the average $\delta^{13}C_{carb}$ value is -0.9 ± 0.7‰ (1σ) (Figure 4.6). This interval is followed by a negative shift, with the average $\delta^{13}C_{carb}$ value above it being -3.1 ± 0.9‰ (1σ) prior to the excursion interval (Figure 4.6).

Values of $\delta^{13}C_{carb}$ at Mushroom Point South predominantly range between -6.0 – 1.0‰ (90% of 105 data points outside excursion interval), with a negative excursion of approximately 11‰ magnitude where measurements reach around -12‰ (Figure 4.6). The excursion is observed at 161.2 – 170.0 m (Figure 4.6). There are no significant long-term trends between 0.0 – 62.5 m, where the average $\delta^{13}C_{carb}$ value is -0.9 ± 1.2‰ (1σ) (Figure 4.6). From above this interval until the excursion, there is a gradual negative shift from approximately -2‰ to -6‰ (Figure 4.6). There is a positive shift in $\delta^{13}C_{carb}$ values across the top of the excursion interval, with those Rhaetian values above averaging 0.3 ± 0.7‰ (1σ) (Figure 4.6). There is a slight and gradual negative trend in the Norian and Rhaetian $\delta^{13}C_{carb}$ values at Walters Island East from approximately 1‰ to -2‰ (Figure 4.6).

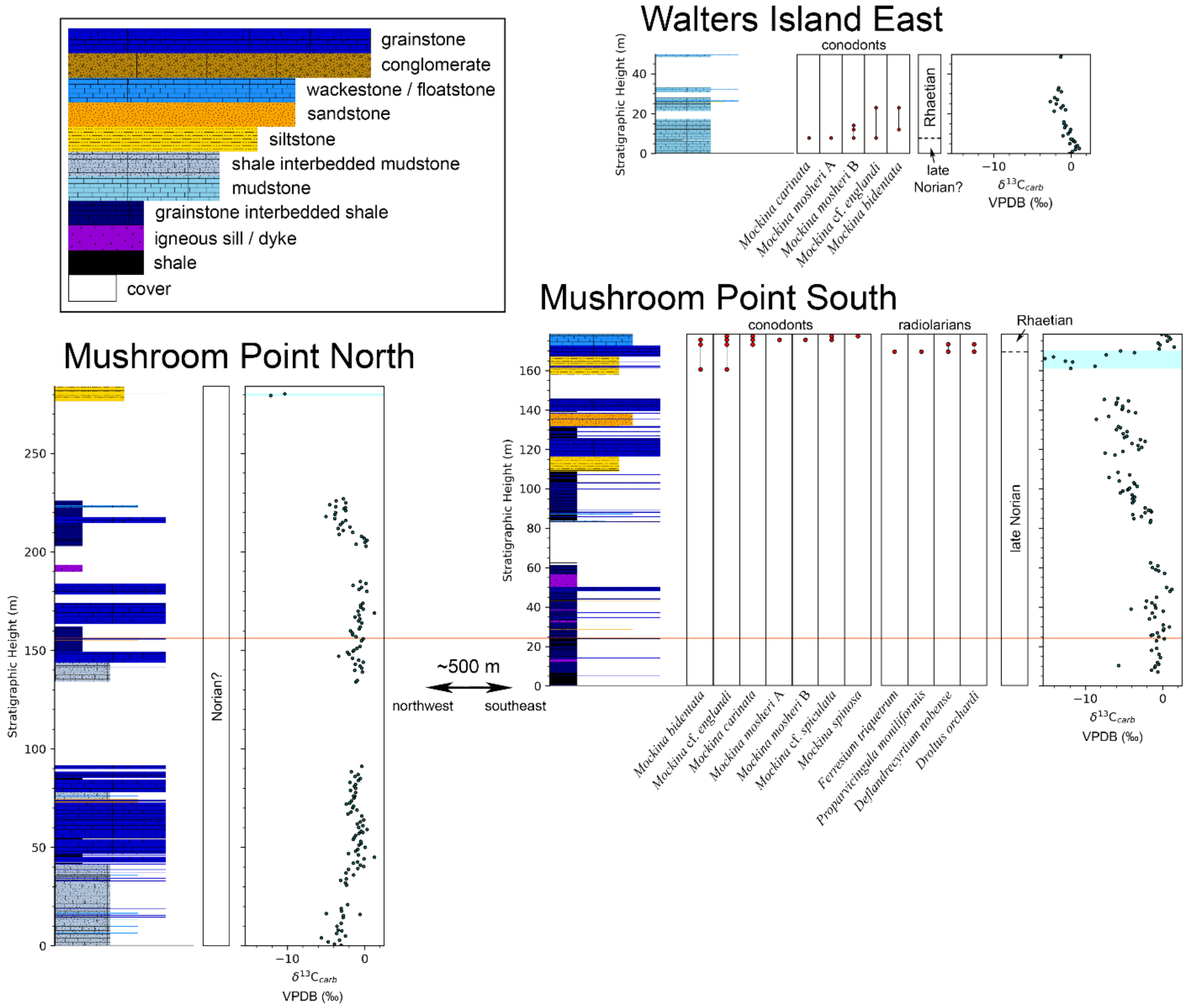

Figure 4.6: Compiled lithostratigraphic, biostratigraphic, and geochemical results from the Kyuquot Sound sections. The Mushroom Point sections are correlated by a distinctive lithological marker bed found in both, where a 50 – 60 cm grainstone bed is

capped with 10 – 20 cm of sandstone, highlighted with an orange line. Excursions in $\delta^{13}C$ values associated with the NRB are highlighted in light blue.

4.6. Discussion

4.6.1. Carbon isotope signatures across the NRB and TJB in western Canada

Overall, negative excursions in $\delta^{13}C_{carb}$ values associated with both the NRB and TJB are largely identifiable within stratigraphic sections across the Canadian Cordillera that span these age boundaries (Figures 4.4, 4.5, 4.6). This pattern of negative carbon isotope excursion is generally consistent with the global carbon cycling disruption hypothesized by prior studies investigating the NRB in western Canada (Ward et al., 2001, 2004; Whiteside & Ward, 2011; Lei et al., 2022). Negative excursions leading up to and coinciding with the TJB in western Canada may also reflect carbon cycling disruption consistent with the global signal (Ward et al., 2001, 2004; Williford et al., 2007b). However, the negative excursions associated with the TJB tend to be proximal to major shifts in lithology (Figures 4.4, 4.5, 4.6), suggesting these excursions may have been diagenetically influenced, or even diagenetic in origin (e.g. Marshall, 1992).

Amongst the Williston Lake sections, negative excursions in $\delta^{13}C_{carb}$ values associated with the NRB as approximated by the top of *Monotis* are observed at the Pardonet Creek section (~4‰ magnitude), and the Black Bear Ridge section (~5‰ magnitude) (Figure 4.4). Also associated with the NRB as placed by the top of *Monotis*, negative excursions in $\delta^{13}C_{carb}$ values are observed at the Holberg section (~8‰ magnitude), and the Michelsen Point section (~5‰ magnitude) (Figure 4.5). Additionally, a negative excursion in $\delta^{13}C_{carb}$ values associated with the NRB based on the first occurrence of *Proparvicingula moniliformis* Zone radiolarians is observed at the Mushroom Point South section (~11‰ magnitude), supported by a likely parallel excursion at the Mushroom Point North section (~9‰ magnitude), although only a small portion of it is observed in the latter (Figure 4.6).

Associated with the TJB as approximated by the top of distinctive phosphatic lag deposits (Larina et al., 2019), the Ne Parle Pas Point section exhibits a negative excursion in $\delta^{13}C_{carb}$ values (~3‰ magnitude), as does the Pardonet Creek section (~15‰ magnitude) (Figure 4.4). This TJB excursion is additionally preceded by an earlier excursion within the Rhaetian at both Ne Parle Pas Point (~3‰ magnitude) and Pardonet Creek (~2‰ magnitude) (Figure 4.4). Also at Williston Lake, a negative excursion in $\delta^{13}C_{carb}$ values is associated with the TJB as placed by the first occurrence of *Psiloceras* (Hall & Pitaru, 2004; Wignall et al., 2007; Greene et al., 2012; Golding et al., 2016) at the Black Bear Ridge section (~5‰ magnitude) (Figure 4.4). At the Holberg section, a negative excursion in $\delta^{13}C_{carb}$ values is associated with the TJB as approximated by the lithological shift from silty grainstone to calcareous siltstone (Nixon et al., 2011) (~8‰ magnitude), with another separate negative excursion following after in the early Hettangian (~8‰ magnitude) (Figure 4.5). At the Michelsen Point section, two negative excursions (~5‰ magnitude) are observed in the Rhaetian, with the upper excursion potentially proximal to and associated with the TJB (Figure 4.5).

In addition to the variable magnitudes of all these carbon isotope excursions, their positions relative to age boundary proxies also differ, even amongst stratigraphic sections in close proximity. For example, the top of *Monotis* is observed in all five Williston Lake and Holberg Inlet sections, but the expression of associated carbon isotope value excursion varies widely between them (Figures 4.4, 4.5, 4.6). Amongst the Williston Lake sections, no significant NRB excursion is observed at Ne Parle Pas Point, a negative excursion begins just above the top of *Monotis* at Pardonet Creek, and the top of *Monotis* roughly coincides with the uppermost portion of a negative excursion interval at Black Bear Ridge (Figure 4.4). For Holberg Inlet, a negative excursion begins just above the top of *Monotis* at the Holberg section, and a negative excursion interval overlaps the top of *Monotis* at Michelsen Point (Figure 4.5). These observations suggest that these carbon isotope excursions and/or these age boundary proxies are occurring asynchronously.

As the $\delta^{18}O$ record is more susceptible to diagenetic influence, a strong correlation between $\delta^{13}C$ and $\delta^{18}O$ is an indicator of the $\delta^{13}C$ signal being diagenetically altered (e.g. Marshall, 1992). Across all localities, there is no correlation between $\delta^{13}C_{carb}$ and $\delta^{18}O_{carb}$, with $R^2 = 0.0001$ for Triassic data, and $R^2 = 0.0603$ for Jurassic data (Figure 4.7). Additionally, the datapoints within excursion intervals are not limited to any particular lithology, further countering the prospect of a purely diagenetic $\delta^{13}C_{carb}$ signal. The more positive $\delta^{13}C_{carb}$ values between around 0.0 – 3.0‰ are predominantly from Triassic packstone/grainstone/floatstone/rudstone samples, which are lithologies largely not observed in the Jurassic, with the latter displaying a much higher proportion of calcareous siltstone samples (Figure 4.7). However, the anomalously negative $\delta^{13}C_{carb}$ values which create the negative excursions include samples from all lithology categories (Figure 4.7).

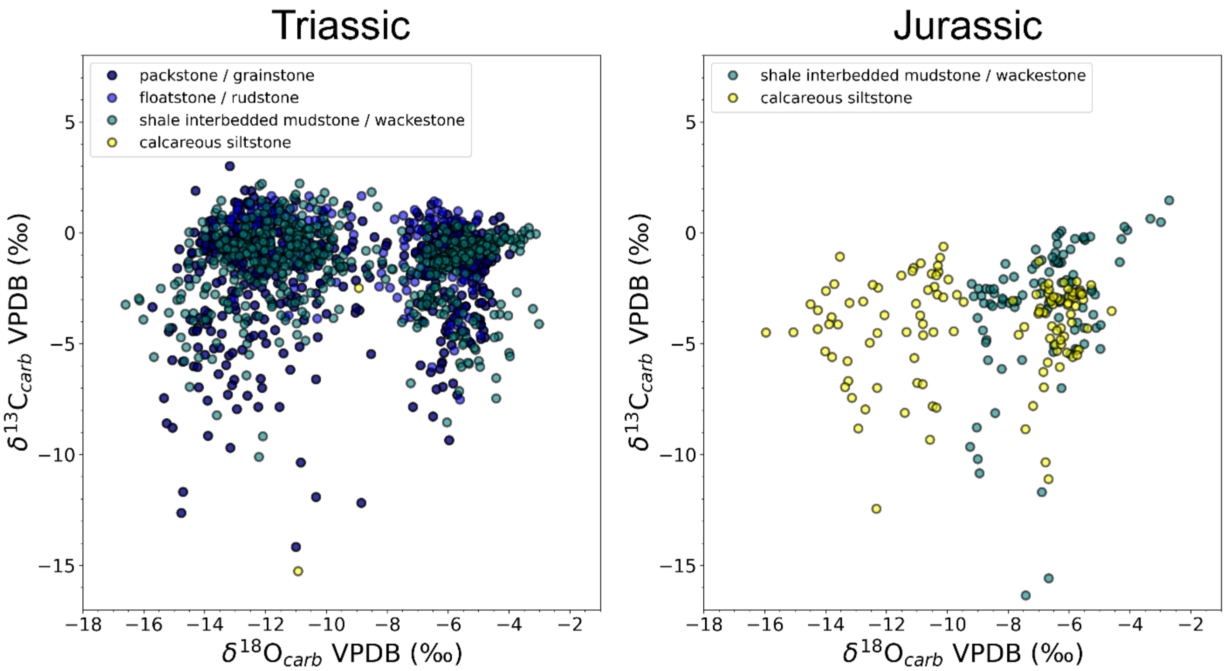

Figure 4.7: Comparison of Triassic and Jurassic $\delta^{13}C_{carb}$ vs $\delta^{18}O_{carb}$ for the Williston Lake, Holberg Inlet, and Kyuquot Sound sections. Each sample is colour-coded by its generalized lithology.

Assuming these patterns of $\delta^{13}C_{carb}$ values are primary, the very large magnitude of many negative excursions observed in the present study is problematic under the current understanding of global $\delta^{13}C$ mass balance (e.g. Kump & Arthur, 1999; Ripperdan, 2001). Despite volcanic carbon input into the ocean-atmosphere system being approximately -5‰, the $\delta^{13}C$ value of Phanerozoic carbonates average around

0‰ (e.g. Kump & Arthur, 1999; Ripperdan, 2001). Assuming a 25‰ offset between organic carbon and global ocean DIC, carbon burial should roughly be 20% organic and 80% carbonate (e.g. Kump & Arthur, 1999; Ripperdan, 2001). Thus, even if fractional organic carbon burial drops to zero, the δ^{13}C of global ocean DIC should not decrease beyond -5‰. The regularity in which δ^{13}C$_{carb}$ values from the present study fall below -10‰ therefore cannot reflect global DIC values, but instead likely represent some local mechanism of isotopically light carbon input. Given how these large magnitude excursion intervals are observed coinciding with the NRB/TJB, or are within the Rhaetian Stage, this local mechanism of carbon influx is likely associated with the environmental distress around these boundaries. These shifts in δ^{13}C values do still potentially record global trends, albeit amplified by local processes.

A large influx of respired terrestrial organic carbon is a tempting explanation for the nearshore Holberg Inlet and Kyuquot Sound sections where terrestrial influence is evident from the lithologies present (e.g. Nixon & Orr, 2007; Nixon et al., 2011), but the same extreme magnitude shifts are observed at the Williston Lake sections which are interpreted to have been deposited in a much more offshore setting (e.g. Orchard et al., 2001; Wignall et al., 2007; Zonneveld et al., 2010; McRoberts, 2011). The Williston Lake sections are notably bioclast-rich, with thick intervals of densely layered bivalve packstone/rudstone highly prevalent in the Norian strata which then largely disappear across the NRB (Figure 4.4). The large magnitude excursions in δ^{13}C$_{carb}$ values may therefore generally be the result of amplification via organic carbon respiration from mass die-offs around both the NRB and TJB, including from terrestrial sources but not needing to be exclusively so. In order for this light carbon input to be recorded by very negative $\delta^{13}C$ values in carbonate, a restricted environment would be required, or otherwise the signal would be drowned-out by mixing with global ocean DIC. A restricted circulation environment would not be unexpected for the Williston Lake sections, due to the imminent accretion of the Stikine and Quesnel terranes (e.g. Colpron & Nelson, 2009, 2011). Comparable signals in the Holberg Inlet and Kyuquot Sound sections suggest that restricted marine settings were also prominent along the margins of the Wrangell Terrane during this time, although the pre-accretionary configuration and paleogeographic positions of this terrane are highly uncertain (e.g. Colpron & Nelson, 2009, 2011).

4.6.2. Correlation of carbon isotope anomalies associated with the NRB

Currently, a Global Boundary Stratotype Section and Point (GSSP) has not been selected for the base of the Rhaetian stage, although candidates have been proposed in Austria (Krystyn et al., 2007a, b) and Italy (Rigo et al., 2016). The base of the Rhaetian stage is commonly defined by the First Appearance Datum (FAD) of the conodont species *Misikella posthernsteini* (e.g. Krystyn, 2010; Rigo et al., 2016). This genus is rare in North America, but several more readily utilized latest Norian proxies have been established reflecting close proximity to the base of the Rhaetian, including the FAD of the conodont *Mockina mosheri* (e.g. Carter & Orchard, 2007; Orchard et al., 2007; Lei et al. 2022), the *Pr. moniliformis* Zone radiolarians (e.g. Carter, 1994; Carter & Orchard, 2007), and the Last Appearance Datum (LAD) of the bivalve *Monotis* (e.g. Ward et al., 2001, 2004; Wignall et al., 2007). Temporal offset does exist between some if not all of these proxies, the extent of which remains somewhat uncertain. Generally, the top of non-dwarf *Monotis* is considered the stratigraphically lowest of these proxies, followed by the FAD of *Mo. mosheri* B, then the FAD of *Mo. mosheri* A coinciding with the base of the *Pr. moniliformis* Zone, with the FAD of *Mi. posthernsteini* being the stratigraphic highest (Figure 4.8; e.g. Carter & Orchard, 2007; Krystyn et al., 2007a, b; Orchard et al., 2007; Tackett et al., 2014; Rigo et al., 2016, 2018).

Given the substantial uncertainty in biostratigraphic correlation between different NRB proxies, and especially between the Panthalassan and Tethyan realms, the apparent asynchroneity of associated negative excursions in $\delta^{13}C$ values between sections is not unexpected (Figure 4.8). However, the position and magnitude of the negative excursion greatly varies even between neighbouring sections, as discussed prior for the carbon isotope signature in western Canada (Figure 4.8). If the negative excursion in $\delta^{13}C$ values associated with the NRB is indeed a signal reflecting a global shift in ocean water chemistry (e.g. Maron et al., 2015; Rigo et al., 2016), the results from western Canada would suggest widespread diachroneity amongst biotic markers currently associated with the same disturbance event. The negative excursion in $\delta^{13}C$ values commonly proximal to the NRB may also be diachronous to some degree, given how variable the signal can be, as discussed above.

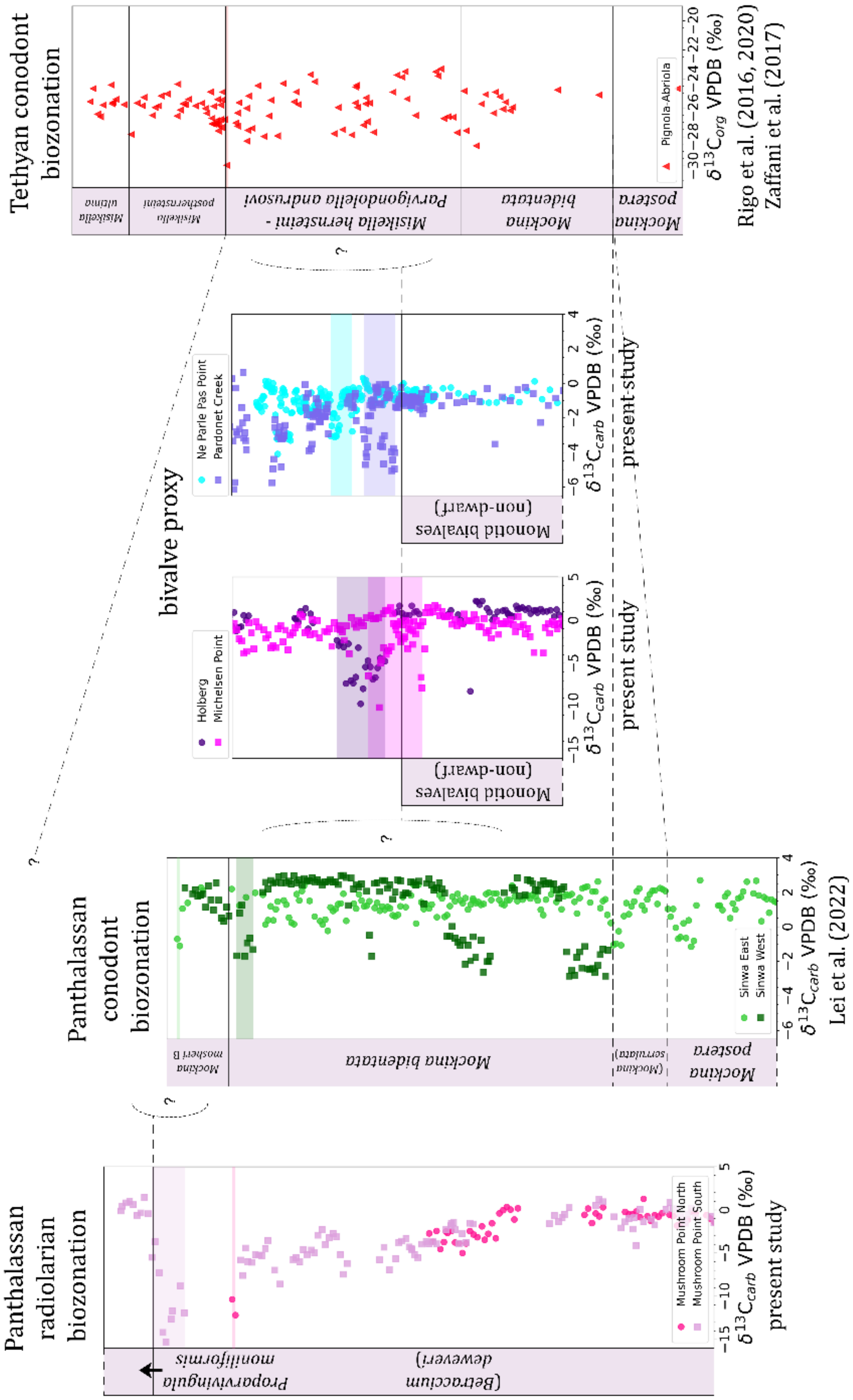
Panthalassan radiolarian biozonation
Panthalassan conodont biozonation
bivalve proxy
Tethyan conodont biozonation
Proparvicingula moniliformis
(Betraccium deweeri)
Mushroom Point North
Mushroom Point South
$\delta^{13}C_{carb}$ VPDB (‰)
present study
Mockina mosheri B
Mockina bidentata
(Mockina serrulata)
Mockina postera
Sinwa East
Sinwa West
Lei et al. (2022)
Monotid bivalves (non-dwarf)
Holberg
Michelsen Point
Ne Parle Pas Point
Pardonet Creek
Misikella ultima
Misikella posthernsteini
Misikella hernsteini - Parvigondolella andrusovi
Mockina bidentata
Mockina postera
Pignola-Abriola
$\delta^{13}C_{org}$ VPDB (‰)
Rigo et al. (2016, 2020)
Zaffani et al. (2017)
?

Figure 4.8: Correlation between select sections with δ^{13}C values exhibiting excursions proposed to be related to disturbance at the NRB interval aligned by various biostratigraphic proxies. The offsets between these proxies are approximated from relative positionings in prior studies (Carter & Orchard, 2007; Krystyn et al., 2007a, b; Orchard et al., 2007; Tackett et al., 2014; Rigo et al., 2016, 2018). The Sinwa East and Sinwa West data are from Lei et al. (2022). The Pignola-Abriola data are from Rigo et al. (2016, 2020) and Zaffani et al. (2017). Proposed excursion intervals are highlighted in the same colours as the datapoint markers of each section.

4.6.3. Correlation of carbon isotope anomalies leading into and across the TJB

The TJB is defined by the FAD of the ammonite *Psiloceras spelae* at Kuhjoch, Austria, the GSSP for the base of the Hettangian (Hillebrandt et al., 2013). A multitude of ammonite and radiolarian proxies are commonly utilized to identify the TJB in North America, including the cosmopolitan *Ps. spelae* (Tozer, 1994; Guex et al., 2004; Longridge et al., 2007; Taylor et al., 2021). As introduced prior, discussion of the ETME within the present study refers to a protracted event that includes not just the faunal turnover coinciding with the TJB, but also periods of biotic distress that preceded it during the Rhaetian Stage.

Within stratigraphic sections with substantial sedimentation spanning the Rhaetian and/or early Hettangian like Ne Parle Pas Point, Pardonet Creek, Holberg, and Michelsen Point, two distinct negative excursions in δ^{13}C values are observed in this time span (Figures 4.4, 4.5). The upper of these two excursions is likely associated with the TJB, with the lower within the Rhaetian, but uncertainty amongst the various TJB proxies utilized across these sections adds ambiguity (Figures 4.4, 4.5). Regardless, this multitude of negative excursions leading into a “main” excursion coinciding with the TJB is generally consistent with many prior studies which propose a “precursor” excursion as well as an “initial” excursion both in the Rhaetian (Figure 4.9; e.g. Hesselbo et al., 2002; Ward et al., 2004; Ruhl et al., 2009; Ruhl & Kürschner, 2011; Fujisaki et al., 2018; Zaffani et al., 2018; Du et al., 2020b; de Graaff et al., 2022). Within the sections from the present study, the positions of the Rhaetian excursions suggest that the “precursor” excursion associated with the ETME may be indistinguishable from one associated with the NRB. Ambiguity in the exact placement of the NRB, which would potentially shift the boundary higher in the Canadian sections than displayed in Figure 4.9, makes this differentiation even more ambiguous.

This series of globally correlatable Rhaetian $\delta^{13}C$ value excursions preceding the TJB provides strong evidence suggesting the paleoenvironmental disturbance associated with the ETME had roots extending earlier than commonly established (Figure 4.9). This would necessitate a trigger predating eruptive CAMP volcanism (Marzoli et al., 1999; 2004; Blackburn et al., 2013), such as non-eruptive outgassing (Ruhl & Kürschner, 2011; Davies et al., 2017), or perhaps even the underexplored cause of the NRB faunal turnover. Widespread uncertainty in the biostratigraphic placement of the NRB makes it difficult to assess whether this chain of negative excursions can be considered to start at the NRB, but repeated carbon cycling disruption on a global scale throughout the

Rhaetian – Hettangian interval does lead up to the traditional placement of a geologically instantaneous ETME at the TJB (Figure 4.9). This evidence supports the concept of a multiphase ETME spanning millions of years across much of (if not all of) the Rhaetian Stage, with a climax at the TJB, and ecological instability persisting well into the Hettangian afterwards.

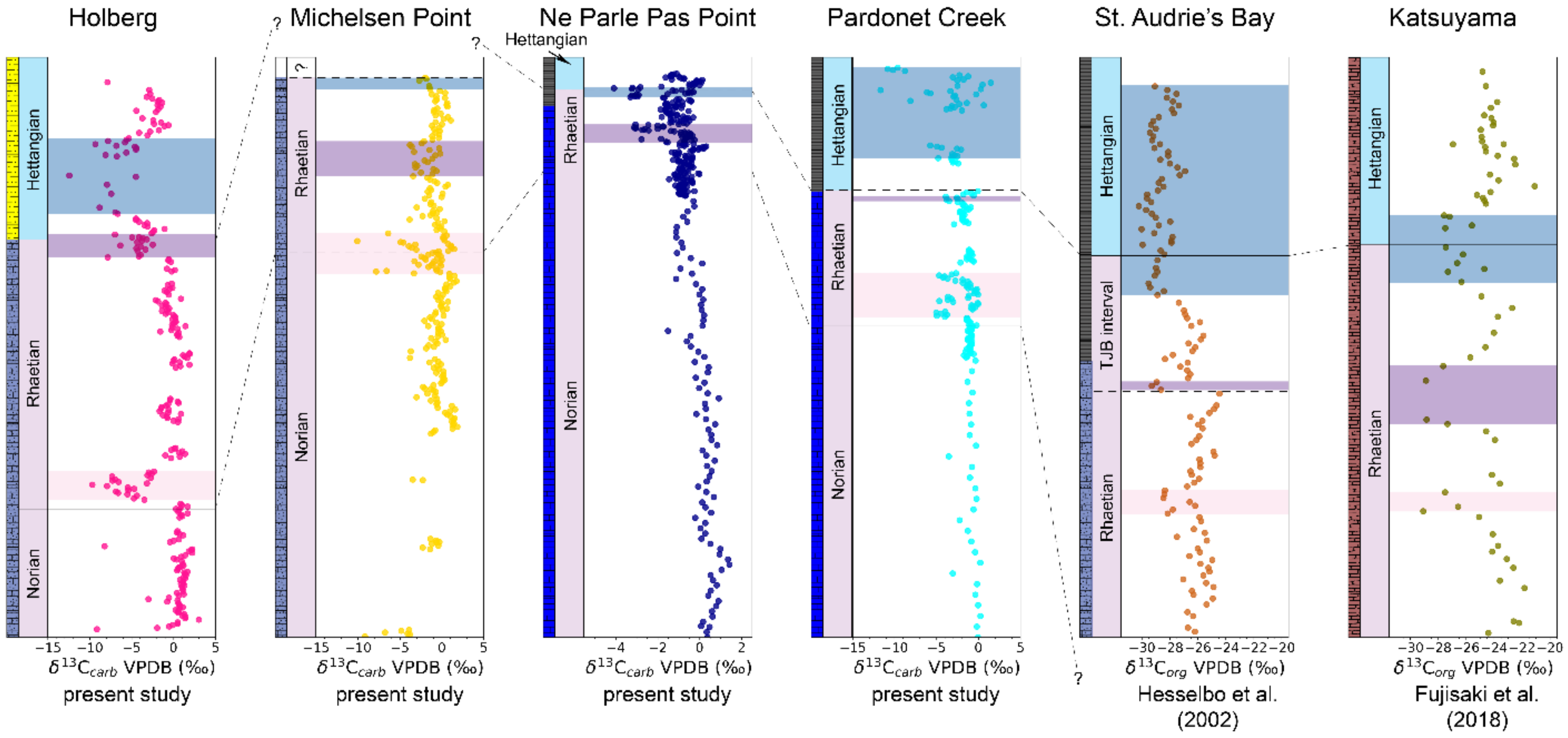
Holberg
Michelsen Point
Ne Parle Pas Point
Pardonet Creek
St. Audrie's Bay
Katsuyama
Hettangian
Rhaetian
Norian
TJB interval
?
−15 −10 −5 0 5
−4 −2 0 2
−30 −28 −26 −24 −22 −20
$\delta^{13}C_{carb}$ VPDB (‰)
$\delta^{13}C_{org}$ VPDB (‰)
present study
Hesselbo et al. (2002)
Fujisaki et al. (2018)

Figure 4.9: Correlation between select sections with $\delta^{13}C$ values exhibiting excursions proposed to be related to the ETME. All sections are displayed alongside a simplified lithostratigraphy, accentuating how the TJB as placed in each section is often proximal to a significant reduction of carbonate lithologies. The Holberg section transitions from impure limestone to siltstone, the Ne Parle Pas Point and Pardonet Creek sections transition from limestone to shale, and the St. Audrie’s Bay sections transitions from impure limestone to shale. The St. Audrie’s Bay data are from Hesselbo et al. (2002), and the Katsuyama data are from Fujisaki et al. (2018). Proposed excursion intervals are highlighted in consistent colours across all sections, with the NRB or “precursor” excursion in pink, the “initial” excursion in purple, and the “main” excursion in blue.

4.7. Conclusions

Through the investigation of eight Late Triassic stratigraphic sections across western Canada, the compilation of $\delta^{13}C_{carb}$ measurements present a comprehensive Panthalassan record spanning the Norian – Hettangian interval. Negative excursions in $\delta^{13}C_{carb}$ values associated with the NRB are observed in the sections: Pardonet Creek (~4‰ magnitude), Black Bear Ridge (~5‰ magnitude), Holberg (~8‰ magnitude), Michelsen Point (~5‰ magnitude), Mushroom Point North (~9‰ magnitude), and Mushroom Point South (~11‰ magnitude). Two distinct negative excursions in $\delta^{13}C_{carb}$ values are observed during the Rhaetian to early Hettangian interval (with the latter of the two likely associated with the TJB) of the sections: Ne Parle Pas Point (both ~3‰ magnitude), Pardonet Creek (~2‰ magnitude followed by ~15‰ magnitude), Holberg (both ~8‰ magnitude), and Michelsen Point (both ~5‰ magnitude). A negative excursion in $\delta^{13}C_{carb}$ values is also associated with the TJB at the Black Bear Ridge section (~5‰ magnitude).

The variable and sometimes extreme magnitude displayed by these excursions is problematic given the current conceptualization of $\delta^{13}C_{carb}$ values as an accurate preservation of average global ocean $\delta^{13}C$ values (e.g. Kump & Arthur, 1999; Ripperdan, 2001), suggesting some manner of local mechanism can amplify these global signals in restricted marine environments. Additionally, excursions associated with the TJB tend to occur near a pronounced shift away from carbonate lithologies, indicating these particular excursions are more likely to have been altered or driven by diagenesis than the older excursions also investigated. Regardless, comparing this new Panthalassan record with the global record (e.g. Hesselbo et al., 2002; Fujisaki et al., 2018) does illustrate a global series of negative excursions in $\delta^{13}C_{carb}$ values spanning much of the Rhaetian, if not all of it. Carbon isotope excursion intervals previously interpreted as Rhaetian “precursor” to the TJB may in actuality be more associated with the NRB. A variety of biostratigraphic proxies are utilized to approximate the NRB, and uncertainty in the correlation between these proxies make this distinction in attribution further unclear.

Overall, these results can be interpreted as reflecting an enduring state of ecosystem instability encompassing the latest Norian to early Hettangian interval, supporting the concept of a multiphase ETME initiating as early as the NRB (e.g. Hallam, 2002; Tanner et al., 2004; Rigo et al., 2018, 2020), followed by a drawn-out recovery extending into the Hettangian. Reframing the relatively enigmatic NRB faunal turnover as a pivotal event leading into the ETME increases the significance of the NRB, motivating further attention and research.

Chapter 5

Conclusions

5.1. Research overview and impact

The research detailed in this dissertation investigates the paleoenvironmental conditions leading up to and across the end-Triassic mass extinction (ETME), as preserved in the rock record of western Canada. A wide variety of sedimentological, paleontological, and geochemical approaches are utilized to this end. First focusing on the Norian/Rhaetian boundary (NRB) interval in chapter two, the boundary is identified within the two Mount Sinwa sections via conodont biostratigraphy and Re–Os isochron ages, coinciding with the collapse of a coral reef. Although regional base level rise cannot be ruled out as the cause of this, the reef collapse could instead be indicative of substantial ecological distress. A slight increasing trend in $^{87}Sr/^{86}Sr$ ratios is observed across the middle to latest Norian, documenting the first values measured for this time interval in Panthalassa, and failing to replicate the $^{87}Sr/^{86}Sr$ ratio decrease across the NRB interpreted from Tethyan data. The lack of a convincing global shift in $^{87}Sr/^{86}Sr$ ratios across the NRB suggests against global scale mantle-derived volcanism as the trigger of the NRB event, prompting re-evaluation of causal mechanism hypotheses. A negative excursion in $\delta^{13}C$ values of 3 – 4‰ is observed proximal to the NRB at Mount Sinwa, consistent with prior studies asserting global carbon cycling disruption at the NRB.

Chapter three shifts focus to paleontological evidence for ecosystem disturbance across the NRB and into the Rhaetian Stage. A morphological shift of platform width reduction is demonstrated in two conodont species that are particularly abundant in the Norian and Rhaetian stages of Panthalassa: *Mockina carinata* and *Mockina englandi*. Specimens of these two species with a mid-platform length to breadth ratio greater than 3:1 are shown to be exclusively found in the Rhaetian, facilitating identification of potential morphotypes/subspecies, which have new biostratigraphic utility. Intergeneric platform reduction is fairly evident amongst Tethyan conodonts, but with the rarity of those forms in Panthalassa, these intraspecific results offer the first concrete evidence of this trend being global in scale. This shift in morphology can be interpreted as reflecting a change in the primary diet of conodonts from mineralized to soft-bodied food sources, suggesting that the carbonate biomineralization pressure typically associated with the ETME around the Triassic/Jurassic boundary (TJB) began at a lesser severity as early as the NRB.

Zooming out temporally to view the Norian through Hettangian stages more broadly, chapter four compiles a Panthalassan record of $\delta^{13}C$ values from eight sections across Williston Lake, Holberg Inlet, and Kyuquot Sound. Together, these sections represent a variety of depositional settings across a wide paleogeographic area, as well as the most comprehensive Panthalassan record produced to date. Three negative excursions are observed, with one proximal to the NRB, another within the Rhaetian, and one coinciding with the TJB. The apparently variable position of the NRB excursion relative to various proxies for the boundary suggests there may be little distinction between this excursion and the Rhaetian “precursor” excursion identified in prior studies. The magnitude of the observed excursions include very large shifts of over 10‰, which are not likely to represent changes in ocean water chemistry on a global scale. A potential local amplification mechanism would be the disturbance-triggered increase of organic carbon respiration in the water column, but this would require restricted circulation environments, suggesting such settings were common across Panthalassa. The sequential nature of these excursions in $\delta^{13}C$ values from the NRB to the TJB can be interpreted as persistent ecosystem instability across this time interval.

Chapters two through four present Panthalassan evidence for the ETME being a protracted and multi-phased event. Even some faunal groups considered the most strongly affected by the ETME, such as conodonts, show declining biodiversity and morphological signs of distress long-preceding the TJB. Global carbon cycle disruption is evidently associated with the NRB faunal turnover, and this is followed by persistent ecological instability manifesting as a series of negative excursions in $\delta^{13}C$ values. Investigation from both paleontological and geochemical approaches independently recognize how the paleoenvironmental disturbance that started at the NRB cascaded forward through the Rhaetian.

5.2. Limitations and future research

Despite the contributions of the research presented in this dissertation, substantial aspects of the Late Triassic paleoenvironmental disturbances remain unknown or underdeveloped. Much work remains to be done in refining Panthalassan Late Triassic conodont taxonomic concepts and biozonation, as the current diagnoses for many genera and species are potentially too broad. The morphometric analyses of chapter three address only two species that are particularly abundant in Panthalassa, so much work remains to be done using similar methodology on other conodont species. The expansion of Late Triassic conodont taxonomy has the potential to facilitate even more precise age determinations across stratigraphic sections. Exact correlations between the Panthalassan and Tethyan conodont biozonations also remain uncertain, encouraging additional efforts to intercalibrate these biozonations with other means of geochronology, such as the biostratigraphy of other faunal groups or radiometric dating.

Some of the geochemical results from chapters two and four were unexpected, suggesting prior conceptions of Late Triassic paleoenvironmental conditions and/or these geochemical proxies are incomplete. Despite the current lack of strong evidence for a global shift in $^{87}Sr/^{86}Sr$ ratios across the NRB, enhanced volcanism in some form remains the most likely trigger for the faunal turnover based on a variety of other proxies. Measurement of $^{87}Sr/^{86}Sr$ ratios across a section in western Canada that spans the NRB as well as considerable portions of the Rhaetian Stage would clarify whether or not a shift can be observed, countering the current uncertainty of identifying the NRB in Panthalassa. The smoking gun for establishing causal mechanism would ultimately be the precise dating of a large igneous province (LIP) coinciding with the NRB, whether it is improved dating of the Angayucham Province, or the discovery of another LIP that has not been previously linked to the NRB.

In chapter four especially, the presence of apparently asynchronous negative excursions in $\delta^{13}C$ values, that also can reach very large magnitudes, highlights multiple limitations of the carbon isotope system as a proxy for paleoenvironmental disturbance. Separate instances of carbon cycling disruption do not have reliably unique identifiers, such that excursions can only be attributed to specific events when contextualized by independent age constraints. Therefore, when the correlation between disparate biostratigraphic proxies is uncertain, as it is for the NRB, ascertaining the timing of carbon isotope excursions is inevitably also uncertain. A large variety of factors can influence the carbon isotope system, such that the assumption of carbonate $\delta^{13}C$ measurements reflecting unadulterated global ocean seawater values may be so tenuous that it can be considered mostly untrue. Further investigation of how carbon isotopes behave across the full range of diverse oceanic settings could contribute to disentangling the globally averaged signal from local influences.

Bibliography

Adams, J.F., and Rhodes, M.L. (1960). Dolomitization by seepage refluxion. AAPG Bulletin, v. 44(12), p. 1912–1920.

Allan, J.R., and Matthews, R.K. (1982). Isotope signatures associated with early meteoric diagenesis. Sedimentology, v. 29, p. 797–817.

Bachan, A., Van De Schootbrugge, B., Fiebig, J., McRoberts, C.A., Ciarapica, G., and Payne, J.L. (2012). Carbon cycle dynamics following the end-Triassic mass extinction: Constraints from paired $\delta^{13}C_{carb}$ and $\delta^{13}C_{org}$ records. Geochemistry, Geophysics, Geosystems, v. 13(9), p. 1–24.

Banner, J.L., and Hanson, G.N. (1990). Calculation of simultaneous isotopic and trace element variations during water-rock interaction with applications to carbonate diagenesis. Geochimica et Cosmochimica Acta, v. 54, p. 3123–3137.

Baud, A., Magaritz, M., and Holser, W.T. (1989). Permian-Triassic of the Tethys: Carbon isotope studies. Geologische Rundschau, v. 78, p. 649–677.

Baumiller, T.K., Salamon, M.A., Gorzelak, P., Mooi, R., Messing, C.G., and Gahn, F.J. (2010). Post-Paleozoic crinoid radiation in response to benthic predation preceded the Mesozoic marine revolution. Proceedings of the National Academy of Sciences of the United States of America, v. 107(13), p. 5893–5896.

Bazzucchi, P., Bertinelli, A., Ciarapica, G., Marcucci, M., Passeri, L., Rigo, M., and Roghi, G. (2005). The Late Triassic-Jurassic stratigraphic succession of Pignola

(Lagonegro-Molise Basin, Southern Apennines, Italy). Bollettino Della Società Geologica Italiana, v. 124, p. 143–153.

Belasky, P., Stevens, C.H., and Hanger, R.A. (2002). Early Permian location of western North American terranes based on brachiopod, fusulinid, and coral biogeography. Palaeogeography, Palaeoclimatology, Palaeoecology, v. 179(3–4), p. 245–266.

Beranek, L.P., and Mortensen, J.K. (2011). The timing and provenance record of the Late Permian Klondike orogeny in northwestern Canada and arc-continent collision along western North America. Tectonics, v. 30(5), p. 1–23.

Bertinelli, A., Casacci, M., Concheri, G., Gattolin, G., Godfrey, L., Katz, M.E., Maron, M., Mazza, M., Mietto, P., Muttoni, G., Rigo, M., Sprovieri, M., Stellin, F., and Zaffani, M. (2016). The Norian/Rhaetian boundary interval at Pignola-Abriola section (Southern Apennines, Italy) as a GSSP candidate for the Rhaetian Stage: an update. Albertiana, v. 43, p. 5–18.

Blackburn, T.J., Olsen, P.E., Bowring, S.A., McLean, N.M., Kent, D. V., Puffer, J., McHone, G., Rasbury, E.T., and Et-Touhami, M. (2013). Zircon U-Pb geochronology links the end-Triassic extinction with the Central Atlantic Magmatic Province. Science, v. 340(6135), p. 941–945.

Bookstein, F. P. 1991. Morphometric tools for landmark data. Geometry and Biology. Cambridge University Press, 435 p.

Briggs, D.E.G., Clarkson, E.N.K., and Aldridge, R.J. (1983). The conodont animal. Lethaia, v. 16(1), p. 1–14.

Callegaro, S., Rigo, M., Chiaradia, M., and Marzoli, A. (2012). Latest Triassic marine Sr isotopic variations, possible causes and implications. Terra Nova, v. 24(2), p. 130–135.

Carter, E.S. (1994). Evolutionary trends in latest Norian through Hettangian radiolarians from the Queen Charlotte Islands, British Columbia. Geobios Mémoire Spécial, v. 17, p. 111–119.

Carter, E.S., and Orchard, M.J. (2007). Radiolarian - conodont - ammonoid intercalibration around the Norian-Rhaetian boundary and implications for trans-Panthalassan correlation. Albertiana, v. 36, p. 149–163.

Caruthers, A.H., Marroquín, S.M., Gröcke, D.R., Golding, M.L., Aberhan, M., Them, T.R., Veenma, Y.P., Owens, J.D., McRoberts, C.A., Friedman, R.M., Trop, J.M., Szűcs, D., Pálfy, J., Rioux, M., Trabucho-Alexandre, J.P., and Gill, B.C. (2022). New evidence for a long Rhaetian from a Panthalassan succession (Wrangell Mountains, Alaska) and regional differences in carbon cycle perturbations at the Triassic-Jurassic transition. Earth and Planetary Science Letters, v. 577(117262), 14 p.

Charlson, R.J., Lovelock, J.E., Andreaei, M.O., and Warren, S.G. (1987). Oceanic phytoplankton, atmospheric sulphur, cloud albedo and climate. Nature, v. 326(6114), p. 655–661.

Clapham, M.E., Shen, S., and Bottjer, D.J. (2009). The double mass extinction revisited: reassessing the severity, selectivity, and causes of the end-Guadalupian biotic crisis (Late Permian). Paleobiology, v. 35(1), p. 32–50.

Clark, D.L. (1983). Extinction of conodonts. Journal of Paleontology, v. 57(4), p. 652–661.

Clark, D.L., Wang, C.Y., Orth, C.J., and Gilmore, J.S. (1986). Conodont survival and low iridium abundances across the Permian-Triassic boundary in south China. Science, v. 233(4767), p. 984–986.

Colpron, M., and Nelson, J.L. (2009). A Palaeozoic Northwest Passage: Incursion of Caledonian, Baltican and Siberan terranes into eastern Panthalassa, and the early evolution of the North American Cordillera. Geological Society Special Publication, v. 318(1), p. 273–307.

Colpron, M., and Nelson, J. (2011). A digital atlas of terranes for the northern Cordillera. British Columbia Ministry of Energy and Mines, BCGS Geofile 11.

Colpron, M., Crowley, J.L., Gehrels, G., Long, D.G.F., Murphy, D.C., Beranek, L., and Bickerton, L. (2015). Birth of the northern Cordilleran orogen, as recorded by detrital zircons in Jurassic synorogenic strata and regional exhumation in Yukon. Lithosphere, v. 7, p. 541–562.

Črne, A.E., Weissert, H., Goričan, Š., and Bernasconi, S.M. (2011). A biocalcification crisis at the Triassic-Jurassic boundary recorded in the Budva Basin (Dinarides, Montenegro). Bulletin of the Geological Society of America, v. 123, p. 40–50.

Davies, J.H.F.L., Marzoli, A., Bertrand, H., Youbi, N., Ernesto, M., and Schaltegger, U. (2017). End-Triassic mass extinction started by intrusive CAMP activity. Nature Communications, v. 8(15596), p. 1–8.

de Graaff, S.J., Percival, L.M.E., Kaskes, P., Déhais, T., de Winter, N.J., Jansen, M.N., Smit, J., Sinnesael, M., Vellekoop, J., Sato, H., Ishikawa, A., Spassov, S., Claeys, P., and Goderis, S. (2022). Geochemical records of the end-Triassic Crisis preserved in a deep marine section of the Budva Basin, Dinarides, Montenegro. Palaeogeography, Palaeoclimatology, Palaeoecology, v. 606(111250), p. 1–17.

Deniel, C., and Pin, C. (2001). Single-stage method for the simultaneous isolation of lead and strontium from silicate samples for isotopic measurements. Analytica Chimica Acta, v. 426, p. 95–103.

Derry, L.A. (2010). A burial diagenesis origin for the Ediacaran Shuram-Wonoka carbon isotope anomaly. Earth and Planetary Science Letters, v. 294, p. 152–162.

Desrochers, A., and Orchard, M.J. (1991). Stratigraphic revisions and carbonate sedimentology of the Kunga Group Upper Triassic-Lower Jurassic], Queen Charlotte Islands, British Columbia. Geological Survey of Canada Paper 90-10, p. 163–172.

Donoghue, P.C.J., and Purnell, M.A. (1999). Mammal-like occlusion in conodonts. Paleobiology, v. 25(1), p. 58–74.

Du, Y., Bertinelli, A., Jin, X., Shi, Z., Karádi, V., Yin, H., Han, L., Wu, Q., and Rigo, M. (2020a). Integrated conodont and radiolarian biostratigraphy of the upper Norian in Baoshan Block, Southwestern China. Lethaia, v. 53(4), p. 533–545.

Du, Y., Chiari, M., Karádi, V., Nicora, A., Onoue, T., Pálfy, J., Roghi, G., Tomimatsu, Y., and Rigo, M. (2020b). The asynchronous disappearance of conodonts: New constraints from Triassic-Jurassic boundary sections in the Tethys and Panthalassa. Earth-Science Reviews, v. 203(103176), p. 1–18.

Du, Y., Onoue, T., Karádi, V., Williams, I.S., and Rigo, M. (2021). Evolutionary process from *Mockina bidentata* to *Parvigondolella andrusovi*: Evidence from the Pizzo Mondello section, Sicily, Italy. Journal of Earth Science, v. 32(3), p. 667–676.

Du, Y., Onoue, T., Tomimatsu, Y., Wu, Q., and Rigo, M. (2023). Lower Jurassic conodonts from the Inuyama area of Japan: Implications for conodont extinction. Frontiers in Ecology and Evolution, v. 11 (113578), p. 1–10.

Dunham, R.J. (1962). Classification of carbonate rocks according to depositional textures. Classification of Carbonate Rocks--A Symposium, p. 108–121.

Embry, A.F. (1988). Triassic sea-level changes. Sea-level changes: An integrated approach, v. 42, p. 249–259.

Embry, A.F., and Klovan, J.E. (1971). A Late Devonian reef tract on northeastern Banks Island, NWT. Bulletin of Canadian Petroleum Geology, v. 19, p. 730–781.

English, J.M., and Johnston, S.T. (2005). Collisional orogenesis in the northern Canadian Cordillera: Implications for Cordilleran crustal structure, ophiolite emplacement, continental growth, and the terrane hypothesis. Earth and Planetary Science Letters, v. 232, p. 333–344.

English, J.M., Johannson, G.G., Johnston, S.T., Mihalynuk, M.G., Fowler, M., and Wight, K.L. (2005). Structure, stratigraphy and petroleum resource potential of the Central Whitehorse Trough, Northern Canadian Cordillera. Bulletin of Canadian Petroleum Geology, v. 53, p. 130–153.

Ernst, R.E., and Buchan, K.L. (2001). Mantle plumes: Their identification through time. Geological Society of America Special Paper 352, 593p.

Flügel, E., and Kiessling, W. (2002). Patterns of Phanerozoic Reef Crises. Phanerozoic Reef Patterns, SEPM Special Publication, v. 72, p. 691–733.

Folk, R.L. (1959). Practical petrographic classification of limestones. AAPG Bulletin, v. 43(1), p. 1–38.

Fölling, P.G., and Frimmel, H.E. (2002). Chemostratigraphic correlation of carbonate successions in the Gariep and Saldania Belts, Namibia and South Africa. Basin Research, v. 14, p. 69–88.

Fourny, A., Weis, D., and Scoates, J.S. (2016). Comprehensive Pb-Sr-Nd-Hf isotopic, trace element, and mineralogical characterization of mafic to ultramafic rock reference materials. Geochemistry, Geophysics, Geosystems, v. 17, p. 739–773.

Fujisaki, W., Matsui, Y., Asanuma, H., Sawaki, Y., Suzuki, K., and Maruyama, S. (2018). Global perturbations of carbon cycle during the Triassic–Jurassic transition recorded in the mid-Panthalassa. Earth and Planetary Science Letters, v. 500, p. 105–116.

Gabrielse, H. (1998). Geology of Cry Lake and Dease Lake map areas, north-central British Columbia. Bulletin of the Geological Survey of Canada, v. 504, p. 1–147.

Galbrun, B., Boulila, S., Krystyn, L., Richoz, S., Gardin, S., Bartolini, A., and Maslo, M. (2020). “Short” or “long” Rhaetian? Astronomical calibration of Austrian key sections. Global and Planetary Change, v. 192(103253), 20 p.

Galli, M.T., Jadoul, F., Bernasconi, S.M., and Weissert, H. (2005). Anomalies in global carbon cycling and extinction at the Triassic/Jurassic boundary: Evidence from a marine C-isotope record. Palaeogeography, Palaeoclimatology, Palaeoecology, v. 216, p. 203–214.

George, S.W.M., Nelson, J.L., Alberts, D., Greig, C.J., and Gehrels, G.E. (2021). Triassic–Jurassic Accretionary History and Tectonic Origin of Stikinia From U-Pb Geochronology and Lu-Hf Isotope Analysis, British Columbia. Tectonics, v. 40(4), 28 p.

Ginot, S., and Goudemand, N. (2019). Conodont size, trophic level, and the evolution of platform elements. Paleobiology, v. 45(3), p. 458–468.

Giordano, N., Rigo, M., Ciarapica, G., and Bertinelli, A. (2010). New biostratigraphical constraints for the Norian/Rhaetian boundary: Data from Lagonegro Basin, Southern Apennines, Italy. Lethaia, v. 43(4), p. 573–586.

Girard, C., Renaud, S., and Feist, R. (2007). Morphometrics of the Late Devonian conodont genus *Palmatolepis*: Phylogenetic, geographical and ecological contributions of a generic approach. Journal of Micropalaeontology, v. 26(1), p. 61–72.

Golding, M.L., and Orchard, M.J. (2021). Diverse Late Paleozoic and Triassic conodont faunas from the Cache Creek Terrane, central British Columbia, Canada. Palaeontographica Canadiana, n. 39, 93 p.

Golding, M.L., Mortensen, J.K., Zonneveld, J.P., and Orchard, M.J. (2016). U-Pb isotopic ages of euhedral zircons in the Rhaetian of British Columbia: Implications for Cordilleran tectonics during the Late Triassic. Geosphere, v. 12, p. 1606–1616.

Greene, S.E., Bottjer, D.J., Corsetti, F.A., Berelson, W.M., and Zonneveld, J.P. (2012). A subseafloor carbonate factory across the Triassic-Jurassic transition. Geology, v. 40, p. 1043–1046.

Guenser, P., Souquet, L., Dolédec, S., Mazza, M., Rigo, M., and Goudemand, N. (2019). Deciphering the roles of environment and development in the evolution of a Late Triassic assemblage of conodont elements. Paleobiology, v. 45(3), p. 440–457.

Guex, J., Bartolini, A., Atudorei, V., and Taylor, D. (2004). High-resolution ammonite and carbon isotope stratigraphy across the Triassic-Jurassic boundary at New York Canyon (Nevada). Earth and Planetary Science Letters, v. 225, p. 29–41.

Hall, R., and Pitaru, S. (2004). New Hettangian ammonite faunas and a Triassic Jurassic boundary succession, Fernie formation, Williston lake, British Columbia. Rivista Italiana Di Paleontologia e Stratigrafia, v. 110, p. 53–60.

Hallam, A. (2002). How catastrophic was the end-Triassic mass extinction? Lethaia, v. 35(2), p. 147–157.

Haq, B.U., Hardenbol, J., and Vail, P.R. (1988). Mesozoic and Cenozoic chronostratigraphy and cycles of sea-level change. Sea-Level Changes: An Integrated Approach, p. 71–108.

Hart, C.J.R. (1997). A Transect Across Stikinia: Geology of the Northern Whitehorse Map Area, Southern Yukon Territory. Exploration and Geological Services Division, Yukon, Indian and Northern Affairs Canada, v. 8, 112 p.

Hautmann, M. (2004). Effect of end-Triassic CO_2 maximum on carbonate sedimentation and marine mass extinction. Facies, v. 50(2), p. 257–261.

Hesselbo, S.P., Robinson, S.A., Surlyk, F., and Piasecki, S. (2002). Terrestrial and marine extinction at the Triassic-Jurassic boundary synchronized with major carbon-cycle perturbation: A link to initiation of massive volcanism? Geology, v. 30(3), p. 251–254.

Hillebrandt, A. V., Krystyn, L., Kürschner, W.M., Bonis, N.R., Ruhl, M., Richoz, S., Schobben, M.A., Urlichs, M., Bown, P.R., Kment, K., McRoberts, C.A., Simms, M., and Tomãsových, A. (2013). The global stratotype sections and point (GSSP) for the base of the Jurassic system at Kuhjoch (Karwendel Mountains, Northern Calcareous Alps, Tyrol, Austria). Episodes, v. 36(3), p. 162–198.

Hogancamp, N.J. (2020). P1 element morphological variability within the Late Pennsylvanian asymmetrical *Idiognathodus* clade from the Midcontinent, U.S.A. and implications for ontogeny, taxonomy, phylogeny, and function. Palaeogeography, Palaeoclimatology, Palaeoecology, v. 549(109090), p. 1–16.

Hogancamp, N., and Barrick, J. (2018). Morphometric analysis and taxonomic revision of North American species of the *Idiognathodus eudoraensis* Barrick, Heckel, & Boardman, 2008 group (Missourian, Upper Pennsylvanian Conodonts). Bulletins of American Paleontology, v. 395–396, p. 35–69.

Hogancamp, N.J., and Manship, L.L. (2016). Comparison of morphometric techniques and the ability to accurately reconstruct the form and distinguish between species of the

Palmatolepis winchelli group - Conodonta, Upper Devonian. Micropaleontology, v. 62(6), p. 439–451.

Hogancamp, N.J., Barrick, J.E., and Strauss, R.E. (2016). Geometric morphometric analysis and taxonomic revision of the Gzhelian (Late Pennsylvanian) conodont *Idiognathodus simulator* from North America. Acta Palaeontologica Polonica, v. 61(3), p. 477–502.

Hu, S.X., Zhang, Q.Y., Chen, Z.Q., Zhou, C.Y., Lü, T., Xie, T., Wen, W., Huang, J.Y., and Benton, M.J. (2011). The Luoping biota: Exceptional preservation, and new evidence on the Triassic recovery from end-Permian mass extinction. Proceedings of the Royal Society B: Biological Sciences, v. 278, p. 2274–2282.

Huckriede, R. (1958). Die Conodonten der mediterranen Trias und ihr stratigraphischer Wert. Paläontologische Zeitschrift, v. 32, p. 141–175.

Hüsing, S.K., Deenen, M.H.L., Koopmans, J.G., and Krijgsman, W. (2011). Magnetostratigraphic dating of the proposed Rhaetian GSSP at Steinbergkogel (Upper Triassic, Austria): Implications for the Late Triassic time scale. Earth and Planetary Science Letters, v. 302, p. 203–216.

Jacobsen, S.B., and Kaufman, A.J. (1999). The Sr, C and O isotopic evolution of Neoproterozoic seawater. Chemical Geology, v. 161, p. 37–57.

Jeletzky, J.A. (1970). Some salient features of early Mesozoic history of Insular tectonic belt, western British Columbia. Geological Survey of Canada Paper 69-14, 25 p.

Johnston, S.T. (2008). The cordilleran ribbon continent of North America. Annual Review of Earth and Planetary Sciences, v. 36(1), p. 495–530.

Johnston, S.T., and Borel, G.D. (2007). The odyssey of the Cache Creek terrane, Canadian Cordillera: Implications for accretionary orogens, tectonic setting of Panthalassa, the Pacific superwell, and break-up of Pangea. Earth and Planetary Science Letters, v. 253(3–4), p. 415–428.

Johnston, D.T., MacDonald, F.A., Gill, B.C., Hoffman, P.F., and Schrag, D.P. (2012). Uncovering the neoproterozoic carbon cycle. Nature, v. 483, p. 320–323.

Jones, D.L., Silberling, N.J., and Hillhouse, J. (1977). Wrangellia - a displaced terrane in northwestern North America. Canadian Journal of Earth Sciences, v. 14(11), p. 2565–2577.

Karádi, V., Cau, A., Mazza, M., and Rigo, M. (2020). The last phase of conodont evolution during the Late Triassic: Integrating biostratigraphic and phylogenetic approaches. Palaeogeography, Palaeoclimatology, Palaeoecology, v. 549(109144), p. 1–12.

Kasprak, A.H., Sepúlveda, J., Price-Waldman, R., Williford, K.H., Schoepfer, S.D., Haggart, J.W., Ward, P.D., Summons, R.E., and Whiteside, J.H. (2015). Episodic photic zone euxinia in the northeastern Panthalassic Ocean during the end-Triassic extinction. Geology, v. 43(4), p. 307–310.

Keith, M.L., and Weber, J.N. (1964). Carbon and oxygen isotopic composition of selected limestones and fossils. Geochimica et Cosmochimica Acta, v. 28, p. 1787–1816.

Keller, G. (2001). The end-Cretaceous mass extinction in the marine realm: Year 2000 assessment. Planetary and Space Science, v. 49, p. 817–830.

Keller, G., and Lindinger, M. (1989). Stable isotope, TOC and $CaCO_3$ record across the cretaceous/tertiary boundary at El Kef, Tunisia. Palaeogeography, Palaeoclimatology, Palaeoecology, v. 73, p. 243–265.

Kelz, V., Guenser, P., Rigo, M., and Jarochowska, E. (2023). Growth allometry and dental topography in Upper Triassic conodonts support trophic differentiation and molar-like element function. Paleobiology, v. 49(4), p. 665–683.

Kent, D. V., and Irving, E. (2010). Influence of inclination error in sedimentary rocks on the Triassic and Jurassic apparent pole wander path for North America and implications for Cordilleran tectonics. Journal of Geophysical Research: Solid Earth, v. 115(10), p. 1–25.

Kent, D. V., Olsen, P.E., and Muttoni, G. (2017). Astrochronostratigraphic polarity time scale (APTS) for the Late Triassic and Early Jurassic from continental sediments and correlation with standard marine stages. Earth-Science Reviews, v. 166, p. 153–180.

Klapper, G., and Foster, C.T. (1986). Quantification of outlines in Frasnian (Upper Devonian) platform conodonts. Canadian Journal of Earth Sciences, v. 23(8), p. 1214–1222.

Klapper, G., and Foster, C.T. (1993). Shape analysis of Frasnian species of the Late Devonian conodont genus *Palmatolepis*. Journal of Paleontology Memoir 32(4), p. 1–35.

Klingenberg, C.P. (2011). MorphoJ: an integrated software package for geometric morphometrics. Molecular Ecology Resources, v. 11, p. 353–357.

Knauth, L.P., and Kennedy, M.J. (2009). The late Precambrian greening of the Earth. Nature, v. 460, p. 728–732.

Korte, C., Kozur, H.W., Bruckschen, P., and Veizer, J. (2003). Strontium isotope evolution of Late Permian and Triassic seawater. Geochimica et Cosmochimica Acta, v. 67(1), p. 47–62.

Korte, C., Kozur, H.W., Joachimski, M.M., Strauss, H., Veizer, J., and Schwark, L. (2004). Carbon, sulfur, oxygen and strontium isotope records, organic geochemistry and biostratigraphy across the Permian/Triassic boundary in Abadeh, Iran. International Journal of Earth Sciences, v. 93, p. 565–581.

Korte, C., Kozur, H.W., and Veizer, J. (2005). $\delta^{13}C$ and $\delta^{18}O$ values of Triassic brachiopods and carbonate rocks as proxies for coeval seawater and palaeotemperature. Palaeogeography, Palaeoclimatology, Palaeoecology, v. 226, p. 287–306.

Kozur, H., and Mostler, H. (1971). Probleme der Conodontenforschung in der Trias. Geologisch-Palaeontologische Mitteilungen Innsbruck., v. 1(4), p. 1–19.

Kozur, H., and Mostler, H. (1976). Neue Conodonten aus dem Jungpaläozoikum und der Trias. Geologisch-Palaontologische Mitteilungen Innsbruck, v. 6(3), p. 1–33.

Kozur, H.W. (1989a). Significance of events in conodont evolution for the Permian and Triassic stratigraphy. Courier Forschungsinstitut Senckenberg, v. 117, p. 385–408.

Kozur, H.W. (1989b). The taxonomy of the Gondolellid conodonts in the Permian and Triassic. Courier Forschungs-Institut Senckenberg, v. 117, p. 409–469.

Krystyn, L. (2010). Decision report on the defining event for the base of the Rhaetian Stage. Albertiana, v. 38, p. 11–12.

Krystyn, L., Bouquerel, H., Kuerschner, W., Richoz, S., and Gallet, Y. (2007a). Proposal for a candidate GSSP for the base of the Rhaetian Stage. New Mexico Museum of Natural History and Science Bulletin, v. 41, p. 189–199.

Krystyn, L., Richoz, S., Gallet, Y., Bouquerel, H., Kürschner, W.M., and Spötl, C. (2007b). Updated bio- and magnetostratigraphy from Steinbergkogel (Austria), candidate GSSP for the base of the Rhaetian stage. Albertiana, v. 36, p. 164–173.

Kump, L.R., and Arthur, M.A. (1999). Interpreting carbon-isotope excursions: Carbonates and organic matter. Chemical Geology, v. 161, p. 181–198.

Kuroda, J., Hori, R.S., Suzuki, K., Gröcke, D.R., and Ohkouchi, N. (2010). Marine osmium isotope record across the Triassic-Jurassic boundary from a Pacific pelagic site. Geology, v. 38, p. 1095–1098.

Kürschner, W.M., Bonis, N.R., and Krystyn, L. (2007). Carbon-isotope stratigraphy and palynostratigraphy of the Triassic-Jurassic transition in the Tiefengraben section - Northern Calcareous Alps (Austria). Palaeogeography, Palaeoclimatology, Palaeoecology, v. 244, p. 257–280.

Lai, X., Jiang, H., and Wignall, P.B. (2018). A review of the Late Permian – Early Triassic conodont record and its significance for the end-Permian mass extinction. Revue de Micropaleontologie, v. 61(3–4), p. 155–164.

Larina, E., Bottjer, D.J., Corsetti, F.A., Zonneveld, J.P., Celestian, A.J., and Bailey, J. V. (2019). Uppermost Triassic phosphorites from Williston Lake, Canada: Link to fluctuating euxinic-anoxic conditions in northeastern Panthalassa before the end-Triassic mass extinction. Scientific Reports, v. 9(18790), p. 1–9.

Lei, J.Z.X., Husson, J.M., Golding, M.L., Orchard, M.J., and Zonneveld, J.-P. (2021). Stable carbon isotope record of carbonate across the Carnian – Norian boundary at the prospective GSSP section at Black Bear Ridge, British Columbia, Canada. Albertiana, v. 46, p. 1–10.

Lei, J.Z.X., Golding, M.L., and Husson, J.M. (2022). Paleoenvironmental interpretation of the Late Triassic Norian – Rhaetian boundary interval in the Whitehorse Trough (Stikine Terrane, northern Canadian Cordillera). Palaeogeography, Palaeoclimatology, Palaeoecology, v. 608(111306), p. 1–17.

Lei, J.Z.X., Golding, M.L., and Husson, J.M. (2024). Morphological trends across the Norian/Rhaetian boundary within Late Triassic conodonts in western Canada: Implications for protracted paleoenvironmental disturbance preceding the end-Triassic mass extinction. Paleobiology, v. 50(1), p. 85–95.

Li, M., Zhang, Y., Huang, C., Ogg, J., Hinnov, L., Wang, Y., Zou, Z., and Li, L. (2017). Astronomical tuning and magnetostratigraphy of the Upper Triassic Xujiahe Formation of South China and Newark Supergroup of North America: Implications for the Late Triassic time scale. Earth and Planetary Science Letters, v. 475, p. 207–223.

Longridge, L.M., Carter, E.S., Smith, P.L., and Tipper, H.W. (2007). Early Hettangian ammonites and radiolarians from the Queen Charlotte Islands, British Columbia and their bearing on the definition of the Triassic-Jurassic boundary. Palaeogeography, Palaeoclimatology, Palaeoecology, v. 244, p. 142–169.

Lowey, G.W., Long, D.G.F., Fowler, M.G., Sweet, A.R., and Orchard, M.J. (2009). Petroleum source rock potential of Whitehorse trough: A frontier basin in south-central Yukon. Bulletin of Canadian Petroleum Geology, v. 57, p. 350–386.

Lucas, S.G. (2018). Late Triassic ammonoids: Distribution, biostratigraphy and biotic events. The Late Triassic World, Topics in Geobiology 46, p. 237–261.

Luo, G., Lai, X., Jiang, H., and Zhang, K. (2006). Size variation of the end Permian conodont *Neogondolella* at Meishan Section, Changxing, Zhejiang and its significance. Science in China, Series D: Earth Sciences, v. 49(4), p. 337–347.

Maron, M., Rigo, M., Bertinelli, A., Katz, M.E., Godfrey, L., Zaffani, M., and Muttoni, G. (2015). Magnetostratigraphy, biostratigraphy, and chemostratigraphy of the Pignola-Abriola section: New constraints for the Norian-Rhaetian boundary. Bulletin of the Geological Society of America, v. 127, p. 962–974.

Maron, M., Muttoni, G., Rigo, M., Gianolla, P., and Kent, D. V. (2019). New magnetobiostratigraphic results from the Ladinian of the Dolomites and implications for the Triassic geomagnetic polarity timescale. Palaeogeography, Palaeoclimatology, Palaeoecology, v. 517, p. 52–73.

Marshall, J.D. (1992). Climatic and oceanographic isotopic signals from the carbonate rock record and their preservation. Geological Magazine, v. 129, p. 143–160.

Martínez-Pérez, C., Plasencia, P., Cascales-Miñana, B., Mazza, M., and Botella, H. (2014a). New insights into the diversity dynamics of Triassic conodonts. Historical Biology, v. 26(5), p. 591–602.

Martínez-Pérez, C., Rayfield, E.J., Purnell, M.A., and Donoghue, P.C.J. (2014b). Finite element, occlusal, microwear and microstructural analyses indicate that conodont microstructure is adapted to dental function. Palaeontology, v. 57(5), p. 1059–1066.

Martínez-Pérez, C., Rayfield, E.J., Botella, H., and Donoghue, P.C.J. (2016). Translating taxonomy into the evolution of conodont feeding ecology. Geology, v. 44(4), p. 247–250.

Marzoli, A., Renne, P.R., Piccirillo, E.M., Ernesto, M., Bellieni, G., and De Min, A. (1999). Extensive 200-million-year-old continental flood basalts of the Central Atlantic Magmatic Province. Science, v. 284(5414), p. 616–618.

Marzoli, A., Bertrand, H., Knight, K.B., Cirilli, S., Buratti, N., Vérati, C., Nomade, S., Renne, P.R., Youbi, N., Martini, R., Allenbach, K., Neuwerth, R., Rapaille, C., Zaninetti, L., and Bellieni, G. (2004). Synchrony of the Central Atlantic magmatic province and the Triassic-Jurassic boundary climatic and biotic crisis. Geology, v. 32(11), p. 973–976.

Massey, N.W.D., Grunsky, E.C., and Desjardins, P.J. (1994). Geological compilation of Vancouver Island. British Columbia Ministry of Energy, Mines and Petroleum Resources, Open File 1994-6.

Mazza, M., Rigo, M., and Gullo, M. (2012). Taxonomy and biostratigraphic record of the Upper Triassic conodonts of the Pizzo Mondello section (western Sicily, Italy), GSSP candidate for the base of the Norian. Rivista Italiana Di Paleontologia e Stratigrafia, v. 118(1), p. 85–130.

McElwain, J.C., Beerling, D.J., and Woodward, F.I. (1999). Fossil plants and global warming at the Triassic-Jurassic boundary. Science, v. 285, p. 1386–1390.

McRoberts, C.A. (2001). Triassic bivalves and the initial marine Mesozoic revolution: A role for predators? Geology, v. 29, p. 359–362.

McRoberts, C.A. (2007). The halobiid bivalve succession across a potential Carnian/Norian GSSP at Black Bear Ridge, Williston Lake, northeast British Columbia, Canada. Albertiana, v. 36, p. 142–145.

McRoberts, C.A. (2011). Late Triassic Bivalvia (chiefly Halobiidae and Monotidae) from the Pardonet Formation, Williston Lake area, northeastern British Columbia, Canada. Journal of Paleontology, v. 85, p. 613–664.

McRoberts, C.A., Furrer, H., and Jones, D.S. (1997). Palaeoenvironmental interpretation of a Triassic-Jurassic boundary section from western Austria based on palaeoecological and geochemical data. Palaeogeography, Palaeoclimatology, Palaeoecology, v. 136, p. 79–95.

Meyer, K.M., Yu, M., Lehrmann, D., van de Schootbrugge, B., and Payne, J.L. (2013). Constraints on Early Triassic carbon cycle dynamics from paired organic and inorganic carbon isotope records. Earth and Planetary Science Letters, v. 361, p. 429–435.

Mihalynuk, M.G. (1999). Geology and Mineral Resources of the Tagish Lake Area (NTS 104M/8, 9, 10E, 15, and 104N/12W) northwestern British Columbia. British Columbia Geological Survey Bulletin, v. 105, 217 p.

Mihalynuk, M.G., Nelson, J.A., and Diakow, L.J. (1994). Cache Creek terrane entrapment: Oroclinal paradox within the Canadian Cordillera. Tectonics, v. 13(3), p. 575–595.

Mihalynuk, M.G., Zagorevski, A., English, J.M., Orchard, M.J., Bidgood, A.K., Joyce, N., and Friedman, R.M. (2017). Geology of the Sinwa Creek area, northwest BC (104K/14). Geological Fieldwork 2016, British Columbia Ministry of Energy and Mines, British Columbia Geological Survey Paper 2017-1, p. 153–178.

Monger, J.W.H. (1997). Plate tectonics and northern cordilleran geology: An unfinished revolution. Geoscience Canada, v. 24, p. 189–198.

Monger, J.W.H., and Ross, C.A. (1971). Distribution of Fusulinaceans in the Western Canadian Cordillera. Canadian Journal of Earth Sciences, v. 8(2), p. 259–278.

Mosher, L.C. (1968). Paleontological Society Triassic Conodonts from western North America and Europe and their correlation. Journal of Paleontology, v. 42, p. 895–946.

Muttoni, G., Mazza, M., Mosher, D., Katz, M.E., Kent, D. V., and Balini, M. (2014). A Middle-Late Triassic (Ladinian-Rhaetian) carbon and oxygen isotope record from the Tethyan Ocean. Palaeogeography, Palaeoclimatology, Palaeoecology, v. 399, p. 246–259.

Nixon, G.T., and Orr, A.J. (2007). Recent revisions to the Early Mesozoic stratigraphy of northern Vancouver Island (NTS 102I; 092L) and metallogenic implications, British Columbia. British Columbia Ministry of Energy, Mines and Petroleum Resources, Geological Fieldwork 2006, p. 163–177.

Nixon, G.T., Hammack, J.L., Koyanagi, V.M., Snyder, L.D., Payie, G.J., Panteleyev, A., Massey, N.W.D., Hamilton, J.V., Orr, A.J., Friedman, R.M., Archibald, D.A., Haggart, J.W., Orchard, M.J., Tozer, E.T., Tipper, H.W., Poulton, T.P., Pálfy, J., and Cordey, F. (2011). Geology, geochronology, lithochemistry and metamorphism of the Holberg-Winter Harbour Area, Northern Vancouver Island. British Columbia Geological Survey, Geoscience Map 2011-1.

Ogg, J.G., Huang, C., and Hinnov, L. (2014). Triassic timescale status: A brief overview. Albertiana, v. 41, p. 3–30.

Ogg, J.G., Chen, Z.-Q., Orchard, M.J., and Jiang, H.S. (2020). The Triassic Period. Geologic Time Scale 2020, Elsevier, p. 903–953.

Onoue, T., Yamashita, K., Fukuda, C., Soda, K., Tomimatsu, Y., Abate, B., and Rigo, M. (2018). Sr isotope variations in the Upper Triassic succession at Pizzo Mondello, Sicily: Constraints on the timing of the Cimmerian Orogeny. Palaeogeography, Palaeoclimatology, Palaeoecology, v. 499, p. 131–137.

Orchard, M.J. (1983). *Epigondolella* populations and their phylogeny and zonation in the Upper Triassic. Fossils and Strata, v. 15, p. 177–192.

Orchard, M.J. (1991a). Upper Triassic conodont biochronology and new index species from the Canadian Cordillera. Geological Survey of Canada Bulletin 417, p. 299–335.

Orchard, M.J. (1991b). Late Triassic conodont biochronology and biostratigraphy of the Kunga Group, Queen Charlotte Islands, British Columbia. Evolution and Hydrocarbon Potential of the Queen Charlotte Basin, British Columbia, Geological Survey of Canada Paper 90–10, p. 173–193.

Orchard, M.J. (1994). Late Triassic (Norian) conodonts from Peru. Paleontology and Stratigraphy of Triassic to Jurassic Rocks of the Peruvian Andes, Palaeontographica Abteilung A Band 233 Lieferung v. 1–6, p. 203–208.

Orchard, M.J. (2007). A proposed Carnian-Norian boundary GSSP at Black Bear Ridge, northeast British Columbia, and a new conodont framework for the boundary interval. Albertiana, v. 36, p. 130–141.

Orchard, M.J. (2014). Conodonts from the Carnian-Norian boundary (Upper Triassic) of Black Bear Ridge, northeastern British Columbia, Canada. New Mexico Museum of Natural History and Science Bulletin 64, 139 p.

Orchard, M.J. (2018). The lower-middle Norian (Upper Triassic) boundary: New conodont taxa and a refined biozonation. Bulletins of American Paleontology, v. 395–396, p. 165–193.

Orchard, M.J. (2019). The Carnian-Norian boundary GSSP candidate at Black Bear Ridge, British Columbia, Canada: update, correlation, and conodont taxonomy. Albertiana, v. 45, p. 50–68.

Orchard, M.J., Zonneveld, J.P., Johns, M.J., McRoberts, C.A., Sandy, M.R., Tozer, E.T., and Carrelli, G.G. (2001). Fossil succession and sequence stratigraphy of the Upper

Triassic of Black Bear Ridge, northeast British Columbia, a GSSP prospect for the Carnian- Norian boundary. Albertiana, v. 25, p. 10–22.

Orchard, M. J., Carter, E.S., Lucas, S.G., and Taylor, D.G. (2007). Rhaetian (Upper Triassic) conodonts and radiolarians from New York Canyon, Nevada, USA. Albertiana, v. 35, p. 59–65.

Pálfy, J., Demény, A., Hass, J., Hetényi, M., Orchard, M.J., and Vetö, I. (2001). Carbon isotope anomaly and other geochemical changes at the Triassic-Jurassic boundary from a marine section in Hungary. Geology, v. 29, p. 1047–1050.

Pálfy, J., Demény, A., Haas, J., Carter, E.S., Görög, Á., Halász, D., Oravecz-Scheffer, A., Hetényi, M., Márton, E., Orchard, M.J., Ozsvárt, P., Veto, I., and Zajzon, N. (2007). Triassic-Jurassic boundary events inferred from integrated stratigraphy of the Csovár section, Hungary. Palaeogeography, Palaeoclimatology, Palaeoecology, v. 244(1–4), p. 11–33.

Patterson, W.P., and Walter, L.M. (1994). Depletion of ^{13}C in seawater ΣCO_2 on modern carbonate platforms: Significance for the carbon isotopic record of carbonates. Geology, v. 22, p. 885–888.

Peters, S.E., Husson, J.M., and Czaplewski, J. (2018). Macrostrat: a platform for geological data integration and deep-time Earth crust research. Geochemistry, Geophysics, Geosystems, v. 19(4), p. 1393–1409.

Pruss, S.B., Corsetti, F.A., and Bottjer, D.J. (2005). The unusual sedimentary rock record of the Early Triassic: A case study from the southwestern United States. Palaeogeography, Palaeoclimatology, Palaeoecology, v. 222, p. 33–52.

Purnell, M.A. (1993). Feeding mechanisms in conodonts and the function of the earliest vertebrate hard tissues. Geology, v. 21(4), p. 375–377.

Purnell, M.A. (1995). Microwear on conodont elements and macrophagy in the first vertebrates. Nature, v. 374(6525), p. 798–800.

Purnell, M.A., and Jones, D. (2012). Quantitative analysis of conodont tooth wear and damage as a test of ecological and functional hypotheses. Paleobiology, v. 38(4), p. 605–626.

Purnell, M.A., and Von Bitter, P.H. (1992). Blade-shaped conodont elements functioned as cutting teeth. Nature, v. 359(6396), p. 629–631.

Raup, D.M., and Sepkoski, J.J. (1982). Mass extinctions in the marine fossil record. Science, v. 215(4539), p. 1501–1503.

Renaud, S., and Girard, C. (1999). Strategies of survival during extreme environmental perturbations: Evolution of conodonts in response to the Kellwasser crisis (Upper Devonian). Palaeogeography, Palaeoclimatology, Palaeoecology, v. 146(1–4), p. 19–32.

Rigo, M., and Campbell, H. (2022). Correlation between the Warepan/Otapirian and the Norian/Rhaetian stage boundary: Implications of a global negative $\delta^{13}C_{org}$ perturbation. New Zealand Journal of Geology and Geophysics, v. 65(3), p. 397–406.

Rigo, M., Bertinelli, A., Concheri, G., Gattolin, G., Godfrey, L., Katz, M.E., Maron, M., Mietto, P., Muttoni, G., Sprovieri, M., Stellin, F., and Zaffani, M. (2016). The Pignola-

Abriola section (southern Apennines, Italy): A new GSSP candidate for the base of the Rhaetian Stage. Lethaia, v. 49(3), p. 287–306.

Rigo, M., Mazza, M., Karádi, V., and Nicora, A. (2018). New Upper Triassic conodont biozonation of the Tethyan realm. The Late Triassic World, Topics in Geobiology 46, p. 189–235.

Rigo, M., Onoue, T., Tanner, L., Lucas, S.G., Godfrey, L., Katz, M.E., Zaffani, M., Grice, K., Cesar, J., Yamashita, D., Maron, M., Tackett, L.S., Campbell, H., Tateo, F., Concheri, G., Agnini, C., Chiari, M., and Bertinelli, A. (2020). The Late Triassic Extinction at the Norian/Rhaetian boundary: Biotic evidence and geochemical analysis. Earth-Science Reviews, v. 204(103180), p. 1–15.

Ripperdan, R.L. (2019). Stratigraphic variation in marine carbonate carbon isotope ratios. Stable Isotope Geochemistry, v. 43, p. 637–662.

Rohlf, F.J. (2010a). TpsDig, version 2.16. Department of Ecology and Evolution, State University of New York, Stony Brook.

Rohlf, F.J. (2010b). TpsUtil, version 1.46. Department of Ecology and Evolution, State University of New York, Stony Brook.

Rooney, A.D., Chew, D.M., and Selby, D. (2011). Re–Os geochronology of the Neoproterozoic-Cambrian Dalradian Supergroup of Scotland and Ireland: Implications for Neoproterozoic stratigraphy, glaciations and Re–Os systematics. Precambrian Research, v. 185, p. 202–214.

Rooney, A.D., Macdonald, F.A., Strauss, J. V., Dudás, F.Ö., Hallmann, C., and Selby, D. (2014). Re–Os geochronology and coupled Os-Sr isotope constraints on the Sturtian snowball Earth. Proceedings of the National Academy of Sciences of the United States of America, v. 111, p. 51–56.

Ruhl, M., and Kürschner, W.M. (2011). Multiple phases of carbon cycle disturbance from large igneous province formation at the Triassic-Jurassic transition. Geology, v. 39(5), p. 431–434.

Ruhl, M., Kürschner, W.M., and Krystyn, L. (2009). Triassic-Jurassic organic carbon isotope stratigraphy of key sections in the western Tethys realm (Austria). Earth and Planetary Science Letters, v. 281, p. 169–187.

Sato, H., Nozaki, T., Onoue, T., Ishikawa, A., Soda, K., Yasukawa, K., Kimura, J.-I., Chang, Q., Kato, Y., and Rigo, M. (2023). Rhenium-osmium isotope evidence for the onset of volcanism in the central Panthalassa Ocean during the Norian “chaotic carbon episode.” Global and Planetary Change, v. 229(104239), p. 1–16.

Schaal, E.K., Clapham, M.E., Rego, B.L., Wang, S.C., and Payne, J.L. (2015). Comparative size evolution of marine clades from the Late Permian through Middle Triassic. Paleobiology, v. 42(1), p. 127–142.

Schlager, W. (1981). The paradox of drowned reefs and carbonate platforms. Geological Society of America Bulletin, v. 92, p. 197–211.

Schoepfer, S.D., Algeo, T.J., Ward, P.D., Williford, K.H., and Haggart, J.W. (2016). Testing the limits in a greenhouse ocean: Did low nitrogen availability limit marine productivity during the end-Triassic mass extinction? Earth and Planetary Science Letters, v. 451, p. 138–148.

Selby, D., and Creaser, R.A. (2003). Re–Os geochronology of organic rich sediments: An evaluation of organic matter analysis methods. Chemical Geology, v. 200, p. 225–240.

Sephton, M.A., Amor, K., Wignall, P.B., Newton, R., and Zonneveld, J.-P. (2002). Carbon and nitrogen isotope disturbances and an end-Norian (Late Triassic) extinction event. Geology, v. 30, p. 1119–1122.

Sepkoski, J.J. (1981). A factor analytic description of the Phanerozoic marine fossil record. Paleobiology, v. 7(1), p. 36–53.

Sepkoski, J.J. (1982). Flat-pebble conglomerates, storm deposits, and the Cambrian bottom fauna. Cyclic and Event Stratification, Springer-Verlag, Berlin, p. 371–385.

Simms, M.J., and Ruffell, A.H. (1989). Synchroneity of climatic change and extinctions in the Late Triassic. Geology, v. 17, p. 265–268.

Souther, J.G. (1971). Geology and Mineral Deposits of Tulsequah Map-Area, British Columbia (104K). Geological Survey of Canada Memoir, v. 362, 84 p.

Stanley, G.D. (1988). The History of Early Mesozoic Reef Communities : A three-step process. Palaios, v. 3(2), p. 170–183.

Stanley, G.D. (2003). The evolution of modern corals and their early history. Earth-Science Reviews, v. 60(3–4), p. 195–225.

Stone, J. (1987). Review of investigative techniques used in the study of conodonts. British Micropalaeontological Society Series, Conodonts: Investigative techniques and applications, p. 17–34.

Tackett, L.S., Kaufman, A.J., Corsetti, F.A., and Bottjer, D.J. (2014). Strontium isotope stratigraphy of the Gabbs Formation (Nevada): Implications for global Norian-Rhaetian correlations and faunal turnover. Lethaia, v. 47, p. 500–511.

Tanner, L.H., Lucas, S.G., and Chapman, M.G. (2004). Assessing the record and causes of Late Triassic extinctions. Earth-Science Reviews, v. 65(4), p. 103–139.

Taylor, D., Guex, J., and Lucas, S.G. (2021). Ammonoids of the latest Triassic Gabbs Formation at New York Canyon, Mineral County, Nevada. Fossil Record, v. 7, p. 393–425.

Tempelman-Kluit, D.J. (1979). Transported cataclasite, ophiolite, and granodiorite in Yukon : evidence of arc-continent collision. Geological Survey of Canada, Paper, v. 79-14, 27 p.

Thibodeau, A.M., Ritterbush, K., Yager, J.A., West, A.J., Ibarra, Y., Bottjer, D.J., Berelson, W.M., Bergquist, B.A., and Corsetti, F.A. (2016). Mercury anomalies and the timing of biotic recovery following the end-Triassic mass extinction. Nature Communications, v. 7(11147), p. 1–8.

Tipper, H.W., Carter, E.S., Orchard, M.J., and Tozer, E.T. (1994). The Triassic-Jurassic boundary in Queen Charlotte Islands, British Columbia defined by ammonites, conodonts and radiolarians. Geobios Mémoire Special, v. 17, p. 485–492.

Tozer, E.T. (1982). Late Triassic (upper Norian) and earliest Jurassic (Hettangian) rocks and ammonoid faunas, Half-way River area and Pine Pass map areas, British Columbia. Geological Survey of Canada Paper 82 (1A), p. 385–391.

Tozer, E.T. (1994). Canadian Triassic ammonoid faunas. Geological Survey of Canada Bulletin 467, 663 p.

Tucker, M.E., and Wright, V.P. (1990). Carbonate Sedimentology. Blackwell, Oxford.

Umhoefer, P.J., and Tipper, H.W. (1998). Stratigraphy, depositional environment, and tectonic setting of the Upper Triassic to Middle Jurassic rocks of the Chilcotin Ranges, southwestern British Columbia. Geological Survey of Canada Bulletin 519, 58 p.

Veevers, J.J. (1994). Pangea: evolution of a supercontinent and its consequences for Earth’s paleoclimate and sedimentary environments. Geological Society of America Special Paper, v. 288, p. 13–23.

Vermeij, G.J. (1977). The Mesozoic marine revolution: Evidence from snails, predators, grazers. Paleobiology, v. 3(3), p. 245–258.

Wagner, P.J., Kosnik, M.A., and Lidgard, S. (2006). Abundance distributions imply elevated complexity of post-Paleozoic marine ecosystems. Science, v. 314, p. 1289–1292.

Walker, J.C.G., Hays, P.B., and Kasting, J.F. (1981). A negative feedback mechanism for the long-term stabilization of Earth’s surface temperature. Journal of Geophysical Research, v. 86, p. 9776–9782.

Ward, P.D., Haggart, J.W., Carter, E.S., Wilbur, D., Tipper, H.W., and Evans, T. (2001). Sudden productivity collapse associated with the Triassic-Jurassic boundary mass extinction. Science, v. 292(5519), p. 1148–1151.

Ward, P.D., Garrison, G.H., Haggart, J.W., Kring, D.A., and Beattie, M.J. (2004). Isotopic evidence bearing on Late Triassic extinction events, Queen Charlotte Islands, British Columbia, and implications for the duration and cause of the Triassic/Jurassic mass extinction. Earth and Planetary Science Letters, v. 224(3–4), p. 589–600.

Ward, P.D., Garrison, G.H., Williford, K.H., Kring, D.A., Goodwin, D., Beattie, M.J., and McRoberts, C.A. (2007). The organic carbon isotopic and paleontological record across the Triassic-Jurassic boundary at the candidate GSSP section at Ferguson Hill, Muller Canyon, Nevada, USA. Palaeogeography, Palaeoclimatology, Palaeoecology, v. 244, p. 281–289.

Warren, J. (2000). Dolomite: occurrence, evolution and economically important associations. Earth-Science Reviews, v. 52, p. 1–81.

Whiteside, J.H., and Ward, P.D. (2011). Ammonoid diversity and disparity track episodes of chaotic carbon cycling during the early Mesozoic. Geology, v. 39, p. 99–102.

Wignall, P.B., and Atkinson, J.W. (2020). A two-phase end-Triassic mass extinction. Earth-Science Reviews, v. 208 (103282), 16 p.

Wignall, P.B., and Twitchett, R.J. (1999). Unusual intraclastic limestones in Lower Triassic carbonates and their bearing on the aftermath of the end-Permian mass extinction. Sedimentology, v. 46, p. 303–316.

Wignall, P.B., Zonneveld, J.P., Newton, R.J., Amor, K., Sephton, M.A., and Hartley, S. (2007). The end Triassic mass extinction record of Williston Lake, British Columbia. Palaeogeography, Palaeoclimatology, Palaeoecology, v. 253(3–4), p. 385–406.

Williford, K.H., Orchard, M.J., Zonneveld, J.-P., McRoberts, C.A., and Beatty, T.W. (2007a). A record of stable organic carbon isotopes from the Carnian-Norian boundary section at Black Bear Ridge, Williston Lake, British Columbia. Albertiana, v. 36, p. 146–148.

Williford, K.H., Ward, P.D., Garrison, G.H., and Buick, R. (2007b). An extended organic carbon-isotope record across the Triassic – Jurassic boundary in the Queen Charlotte Islands , British Columbia , Canada. Palaeogeography, Palaeoclimatology, Palaeoecology, v. 244, p. 290–296.

Williford, K.H., Foriel, J., Ward, P.D., and Steig, E.J. (2009). Major perturbation in sulfur cycling at the Triassic-Jurassic boundary. Geology, v. 37(9), p. 835–838.

Wilson, J.L. (1975). Carbonate Facies in Geologic History. Springer-Verlag, New York.

Woods, A.D. (2009). Anatomy of an anachronistic carbonate platform: Lower Triassic carbonates of the southwestern United States. Australian Journal of Earth Sciences, v. 56, p. 825–839.

Wotzlaw, J.F., Guex, J., Bartolini, A., Gallet, Y., Krystyn, L., McRoberts, C.A., Taylor, D., Schoene, B., and Schaltegger, U. (2014). Towards accurate numerical calibration of the Late Triassic: High-precision U-Pb geochronology constraints on the duration of the Rhaetian. Geology, v. 42, p. 571–574.

Wright, N., Zahirovic, S., and Seton, M. (2013). Towards community-driven paleogeographic reconstructions: Integrating open-access paleogeographic and paleobiology data with plate tectonics. Biogeosciences, v. 10(3), p. 1529–1541.

Yager, J.A., West, A.J., Corsetti, F.A., Berelson, W.M., Rollins, N.E., Rosas, S., and Bottjer, D.J. (2017). Duration of and decoupling between carbon isotope excursions during the end-Triassic mass extinction and Central Atlantic Magmatic Province emplacement. Earth and Planetary Science Letters, v. 473, p. 227–236.

Zaffani, M., Agnini, C., Concheri, G., Godfrey, L., Katz, M., Maron, M., and Rigo, M. (2017). The Norian "chaotic carbon interval": New clues from the $\delta^{13}C_{org}$ record of the Lagonegro Basin (southern Italy). Geosphere, v. 13(4), p. 1–16.

Zaffani, M., Jadoul, F., and Rigo, M. (2018). A new Rhaetian $\delta^{13}C_{org}$ record: Carbon cycle disturbances, volcanism, end-Triassic mass extinction (ETE). Earth-Science Reviews, v. 178, p. 92–104.

Zhang, M., Jiang, H., Purnell, M.A., and Lai, X. (2017). Testing hypotheses of element loss and instability in the apparatus composition of complex conodonts: articulated skeletons of *Hindeodus*. Palaeontology, v. 60(4), p. 595–608.

Zimmerman, A.N., Johnson, C.C., and Polly, P.D. (2018). Taxonomic and evolutionary pattern revisions resulting from geometric morphometric analysis of Pennsylvanian *Neognathodus* conodonts, Illinois Basin. Paleobiology, v. 44(4), p. 660–683.

Zonneveld, J.P., Beatty, T.W., Williford, K.H., Orchard, M.J., and McRoberts, C.A. (2010). Stratigraphy and sedimentology of the lower Black Bear Ridge section, British Columbia: Candidate for the base-Norian GSSP. Stratigraphy, v. 7, p. 61–82.

Appendix A: Chapter two supplementary material

Appendix A1: Mount Sinwa thin section summary.

Thin Section	Section	Height (m)	Field Lithology	Field Facies
V-003818	Sinwa East	0	Massive mudstone	1
V-003821	Sinwa East	44	Bedded wackestone with mudchips	2
V-003822	Sinwa East	72	Laminated massive mudstone with mudchips	2
V-003823	Sinwa East	92	Massive mudstone	1
V-003826	Sinwa East	114	Silicified bedded bivalve coral floatstone	3
V-003827	Sinwa East	118	Silicified bedded bivalve coral wackestone	3
V-003834	Sinwa East	231	Highly silicified bedded intact coral boundstone	4
SW-0.0	Sinwa West	0	Recrystallized mudstone	6
SW-40.0	Sinwa West	40	Bivalve floatstone	3
SW-60.0	Sinwa West	60	Mudstone	1
SW-90.0	Sinwa West	90	Mudstone	1
SW-140.0	Sinwa West	140	Mudstone	1
SW-150.0	Sinwa West	150	Bivalve coral floatstone with shale interbeds	4
SW-153.0	Sinwa West	153	Bivalve coral floatstone with shale interbeds	4

Thin Section	Folk	Dunham
V-003818	Intrapelbiomicrite	Bioclastic wackestone
V-003821	Intrabiomicrite	Bioclastic wackestone
V-003822	Micrite	Mudstone
V-003823	Micrite	Mudstone
V-003826	Biomicrite	Bioclastic wackestone
V-003827	Biomicrite	Bioclastic wackestone
V-003834	Biomicrite	Bioclastic wackestone
SW-0.0	Intrabiomicrite	Bioclastic wackestone
SW-40.0	Pelbiomicrite	Bioclastic wackestone
SW-60.0	Intrabiomicrite	Bioclastic wackestone
SW-90.0	Micrite	Mudstone
SW-140.0	Micrite	Mudstone
SW-150.0	Micrite	Mudstone
SW-153.0	Biointramicrite	Lithoclast wackestone

Thin Section	Misc.
V-003818	bivalves common, peloids common, 1 large spar intraclast
V-003821	arc regions of spar common, large bivalves? Spar clasts common in matrix
V-003822	
V-003823	arc regions of spar uncommon, large bivalves?
V-003826	very dark matrix, bivalves and coral common, single crinoid
V-003827	very dark matrix, bryozoans and gastropods common
V-003834	circular regions of spar common, single bivalve
SW-0.0	bivalves common, highly veined
SW-40.0	subrounded dark opaque clasts common, bivalves common with 1 very large? 1 bryozoan
SW-60.0	bivalves and bryozoans common, crinoids uncommon, spar clasts common
SW-90.0	large vein
SW-140.0	highly veined
SW-150.0	
SW-153.0	bivalves common, 1 large bryozoan, large spar intraclasts and smaller quartz common

Appendix A2: Mount Sinwa conodont recovery.

Section	**Height (m)**	***M. bidentata***	***M. carinata***	***M. englandi***	***M.* cf. *englandi***	***M. mosheri* B**	***M. postera***
Sinwa East	5	0	0	0	2	0	0
Sinwa East	42	0	0	0	4	0	1
Sinwa East	106	0	5	0	15	0	0
Sinwa East	112	0	4	1	12	0	0
Sinwa East	114	2	12	0	14	0	0
Sinwa East	118	0	0	0	1	0	0
Sinwa East	120	2	9	3	25	0	0
Sinwa East	127	0	7	1	15	0	0
Sinwa East	164	0	1	3	5	0	0
Sinwa East	179	0	3	1	6	0	0
Sinwa East	188	0	9	0	2	0	0
Sinwa East	205	1	0	0	0	0	0
Sinwa East	208	0	6	0	2	0	0
Sinwa East	211	1	23	3	21	1	0
Sinwa East	231	2	3	1	1	0	0
Sinwa East	231	2	5	2	11	2	0
Sinwa West	138	0	0	0	2	0	0
Sinwa West	146	0	6	0	2	1	0
Sinwa West	148	0	0	0	1	0	0
Sinwa West	163	0	0	0	2	0	0
		10	93	15	143	4	1

Section	**Height (m)**	***M.* cf. *spiculata***	***M. spinosa***	***M.* sp.**	**ramiform**	**sample total**
Sinwa East	5	0	0	1	0	3
Sinwa East	42	0	0	2	0	7
Sinwa East	106	1	0	16	7	44
Sinwa East	112	1	0	12	3	33
Sinwa East	114	0	0	26	7	61
Sinwa East	118	0	0	7	3	11
Sinwa East	120	0	0	24	19	82
Sinwa East	127	0	0	6	9	38
Sinwa East	164	0	2	9	0	20
Sinwa East	179	0	0	7	3	20
Sinwa East	188	0	0	4	0	15
Sinwa East	205	2	0	3	1	7
Sinwa East	208	0	0	2	0	10
Sinwa East	211	6	3	43	7	108
Sinwa East	231	0	0	2	1	10
Sinwa East	231	2	0	13	1	38
Sinwa West	138	1	0	4	1	8
Sinwa West	146	0	0	12	0	21
Sinwa West	148	0	0	1	0	2
Sinwa West	163	0	1	2	0	5
		13	6	196	62	grand total: 543

Appendix A3: Sinwa East geochemical data.

Height (m)	d13C (carb)	d18O (carb)	d13C (org)	% carb	Sr (ppm)	Sr/Ca	Mg/Ca	Mn/Ca
0	1.39	-13.34	-23.38	99.65	1295.84	1.48E-03	4.69E-03	8.54E-05
1	1.47	-12.51						
2.1	1.58	-6.08						
3	0.81	-10.84						
4	1.60	-12.54			1396.42	1.60E-03	5.39E-03	9.58E-05
5	1.72	-15.61						
6	0.32	-11.40						
7	1.82	-6.67						
8	2.66	-10.71			1019.52	1.36E-03	2.01E-01	5.41E-04
9	1.94	-5.77						
11.6	2.61	-7.47						
13	2.03	-6.02	-28.06	98.23	974.24	1.52E-03	4.29E-01	3.36E-04
13.9	1.72	-7.29						
15	1.65	-6.50						
16	1.00	-13.09						
17	1.36	-14.80			366.95	4.19E-04	3.59E-03	4.97E-04
18	0.50	-12.61						
19	1.94	-11.73						
20	1.75	-12.45			2114.46	2.42E-03	4.48E-03	1.44E-04
21	0.97	-12.48						
22	1.24	-12.35						
22.6	1.23	-15.18						
29.6	2.69	-6.84	-27.35	97.26	1029.72	1.61E-03	4.39E-01	3.19E-04
31	1.23	-8.99						
32	-0.82	-9.34	-27.78	99.15				
33	-1.15	-13.17						
34	0.38	-11.28	-26.09	99.75	1178.92	1.58E-03	2.02E-01	3.23E-04
35	-0.65	-8.81						
36	0.20	-9.43	-26.08	98.51				
37.2	-0.59	-10.11						
38	-0.70	-10.16	-24.91	99.92	965.17	1.10E-03	4.80E-03	3.95E-05
39	-0.05	-10.88						
40	1.03	-9.92						
41	0.58	-10.84	-24.77	98.03	2165.08	2.47E-03	6.45E-03	8.19E-05
42	1.03	-10.50						
43	2.07	-9.32	-24.72	98.89	3028.04	3.46E-03	7.09E-03	4.22E-05
44	2.17	-10.27						
45	2.23	-11.63						

Height (m)	d13C (carb)	d18O (carb)	d13C (org)	% carb	Sr (ppm)	Sr/Ca	Mg/Ca	Mn/Ca
46	1.32	-10.56						
47	2.10	-8.89			1261.60	1.44E-03	6.02E-03	2.64E-05
48	2.08	-8.18						
49	1.88	-8.49						
50	1.58	-10.01						
51	0.97	-8.50	-26.18	99.89	2278.03	2.60E-03	7.51E-03	3.73E-05
52	1.22	-8.93						
53	2.22	-8.44						
54	2.04	-8.86						
55	1.46	-8.83			2102.79	2.40E-03	5.99E-03	1.79E-05
56	1.19	-6.85						
57	0.73	-12.61						
58	1.37	-14.91	-22.61	97.92	6600.59	7.54E-03	4.18E-03	1.08E-04
59	0.61	-9.93						
60	-1.07	-10.34	-25.64	99.82				
61	-0.26	-10.83						
62	-0.97	-12.27	-26.03	99.65	1559.39	1.78E-03	4.94E-03	4.38E-05
63	-1.06	-11.09						
64	0.22	-13.66	-26.98	98.85				
65.3	0.69	-10.22						
66.1	1.60	-7.01	-24.36	99.89	1186.16	1.35E-03	1.58E-02	7.00E-05
67	1.48	-11.38						
68	1.09	-14.10						
69	2.62	-10.43						
69.9	2.04	-11.44			9834.43	1.12E-02	6.85E-03	7.65E-05
71	2.04	-7.28						
72	1.41	-11.44						
73	2.33	-8.87			2454.51	2.80E-03	7.46E-03	6.77E-05
74	2.29	-6.71						
75	2.22	-9.32						
76	1.66	-8.46	-27.67	99.90	1890.34	2.16E-03	5.73E-03	6.31E-05
77	0.77	-10.12						
78	1.45	-7.45						
79	1.89	-9.35						
80	1.81	-8.09			971.29	1.11E-03	5.14E-03	1.22E-04
81	1.86	-8.46						
82	1.77	-9.95						
83	1.01	-9.25			1540.40	1.76E-03	5.23E-03	7.03E-05
84	1.95	-9.79						
85	1.43	-10.01						
86.2	2.16	-11.45	-26.07	99.88	1684.10	1.92E-03	5.51E-03	5.39E-05

Height (m)	d13C (carb)	d18O (carb)	d13C (org)	% carb	Sr (ppm)	Sr/Ca	Mg/Ca	Mn/Ca
87	1.89	-10.88						
89	1.57	-10.55						
90	0.68	-10.92						
91	0.99	-9.40			1259.97	1.44E-03	4.35E-03	3.57E-05
92.2	1.52	-10.69						
93	1.77	-13.61						
94.2	1.84	-12.60			1260.55	1.44E-03	4.63E-03	6.35E-05
95	1.63	-10.53						
96	1.80	-9.09						
97	1.74	-8.23	-27.26	99.85	1808.64	2.07E-03	7.69E-03	2.65E-05
98	1.58	-8.92						
100	1.49	-9.67			1941.32	2.22E-03	6.82E-03	2.18E-05
101	1.75	-9.13						
102	2.38	-9.89						
103	1.55	-11.49			1677.03	1.92E-03	6.71E-03	3.32E-05
104	1.55	-14.29						
105	1.26	-14.34						
106	1.32	-13.82						
107	1.55	-14.56	-23.94	99.11	1405.02	1.60E-03	4.74E-03	5.04E-05
108	1.93	-14.23						
109	1.92	-15.79						
110	1.54	-14.54						
111	1.97	-12.65			1606.17	1.83E-03	5.05E-03	2.90E-05
112	1.89	-13.39						
113	1.32	-11.78						
114	1.27	-12.55			2086.63	2.38E-03	7.03E-03	4.04E-05
115	1.44	-13.36						
116	1.38	-12.59						
117	1.53	-15.02						
117.1	1.64	-10.90	-26.84	99.77	1964.59	2.24E-03	8.19E-03	4.71E-05
118	1.28	-14.54						
119	1.00	-11.39						
120	1.66	-10.39			2160.91	2.47E-03	6.84E-03	3.42E-05
121	1.36	-11.16						
122	1.54	-9.12						
123	1.91	-8.39			2581.74	2.95E-03	8.93E-03	3.37E-05
124	1.48	-8.83						
125	1.73	-9.23						

Height (m)	d13C (carb)	d18O (carb)	d13C (org)	% carb	Sr (ppm)	Sr/Ca	Mg/Ca	Mn/Ca
126	1.20	-8.72	-27.70	99.84	2289.08	2.61E-03	6.71E-03	2.92E-05
127	0.68	-13.91						
128	0.58	-8.94						
129	1.65	-7.55						
130	1.84	-9.23			2180.61	2.49E-03	6.88E-03	2.33E-05
131	0.56	-11.38						
132	2.22	-7.81						
133	1.29	-8.15						
134	1.07	-6.88			2343.57	2.68E-03	7.58E-03	2.74E-05
135.1	1.31	-13.80						
136	1.02	-11.94						
137	1.43	-9.93	-27.79	99.75	2261.90	2.58E-03	6.84E-03	2.90E-05
138	2.44	-10.91						
139	0.18	-8.39						
140	2.44	-9.59			2016.73	2.30E-03	8.86E-03	4.95E-05
141	1.81	-9.95						
143	1.13	-10.63						
144.1	1.72	-8.51			2330.09	2.66E-03	7.45E-03	6.37E-05
145	1.19	-11.23						
146	0.69	-10.35						
147	0.59	-10.16	-26.66	99.33	1815.33	2.07E-03	6.24E-03	5.17E-05
148	0.67	-10.69						
149	1.08	-9.91						
150	1.15	-13.91						
151	0.98	-9.21			2164.74	2.47E-03	7.20E-03	4.21E-05
152	1.18	-8.41						
153	0.93	-13.28						
154	1.38	-11.31						
155	1.09	-11.97			2822.44	3.22E-03	7.13E-03	8.80E-05
157	1.48	-12.87						
158	1.21	-10.82						
159	1.18	-13.35	-27.07	99.44	1652.55	1.89E-03	7.73E-03	7.55E-05
160	1.52	-9.78						
161	1.87	-10.45						
162.1	1.05	-9.34						
163	1.34	-11.21			2424.42	2.77E-03	6.27E-03	3.02E-05
165.9	0.35	-20.85						
167	1.91	-9.00						
168	1.36	-10.31			2700.16	3.08E-03	4.26E-03	3.37E-05
169	1.31	-15.26						
170	1.03	-13.14						

Height (m)	d13C (carb)	d18O (carb)	d13C (org)	% carb	Sr (ppm)	Sr/Ca	Mg/Ca	Mn/Ca
171	0.91	-12.16	-23.48	97.15	7704.69	8.80E-03	6.24E-03	4.55E-05
172	1.12	-16.27						
173	-0.23	-13.39						
174	0.41	-14.07			1164.22	1.33E-03	6.41E-03	6.82E-05
175	0.14	-12.62						
176	0.33	-12.81						
178.1	0.59	-14.01						
180	1.49	-10.34			6501.55	7.43E-03	8.52E-03	1.94E-04
181	2.61	-9.88						
182.2	2.35	-12.99						
183	2.06	-10.54						
184	1.53	-8.87	-25.41	87.95	2925.13	3.34E-03	1.06E-02	1.96E-04
185	1.90	-10.23						
186	0.15	-11.67						
187	0.23	-9.57						
188	0.54	-15.88			1586.52	1.81E-03	5.97E-03	5.09E-05
189	1.28	-8.71						
190	1.53	-11.76						
192.3	1.46	-16.15			1719.83	1.96E-03	8.70E-03	1.15E-04
193	1.01	-10.42						
194	0.37	-9.96						
195	1.18	-15.81						
196	0.38	-15.05	-25.54	95.42	2196.33	2.51E-03	5.36E-03	8.94E-05
197	0.14	-18.76						
198	1.85	-10.21						
201	1.96	-12.02			5596.15	6.39E-03	8.38E-03	4.08E-05
204.5	1.71	-11.61						
207	1.22	-9.96	-25.65	99.35	2929.39	3.35E-03	8.76E-03	4.30E-05
210	2.18	-9.83						
221.1	2.10	-8.89	-23.72	98.50	6288.19	7.18E-03	9.53E-03	2.58E-05
221.8	2.27	-9.25						
227	1.38	-12.13						
229	1.05	-10.38	-22.88	99.96	11266.02	1.29E-02	7.13E-03	2.12E-05
230	-1.11	-11.50						
231	-0.71	-10.17	-24.95	98.69	2779.81	3.18E-03	6.96E-03	2.34E-04

Height (m)	Mn (ppm)	Mn/Sr	87/86Sr	Height (m)	Mn (ppm)	Mn/Sr	87/86Sr
0	46.89	5.77E-02	0.707727	48			
1				49			
2.1				50			
3				51	20.48	1.43E-02	
4	52.61	6.01E-02		52			
5				53			
6				54			
7				55	9.83	7.45E-03	
8	254.10	3.97E-01		56			
9				57			
11.6				58	59.21	1.43E-02	
13	135.16	2.21E-01		59			
13.9				60			
15				61			
16				62	24.02	2.46E-02	
17	272.56	1.18E+00		63			
18				64			
19				65.3			
20	78.85	5.95E-02		66.1	38.40	5.16E-02	
21				67			
22				68			
22.6				69			
29.6	127.56	1.98E-01		69.9	42.00	6.81E-03	0.707759
31				71			
32				72			
33				73	37.14	2.41E-02	
34	151.57	2.05E-01		74			
35				75			
36				76	34.63	2.92E-02	
37.2				77			
38	21.68	3.58E-02	0.707727	78			
39				79			
40				80	66.93	1.10E-01	
41	44.96	3.31E-02		81			
42				82			
43	23.17	1.22E-02		83	38.59	4.00E-02	
44				84			
45				85			
46				86.2	29.61	2.80E-02	
47	14.46	1.83E-02		87			

Height (m)	Mn (ppm)	Mn/Sr	87/86Sr	Height (m)	Mn (ppm)	Mn/Sr	87/86Sr
89				129			
90				130	12.77	9.34E-03	
91	19.59	2.48E-02	0.707590	131			
92.2				132			
93				133			
94.2	34.87	4.41E-02		134	15.03	1.02E-02	
95				135.1			
96				136			
97	14.54	1.28E-02		137	15.90	1.12E-02	
98				138			
100	11.96	9.83E-03		139			
101				140	27.14	2.15E-02	
102				141			
103	18.23	1.73E-02		143			
104				144.1	34.94	2.39E-02	0.707797
105				145			
106				146			
107	27.69	3.14E-02		147	28.36	2.49E-02	
108				148			
109				149			
110				150			
111	15.92	1.58E-02	0.707837	151	23.09	1.70E-02	
112				152			
113				153			
114	22.16	1.69E-02		154			
115				155	48.29	2.73E-02	
116				157			
117				158			
117.1	25.83	2.10E-02		159	41.42	4.00E-02	
118				160			
119				161			
120	18.79	1.39E-02		162.1			
121				163	16.56	1.09E-02	
122				165.9			
123	18.50	1.14E-02		167			
124				168	18.49	1.09E-02	
125				169			
126	16.05	1.12E-02	0.707831	170			
127				171	24.96	5.17E-03	0.707701
128				172			

Height (m)	**Mn (ppm)**	**Mn/Sr**	**87/86Sr**
173			
174	37.46	5.13E-02	
175			
176			
178.1			
180	106.55	2.61E-02	
181			
182.2			
183			
184	107.48	5.86E-02	0.707809
185			
186			
187			
188	27.95	2.81E-02	
189			
190			
192.3	63.30	5.87E-02	
193			
194			
195			
196	49.06	3.56E-02	
197			
198			
201	22.39	6.38E-03	0.707877
204.5			
207	23.61	1.29E-02	
210			
221.1	14.14	3.59E-03	
221.8			
227			
229	11.65	1.65E-03	0.707902
230			
231	128.34	7.36E-02	0.707759

Appendix A4: Sinwa West geochemical data.

Height (m)	d13C (carb)	d18O (carb)	d13C (org)	% carb	Sr (ppm)	Sr/Ca	Mg/Ca	Mn/Ca
0	-1.35	-13.28	-25.52	98.61	1380.48	1.58E-03	5.58E-03	1.17E-04
1	-2.85	-8.13						
2	-1.29	-12.41	-27.53	97.20				
3	-1.60	-8.56						
4	-2.23	-9.64	-26.93	98.73	2349.37	2.68E-03	4.37E-03	9.25E-05
5	-2.63	-7.50						
6	-2.42	-6.59	-27.15	99.79				
7	-2.43	-6.89						
8	-2.43	-8.91	-28.34	99.24	1266.19	1.45E-03	4.37E-03	1.33E-04
9	-1.14	-10.76						
10	-2.38	-7.68	-26.60	99.54				
11	-1.44	-9.00						
12	-1.76	-8.94	-27.50	98.13	1509.45	1.72E-03	5.39E-03	1.65E-04
13	-2.80	-6.78						
14	-2.54	-7.56	-26.87	97.48				
15	-2.85	-7.03						
16	-1.44	-7.15	-28.36	99.69	1177.91	1.35E-03	4.95E-03	1.01E-04
17	2.33	-5.22						
18	2.18	-5.45	-26.98	99.81	914.70	1.04E-03	5.08E-03	1.01E-04
19	1.66	-13.26						
20	2.16	-8.49						
21	2.51	-12.32			1355.08	1.55E-03	6.79E-03	1.47E-04
22	2.46	-8.80						
23	2.56	-8.51						
24	2.48	-7.07			873.71	9.98E-04	3.91E-03	9.73E-05
25	2.67	-9.82						
26	2.45	-5.84						
27	2.09	-12.64	-27.59	98.81	1267.56	1.45E-03	4.62E-03	1.39E-04
28	2.14	-14.13						
29	2.52	-15.26						
30	2.67	-6.18						
31	2.73	-5.60			851.16	9.72E-04	4.12E-03	1.07E-04
32	1.84	-14.97						
34.25	1.81	-14.93						
35	2.84	-9.61			1194.69	1.36E-03	3.84E-03	7.57E-05
36	2.16	-7.89						
37	2.26	-15.50						
40	1.99	-7.79	-23.37	92.32	5803.40	6.63E-03	6.39E-03	1.06E-04

Height (m)	d13C (carb)	d18O (carb)	d13C (org)	% carb	Sr (ppm)	Sr/Ca	Mg/Ca	Mn/Ca
45.5	-1.69	-11.08						
46	-2.01	-8.78	-26.45	98.31				
46.5	-2.02	-9.99						
48	-2.61	-6.61	-25.04	99.08	913.10	1.04E-03	4.96E-03	4.92E-05
49	-0.78	-12.00						
51	-1.76	-12.77	-24.42	99.17				
52	-0.56	-10.93						
53	-1.96	-6.57	-26.69	97.61	1435.73	1.64E-03	6.09E-03	1.06E-04
54	-1.04	-5.94						
55	-2.16	-6.90	-27.72	99.07				
56	-0.76	-8.17						
57	-1.08	-4.39	-27.92	99.78	900.83	1.03E-03	5.39E-03	1.08E-04
58	-0.87	-12.68						
59	-0.65	-7.07	-26.64	98.39				
60	0.02	-12.14						
61	-0.55	-10.34	-27.45	99.49	1087.99	1.24E-03	7.06E-03	1.36E-04
62	-0.53	-6.94						
63	1.94	-11.94	-23.17	99.65	1094.92	1.25E-03	5.51E-03	1.85E-04
64	2.18	-8.81						
65	2.56	-6.97						
66	2.25	-9.72						
67	2.13	-11.17			665.64	7.60E-04	3.46E-03	3.15E-04
68	2.42	-6.83						
69	2.78	-9.29						
70	2.52	-10.09	-23.11	98.96	661.68	7.56E-04	5.29E-03	1.38E-04
71	1.33	-18.20						
73	2.64	-10.42						
74	2.42	-10.52			1028.95	1.18E-03	3.79E-03	1.44E-04
75	2.58	-6.03						
76	2.59	-7.57						
77	1.93	-15.05			1061.73	1.21E-03	4.36E-03	1.92E-04
78	1.95	-9.15						
79	1.84	-12.74						
80	2.67	-6.93	-25.68	94.26	635.23	7.26E-04	2.82E-03	9.54E-05
81	2.72	-7.58						
82	2.01	-8.03						
83	1.59	-10.13						
84	2.44	-10.00			1061.93	1.21E-03	3.45E-03	1.14E-04
85	2.23	-11.17						
86	2.69	-6.25						
87	2.70	-7.78			1104.45	1.26E-03	4.13E-03	6.79E-05

Height (m)	d13C (carb)	d18O (carb)	d13C (org)	% carb	Sr (ppm)	Sr/Ca	Mg/Ca	Mn/Ca
88	2.05	-12.65						
89	2.55	-7.17						
90	2.51	-13.80	-21.30	98.87	587.55	6.71E-04	2.77E-03	1.37E-04
91	-1.69	-8.89						
92	-0.49	-9.12	-28.02	97.34				
93	2.06	-6.81						
95	2.48	-7.17	-28.59	99.66	1008.56	1.15E-03	4.68E-03	1.49E-04
96	2.32	-10.40						
97	2.45	-10.90						
98	2.20	-10.25			1021.64	1.17E-03	3.78E-03	1.26E-04
99	2.83	-16.03						
100	1.24	-19.16						
101	2.85	-12.89			550.80	6.29E-04	2.61E-03	2.32E-04
102	2.99	-14.70						
103	2.96	-10.35						
104	2.45	-7.74						
105	2.59	-11.51	-25.48	99.75	896.05	1.02E-03	3.53E-03	1.09E-04
106	2.59	-8.07						
107	2.74	-10.41						
108	2.63	-12.79			1029.18	1.18E-03	3.81E-03	1.51E-04
109	2.59	-8.33						
110	2.44	-8.12						
111	2.58	-8.49			1125.47	1.29E-03	4.43E-03	9.42E-05
112	2.74	-10.79						
113	2.62	-11.61						
114	2.83	-13.63	-24.52	99.50	933.01	1.07E-03	3.90E-03	1.44E-04
115	2.68	-7.79						
116	2.69	-11.36						
117	2.81	-9.79			899.24	1.03E-03	3.74E-03	8.90E-05
118	2.44	-12.39						
119	2.72	-11.30						
120	2.56	-7.51			947.30	1.08E-03	4.44E-03	7.45E-05
121	2.96	-8.39						
122	2.49	-8.31						
123	2.64	-9.14	-26.51	98.62	826.80	9.44E-04	5.10E-03	6.78E-05
124	2.56	-12.52						
125	2.97	-10.78						
126	2.55	-11.28			991.82	1.13E-03	3.66E-03	1.40E-04

Height (m)	d13C (carb)	d18O (carb)	d13C (org)	% carb	Sr (ppm)	Sr/Ca	Mg/Ca	Mn/Ca
127	2.90	-13.92						
128	2.58	-15.79						
129	2.52	-10.34			780.12	8.91E-04	3.88E-03	1.11E-04
130	2.69	-10.23						
131	2.19	-12.24						
132	2.58	-14.75	-24.58	99.29	615.49	7.03E-04	2.61E-03	3.89E-04
133	2.00	-19.06						
136.75	-1.31	-11.38	-28.11	86.34				
138	-0.65	-11.32						
139	-0.93	-9.86	-26.76	88.01	2498.97	2.85E-03	8.19E-03	3.72E-04
140	-1.69	-10.45						
141	1.25	-12.44	-27.63	88.56				
142	0.80	-11.22						
143	-1.67	-16.54	-23.00	96.19	1834.46	2.10E-03	4.88E-03	3.20E-04
146	0.64	-7.94						
147	1.15	-7.68	-27.01	97.21	1582.10	1.81E-03	7.41E-03	1.10E-04
148	0.33	-6.03						
149	0.51	-10.96						
150	1.54	-10.68			2394.28	2.73E-03	7.29E-03	1.22E-04
151	2.54	-5.99						
152	0.97	-16.68						
153	1.57	-7.48						
154	2.37	-7.93	-20.81		7599.84	8.68E-03	6.60E-03	1.40E-04
155	1.14	-18.25						
156	1.92	-14.07						
157	1.84	-6.88						
158	1.78	-12.38			3035.40	3.47E-03	1.23E-02	6.83E-05
159	2.15	-5.50						
160	1.92	-4.88						
163	2.27	-9.58	-22.83	83.80	4402.58	5.03E-03	7.74E-03	2.25E-04

Height (m)	Mn (ppm)	Mn/Sr	87/86Sr	Height (m)	Mn (ppm)	Mn/Sr	87/86Sr
0	64.34	7.43E-02		49			
1				51			
2				52			
3				53	57.95	6.44E-02	
4	50.78	3.45E-02	0.707719	54			
5				55			
6				56			
7				57	59.33	1.05E-01	
8	73.12	9.21E-02		58			
9				59			
10				60			
11				61	74.53	1.09E-01	
12	90.66	9.58E-02		62			
13				63	101.33	1.48E-01	0.707579
14				64			
15				65			
16	55.18	7.47E-02		66			
17				67	172.79	4.14E-01	
18	55.59	9.69E-02	0.707593	68			
19				69			
20				70	75.81	1.83E-01	
21	80.90	9.52E-02		71			
22				73			
23				74	79.08	1.23E-01	
24	53.43	9.75E-02		75			
25				76			
26				77	105.52	1.59E-01	0.707539
27	76.08	9.57E-02		78			
28				79			
29				80	52.34	1.31E-01	
30				81			
31	58.69	1.10E-01		82			
32				83			
34.25				84	62.81	9.43E-02	
35	41.55	5.55E-02		85			
36				86			
37				87	37.29	5.39E-02	
40	58.28	1.60E-02	0.707485	88			
45.5				89			
46				90	75.12	2.04E-01	
46.5				91			
48	27.00	4.72E-02		92			

Height (m)	Mn (ppm)	Mn/Sr	87/86Sr	Height (m)	Mn (ppm)	Mn/Sr	87/86Sr
93				133			
95	81.94	1.30E-01		136.75			
96				138			
97				139	204.15	1.30E-01	0.707760
98	68.93	1.08E-01	0.707521	140			
99				141			
100				142			
101	127.33	3.69E-01		143	175.90	1.53E-01	
102				146			
103				147	60.23	6.07E-02	0.707641
104				148			
105	59.65	1.06E-01		149			
106				150	66.95	4.46E-02	
107				151			
108	82.62	1.28E-01		152			
109				153			
110				154	76.58	1.61E-02	0.707812
111	51.71	7.33E-02		155			
112				156			
113				157			
114	79.10	1.35E-01	0.707536	158	37.50	1.97E-02	
115				159			
116				160			
117	48.84	8.66E-02		163	123.74	4.48E-02	0.707813
118							
119							
120	40.91	6.89E-02					
121							
122							
123	37.23	7.18E-02					
124							
125							
126	76.65	1.23E-01	0.707532				
127							
128							
129	60.98	1.25E-01					
130							
131							
132	213.78	5.54E-01					

Appendix A5: Mount Sinwa Re–Os isochrons

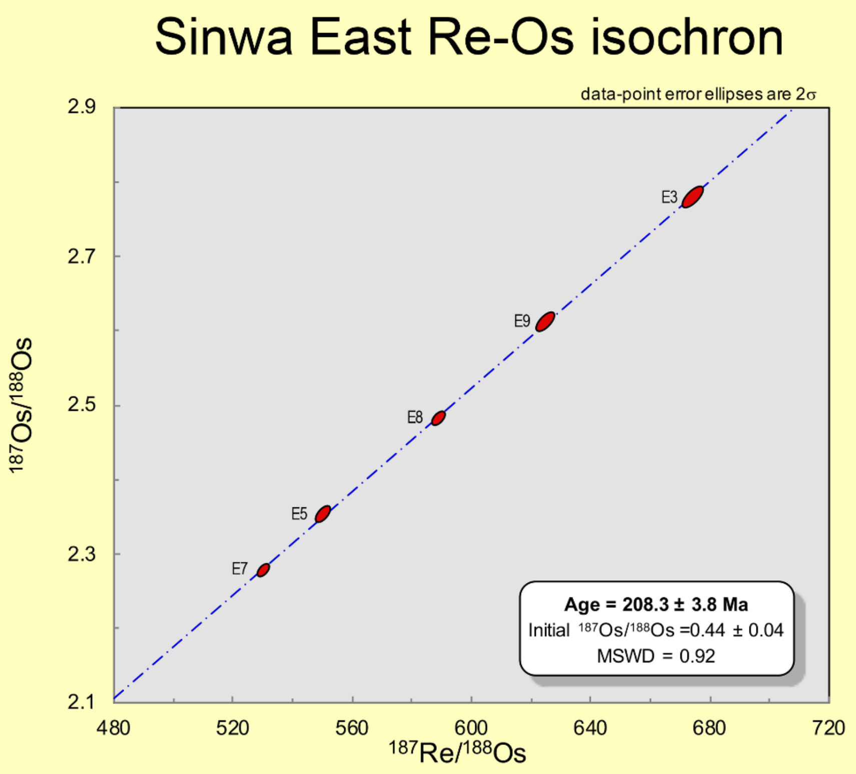

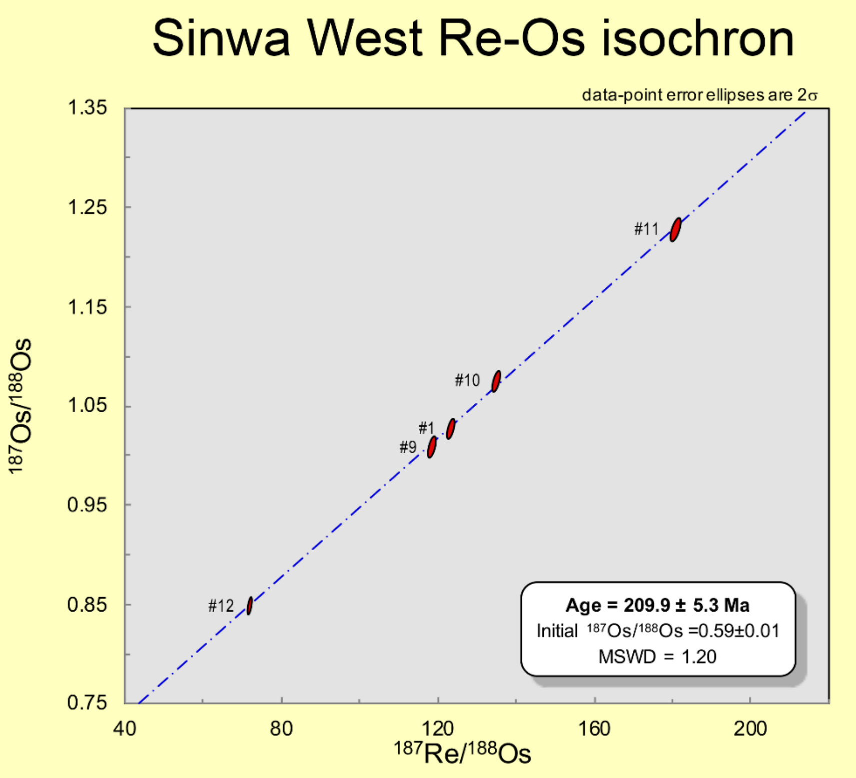

Appendix B: Chapter three supplementary material

Appendix B: Morphometric analyses specimen pool.

Sample name	Ref	UTM zone	UTM Easting	UTM Northing	Formation
81-MJO-BBR-242A	C-101108	10	497550	6215500	Pardonet
82-MJO-BBR-22	C-101027	10	497550	6215500	Pardonet
NPP-82-206C1	C-101764	10	494650	6207625	Pardonet
NPP-82-206C3	C-101766	10	494650	6207625	Pardonet
96-OF-BBR-242A	C-305207	10	497550	6215500	Pardonet
81-MJO-PH-227A	C-101778	10	497950	6212980	Pardonet
91-GK-38	C-197165	10	504400	6183200	Pardonet
93-OF-BBR-BF	C-301184	10	497725	6215525	Pardonet
94-GK-69-5-1A	C-197180	10	504900	6191900	Bocock
01-OF-NPP-4	C-305823	10	494700	6207625	Pardonet
79-TOT-10-10	C-087002	8	499102	6781151	Aksala
79-TOT-10-4	C-086449	8	500000	6781151	Aksala
79-TOT-10-8	C-086450	8	499102	6781151	Aksala
79-TOT-10-9	C-087001	8	499102	6781151	Aksala
79-TOT-11-14	C-087003	8	498957	6781151	Aksala
79-TOT-11-19	C-087005	8	499090	6781452	Aksala
79-TOT-11-20	C-087006	8	498957	6781452	Aksala
16-EB-018-1	V-003787	8	509331	6762978	Aksala
16-EB-539-2	V-003809	8	496603	6772368	Aksala
17-SIN-7	V-003824	8	597187	6526223	Sinwa
17-SIN-8	V-003825	8	597186	6526232	Sinwa
17-SIN-9	V-003826	8	597188	6526234	Sinwa
17-SIN-11	V-003828	8	597190	6526241	Sinwa
17-SIN-12	V-003829	8	597190	6526249	Sinwa
17-SIN-13	V-003830	8	597237	6526270	Sinwa
17-SIN-15	V-003832	8	597216	6526304	Sinwa
17-SIN-16	V-003833	8	597242	6526302	Sinwa
17-SIN-17	V-003834	8	597266	6526340	Sinwa
18-SIN-1	V-012679	8	597274	6526336	Sinwa
18-SIN-3	V-012681	8	597263	6526304	Sinwa
18-SIN-4	V-012682	8	597266	6526304	Sinwa
18-SIN-5	V-012683	8	597258	6526299	Sinwa
18-WEST-7	V-012698	8	594052	6527695	Sinwa
18-WEST-8	V-012699	8	594055	6527704	Sinwa
18-HILL-0	V-012729	8	498312	6781489	Aksala
18-HILL-2	V-012720	8	498187	6781492	Aksala
18-HILL-3	V-012721	8	498143	6781465	Aksala

Sample name	Ref	UTM zone	UTM Easting	UTM Northing	Formation
18-HILL-5	V-012723	8	498125	6781493	Aksala
18-HILL-6	V-012724	8	498126	6781527	Aksala
18-LPC-2	V-012709	8	504632	6770152	Aksala
16-ZE-MG-SIN-2	V-003709	8	597169	6526078	Sinwa
16-ZE-MG-WB-10	V-003682	8	556306	6571636	Sinwa
16-ZE-MG-WB-11	V-003683	8	556306	6571636	Sinwa
17-ZE-BVS-23-212	V-003860	9	500535	6443750	Sinwa
17-SIN-2	V-003819	8	597172	6526084	Sinwa
17-SIN-3	V-003820	8	597186	6526120	Sinwa
17-ZE-MG-EL-2	V-003841	8	513446	6680660	Aksala
87-OF-EC-KPJA-5	C-140477	8	621160	5975325	Sandilands
88-OF-KPA-R3A	C-158533	8	621160	5975325	Sandilands
88-OF-KP-M3A	C-156504	8	621170	5975500	Peril
88-OF-KP-M7	C-156509	8	621170	5975500	Peril
89-CNA-KPX-1	C-159337	8	621200	5975300	Sandilands
90-JF-KPMM-SH1	C-173156	8	621200	5975300	Sandilands
90-OF-KP-1	C-176949	8	621160	5975325	Sandilands
90-OF-KP-M17	C-176895	8	621160	5975325	Peril
92-OF-MUP-A1	C-202796	9	628100	5532275	Parson Bay
92-OF-MUP-A7	C-202702	9	628100	5532275	Parson Bay
20-MP3-75.3	V-016845	9	591557	5603523	Parson Bay
21-MUP2-176	V-016998	9	627915	5532553	Parson Bay
88-OF-FI-30	C-156590	8	620875	5976630	Peril
88-OF-FI-31	C-156591	8	620875	5976630	Peril
88-OF-FI-31A	C-156597	8	620875	5976630	Peril
88-OF-FI-32	C-156592	8	620875	5976630	Peril
92-OF-UNI-B6	C-202757	9	620675	5539625	Parson Bay
92-OF-UNI-B8	C-202759	9	620675	5539625	Parson Bay
19-H2-1	V-016679	9	573586	5609426	Parson Bay
20-MP2B-2.7	V-016842	9	591571	5603744	Parson Bay
88-CNA-KPA-E	C-156793	8	621160	5975325	Sandilands
88-OF-KPA-R5C	C-156513	8	621160	5975325	Sandilands
89-CNA-KPA-3	C-159341	8	621200	5975300	Sandilands
89-CNA-KPX-3	C-164737	8	621200	5975300	Sandilands
89-CNA-KPX-4	C-164738	8	621200	5975300	Sandilands
89-CNA-KPX-6	C-164740	8	621200	5975300	Sandilands
90-OF-KP-X13	C-176903	8	621160	5975325	Sandilands
90-OF-KP-X14	C-176904	8	621160	5975325	Sandilands
90-OF-KP-X15	C-176905	8	621160	5975325	Sandilands

Sample name	Ref	UTM zone	UTM Easting	UTM Northing	Formation
90-OF-KP-X16	C-176906	8	621160	5975325	Sandilands
90-OF-KP-X17	C-176907	8	621160	5975325	Sandilands
90-OF-KP-X2	C-176898	8	621160	5975325	Sandilands
90-OF-KP-X6	C-176900	8	621160	5975325	Sandilands
90-OF-KP-X9	C-176901	8	621160	5975325	Sandilands
92-OF-MUP-D17	C-202712	9	628100	5532000	Parson Bay
92-OF-WAI-B2	C-202781	9	616075	5542750	Parson Bay
92-OF-WAI-C4	C-202783	9	616925	5542275	Parson Bay
92-OF-WAI-C8	C-202787	9	616925	5542275	Parson Bay

Sample name	Age	Terrane	*M.* ex gr. *carinata*	*M.* ex gr. *englandi*
81-MJO-BBR-242A	late Norian	Laurentia	5	10
82-MJO-BBR-22	late Norian	Laurentia	10	24
NPP-82-206C1	late Norian	Laurentia	2	11
NPP-82-206C3	late Norian	Laurentia	0	1
96-OF-BBR-242A	late Norian	Laurentia	7	23
81-MJO-PH-227A	mid Norian	Laurentia	5	0
91-GK-38	Rhaetian	Laurentia	1	0
93-OF-BBR-BF	Rhaetian	Laurentia	2	0
94-GK-69-5-1A	Rhaetian	Laurentia	0	1
01-OF-NPP-4	Rhaetian	Laurentia	1	0
79-TOT-10-10	late Norian	Stikine	0	13
79-TOT-10-4	late Norian	Stikine	0	1
79-TOT-10-8	late Norian	Stikine	0	1
79-TOT-10-9	late Norian	Stikine	0	1
79-TOT-11-14	late Norian	Stikine	0	3
79-TOT-11-19	late Norian	Stikine	1	28
79-TOT-11-20	late Norian	Stikine	0	1
16-EB-018-1	late Norian	Stikine	0	1
16-EB-539-2	late Norian	Stikine	0	9
17-SIN-7	late Norian	Stikine	5	6
17-SIN-8	late Norian	Stikine	3	4
17-SIN-9	late Norian	Stikine	9	11
17-SIN-11	late Norian	Stikine	7	12
17-SIN-12	late Norian	Stikine	3	11
17-SIN-13	late Norian	Stikine	1	4
17-SIN-15	late Norian	Stikine	4	3

Sample name	Age	Terrane	*M.* ex gr. *carinata*	*M.* ex gr. *englandi*
17-SIN-16	late Norian	Stikine	3	1
17-SIN-17	late Norian	Stikine	2	6
18-SIN-1	late Norian	Stikine	1	1
18-SIN-3	late Norian	Stikine	13	14
18-SIN-4	late Norian	Stikine	3	0
18-SIN-5	late Norian	Stikine	0	2
18-WEST-7	late Norian	Stikine	0	2
18-WEST-8	late Norian	Stikine	4	1
18-HILL-0	late Norian	Stikine	0	3
18-HILL-2	late Norian	Stikine	0	12
18-HILL-3	late Norian	Stikine	0	3
18-HILL-5	late Norian	Stikine	2	16
18-HILL-6	late Norian	Stikine	0	2
18-LPC-2	late Norian	Stikine	0	1
16-ZE-MG-SIN-2	mid Norian	Stikine	6	3
16-ZE-MG-WB-10	mid Norian	Stikine	2	0
16-ZE-MG-WB-11	mid Norian	Stikine	7	0
17-ZE-BVS-23-212	mid Norian	Stikine	0	1
17-SIN-2	mid Norian	Stikine	0	1
17-SIN-3	mid Norian	Stikine	0	1
17-ZE-MG-EL-2	Rhaetian	Stikine	2	2
87-OF-EC-KPJA-5	late Norian	Wrangell	1	1
88-OF-KPA-R3A	late Norian	Wrangell	0	1
88-OF-KP-M3A	late Norian	Wrangell	2	7
88-OF-KP-M7	late Norian	Wrangell	0	1
89-CNA-KPX-1	late Norian	Wrangell	1	1
90-JF-KPMM-SH1	late Norian	Wrangell	0	1
90-OF-KP-1	late Norian	Wrangell	1	1
90-OF-KP-M17	late Norian	Wrangell	3	8
92-OF-MUP-A1	late Norian	Wrangell	0	1
92-OF-MUP-A7	late Norian	Wrangell	0	1
20-MP3-75.3	late Norian	Wrangell	1	0
21-MUP2-176	late Norian	Wrangell	0	1
88-OF-FI-30	mid Norian	Wrangell	0	2
88-OF-FI-31	mid Norian	Wrangell	1	1
88-OF-FI-31A	mid Norian	Wrangell	3	3
88-OF-FI-32	mid Norian	Wrangell	4	0
92-OF-UNI-B6	mid Norian	Wrangell	1	1
92-OF-UNI-B8	mid Norian	Wrangell	1	1

Sample name	**Age**	**Terrane**	***M.* ex gr. *carinata***	***M.* ex gr. *englandi***
19-H2-1	mid Norian	Wrangell	1	0
20-MP2B-2.7	mid Norian	Wrangell	0	1
88-CNA-KPA-E	Rhaetian	Wrangell	3	6
88-OF-KPA-R5C	Rhaetian	Wrangell	0	4
89-CNA-KPA-3	Rhaetian	Wrangell	2	1
89-CNA-KPX-3	Rhaetian	Wrangell	0	1
89-CNA-KPX-4	Rhaetian	Wrangell	0	1
89-CNA-KPX-6	Rhaetian	Wrangell	2	7
90-OF-KP-X13	Rhaetian	Wrangell	0	1
90-OF-KP-X14	Rhaetian	Wrangell	0	4
90-OF-KP-X15	Rhaetian	Wrangell	0	1
90-OF-KP-X16	Rhaetian	Wrangell	5	9
90-OF-KP-X17	Rhaetian	Wrangell	0	1
90-OF-KP-X2	Rhaetian	Wrangell	4	1
90-OF-KP-X6	Rhaetian	Wrangell	1	2
90-OF-KP-X9	Rhaetian	Wrangell	2	8
92-OF-MUP-D17	Rhaetian	Wrangell	1	1
92-OF-WAI-B2	Rhaetian	Wrangell	2	4
92-OF-WAI-C4	Rhaetian	Wrangell	1	2
92-OF-WAI-C8	Rhaetian	Wrangell	0	1
species totals			154	339

Appendix C: Chapter four supplementary material

Appendix C1: Williston Lake and Holberg Inlet ammonoid recovery.

Sample Name	**Section**	**Height (m)**	**Identification**
20-H10-18.5	Holberg	550	*Discamphiceras* aff. *antiquum*
20-NPP-86.3	Ne Parle Pas Point	86.3	*Sagenites minaensis*
20-NPP-89.7	Ne Parle Pas Point	89.7	*Sagenites minaensis*
20-NPP-89.8	Ne Parle Pas Point	89.8	*Sagenites minaensis*
20-NPP-100.1	Ne Parle Pas Point	100.1	*Placites* cf. *polydactylus*
20-PC-32.7	Pardonet Creek	32.7	*Cladiscites tornatus*
20-BU-13.8-sp.1	Black Bear Ridge	201.4	*Psiloceras* cf. *tibeticum*
20-BU-13.8-sp.2	Black Bear Ridge	201.4	*Psiloceras* cf. *tibeticum*
20-BU-17	Black Bear Ridge	204.6	*Choristoceras* cf. *minutum*
20-BU-18-sp.1	Black Bear Ridge	205.6	*Psiloceras* cf. *tilmanni*
20-BU-18-sp.2	Black Bear Ridge	205.6	*Psiloceras tilmanni*
20-BU-18.6	Black Bear Ridge	206.2	*Psiloceras tilmanni*

Appendix C2: Williston Lake, Holberg Inlet, and Kyuquot Sound conodont recovery.

Sample Name	**Section**	**Height (m)**	***Epigondolella* cf. *spiculata***	***Mockina bidentata***	***Mockina carinata***	***Mockina* cf. *englandi***
20-ZE-JL-PC-18	Pardonet Creek	18	0	0	0	0
20-ZE-JL-PC-29.7	Pardonet Creek	29.7	0	0	0	0
20-ZE-JL-BL-124	Black Bear Ridge	124	0	0	3	0
20-ZE-JL-BL-167.6	Black Bear Ridge	167.6	0	1	0	0
19-ZE-JL-H2-1	Holberg	187	0	0	1	0
19-ZE-JL-H3-25	Holberg	271.8	0	0	0	0
20-ZE-JL-MP2B-2.7	Michelsen Point	143.1	0	0	1	0
20-ZE-JL-MP3-75.3	Michelsen Point	332.8	0	2	1	0
92-OF-MUP-A1	Mushroom Point South	161.5	0	0	0	2
92-OF-MUP-A4	Mushroom Point South	168.5	0	0	0	0
92-OF-MUP-A7	Mushroom Point South	173	0	0	1	1
92-OF-MUP-A8	Mushroom Point South	175.25	1	0	0	0
92-OF-MUP-A9	Mushroom Point South	177.25	1	0	2	1
92-OF-MUP-A10	Mushroom Point South	180.25	0	1	0	0
92-OF-WAI-C4	Walters Island East	8	0	0	2	2
92-OF-WAI-C5	Walters Island East	12	0	1	0	0
92-OF-WAI-C6	Walters Island East	14	0	0	0	0
92-OF-WAI-C8	Walters Island East	23	0	1	0	1
92-OF-WAI-C13	Walters Island East	42	0	0	1	0
21-ZE-JL-MUP2-161.2	Mushroom Point South	161.2	0	1	0	0
21-ZE-JL-MUP2-176	Mushroom Point South	176	0	1	2	2
species total			2	8	14	9

Sample Name	*Mockina mosheri* A	*Mockina mosheri* B	*Mockina postera*	*Mockina spinosa*	*Mockina* sp.	*Norigondolella* cf. *navicula*
20-ZE-JL-PC-18	0	0	0	0	0	0
20-ZE-JL-PC-29.7	0	0	0	0	0	0
20-ZE-JL-BL-124	0	0	1	0	1	0
20-ZE-JL-BL-167.6	0	0	0	0	0	0
19-ZE-JL-H2-1	0	0	0	0	0	0
19-ZE-JL-H3-25	0	0	0	0	0	1
20-ZE-JL-MP2B-2.7	0	0	0	1	0	0
20-ZE-JL-MP3-75.3	0	0	0	0	0	0
92-OF-MUP-A1	0	0	0	0	0	0
92-OF-MUP-A4	0	0	0	0	1	0
92-OF-MUP-A7	0	0	0	0	1	0
92-OF-MUP-A8	2	1	0	0	0	0
92-OF-MUP-A9	0	0	0	0	1	0
92-OF-MUP-A10	0	0	0	0	1	0
92-OF-WAI-C4	1	1	0	0	3	0
92-OF-WAI-C5	0	1	0	0	1	0
92-OF-WAI-C6	0	2	0	0	0	0
92-OF-WAI-C8	0	0	0	0	0	0
92-OF-WAI-C13	0	0	0	0	0	0
21-ZE-JL-MUP2-161.2	0	0	0	0	0	0
21-ZE-JL-MUP2-176	0	0	0	1	3	0
species total	3	5	1	2	12	1

Sample Name	*Norigondolella steinbergensis*	*Norigondolella* sp.	*Orchardella elongata*	ramiform	sample total
20-ZE-JL-PC-18	0	0	1	0	1
20-ZE-JL-PC-29.7	13	10	0	30	53
20-ZE-JL-BL-124	0	0	2	0	7
20-ZE-JL-BL-167.6	11	19	0	11	42
19-ZE-JL-H2-1	0	0	0	0	1
19-ZE-JL-H3-25	0	1	0	0	2
20-ZE-JL-MP2B-2.7	0	0	0	1	3
20-ZE-JL-MP3-75.3	0	0	0	0	3
92-OF-MUP-A1	0	0	0	0	2
92-OF-MUP-A4	0	0	0	0	1
92-OF-MUP-A7	0	0	0	0	3
92-OF-MUP-A8	0	0	0	0	3
92-OF-MUP-A9	0	0	0	0	4
92-OF-MUP-A10	0	0	0	11	13
92-OF-WAI-C4	0	0	0	2	11
92-OF-WAI-C5	0	0	0	1	4
92-OF-WAI-C6	0	0	0	0	2
92-OF-WAI-C8	0	0	0	1	3
92-OF-WAI-C13	0	0	0	0	1
21-ZE-JL-MUP2-161.2	0	0	0	0	1
21-ZE-JL-MUP2-176	0	0	0	3	12
species total	24	30	3	60	grand total: 174

Appendix C3: Williston Lake geochemical data.

Section	Section Height (m)	Subsection	Subsection Height (m)	d13C (carb)	d18O (carb)
Black Bear Ridge	100	BL	100	-5.41	-3.99
Black Bear Ridge	101	BL	101	-4.11	-3.02
Black Bear Ridge	102	BL	102	-2.78	-4.67
Black Bear Ridge	103	BL	103	-3.22	-4.27
Black Bear Ridge	104	BL	104	-6.55	-4.42
Black Bear Ridge	105	BL	105	-3.67	-4.30
Black Bear Ridge	106	BL	106	-7.47	-4.42
Black Bear Ridge	107.6	BL	107.6	-3.42	-3.22
Black Bear Ridge	108	BL	108	-2.69	-3.75
Black Bear Ridge	109	BL	109	-3.74	-4.03
Black Bear Ridge	110	BL	110	-5.57	-3.97
Black Bear Ridge	111	BL	111	-4.66	-4.35
Black Bear Ridge	112	BL	112	-4.71	-4.48
Black Bear Ridge	113	BL	113	-3.69	-4.49
Black Bear Ridge	114	BL	114	-5.28	-5.10
Black Bear Ridge	115	BL	115	-5.19	-5.14
Black Bear Ridge	116	BL	116	-5.77	-4.99
Black Bear Ridge	117	BL	117	-6.04	-4.95
Black Bear Ridge	118	BL	118	-4.72	-5.41
Black Bear Ridge	119	BL	119	-5.91	-5.31
Black Bear Ridge	120	BL	120	-5.85	-5.35
Black Bear Ridge	121	BL	121	-5.88	-5.61
Black Bear Ridge	122	BL	122	-7.14	-5.64
Black Bear Ridge	123	BL	123	-6.04	-5.57
Black Bear Ridge	124	BL	124	-3.83	-5.05
Black Bear Ridge	125	BL	125	-4.62	-5.64
Black Bear Ridge	126	BL	126	-3.61	-5.51
Black Bear Ridge	126.5	BL	126.5	-8.55	-6.04
Black Bear Ridge	132	BL	132	-5.01	-5.24
Black Bear Ridge	133	BL	133	-4.14	-4.92
Black Bear Ridge	134	BL	134	-3.30	-4.77
Black Bear Ridge	135	BL	135	-3.14	-4.56
Black Bear Ridge	136	BL	136	-4.40	-4.84
Black Bear Ridge	137	BL	137	-4.71	-4.79
Black Bear Ridge	138	BL	138	-4.91	-5.30
Black Bear Ridge	139	BL	139	-2.46	-4.87
Black Bear Ridge	140	BL	140	-3.17	-4.97
Black Bear Ridge	141	BL	141	-4.78	-4.92

Section	Section Height (m)	Subsection	Subsection Height (m)	d13C (carb)	d18O (carb)
Black Bear Ridge	142	BL	142	-3.77	-5.13
Black Bear Ridge	143	BL	143	-3.14	-4.89
Black Bear Ridge	144	BL	144	-6.79	-5.84
Black Bear Ridge	145	BL	145	-2.65	-4.85
Black Bear Ridge	146	BL	146	-6.94	-6.17
Black Bear Ridge	147	BL	147	-2.43	-5.08
Black Bear Ridge	148	BL	148	-2.75	-4.65
Black Bear Ridge	149	BL	149	-2.80	-5.17
Black Bear Ridge	150	BL	150	-3.32	-5.42
Black Bear Ridge	151	BL	151	-3.41	-5.57
Black Bear Ridge	152	BL	152	-2.82	-5.56
Black Bear Ridge	153	BL	153	-5.83	-6.20
Black Bear Ridge	154	BL	154	-4.13	-5.09
Black Bear Ridge	155	BL	155	-3.46	-6.07
Black Bear Ridge	156	BL	156	-4.03	-7.52
Black Bear Ridge	157	BL	157	-4.46	-5.58
Black Bear Ridge	158	BL	158	-4.19	-5.70
Black Bear Ridge	159	BL	159	-5.31	-5.80
Black Bear Ridge	160	BL	160	-4.62	-4.94
Black Bear Ridge	161	BL	161	-2.64	-4.80
Black Bear Ridge	162	BL	162	-4.50	-5.96
Black Bear Ridge	163	BL	163	-7.52	-5.61
Black Bear Ridge	164	BL	164	-2.05	-4.96
Black Bear Ridge	165	BL	165	-2.23	-5.56
Black Bear Ridge	166	BL	166	-2.06	-5.53
Black Bear Ridge	167	BL	167	-2.59	-5.20
Black Bear Ridge	168	BL	168	-4.19	-5.57
Black Bear Ridge	169	BL	169	-6.05	-6.53
Black Bear Ridge	170	BL	170	-2.01	-5.18
Black Bear Ridge	171	BL	171	-2.52	-5.82
Black Bear Ridge	172	BL	172	-3.83	-5.33
Black Bear Ridge	173	BL	173	-4.15	-5.92
Black Bear Ridge	174	BL	174	-1.51	-5.47
Black Bear Ridge	175	BL	175	-2.13	-5.47
Black Bear Ridge	176	BL	176	-3.65	-5.65
Black Bear Ridge	177	BL	177	-3.11	-5.71
Black Bear Ridge	178	BL	178	-1.99	-5.86
Black Bear Ridge	179	BL	179	-3.04	-5.87
Black Bear Ridge	180	BL	180	-1.76	-5.48
Black Bear Ridge	181	BL	181	-2.56	-6.55
Black Bear Ridge	182	BL	182	-1.53	-5.19

Section	Section Height (m)	Subsection	Subsection Height (m)	d13C (carb)	d18O (carb)
Black Bear Ridge	183	BL	183	-3.70	-5.52
Black Bear Ridge	184	BL	184	-1.26	-5.51
Black Bear Ridge	185	BL	185	-1.02	-5.61
Black Bear Ridge	186	BL	186	-1.58	-5.42
Black Bear Ridge	187	BL	187	-1.50	-5.57
Black Bear Ridge	187.6	BU	0	-4.57	-6.03
Black Bear Ridge	187.7	BU	0.1	-3.79	-5.74
Black Bear Ridge	187.8	BU	0.2	-3.49	-5.68
Black Bear Ridge	187.9	BU	0.3	-3.16	-6.76
Black Bear Ridge	188	BU	0.4	-5.41	-6.14
Black Bear Ridge	188.1	BU	0.5	-5.89	-6.21
Black Bear Ridge	188.2	BU	0.6	-1.63	-4.99
Black Bear Ridge	188.3	BU	0.7	-1.62	-5.01
Black Bear Ridge	188.4	BU	0.8	-1.82	-4.90
Black Bear Ridge	188.5	BU	0.9	-1.79	-5.23
Black Bear Ridge	188.6	BU	1	-1.20	-4.82
Black Bear Ridge	188.7	BU	1.1	-1.10	-5.20
Black Bear Ridge	188.8	BU	1.2	-4.42	-6.08
Black Bear Ridge	188.9	BU	1.3	-4.22	-6.05
Black Bear Ridge	189	BU	1.4	-6.14	-6.27
Black Bear Ridge	189.1	BU	1.5	-4.89	-6.24
Black Bear Ridge	189.2	BU	1.6	-1.47	-4.79
Black Bear Ridge	189.3	BU	1.7	-2.28	-5.20
Black Bear Ridge	189.4	BU	1.8	-4.04	-5.94
Black Bear Ridge	189.5	BU	1.9	-1.64	-5.13
Black Bear Ridge	189.6	BU	2	-1.79	-5.08
Black Bear Ridge	189.7	BU	2.1	-1.20	-4.67
Black Bear Ridge	189.8	BU	2.2	-1.73	-4.98
Black Bear Ridge	189.9	BU	2.3	-5.05	-5.89
Black Bear Ridge	190	BU	2.4	-1.18	-5.21
Black Bear Ridge	190.1	BU	2.5	-3.33	-5.43
Black Bear Ridge	190.2	BU	2.6	-1.30	-4.58
Black Bear Ridge	190.3	BU	2.7	-1.27	-4.93
Black Bear Ridge	190.4	BU	2.8	-1.52	-5.20
Black Bear Ridge	190.5	BU	2.9	-1.53	-4.99
Black Bear Ridge	190.6	BU	3	-1.42	-4.75
Black Bear Ridge	190.7	BU	3.1	-1.46	-4.99
Black Bear Ridge	190.8	BU	3.2	-7.06	-6.39

Section	Section Height (m)	Subsection	Subsection Height (m)	d13C (carb)	d18O (carb)
Black Bear Ridge	190.9	BU	3.3	-1.88	-5.45
Black Bear Ridge	191	BU	3.4	-1.52	-5.11
Black Bear Ridge	191.1	BU	3.5	-3.83	-5.83
Black Bear Ridge	191.2	BU	3.6	-3.38	-5.87
Black Bear Ridge	191.3	BU	3.7	-1.05	-5.36
Black Bear Ridge	191.4	BU	3.8	-1.09	-5.41
Black Bear Ridge	191.5	BU	3.9	-0.97	-5.34
Black Bear Ridge	191.6	BU	4	-1.19	-4.92
Black Bear Ridge	191.7	BU	4.1	-1.37	-5.45
Black Bear Ridge	191.8	BU	4.2	-1.24	-5.41
Black Bear Ridge	191.9	BU	4.3	-1.26	-5.07
Black Bear Ridge	192	BU	4.4	-1.49	-5.62
Black Bear Ridge	192.1	BU	4.5	-1.36	-5.54
Black Bear Ridge	192.2	BU	4.6	-1.22	-5.39
Black Bear Ridge	192.3	BU	4.7	-7.84	-7.16
Black Bear Ridge	192.4	BU	4.8	-4.42	-5.55
Black Bear Ridge	192.5	BU	4.9	-3.91	-4.95
Black Bear Ridge	192.6	BU	5	-4.15	-4.93
Black Bear Ridge	192.7	BU	5.1	-3.90	-5.02
Black Bear Ridge	192.8	BU	5.2	-4.46	-5.44
Black Bear Ridge	192.9	BU	5.3	-5.97	-6.91
Black Bear Ridge	193	BU	5.4	-6.28	-6.57
Black Bear Ridge	193.1	BU	5.5	-3.30	-6.71
Black Bear Ridge	193.2	BU	5.6	-0.94	-6.89
Black Bear Ridge	193.3	BU	5.7	-1.13	-4.43
Black Bear Ridge	193.4	BU	5.8	-1.90	-7.24
Black Bear Ridge	193.5	BU	5.9	-3.99	-6.84
Black Bear Ridge	193.6	BU	6	-4.00	-6.84
Black Bear Ridge	193.7	BU	6.1	-3.16	-7.00
Black Bear Ridge	193.8	BU	6.2	-2.65	-6.14
Black Bear Ridge	193.9	BU	6.3	-1.94	-5.42
Black Bear Ridge	194	BU	6.4	-2.91	-6.10
Black Bear Ridge	194.1	BU	6.5	-1.70	-5.60
Black Bear Ridge	194.2	BU	6.6	-1.27	-4.69
Black Bear Ridge	194.3	BU	6.7	-9.36	-5.96
Black Bear Ridge	194.4	BU	6.8	-1.71	-4.80
Black Bear Ridge	194.5	BU	6.9	-0.96	-3.98
Black Bear Ridge	194.6	BU	7	-8.28	-6.50
Black Bear Ridge	194.7	BU	7.1	-1.31	-4.34
Black Bear Ridge	194.8	BU	7.2	-5.24	-4.97
Black Bear Ridge	194.9	BU	7.3	-4.29	-5.11

Section	Section Height (m)	Subsection	Subsection Height (m)	d13C (carb)	d18O (carb)
Black Bear Ridge	195	BU	7.4	-4.15	-4.97
Black Bear Ridge	195.1	BU	7.5	-5.09	-6.50
Black Bear Ridge	195.2	BU	7.6	-5.37	-6.51
Black Bear Ridge	195.3	BU	7.7	-7.00	-6.25
Black Bear Ridge	195.4	BU	7.8	-4.04	-5.73
Black Bear Ridge	195.5	BU	7.9	-4.29	-5.51
Black Bear Ridge	195.6	BU	8	-5.01	-5.50
Black Bear Ridge	195.7	BU	8.1	-5.23	-5.80
Black Bear Ridge	195.8	BU	8.2	-5.46	-5.96
Black Bear Ridge	195.9	BU	8.3	-4.37	-5.82
Black Bear Ridge	196	BU	8.4	-3.82	-6.34
Black Bear Ridge	196.1	BU	8.5	-3.12	-6.31
Black Bear Ridge	196.2	BU	8.6	-2.55	-5.26
Black Bear Ridge	196.3	BU	8.7	-2.13	-6.09
Black Bear Ridge	196.4	BU	8.8	-1.89	-5.86
Black Bear Ridge	196.5	BU	8.9	-2.24	-6.25
Black Bear Ridge	196.6	BU	9	-3.17	-6.67
Black Bear Ridge	196.7	BU	9.1	-3.43	-6.70
Black Bear Ridge	196.8	BU	9.2	-2.22	-5.92
Black Bear Ridge	196.9	BU	9.3	-2.24	-6.89
Black Bear Ridge	197	BU	9.4	-2.78	-5.15
Black Bear Ridge	197.1	BU	9.5	-2.77	-5.71
Black Bear Ridge	197.2	BU	9.6	-2.62	-5.26
Black Bear Ridge	197.3	BU	9.7	-2.24	-5.95
Black Bear Ridge	197.4	BU	9.8	-2.68	-5.95
Black Bear Ridge	197.5	BU	9.9	-2.76	-5.99
Black Bear Ridge	197.6	BU	10	-2.98	-6.25
Black Bear Ridge	197.7	BU	10.1	-3.07	-6.38
Black Bear Ridge	197.8	BU	10.2	-2.73	-6.94
Black Bear Ridge	197.9	BU	10.3	-3.69	-5.20
Black Bear Ridge	198	BU	10.4	-3.37	-5.55
Black Bear Ridge	198.1	BU	10.5	-4.31	-5.40
Black Bear Ridge	198.2	BU	10.6	-3.53	-4.60
Black Bear Ridge	198.3	BU	10.7	-4.67	-6.17
Black Bear Ridge	198.4	BU	10.8	-5.40	-6.07
Black Bear Ridge	198.5	BU	10.9	-5.29	-5.73
Black Bear Ridge	198.6	BU	11	-5.26	-5.68
Black Bear Ridge	198.7	BU	11.1	-5.60	-5.88

Section	Section Height (m)	Subsection	Subsection Height (m)	d13C (carb)	d18O (carb)
Black Bear Ridge	198.8	BU	11.2	-5.51	-5.74
Black Bear Ridge	198.9	BU	11.3	-4.04	-5.92
Black Bear Ridge	199	BU	11.4	-4.30	-6.27
Black Bear Ridge	199.1	BU	11.5	-2.74	-5.55
Black Bear Ridge	199.2	BU	11.6	-3.01	-5.53
Black Bear Ridge	199.3	BU	11.7	-2.94	-5.83
Black Bear Ridge	199.4	BU	11.8	-2.76	-5.77
Black Bear Ridge	199.5	BU	11.9	-3.22	-6.53
Black Bear Ridge	199.6	BU	12	-2.58	-5.64
Black Bear Ridge	199.7	BU	12.1	-2.98	-6.63
Black Bear Ridge	199.8	BU	12.2	-2.87	-6.01
Black Bear Ridge	199.9	BU	12.3	-3.25	-6.05
Black Bear Ridge	200	BU	12.4	-3.66	-5.95
Black Bear Ridge	200.2	BU	12.6	-3.05	-6.30
Black Bear Ridge	200.3	BU	12.7	-2.75	-5.82
Black Bear Ridge	200.4	BU	12.8	-2.87	-5.90
Black Bear Ridge	200.5	BU	12.9	-3.18	-6.03
Black Bear Ridge	200.6	BU	13	-4.76	-6.63
Black Bear Ridge	200.7	BU	13.1	-5.32	-6.40
Black Bear Ridge	200.8	BU	13.2	-5.03	-6.46
Black Bear Ridge	200.9	BU	13.3	-4.21	-6.56
Black Bear Ridge	201	BU	13.4	-2.93	-6.39
Black Bear Ridge	201.1	BU	13.5	-4.60	-7.66
Black Bear Ridge	201.2	BU	13.6	-3.40	-6.95
Black Bear Ridge	201.3	BU	13.7	-10.35	-6.78
Black Bear Ridge	201.4	BU	13.8	-11.11	-6.68
Black Bear Ridge	201.5	BU	13.9	-3.62	-6.77
Black Bear Ridge	201.6	BU	14	-2.67	-5.88
Black Bear Ridge	201.7	BU	14.1	-2.52	-6.04
Black Bear Ridge	201.8	BU	14.2	-2.68	-5.64
Black Bear Ridge	201.9	BU	14.3	-2.73	-6.69
Black Bear Ridge	202	BU	14.4	-3.30	-5.78
Black Bear Ridge	202.1	BU	14.5	-2.77	-7.08
Black Bear Ridge	202.2	BU	14.6	-3.08	-6.60
Black Bear Ridge	202.3	BU	14.7	-3.58	-6.84
Black Bear Ridge	202.4	BU	14.8	-2.88	-6.52
Black Bear Ridge	202.5	BU	14.9	-2.41	-6.81
Black Bear Ridge	202.6	BU	15	-2.55	-6.67
Black Bear Ridge	203.6	BU	16	-5.04	-6.26
Black Bear Ridge	204.6	BU	17	-8.85	-7.43
Black Bear Ridge	205.6	BU	18	-2.23	-6.17

Section	Section Height (m)	Subsection	Subsection Height (m)	d13C (carb)	d18O (carb)
Black Bear Ridge	206.6	BU	19	-4.41	-6.40
Black Bear Ridge	207.6	BU	20	-2.20	-5.76
Black Bear Ridge	208.6	BU	21	-6.05	-6.31
Black Bear Ridge	209.6	BU	22	-4.82	-6.29
Black Bear Ridge	210.6	BU	23	-2.28	-6.68
Black Bear Ridge	211.6	BU	24	-3.06	-7.85
Black Bear Ridge	212.6	BU	25	-7.81	-7.19
Black Bear Ridge	213.5	BU	25.9	-3.65	-7.01
Black Bear Ridge	214.6	BU	27	-4.24	-7.47
Black Bear Ridge	215.6	BU	28	-6.96	-6.83
Black Bear Ridge	216.6	BU	29	-5.84	-6.71
Black Bear Ridge	217.6	BU	30	-3.55	-6.98
Black Bear Ridge	218.6	BU	31	-6.27	-6.85
Black Bear Ridge	219.6	BU	32	-1.28	-6.99
Black Bear Ridge	220.6	BU	33	-2.36	-5.28
Black Bear Ridge	220.9	BU	33.3	-2.78	-5.59
Ne Parle Pas Point	0	NPP	0	0.37	-6.51
Ne Parle Pas Point	1	NPP	1	0.33	-6.12
Ne Parle Pas Point	2	NPP	2	0.47	-5.10
Ne Parle Pas Point	2.15	NPP	2.15	0.06	-6.81
Ne Parle Pas Point	3	NPP	3	0.16	-6.97
Ne Parle Pas Point	4	NPP	4	0.61	-6.44
Ne Parle Pas Point	5	NPP	5	0.59	-6.65
Ne Parle Pas Point	6	NPP	6	0.78	-7.48
Ne Parle Pas Point	7	NPP	7	0.91	-6.60
Ne Parle Pas Point	8	NPP	8	0.41	-6.07
Ne Parle Pas Point	9	NPP	9	0.53	-5.89
Ne Parle Pas Point	10	NPP	10	0.82	-5.01
Ne Parle Pas Point	11	NPP	11	0.63	-5.73
Ne Parle Pas Point	12	NPP	12	0.52	-6.15
Ne Parle Pas Point	13	NPP	13	1.04	-6.33
Ne Parle Pas Point	14	NPP	14	1.42	-6.46
Ne Parle Pas Point	15	NPP	15	1.35	-6.35
Ne Parle Pas Point	16	NPP	16	0.95	-6.18
Ne Parle Pas Point	17	NPP	17	0.98	-5.68
Ne Parle Pas Point	18	NPP	18	0.51	-5.54
Ne Parle Pas Point	19	NPP	19	0.08	-6.22
Ne Parle Pas Point	20	NPP	20	0.27	-6.14

Section	Section Height (m)	Subsection	Subsection Height (m)	d13C (carb)	d18O (carb)
Ne Parle Pas Point	21	NPP	21	0.04	-6.04
Ne Parle Pas Point	22	NPP	22	0.26	-5.75
Ne Parle Pas Point	23	NPP	23	-0.22	-6.70
Ne Parle Pas Point	24	NPP	24	0.54	-5.74
Ne Parle Pas Point	25	NPP	25	0.27	-5.93
Ne Parle Pas Point	26	NPP	26	0.12	-5.90
Ne Parle Pas Point	27	NPP	27	0.67	-6.60
Ne Parle Pas Point	28	NPP	28	0.32	-5.37
Ne Parle Pas Point	29	NPP	29	-0.08	-6.41
Ne Parle Pas Point	30	NPP	30	0.33	-6.12
Ne Parle Pas Point	31	NPP	31	0.46	-7.27
Ne Parle Pas Point	32	NPP	32	0.57	-5.05
Ne Parle Pas Point	33	NPP	33	0.35	-5.68
Ne Parle Pas Point	34	NPP	34	0.71	-4.31
Ne Parle Pas Point	35	NPP	35	0.32	-5.53
Ne Parle Pas Point	36	NPP	36	0.14	-6.74
Ne Parle Pas Point	37	NPP	37	0.83	-6.02
Ne Parle Pas Point	38	NPP	38	0.56	-4.51
Ne Parle Pas Point	39	NPP	39	0.55	-5.78
Ne Parle Pas Point	40	NPP	40	0.42	-5.80
Ne Parle Pas Point	41	NPP	41	0.74	-6.95
Ne Parle Pas Point	42	NPP	42	0.30	-5.58
Ne Parle Pas Point	43	NPP	43	-0.15	-6.13
Ne Parle Pas Point	44	NPP	44	0.29	-6.19
Ne Parle Pas Point	45	NPP	45	0.25	-6.47
Ne Parle Pas Point	46	NPP	46	0.91	-7.03
Ne Parle Pas Point	47	NPP	47	0.38	-5.53
Ne Parle Pas Point	48	NPP	48	-0.03	-5.37
Ne Parle Pas Point	49	NPP	49	0.22	-5.38
Ne Parle Pas Point	50	NPP	50	-0.19	-5.29
Ne Parle Pas Point	51	NPP	51	0.39	-6.72
Ne Parle Pas Point	52	NPP	52	0.43	-5.77
Ne Parle Pas Point	53	NPP	53	-0.24	-6.11
Ne Parle Pas Point	54	NPP	54	0.22	-6.64
Ne Parle Pas Point	55	NPP	55	-0.07	-5.78
Ne Parle Pas Point	56	NPP	56	-0.42	-6.06
Ne Parle Pas Point	57	NPP	57	-0.61	-6.03
Ne Parle Pas Point	58	NPP	58	-0.44	-6.05
Ne Parle Pas Point	59	NPP	59	-1.52	-6.44
Ne Parle Pas Point	60	NPP	60	0.14	-4.36
Ne Parle Pas Point	61	NPP	61	0.18	-5.53

Section	Section Height (m)	Subsection	Subsection Height (m)	d13C (carb)	d18O (carb)
Ne Parle Pas Point	62	NPP	62	0.21	-6.53
Ne Parle Pas Point	63	NPP	63	0.09	-6.86
Ne Parle Pas Point	64	NPP	64	0.07	-5.55
Ne Parle Pas Point	65	NPP	65	0.17	-6.84
Ne Parle Pas Point	66	NPP	66	-0.01	-5.61
Ne Parle Pas Point	67	NPP	67	0.12	-6.06
Ne Parle Pas Point	68	NPP	68	-0.18	-5.23
Ne Parle Pas Point	69	NPP	69	-1.13	-6.31
Ne Parle Pas Point	70	NPP	70	-0.37	-5.81
Ne Parle Pas Point	71	NPP	71	-0.92	-7.07
Ne Parle Pas Point	72	NPP	72	0.12	-7.26
Ne Parle Pas Point	73	NPP	73	-0.43	-6.43
Ne Parle Pas Point	74	NPP	74	-1.09	-6.78
Ne Parle Pas Point	75	NPP	75	-0.81	-5.69
Ne Parle Pas Point	76	NPP	76	-0.88	-7.07
Ne Parle Pas Point	77	NPP	77	-1.11	-6.50
Ne Parle Pas Point	78	NPP	78	-1.12	-6.26
Ne Parle Pas Point	79	NPP	79	-1.09	-5.63
Ne Parle Pas Point	80	NPP	80	-0.59	-6.56
Ne Parle Pas Point	81	NPP	81	-0.78	-5.85
Ne Parle Pas Point	82	NPP	82	-0.58	-5.65
Ne Parle Pas Point	83	NPP	83	-0.25	-6.04
Ne Parle Pas Point	84	NPP	84	-0.29	-5.02
Ne Parle Pas Point	85	NPP	85	-0.69	-6.41
Ne Parle Pas Point	85.1	NPP	85.1	-0.65	-6.88
Ne Parle Pas Point	85.2	NPP	85.2	-0.73	-6.58
Ne Parle Pas Point	85.3	NPP	85.3	-0.94	-6.67
Ne Parle Pas Point	85.4	NPP	85.4	-0.90	-6.07
Ne Parle Pas Point	85.5	NPP	85.5	-0.99	-6.71
Ne Parle Pas Point	85.6	NPP	85.6	-0.99	-6.19
Ne Parle Pas Point	85.7	NPP	85.7	-0.75	-6.75
Ne Parle Pas Point	85.8	NPP	85.8	-0.57	-6.86
Ne Parle Pas Point	85.9	NPP	85.9	-0.26	-6.63
Ne Parle Pas Point	86	NPP	86	-0.86	-5.89
Ne Parle Pas Point	86.1	NPP	86.1	-0.74	-6.44
Ne Parle Pas Point	86.2	NPP	86.2	-0.97	-6.86
Ne Parle Pas Point	86.3	NPP	86.3	-0.80	-6.22
Ne Parle Pas Point	86.4	NPP	86.4	-0.95	-6.15

Section	Section Height (m)	Subsection	Subsection Height (m)	d13C (carb)	d18O (carb)
Ne Parle Pas Point	86.5	NPP	86.5	-0.76	-6.07
Ne Parle Pas Point	86.6	NPP	86.6	-1.05	-5.88
Ne Parle Pas Point	86.7	NPP	86.7	-0.77	-6.66
Ne Parle Pas Point	86.8	NPP	86.8	-0.60	-5.22
Ne Parle Pas Point	86.9	NPP	86.9	-0.97	-5.88
Ne Parle Pas Point	87	NPP	87	-1.16	-5.87
Ne Parle Pas Point	87.1	NPP	87.1	-0.95	-5.81
Ne Parle Pas Point	87.2	NPP	87.2	-0.85	-6.12
Ne Parle Pas Point	87.3	NPP	87.3	-0.68	-5.38
Ne Parle Pas Point	87.4	NPP	87.4	-0.71	-5.18
Ne Parle Pas Point	87.5	NPP	87.5	-0.35	-4.89
Ne Parle Pas Point	87.6	NPP	87.6	-0.79	-6.26
Ne Parle Pas Point	87.7	NPP	87.7	-0.35	-5.16
Ne Parle Pas Point	87.8	NPP	87.8	-0.44	-5.81
Ne Parle Pas Point	87.9	NPP	87.9	-0.38	-5.30
Ne Parle Pas Point	88	NPP	88	-0.58	-8.04
Ne Parle Pas Point	88.1	NPP	88.1	-0.77	-5.61
Ne Parle Pas Point	88.2	NPP	88.2	-1.46	-6.24
Ne Parle Pas Point	88.3	NPP	88.3	-1.06	-6.34
Ne Parle Pas Point	88.4	NPP	88.4	-1.15	-6.47
Ne Parle Pas Point	88.5	NPP	88.5	-0.88	-5.94
Ne Parle Pas Point	88.6	NPP	88.6	-0.62	-5.90
Ne Parle Pas Point	88.7	NPP	88.7	-0.38	-5.91
Ne Parle Pas Point	88.8	NPP	88.8	-1.03	-7.45
Ne Parle Pas Point	88.9	NPP	88.9	-0.79	-6.41
Ne Parle Pas Point	89	NPP	89	-1.17	-5.85
Ne Parle Pas Point	89.1	NPP	89.1	-1.20	-6.25
Ne Parle Pas Point	89.2	NPP	89.2	-0.01	-4.88
Ne Parle Pas Point	89.3	NPP	89.3	-0.08	-5.66
Ne Parle Pas Point	89.4	NPP	89.4	-0.73	-6.34
Ne Parle Pas Point	89.5	NPP	89.5	-1.05	-6.06
Ne Parle Pas Point	89.6	NPP	89.6	-0.90	-5.61
Ne Parle Pas Point	89.7	NPP	89.7	-0.54	-5.63
Ne Parle Pas Point	89.8	NPP	89.8	-0.63	-5.32
Ne Parle Pas Point	89.9	NPP	89.9	-0.86	-6.15
Ne Parle Pas Point	90	NPP	90	-0.82	-5.63
Ne Parle Pas Point	90.1	NPP	90.1	-0.84	-6.41
Ne Parle Pas Point	90.2	NPP	90.2	-0.98	-6.31
Ne Parle Pas Point	90.3	NPP	90.3	-0.84	-5.38
Ne Parle Pas Point	90.4	NPP	90.4	-0.95	-5.83
Ne Parle Pas Point	90.5	NPP	90.5	-0.31	-6.13

Section	Section Height (m)	Subsection	Subsection Height (m)	d13C (carb)	d18O (carb)
Ne Parle Pas Point	90.6	NPP	90.6	-0.45	-5.31
Ne Parle Pas Point	90.7	NPP	90.7	-0.41	-5.88
Ne Parle Pas Point	90.8	NPP	90.8	-0.49	-5.47
Ne Parle Pas Point	90.9	NPP	90.9	-0.50	-6.31
Ne Parle Pas Point	91	NPP	91	-0.71	-5.89
Ne Parle Pas Point	91.1	NPP	91.1	-0.60	-5.69
Ne Parle Pas Point	91.2	NPP	91.2	-0.39	-5.16
Ne Parle Pas Point	91.3	NPP	91.3	-0.71	-5.68
Ne Parle Pas Point	91.4	NPP	91.4	-0.78	-5.57
Ne Parle Pas Point	91.5	NPP	91.5	-0.91	-6.52
Ne Parle Pas Point	91.6	NPP	91.6	-1.02	-5.72
Ne Parle Pas Point	91.7	NPP	91.7	-0.94	-5.89
Ne Parle Pas Point	91.8	NPP	91.8	-1.03	-6.02
Ne Parle Pas Point	91.9	NPP	91.9	-1.26	-6.82
Ne Parle Pas Point	92	NPP	92	-0.38	-4.74
Ne Parle Pas Point	92.1	NPP	92.1	-0.42	-4.69
Ne Parle Pas Point	92.2	NPP	92.2	-0.62	-5.06
Ne Parle Pas Point	92.3	NPP	92.3	-0.33	-5.27
Ne Parle Pas Point	92.4	NPP	92.4	-0.67	-6.56
Ne Parle Pas Point	92.5	NPP	92.5	-0.35	-4.46
Ne Parle Pas Point	92.6	NPP	92.6	-0.58	-5.49
Ne Parle Pas Point	92.7	NPP	92.7	-0.70	-4.47
Ne Parle Pas Point	92.8	NPP	92.8	-1.15	-6.94
Ne Parle Pas Point	92.9	NPP	92.9	-1.02	-5.69
Ne Parle Pas Point	93	NPP	93	-1.13	-5.78
Ne Parle Pas Point	93.2	NPP	93.2	-1.00	-6.70
Ne Parle Pas Point	93.3	NPP	93.3	-1.18	-6.33
Ne Parle Pas Point	93.4	NPP	93.4	-1.33	-6.33
Ne Parle Pas Point	93.5	NPP	93.5	-1.01	-5.31
Ne Parle Pas Point	93.6	NPP	93.6	-0.45	-4.43
Ne Parle Pas Point	93.7	NPP	93.7	-0.35	-4.26
Ne Parle Pas Point	93.8	NPP	93.8	-0.31	-3.52
Ne Parle Pas Point	93.9	NPP	93.9	-0.07	-3.61
Ne Parle Pas Point	94	NPP	94	-0.30	-4.01
Ne Parle Pas Point	94.1	NPP	94.1	0.18	-4.19
Ne Parle Pas Point	94.2	NPP	94.2	-0.03	-3.95
Ne Parle Pas Point	94.3	NPP	94.3	0.10	-3.50
Ne Parle Pas Point	94.4	NPP	94.4	0.23	-3.35

Section	Section Height (m)	Subsection	Subsection Height (m)	d13C (carb)	d18O (carb)
Ne Parle Pas Point	94.5	NPP	94.5	0.31	-5.68
Ne Parle Pas Point	94.6	NPP	94.6	-0.73	-5.41
Ne Parle Pas Point	94.7	NPP	94.7	-0.95	-5.41
Ne Parle Pas Point	94.8	NPP	94.8	-0.79	-5.49
Ne Parle Pas Point	94.9	NPP	94.9	-0.64	-4.71
Ne Parle Pas Point	95	NPP	95	-0.29	-3.63
Ne Parle Pas Point	95.1	NPP	95.1	-0.75	-5.54
Ne Parle Pas Point	95.2	NPP	95.2	-0.94	-5.28
Ne Parle Pas Point	95.3	NPP	95.3	-1.54	-6.13
Ne Parle Pas Point	95.4	NPP	95.4	-1.60	-6.19
Ne Parle Pas Point	95.5	NPP	95.5	-0.72	-4.92
Ne Parle Pas Point	95.6	NPP	95.6	-0.72	-4.52
Ne Parle Pas Point	95.7	NPP	95.7	-0.40	-3.77
Ne Parle Pas Point	95.8	NPP	95.8	-0.24	-3.81
Ne Parle Pas Point	95.9	NPP	95.9	-2.78	-6.89
Ne Parle Pas Point	96	NPP	96	-1.84	-5.44
Ne Parle Pas Point	96.1	NPP	96.1	-0.70	-5.88
Ne Parle Pas Point	96.2	NPP	96.2	-0.62	-5.83
Ne Parle Pas Point	96.3	NPP	96.3	-0.83	-5.63
Ne Parle Pas Point	96.4	NPP	96.4	-0.52	-5.55
Ne Parle Pas Point	96.5	NPP	96.5	-0.34	-5.54
Ne Parle Pas Point	96.6	NPP	96.6	-0.46	-5.19
Ne Parle Pas Point	96.7	NPP	96.7	-0.48	-5.40
Ne Parle Pas Point	96.8	NPP	96.8	-0.89	-5.48
Ne Parle Pas Point	96.9	NPP	96.9	-0.44	-5.05
Ne Parle Pas Point	97	NPP	97	-0.68	-5.20
Ne Parle Pas Point	97.1	NPP	97.1	-0.52	-5.05
Ne Parle Pas Point	97.2	NPP	97.2	-0.91	-5.67
Ne Parle Pas Point	97.3	NPP	97.3	-0.72	-5.50
Ne Parle Pas Point	97.4	NPP	97.4	-1.22	-6.00
Ne Parle Pas Point	97.5	NPP	97.5	-1.37	-6.20
Ne Parle Pas Point	97.6	NPP	97.6	-2.44	-6.39
Ne Parle Pas Point	97.7	NPP	97.7	-2.74	-6.64
Ne Parle Pas Point	97.8	NPP	97.8	-2.64	-6.57
Ne Parle Pas Point	97.9	NPP	97.9	-2.00	-5.07
Ne Parle Pas Point	98	NPP	98	-3.06	-5.87
Ne Parle Pas Point	98.1	NPP	98.1	-3.03	-6.29
Ne Parle Pas Point	98.2	NPP	98.2	-3.13	-6.20
Ne Parle Pas Point	98.3	NPP	98.3	-1.73	-7.22
Ne Parle Pas Point	98.4	NPP	98.4	-1.75	-5.74
Ne Parle Pas Point	98.5	NPP	98.5	-2.01	-6.21

Section	Section Height (m)	Subsection	Subsection Height (m)	d13C (carb)	d18O (carb)
Ne Parle Pas Point	98.6	NPP	98.6	-2.46	-6.44
Ne Parle Pas Point	98.7	NPP	98.7	-3.06	-6.77
Ne Parle Pas Point	98.8	NPP	98.8	-1.00	-5.42
Ne Parle Pas Point	98.9	NPP	98.9	-0.62	-5.06
Ne Parle Pas Point	99	NPP	99	-0.75	-5.13
Ne Parle Pas Point	99.1	NPP	99.1	-1.40	-5.82
Ne Parle Pas Point	99.2	NPP	99.2	-1.32	-6.14
Ne Parle Pas Point	99.3	NPP	99.3	-1.00	-5.96
Ne Parle Pas Point	99.4	NPP	99.4	-0.89	-5.09
Ne Parle Pas Point	99.5	NPP	99.5	-0.48	-4.89
Ne Parle Pas Point	99.6	NPP	99.6	-1.25	-5.73
Ne Parle Pas Point	99.7	NPP	99.7	-1.39	-5.95
Ne Parle Pas Point	99.8	NPP	99.8	-0.74	-4.51
Ne Parle Pas Point	99.9	NPP	99.9	-0.65	-4.88
Ne Parle Pas Point	100	NPP	100	-0.55	-4.99
Ne Parle Pas Point	100.1	NPP	100.1	-0.31	-4.58
Ne Parle Pas Point	100.2	NPP	100.2	-1.81	-8.20
Ne Parle Pas Point	100.3	NPP	100.3	-0.80	-4.62
Ne Parle Pas Point	100.4	NPP	100.4	-1.38	-5.32
Ne Parle Pas Point	100.5	NPP	100.5	-1.07	-4.57
Ne Parle Pas Point	100.6	NPP	100.6	-1.10	-6.22
Ne Parle Pas Point	100.7	NPP	100.7	-1.44	-6.17
Ne Parle Pas Point	100.8	NPP	100.8	-1.36	-6.48
Ne Parle Pas Point	100.9	NPP	100.9	-1.28	-5.83
Ne Parle Pas Point	101	NPP	101	-1.57	-6.19
Ne Parle Pas Point	101.2	NPP	101.2	-1.59	-5.94
Ne Parle Pas Point	101.3	NPP	101.3	-0.53	-3.63
Ne Parle Pas Point	101.4	NPP	101.4	-1.61	-6.28
Ne Parle Pas Point	101.5	NPP	101.5	-1.66	-6.44
Ne Parle Pas Point	101.6	NPP	101.6	-1.87	-7.00
Ne Parle Pas Point	101.7	NPP	101.7	-1.45	-6.34
Ne Parle Pas Point	101.8	NPP	101.8	-1.59	-6.41
Ne Parle Pas Point	101.9	NPP	101.9	-0.88	-5.89
Ne Parle Pas Point	102	NPP	102	-1.14	-5.89
Ne Parle Pas Point	102.1	NPP	102.1	-1.33	-6.70
Ne Parle Pas Point	102.2	NPP	102.2	-1.15	-6.37
Ne Parle Pas Point	102.3	NPP	102.3	-1.12	-5.24
Ne Parle Pas Point	102.4	NPP	102.4	-0.83	-5.09

Section	Section Height (m)	Subsection	Subsection Height (m)	d13C (carb)	d18O (carb)
Ne Parle Pas Point	102.5	NPP	102.5	-1.56	-7.43
Ne Parle Pas Point	102.6	NPP	102.6	-1.64	-7.82
Ne Parle Pas Point	102.7	NPP	102.7	-1.63	-7.86
Ne Parle Pas Point	102.8	NPP	102.8	-1.56	-6.91
Ne Parle Pas Point	102.9	NPP	102.9	-1.31	-6.28
Ne Parle Pas Point	103	NPP	103	-1.02	-5.53
Ne Parle Pas Point	103.1	NPP	103.1	-0.83	-5.66
Ne Parle Pas Point	103.2	NPP	103.2	-0.41	-4.63
Ne Parle Pas Point	103.3	NPP	103.3	-0.42	-4.33
Ne Parle Pas Point	103.4	NPP	103.4	-0.52	-5.32
Ne Parle Pas Point	103.5	NPP	103.5	-1.10	-6.07
Ne Parle Pas Point	103.6	NPP	103.6	-0.99	-5.68
Ne Parle Pas Point	103.8	NPP	103.8	-1.69	-6.07
Ne Parle Pas Point	103.9	NPP	103.9	-1.73	-6.55
Ne Parle Pas Point	104	NPP	104	-3.31	-6.85
Ne Parle Pas Point	104.1	NPP	104.1	-2.97	-6.58
Ne Parle Pas Point	104.2	NPP	104.2	-3.11	-6.84
Ne Parle Pas Point	104.3	NPP	104.3	-3.24	-6.50
Ne Parle Pas Point	104.4	NPP	104.4	-2.91	-6.57
Ne Parle Pas Point	104.5	NPP	104.5	-3.04	-6.61
Ne Parle Pas Point	104.6	NPP	104.6	-1.53	-5.98
Ne Parle Pas Point	104.7	NPP	104.7	-0.69	-4.91
Ne Parle Pas Point	104.8	NPP	104.8	-0.53	-5.21
Ne Parle Pas Point	104.9	NPP	104.9	-0.37	-4.98
Ne Parle Pas Point	105	NPP	105	-0.30	-5.49
Ne Parle Pas Point	105.1	NPP	105.1	-0.52	-4.94
Ne Parle Pas Point	105.2	NPP	105.2	-1.16	-6.26
Ne Parle Pas Point	105.3	NPP	105.3	-1.30	-6.48
Ne Parle Pas Point	105.4	NPP	105.4	-0.86	-5.14
Ne Parle Pas Point	105.5	NPP	105.5	-2.93	-6.71
Ne Parle Pas Point	105.6	NPP	105.6	-3.24	-6.89
Ne Parle Pas Point	105.7	NPP	105.7	-4.09	-6.98
Ne Parle Pas Point	105.8	NPP	105.8	-3.21	-6.70
Ne Parle Pas Point	105.9	NPP	105.9	-2.84	-7.11
Ne Parle Pas Point	106	NPP	106	-1.83	-6.47
Ne Parle Pas Point	106.1	NPP	106.1	-0.32	-5.22
Ne Parle Pas Point	106.2	NPP	106.2	-0.50	-5.47
Ne Parle Pas Point	106.3	NPP	106.3	0.00	-4.57
Ne Parle Pas Point	106.4	NPP	106.4	-0.27	-5.51
Ne Parle Pas Point	106.5	NPP	106.5	-0.50	-6.39
Ne Parle Pas Point	106.6	NPP	106.6	-0.32	-5.48

Section	Section Height (m)	Subsection	Subsection Height (m)	d13C (carb)	d18O (carb)
Ne Parle Pas Point	106.7	NPP	106.7	-0.26	-5.81
Ne Parle Pas Point	106.8	NPP	106.8	-0.16	-5.30
Ne Parle Pas Point	106.9	NPP	106.9	0.09	-6.25
Ne Parle Pas Point	107	NPP	107	-0.19	-5.52
Ne Parle Pas Point	107.1	NPP	107.1	-0.03	-6.33
Ne Parle Pas Point	107.2	NPP	107.2	-0.15	-6.42
Ne Parle Pas Point	107.3	NPP	107.3	0.12	-4.09
Ne Parle Pas Point	107.4	NPP	107.4	-1.33	-6.48
Ne Parle Pas Point	107.5	NPP	107.5	-0.75	-7.10
Ne Parle Pas Point	107.6	NPP	107.6	-0.74	-5.96
Ne Parle Pas Point	107.7	NPP	107.7	-0.90	-6.45
Ne Parle Pas Point	107.8	NPP	107.8	-1.63	-7.21
Ne Parle Pas Point	107.9	NPP	107.9	-0.98	-6.19
Ne Parle Pas Point	108	NPP	108	-1.34	-6.26
Ne Parle Pas Point	108.1	NPP	108.1	-1.41	-7.10
Ne Parle Pas Point	108.2	NPP	108.2	-1.36	-6.34
Ne Parle Pas Point	108.3	NPP	108.3	-1.33	-6.37
Ne Parle Pas Point	108.4	NPP	108.4	-1.24	-6.44
Ne Parle Pas Point	108.5	NPP	108.5	-1.10	-6.55
Pardonet Creek	0	PC	0	-0.07	-5.09
Pardonet Creek	1	PC	1	-0.18	-6.21
Pardonet Creek	2	PC	2	0.24	-5.23
Pardonet Creek	3	PC	3	-0.05	-4.67
Pardonet Creek	4	PC	4	-0.37	-5.78
Pardonet Creek	5	PC	5	-0.16	-5.83
Pardonet Creek	6	PC	6	-3.08	-6.42
Pardonet Creek	7	PC	7	0.23	-4.16
Pardonet Creek	8	PC	8	-0.41	-4.84
Pardonet Creek	9	PC	9	-0.85	-5.95
Pardonet Creek	10	PC	10	-1.27	-5.76
Pardonet Creek	11	PC	11	-2.25	-6.41
Pardonet Creek	12	PC	12	-0.60	-6.20
Pardonet Creek	13	PC	13	-0.23	-4.14
Pardonet Creek	14	PC	14	-0.38	-5.23
Pardonet Creek	15	PC	15	-1.00	-6.08
Pardonet Creek	16	PC	16	-0.79	-6.05
Pardonet Creek	17	PC	17	-3.52	-6.51
Pardonet Creek	18	PC	18	-0.30	-5.07

Section	Section Height (m)	Subsection	Subsection Height (m)	d13C (carb)	d18O (carb)
Pardonet Creek	19	PC	19	-1.04	-6.42
Pardonet Creek	20	PC	20	-0.88	-5.78
Pardonet Creek	21	PC	21	-1.06	-6.21
Pardonet Creek	22	PC	22	-1.13	-5.64
Pardonet Creek	23	PC	23	-0.72	-5.72
Pardonet Creek	24	PC	24	-1.30	-5.80
Pardonet Creek	25	PC	25	-0.78	-6.37
Pardonet Creek	26	PC	26	-0.34	-5.27
Pardonet Creek	26.3	PC	26.3	-1.48	-6.31
Pardonet Creek	26.4	PC	26.4	-1.32	-6.37
Pardonet Creek	26.5	PC	26.5	-1.73	-6.36
Pardonet Creek	26.6	PC	26.6	-0.58	-6.00
Pardonet Creek	26.7	PC	26.7	-0.90	-5.77
Pardonet Creek	26.8	PC	26.8	-1.54	-5.99
Pardonet Creek	26.9	PC	26.9	-1.03	-6.06
Pardonet Creek	27	PC	27	-0.92	-5.59
Pardonet Creek	27.1	PC	27.1	-1.39	-6.48
Pardonet Creek	27.2	PC	27.2	-1.07	-5.87
Pardonet Creek	27.3	PC	27.3	-1.08	-6.09
Pardonet Creek	27.4	PC	27.4	-1.02	-6.15
Pardonet Creek	27.5	PC	27.5	-0.79	-5.60
Pardonet Creek	27.6	PC	27.6	-0.85	-5.28
Pardonet Creek	27.7	PC	27.7	-0.90	-5.96
Pardonet Creek	27.8	PC	27.8	-0.78	-5.20
Pardonet Creek	27.9	PC	27.9	-1.26	-5.47
Pardonet Creek	28	PC	28	-1.31	-5.75
Pardonet Creek	28.1	PC	28.1	-1.22	-5.33
Pardonet Creek	28.2	PC	28.2	-0.90	-4.86
Pardonet Creek	28.3	PC	28.3	-0.79	-4.44
Pardonet Creek	28.4	PC	28.4	-0.82	-4.75
Pardonet Creek	28.5	PC	28.5	-0.90	-5.36
Pardonet Creek	28.6	PC	28.6	-0.90	-5.48
Pardonet Creek	28.7	PC	28.7	-1.14	-5.45
Pardonet Creek	28.8	PC	28.8	-1.28	-5.29
Pardonet Creek	28.9	PC	28.9	-0.81	-5.02
Pardonet Creek	29	PC	29	-0.77	-5.75
Pardonet Creek	29.1	PC	29.1	-1.01	-4.97
Pardonet Creek	29.2	PC	29.2	-0.70	-5.10
Pardonet Creek	29.3	PC	29.3	-0.22	-4.41
Pardonet Creek	29.4	PC	29.4	-1.18	-6.21
Pardonet Creek	29.5	PC	29.5	-0.90	-5.88

Section	Section Height (m)	Subsection	Subsection Height (m)	d13C (carb)	d18O (carb)
Pardonet Creek	29.6	PC	29.6	-1.07	-6.15
Pardonet Creek	29.7	PC	29.7	-1.17	-6.29
Pardonet Creek	29.8	PC	29.8	-1.41	-6.19
Pardonet Creek	29.9	PC	29.9	-1.38	-6.11
Pardonet Creek	30	PC	30	-1.37	-6.18
Pardonet Creek	30.1	PC	30.1	-4.00	-5.67
Pardonet Creek	30.2	PC	30.2	-4.95	-5.49
Pardonet Creek	30.3	PC	30.3	-3.76	-7.03
Pardonet Creek	30.4	PC	30.4	-4.44	-5.53
Pardonet Creek	30.5	PC	30.5	-5.04	-5.52
Pardonet Creek	30.6	PC	30.6	-3.98	-5.18
Pardonet Creek	30.8	PC	30.8	-0.69	-3.84
Pardonet Creek	30.9	PC	30.9	-0.85	-5.32
Pardonet Creek	31	PC	31	-0.41	-4.27
Pardonet Creek	31.1	PC	31.1	-0.66	-4.55
Pardonet Creek	31.2	PC	31.2	-0.82	-3.65
Pardonet Creek	31.3	PC	31.3	-0.04	-3.12
Pardonet Creek	31.4	PC	31.4	-0.08	-3.31
Pardonet Creek	31.5	PC	31.5	-3.03	-5.79
Pardonet Creek	31.6	PC	31.6	-4.67	-5.78
Pardonet Creek	31.7	PC	31.7	-3.66	-6.27
Pardonet Creek	31.8	PC	31.8	-3.23	-7.26
Pardonet Creek	31.9	PC	31.9	-1.22	-6.11
Pardonet Creek	32	PC	32	-3.63	-7.13
Pardonet Creek	32.1	PC	32.1	-1.14	-5.81
Pardonet Creek	32.2	PC	32.2	-0.08	-4.19
Pardonet Creek	32.3	PC	32.3	-0.50	-4.73
Pardonet Creek	32.4	PC	32.4	-0.21	-4.68
Pardonet Creek	32.5	PC	32.5	-0.52	-4.88
Pardonet Creek	32.6	PC	32.6	-0.32	-3.97
Pardonet Creek	32.7	PC	32.7	-0.20	-4.13
Pardonet Creek	32.8	PC	32.8	-1.22	-6.19
Pardonet Creek	32.9	PC	32.9	-0.94	-5.84
Pardonet Creek	33	PC	33	-1.43	-6.20
Pardonet Creek	33.1	PC	33.1	-1.30	-5.96
Pardonet Creek	33.2	PC	33.2	-1.00	-5.78
Pardonet Creek	33.3	PC	33.3	-1.88	-6.39
Pardonet Creek	33.4	PC	33.4	-1.25	-6.08

Section	Section Height (m)	Subsection	Subsection Height (m)	d13C (carb)	d18O (carb)
Pardonet Creek	33.5	PC	33.5	-2.76	-5.93
Pardonet Creek	33.6	PC	33.6	-1.89	-6.60
Pardonet Creek	33.7	PC	33.7	-3.68	-6.14
Pardonet Creek	33.8	PC	33.8	-4.26	-7.02
Pardonet Creek	33.9	PC	33.9	-4.05	-6.78
Pardonet Creek	34	PC	34	-4.69	-5.84
Pardonet Creek	34.1	PC	34.1	-3.18	-5.71
Pardonet Creek	34.2	PC	34.2	-2.67	-5.94
Pardonet Creek	35.2	PC	35.2	-2.15	-7.48
Pardonet Creek	35.3	PC	35.3	-0.58	-4.74
Pardonet Creek	35.4	PC	35.4	-0.74	-6.69
Pardonet Creek	35.5	PC	35.5	-1.39	-6.35
Pardonet Creek	35.6	PC	35.6	-1.12	-5.65
Pardonet Creek	35.7	PC	35.7	-1.26	-6.31
Pardonet Creek	35.8	PC	35.8	-1.38	-5.75
Pardonet Creek	35.9	PC	35.9	-0.75	-4.92
Pardonet Creek	36	PC	36	-0.94	-5.26
Pardonet Creek	36.1	PC	36.1	-0.79	-4.96
Pardonet Creek	36.2	PC	36.2	-0.96	-5.55
Pardonet Creek	36.3	PC	36.3	-1.19	-5.74
Pardonet Creek	36.4	PC	36.4	-1.12	-5.43
Pardonet Creek	38.8	PC	38.8	-2.91	-7.67
Pardonet Creek	38.9	PC	38.9	-1.20	-6.81
Pardonet Creek	39	PC	39	-1.65	-6.73
Pardonet Creek	39.1	PC	39.1	-1.47	-5.72
Pardonet Creek	39.2	PC	39.2	-1.91	-6.82
Pardonet Creek	39.3	PC	39.3	-1.89	-6.86
Pardonet Creek	39.4	PC	39.4	-1.94	-6.72
Pardonet Creek	39.5	PC	39.5	-1.90	-6.76
Pardonet Creek	39.6	PC	39.6	-1.93	-6.68
Pardonet Creek	39.7	PC	39.7	-1.67	-6.53
Pardonet Creek	39.8	PC	39.8	-1.94	-6.64
Pardonet Creek	39.9	PC	39.9	-2.23	-7.42
Pardonet Creek	40	PC	40	-2.20	-7.09
Pardonet Creek	40.1	PC	40.1	-1.50	-6.85
Pardonet Creek	40.2	PC	40.2	-1.13	-6.10
Pardonet Creek	40.3	PC	40.3	-1.70	-6.66
Pardonet Creek	40.4	PC	40.4	-0.89	-8.13
Pardonet Creek	40.5	PC	40.5	-1.61	-6.19
Pardonet Creek	40.6	PC	40.6	-1.85	-6.21
Pardonet Creek	40.7	PC	40.7	-1.79	-6.44

Section	Section Height (m)	Subsection	Subsection Height (m)	d13C (carb)	d18O (carb)
Pardonet Creek	40.8	PC	40.8	-1.95	-6.47
Pardonet Creek	40.9	PC	40.9	-2.50	-6.58
Pardonet Creek	41	PC	41	-3.52	-7.30
Pardonet Creek	41.1	PC	41.1	-3.81	-7.24
Pardonet Creek	41.2	PC	41.2	-2.47	-7.92
Pardonet Creek	41.3	PC	41.3	-2.60	-7.37
Pardonet Creek	41.4	PC	41.4	-3.89	-7.46
Pardonet Creek	41.5	PC	41.5	-0.57	-6.16
Pardonet Creek	41.6	PC	41.6	-1.81	-7.09
Pardonet Creek	41.7	PC	41.7	-0.80	-9.33
Pardonet Creek	41.8	PC	41.8	-1.42	-7.48
Pardonet Creek	41.9	PC	41.9	-0.08	-9.10
Pardonet Creek	44.5	PC	44.5	-2.42	-8.27
Pardonet Creek	44.6	PC	44.6	-3.04	-8.16
Pardonet Creek	44.7	PC	44.7	-2.73	-8.47
Pardonet Creek	44.8	PC	44.8	-3.16	-7.97
Pardonet Creek	44.9	PC	44.9	-3.21	-8.21
Pardonet Creek	45	PC	45	-4.82	-8.71
Pardonet Creek	45.1	PC	45.1	-3.21	-8.59
Pardonet Creek	45.2	PC	45.2	-2.51	-8.74
Pardonet Creek	45.3	PC	45.3	-2.86	-9.13
Pardonet Creek	45.4	PC	45.4	-3.12	-7.81
Pardonet Creek	45.8	PC	45.8	-2.09	-8.16
Pardonet Creek	45.9	PC	45.9	-2.54	-8.60
Pardonet Creek	46	PC	46	-4.39	-8.83
Pardonet Creek	46.1	PC	46.1	-4.94	-8.74
Pardonet Creek	46.2	PC	46.2	-5.75	-8.66
Pardonet Creek	49.5	PC	49.5	-1.98	-7.81
Pardonet Creek	49.6	PC	49.6	-3.83	-9.01
Pardonet Creek	49.7	PC	49.7	-3.30	-8.52
Pardonet Creek	49.8	PC	49.8	-2.84	-8.88
Pardonet Creek	49.9	PC	49.9	-3.18	-8.80
Pardonet Creek	50	PC	50	0.64	-3.33
Pardonet Creek	50.1	PC	50.1	-2.30	-9.21
Pardonet Creek	50.2	PC	50.2	-1.39	-8.10
Pardonet Creek	50.4	PC	50.4	-8.12	-8.43
Pardonet Creek	50.5	PC	50.5	-2.64	-5.72
Pardonet Creek	50.8	PC	50.8	-2.96	-8.19

Section	Section Height (m)	Subsection	Subsection Height (m)	d13C (carb)	d18O (carb)
Pardonet Creek	50.9	PC	50.9	-2.81	-7.53
Pardonet Creek	51	PC	51	-0.27	-4.28
Pardonet Creek	51.1	PC	51.1	-5.73	-7.55
Pardonet Creek	51.2	PC	51.2	-6.14	-8.21
Pardonet Creek	51.3	PC	51.3	-3.35	-7.78
Pardonet Creek	51.4	PC	51.4	-11.69	-6.90
Pardonet Creek	51.5	PC	51.5	0.27	-4.19
Pardonet Creek	51.8	PC	51.8	-2.50	-8.98
Pardonet Creek	51.9	PC	51.9	0.49	-2.99
Pardonet Creek	52.1	PC	52.1	1.47	-2.71
Pardonet Creek	52.3	PC	52.3	-2.53	-8.47
Pardonet Creek	52.4	PC	52.4	-1.77	-6.65
Pardonet Creek	52.6	PC	52.6	-3.07	-7.71
Pardonet Creek	52.7	PC	52.7	-1.22	-6.91
Pardonet Creek	52.8	PC	52.8	-2.27	-7.16
Pardonet Creek	53.1	PC	53.1	-15.58	-6.67
Pardonet Creek	53.2	PC	53.2	-8.77	-9.03
Pardonet Creek	53.3	PC	53.3	-10.20	-9.00
Pardonet Creek	53.4	PC	53.4	-10.85	-8.94
Pardonet Creek	53.5	PC	53.5	-9.65	-9.25
Pardonet Creek	53.6	PC	53.6	-16.35	-7.42

Appendix C4: Holberg Inlet geochemical data.

Section	Section Height (m)	Subsection	Subsection Height (m)	d13C (carb)	d18O (carb)
Holberg	185.97	H2	0	-9.15	-13.89
Holberg	186.97	H2	1	-1.95	-12.04
Holberg	187.97	H2	2	-0.53	-12.54
Holberg	188.97	H2	3	-0.12	-12.63
Holberg	189.97	H2	4	0.48	-12.56
Holberg	190.97	H2	5	0.49	-12.31
Holberg	192.97	H2	7	3.01	-13.17
Holberg	193.97	H2	8	1.38	-13.01
Holberg	194.97	H2	9	1.42	-11.97
Holberg	195.97	H2	10	1.02	-11.93
Holberg	196.97	H2	11	1.26	-12.57
Holberg	197.97	H2	12	0.57	-12.08
Holberg	198.97	H2	13	0.52	-12.63
Holberg	199.97	H2	14	0.24	-12.56
Holberg	200.97	H2	15	0.71	-12.06
Holberg	201.97	H2	16	1.10	-11.59
Holberg	202.97	H2	17	0.78	-13.05
Holberg	203.97	H2	18	0.66	-12.75
Holberg	204.97	H2	19	0.56	-10.58
Holberg	206.07	H2	20.1	-0.76	-11.98
Holberg	206.97	H2	21	0.46	-10.19
Holberg	207.97	H2	22	-3.01	-13.04
Holberg	208.97	H2	23	-0.56	-12.33
Holberg	210.47	H2	24.5	0.61	-10.20
Holberg	211.47	H2	25.5	1.23	-12.54
Holberg	212.47	H2	26.5	0.40	-12.29
Holberg	213.97	H2	28	1.15	-10.56
Holberg	215.47	H2	29.5	1.01	-10.15
Holberg	216.97	H2	31	0.99	-11.22
Holberg	217.97	H2	32	1.29	-12.49
Holberg	219.27	H2	33.3	0.87	-9.83
Holberg	219.97	H2	34	1.17	-11.88
Holberg	220.67	H2	34.7	1.12	-12.37
Holberg	222.07	H2	36.1	0.76	-12.76
Holberg	222.97	H2	37	1.36	-12.93
Holberg	224.27	H2	38.3	1.22	-12.89
Holberg	225.47	H2	39.5	1.46	-11.68
Holberg	226.47	H2	40.5	1.36	-12.59

Section	Section Height (m)	Subsection	Subsection Height (m)	d13C (carb)	d18O (carb)
Holberg	227.47	H2	41.5	1.26	-12.49
Holberg	227.97	H2	42	1.65	-10.57
Holberg	228.97	H2	43	0.43	-10.02
Holberg	230.17	H2	44.2	0.53	-11.10
Holberg	231.17	H2	45.2	0.63	-11.50
Holberg	231.37	H2	45.4	0.79	-11.52
Holberg	232.47	H2	46.5	1.17	-12.12
Holberg	233.47	H2	47.5	1.10	-9.99
Holberg	235.67	H2	49.7	0.97	-11.51
Holberg	236.97	H2	51	0.35	-11.85
Holberg	237.77	H2	51.8	0.01	-12.43
Holberg	238.97	H2	53	0.91	-13.65
Holberg	239.97	H2	54	1.37	-12.52
Holberg	241.97	H2	56	2.22	-10.88
Holberg	242.97	H2	57	1.80	-10.07
Holberg	243.97	H2	58	2.13	-12.20
Holberg	244.47	H2	58.5	2.21	-12.12
Holberg	246.77	H3	2.3	-8.23	-13.60
Holberg	249.77	H3	3	-0.44	-11.45
Holberg	250.77	H3	4	0.02	-14.34
Holberg	251.77	H3	5	0.63	-12.08
Holberg	254.77	H3	8	1.14	-11.09
Holberg	255.77	H3	9	0.69	-12.74
Holberg	256.77	H3	10	0.39	-13.67
Holberg	257.77	H3	11	0.46	-13.17
Holberg	267.77	H3	21	0.71	-12.26
Holberg	268.77	H3	22	1.04	-12.92
Holberg	269.77	H3	23	0.91	-12.46
Holberg	270.77	H3	24	1.67	-8.85
Holberg	271.77	H3	25	0.57	-11.07
Holberg	273.17	H3	26.4	0.60	-13.14
Holberg	274.17	H3	27.4	0.27	-12.38
Holberg	274.77	H3	28	0.81	-11.78
Holberg	275.77	H3	29	1.66	-11.81
Holberg	276.77	H3	30	0.97	-11.79
Holberg	277.77	H3	31	0.83	-11.40
Holberg	280.75	H4A	0	-3.48	-12.98
Holberg	281.75	H4A	1	-4.74	-12.52
Holberg	283.75	H4A	3	-4.39	-11.68
Holberg	284.75	H4A	4	-5.53	-13.20
Holberg	285.75	H4A	5	-6.63	-13.03

Section	Section Height (m)	Subsection	Subsection Height (m)	d13C (carb)	d18O (carb)
Holberg	286.75	H4A	6	-6.86	-13.10
Holberg	287.75	H4A	7	-5.41	-13.08
Holberg	288.75	H4A	8	-4.71	-10.29
Holberg	289.75	H4A	9	-5.44	-11.41
Holberg	290.75	H4A	10	-7.95	-12.94
Holberg	291.75	H4A	11	-9.69	-13.15
Holberg	292.75	H4A	12	-3.19	-10.32
Holberg	293.75	H4A	13	-6.58	-12.16
Holberg	294.75	H4A	14	-7.30	-13.24
Holberg	295.75	H4A	15	-6.99	-12.11
Holberg	296.75	H4A	16	-2.73	-10.34
Holberg	297.75	H4A	17	-7.34	-12.60
Holberg	298.75	H4A	18	-3.12	-11.80
Holberg	299.75	H4A	19	-2.61	-13.10
Holberg	300.75	H4A	20	-2.96	-13.13
Holberg	301.45	H4A	20.7	-2.33	-12.70
Holberg	311.27	H5	0	-0.31	-11.06
Holberg	312.27	H5	1	0.74	-12.50
Holberg	313.27	H5	2	-1.00	-12.22
Holberg	314.27	H5	3	1.36	-12.16
Holberg	315.27	H5	4	0.64	-13.48
Holberg	316.27	H5	5	1.03	-12.85
Holberg	317.27	H5	6	-0.26	-11.92
Holberg	318.27	H5	7	0.10	-12.81
Holberg	318.67	H5	7.4	0.23	-12.56
Holberg	337.67	H6	0	0.52	-13.85
Holberg	338.67	H6	1	-0.02	-12.76
Holberg	339.67	H6	2	0.56	-13.76
Holberg	340.67	H6	3	-0.75	-14.83
Holberg	341.67	H6	4	-0.82	-12.79
Holberg	342.67	H6	5	-1.28	-13.14
Holberg	343.67	H6	6	0.88	-11.97
Holberg	344.67	H6	7	-0.65	-13.83
Holberg	345.67	H6	8	-1.68	-12.45
Holberg	346.67	H6	9	-0.59	-13.37
Holberg	347.67	H6	10	-1.49	-11.66
Holberg	348.67	H6	11	-1.42	-11.97
Holberg	349.67	H6	12	-0.93	-12.82

Section	Section Height (m)	Subsection	Subsection Height (m)	d13C (carb)	d18O (carb)
Holberg	350.67	H6	13	-0.65	-13.86
Holberg	351.67	H6	14	0.59	-13.29
Holberg	352.67	H6	15	0.48	-11.74
Holberg	353.67	H6	16	-0.43	-14.15
Holberg	354.67	H6	17	-0.38	-13.52
Holberg	377.57	H7	0	0.28	-12.93
Holberg	378.57	H7	1	0.81	-11.59
Holberg	379.57	H7	2	1.88	-12.47
Holberg	380.57	H7	3	-0.14	-12.16
Holberg	381.57	H7	4	0.71	-13.00
Holberg	382.57	H7	5	-0.05	-13.15
Holberg	383.57	H7	6	0.11	-12.61
Holberg	384.57	H7	7	1.61	-12.39
Holberg	385.57	H7	8	1.31	-12.86
Holberg	386.57	H7	9	1.12	-12.93
Holberg	387.57	H7	10	1.91	-12.67
Holberg	388.07	H7	10.5	1.90	-14.30
Holberg	399.97	H8	0	0.66	-12.26
Holberg	400.97	H8	1	0.45	-12.64
Holberg	401.97	H8	2	0.42	-12.15
Holberg	402.97	H8	3	0.61	-12.27
Holberg	403.97	H8	4	-1.59	-14.91
Holberg	404.97	H8	5	-0.27	-12.30
Holberg	405.97	H8	6	0.46	-11.77
Holberg	406.97	H8	7	-0.19	-12.88
Holberg	407.97	H8	8	1.40	-12.58
Holberg	408.97	H8	9	-0.19	-13.43
Holberg	409.97	H8	10	0.01	-12.92
Holberg	410.97	H8	11	0.25	-12.54
Holberg	411.97	H8	12	0.24	-11.85
Holberg	412.97	H8	13	-0.15	-13.32
Holberg	413.97	H8	14	0.22	-12.58
Holberg	414.97	H8	15	0.14	-12.78
Holberg	415.97	H8	16	-0.01	-12.46
Holberg	416.97	H8	17	-0.94	-14.42
Holberg	417.97	H8	18	-0.65	-12.48
Holberg	418.97	H8	19	-1.40	-14.55
Holberg	419.97	H8	20	-0.75	-13.70
Holberg	420.97	H8	21	-0.53	-11.83
Holberg	421.97	H8	22	-0.93	-12.86
Holberg	422.97	H8	23	-1.38	-13.07

Section	Section Height (m)	Subsection	Subsection Height (m)	d13C (carb)	d18O (carb)
Holberg	423.97	H8	24	-0.83	-12.06
Holberg	424.97	H8	25	-1.00	-12.50
Holberg	425.97	H8	26	-1.86	-13.02
Holberg	426.97	H8	27	-2.14	-13.44
Holberg	427.97	H8	28	0.88	-11.82
Holberg	430.97	H8	31	-0.58	-10.10
Holberg	432.97	H8	33	-0.79	-11.44
Holberg	433.97	H8	34	-1.09	-12.78
Holberg	434.97	H8	35	-0.48	-12.30
Holberg	435.97	H8	36	-0.15	-12.29
Holberg	437.97	H8	38	-0.69	-13.28
Holberg	438.97	H8	39	-0.22	-12.26
Holberg	447.97	H8	48	-0.23	-12.56
Holberg	448.97	H8	49	0.14	-12.96
Holberg	449.97	H8	50	-0.80	-13.38
Holberg	454.97	H8	55	-0.33	-13.12
Holberg	455.97	H8	56	-0.63	-12.54
Holberg	456.97	H8	57	-0.58	-12.56
Holberg	458.27	H8	58.3	-7.85	-12.24
Holberg	458.97	H8	59	-4.13	-13.93
Holberg	459.97	H8	60	-3.93	-13.89
Holberg	462.97	H8	63	-4.29	-15.06
Holberg	463.97	H8	64	-3.35	-15.71
Holberg	464.97	H8	65	-4.45	-15.17
Holberg	465.97	H8	66	-3.89	-14.48
Holberg	466.97	H8	67	-6.37	-13.54
Holberg	467.57	H8	67.6	-2.49	-8.94
Holberg	469.57	H9	0	-4.34	-14.26
Holberg	470.57	H9	1	-3.80	-13.80
Holberg	471.57	H9	2	-3.21	-14.50
Holberg	472.57	H9	3	-3.71	-12.07
Holberg	473.17	H9	3.6	-4.13	-13.60
Holberg	472.87	H9	4.3	-4.95	-12.55
Holberg	474.97	H9	5.4	-6.98	-12.31
Holberg	475.97	H9	6.4	-2.62	-13.99
Holberg	477.17	H9	7.6	-2.48	-12.28
Holberg	478.17	H9	8.6	-2.31	-13.72
Holberg	479.17	H9	9.6	-1.08	-13.53

Section	Section Height (m)	Subsection	Subsection Height (m)	d13C (carb)	d18O (carb)
Holberg	480.87	H9	11.3	-3.10	-12.77
Holberg	481.97	H9	12.4	-3.50	-14.25
Holberg	483.37	H9	13.8	-3.15	-13.22
Holberg	484.37	H9	14.8	-4.12	-13.88
Holberg	485.77	H9	16.2	-4.49	-15.06
Holberg	486.77	H9	17.2	-4.49	-15.96
Holberg	490.27	H9	20.7	-6.67	-13.26
Holberg	491.27	H9	21.7	-6.95	-13.36
Holberg	494.77	H9	25.2	-8.82	-12.92
Holberg	504.97	H9	35.4	-7.45	-13.14
Holberg	511.57	H9	42	-7.96	-12.69
Holberg	517.27	H9	47.7	-4.51	-12.30
Holberg	518.27	H9	48.7	-12.44	-12.34
Holberg	532.37	H10	0.9	-6.76	-10.99
Holberg	533.37	H10	1.9	-8.11	-11.40
Holberg	535.07	H10	3.6	-5.65	-11.09
Holberg	537.37	H10	5.9	-4.48	-10.46
Holberg	538.37	H10	6.9	-4.47	-11.34
Holberg	539.27	H10	7.8	-4.62	-10.80
Holberg	540.07	H10	8.6	-6.82	-10.81
Holberg	541.17	H10	9.7	-9.33	-10.57
Holberg	542.57	H10	11.1	-5.79	-13.28
Holberg	543.57	H10	12.1	-7.82	-10.48
Holberg	544.47	H10	13	-5.60	-13.79
Holberg	545.47	H10	14	-5.35	-14.02
Holberg	547.77	H10	16.3	-3.12	-9.47
Holberg	549.57	H10	18.1	-4.11	-10.81
Holberg	550.47	H10	19	-2.79	-10.33
Holberg	551.47	H10	20	-1.76	-10.29
Holberg	554.47	H10	23	-1.11	-10.24
Holberg	555.27	H10	23.8	-0.62	-10.13
Holberg	556.07	H10	24.6	-2.34	-12.46
Holberg	557.07	H10	25.6	-1.49	-10.31
Holberg	558.77	H10	27.3	-2.43	-10.42
Holberg	560.17	H10	28.7	-3.72	-10.89
Holberg	564.97	H10	33.1	-2.10	-9.97
Holberg	565.67	H10	33.8	-4.44	-9.79
Holberg	566.67	H10	34.8	-1.84	-10.52
Holberg	568.87	H10	37	-1.58	-11.11
Holberg	569.87	H10	38	-1.91	-10.36
Holberg	571.57	H10	39.7	-1.38	-10.87

Section	Section Height (m)	Subsection	Subsection Height (m)	d13C (carb)	d18O (carb)
Holberg	572.57	H10	40.7	-1.92	-11.52
Holberg	573.47	H10	41.6	-1.72	-11.15
Holberg	574.77	H10	42.9	-2.57	-10.63
Holberg	575.87	H10	44	-3.20	-11.03
Holberg	578.17	H10	46.3	-2.79	-9.68
Holberg	580.97	H10	49.1	-2.91	-10.13
Holberg	586.67	H10	54.8	-7.89	-10.36
Michelsen Point	140.7	MP2B	0.3	-9.17	-12.09
Michelsen Point	141.9	MP2B	1.5	-3.84	-12.64
Michelsen Point	142.4	MP2B	2	-4.08	-10.98
Michelsen Point	143.1	MP2B	2.7	-6.78	-7.23
Michelsen Point	144.1	MP2B	3.7	-4.86	-10.69
Michelsen Point	144.6	MP2B	4.2	-3.93	-10.74
Michelsen Point	191	MP2	0	-1.40	-8.17
Michelsen Point	192	MP2	1	-2.28	-11.59
Michelsen Point	193	MP2	2	-0.43	-10.55
Michelsen Point	194	MP2	3	-1.21	-10.36
Michelsen Point	195	MP2	4	-0.66	-12.92
Michelsen Point	195.2	MP2	4.2	-0.30	-9.86
Michelsen Point	196	MP2	5	-0.69	-9.75
Michelsen Point	197	MP2	6	-1.35	-9.67
Michelsen Point	230.8	MPbivalve	0.8	-2.29	-10.19
Michelsen Point	231.1	MPbivalve	1.1	-3.49	-8.92
Michelsen Point	257.5	MP3	0	-1.30	-9.18
Michelsen Point	258.5	MP3	1	-1.04	-10.41
Michelsen Point	259.5	MP3	2	-0.81	-8.70
Michelsen Point	260.5	MP3	3	1.27	-10.75
Michelsen Point	261.5	MP3	4	1.84	-8.52
Michelsen Point	262.5	MP3	5	1.34	-11.38
Michelsen Point	263.5	MP3	6	1.42	-9.77
Michelsen Point	264.5	MP3	7	1.20	-11.55
Michelsen Point	265.5	MP3	8	1.41	-10.44
Michelsen Point	266.5	MP3	9	1.51	-10.19
Michelsen Point	267.5	MP3	10	1.05	-10.30
Michelsen Point	268.5	MP3	11	0.66	-10.09
Michelsen Point	269.5	MP3	12	0.39	-11.15
Michelsen Point	270.5	MP3	13	1.01	-9.34
Michelsen Point	271.5	MP3	14	1.58	-11.07

Section	Section Height (m)	Subsection	Subsection Height (m)	d13C (carb)	d18O (carb)
Michelsen Point	272.5	MP3	15	-0.51	-12.19
Michelsen Point	273.5	MP3	16	1.17	-8.33
Michelsen Point	274.5	MP3	17	-0.63	-11.84
Michelsen Point	275.5	MP3	18	-0.55	-10.35
Michelsen Point	276.5	MP3	19	-1.33	-10.54
Michelsen Point	277.5	MP3	20	-0.60	-10.91
Michelsen Point	278.5	MP3	21	-3.04	-10.22
Michelsen Point	279.5	MP3	22	-0.84	-12.06
Michelsen Point	280.5	MP3	23	-1.74	-9.47
Michelsen Point	281.5	MP3	24	-0.72	-10.62
Michelsen Point	282.5	MP3	25	-1.01	-9.44
Michelsen Point	283.3	MP3	25.8	-1.32	-11.04
Michelsen Point	283.5	MP3	26	-2.01	-10.74
Michelsen Point	284.5	MP3	27	-2.23	-9.68
Michelsen Point	285.5	MP3	28	-1.02	-10.85
Michelsen Point	286.5	MP3	29	-0.11	-10.87
Michelsen Point	287.5	MP3	30	0.05	-10.02
Michelsen Point	288.5	MP3	31	0.34	-9.58
Michelsen Point	289.5	MP3	32	0.21	-10.44
Michelsen Point	290.5	MP3	33	0.01	-11.93
Michelsen Point	291.5	MP3	34	0.16	-10.93
Michelsen Point	292.5	MP3	35	-0.67	-10.93
Michelsen Point	293.5	MP3	36	0.16	-10.65
Michelsen Point	294.5	MP3	37	-0.39	-11.12
Michelsen Point	295.5	MP3	38	-0.98	-10.83
Michelsen Point	296.5	MP3	39	-0.55	-11.24
Michelsen Point	297.5	MP3	40	-0.12	-10.61
Michelsen Point	298.5	MP3	41	-1.49	-9.45
Michelsen Point	299	MP3	41.5	-0.43	-10.78
Michelsen Point	300.4	MP3	42.9	-0.83	-10.30
Michelsen Point	301.2	MP3	43.7	-3.81	-11.34
Michelsen Point	305	MP3	47.5	-3.71	-10.69
Michelsen Point	306.6	MP3	49.1	-1.87	-8.65
Michelsen Point	307.5	MP3	50	-0.95	-11.00
Michelsen Point	308.5	MP3	51	-1.58	-10.64
Michelsen Point	309.5	MP3	52	-0.55	-12.76
Michelsen Point	310.5	MP3	53	-0.77	-11.32
Michelsen Point	311.5	MP3	54	0.46	-11.49
Michelsen Point	312.5	MP3	55	-1.29	-14.52
Michelsen Point	313.5	MP3	56	-0.48	-12.01
Michelsen Point	314.5	MP3	57	0.03	-14.51

Section	Section Height (m)	Subsection	Subsection Height (m)	d13C (carb)	d18O (carb)
Michelsen Point	315.5	MP3	58	-0.42	-10.70
Michelsen Point	316.5	MP3	59	-0.13	-11.11
Michelsen Point	317.5	MP3	60	-0.39	-13.02
Michelsen Point	318.5	MP3	61	-0.42	-11.83
Michelsen Point	319.5	MP3	62	-1.63	-12.23
Michelsen Point	320.5	MP3	63	-0.04	-12.09
Michelsen Point	321.5	MP3	64	-0.66	-12.11
Michelsen Point	322.5	MP3	65	-2.09	-8.06
Michelsen Point	323.5	MP3	66	-1.21	-11.07
Michelsen Point	324.5	MP3	67	-1.42	-12.26
Michelsen Point	325.5	MP3	68	0.21	-10.63
Michelsen Point	326.5	MP3	69	-0.80	-11.55
Michelsen Point	327.5	MP3	70	-0.74	-8.35
Michelsen Point	328.5	MP3	71	0.13	-11.34
Michelsen Point	329.5	MP3	72	0.62	-11.14
Michelsen Point	330.5	MP3	73	-0.10	-10.54
Michelsen Point	331.5	MP3	74	-0.09	-10.93
Michelsen Point	332.5	MP3	75	-0.01	-11.76
Michelsen Point	333.5	MP3	76	0.71	-11.53
Michelsen Point	334.5	MP3	77	-0.44	-12.01
Michelsen Point	335.5	MP3	78	-0.14	-10.07
Michelsen Point	336.5	MP3	79	-0.67	-12.72
Michelsen Point	337.5	MP3	80	0.10	-12.58
Michelsen Point	338.5	MP3	81	-0.46	-14.51
Michelsen Point	339.5	MP3	82	0.51	-11.59
Michelsen Point	340.5	MP3	83	0.39	-11.37
Michelsen Point	341.5	MP3	84	0.39	-10.99
Michelsen Point	342.5	MP3	85	1.01	-11.55
Michelsen Point	343.5	MP3	86	0.55	-11.85
Michelsen Point	344.5	MP3	87	1.43	-11.45
Michelsen Point	345.5	MP3	88	1.73	-11.01
Michelsen Point	346.5	MP3	89	0.98	-11.96
Michelsen Point	347.5	MP3	90	0.90	-12.26
Michelsen Point	348.5	MP3	91	1.46	-12.13
Michelsen Point	349.5	MP3	92	0.89	-12.04
Michelsen Point	350.5	MP3	93	-0.19	-13.82
Michelsen Point	351.5	MP3	94	-0.63	-13.45
Michelsen Point	352.5	MP3	95	-0.67	-12.40

Section	Section Height (m)	Subsection	Subsection Height (m)	d13C (carb)	d18O (carb)
Michelsen Point	353.5	MP3	96	-1.61	-8.70
Michelsen Point	354.5	MP3	97	-1.27	-11.58
Michelsen Point	355.5	MP3	98	-1.08	-11.45
Michelsen Point	356.5	MP3	99	-0.94	-12.00
Michelsen Point	357.5	MP3	100	-0.01	-10.27
Michelsen Point	358.5	MP3	101	-2.11	-12.34
Michelsen Point	359.5	MP3	102	-2.47	-12.12
Michelsen Point	360.5	MP3	103	-1.66	-10.85
Michelsen Point	361.5	MP3	104	-1.10	-11.72
Michelsen Point	362.5	MP3	105	-0.38	-12.30
Michelsen Point	363.5	MP3	106	-3.06	-10.89
Michelsen Point	364.5	MP3	107	-3.56	-10.80
Michelsen Point	365.5	MP3	108	-3.95	-11.34
Michelsen Point	366.5	MP3	109	-3.17	-11.17
Michelsen Point	367.5	MP3	110	-4.60	-10.97
Michelsen Point	368.4	MP3	110.9	-10.10	-12.21
Michelsen Point	349.8	MP4	0	-3.33	-11.07
Michelsen Point	350.8	MP4	1	-7.85	-11.54
Michelsen Point	351.2	MP4	1.4	-6.61	-10.35
Michelsen Point	354.2	MP4	4.4	-0.10	-13.79
Michelsen Point	354.8	MP4	5	-2.79	-12.58
Michelsen Point	355.8	MP4	6	-0.24	-13.90
Michelsen Point	356.8	MP4	7	-3.27	-12.36
Michelsen Point	357.8	MP4	8	-1.94	-11.66
Michelsen Point	358.8	MP4	9	-0.55	-11.21
Michelsen Point	359.8	MP4	10	-0.14	-11.34
Michelsen Point	360.8	MP4	11	-0.42	-12.22
Michelsen Point	361.8	MP4	12	-0.66	-11.16
Michelsen Point	362.8	MP4	13	0.78	-10.80
Michelsen Point	363.8	MP4	14	1.46	-13.45
Michelsen Point	364.8	MP4	15	1.18	-11.97
Michelsen Point	365.8	MP4	16	1.09	-11.20
Michelsen Point	366.8	MP4	17	0.74	-11.34
Michelsen Point	367.8	MP4	18	-4.93	-11.55
Michelsen Point	368.8	MP4	19	0.33	-10.00
Michelsen Point	369.8	MP4	20	0.17	-12.00
Michelsen Point	370.8	MP4	21	0.16	-11.25
Michelsen Point	371.8	MP4	22	0.54	-11.95
Michelsen Point	372.8	MP4	23	-6.43	-12.63
Michelsen Point	373.8	MP4	24	0.29	-10.89
Michelsen Point	374.8	MP4	25	-0.63	-10.98

Section	Section Height (m)	Subsection	Subsection Height (m)	d13C (carb)	d18O (carb)
Michelsen Point	375.8	MP4	26	-0.25	-11.25
Michelsen Point	376.8	MP4	27	-0.07	-11.99
Michelsen Point	377.8	MP4	28	-0.81	-11.26
Michelsen Point	378.8	MP4	29	-0.47	-12.20
Michelsen Point	379.8	MP4	30	0.32	-10.31
Michelsen Point	380.8	MP4	31	-3.85	-9.78
Michelsen Point	381.8	MP4	32	-0.64	-10.33
Michelsen Point	382.8	MP4	33	-2.31	-11.49
Michelsen Point	383.4	MP4	33.6	-1.34	-11.47
Michelsen Point	384.4	MP4	34.6	-1.07	-10.25
Michelsen Point	384.8	MP4	35	-0.58	-10.40
Michelsen Point	385.8	MP4	36	-1.03	-11.62
Michelsen Point	386.8	MP4	37	-0.27	-10.94
Michelsen Point	387.8	MP4	38	-3.01	-10.73
Michelsen Point	388.8	MP4	39	-0.98	-11.22
Michelsen Point	389.8	MP4	40	-1.37	-11.23
Michelsen Point	390.8	MP4	41	-1.28	-10.16
Michelsen Point	392.8	MP4	43	-2.03	-11.45
Michelsen Point	393.8	MP4	44	-0.03	-10.17
Michelsen Point	394.8	MP4	45	-1.53	-9.42
Michelsen Point	395.8	MP4	46	0.08	-11.20
Michelsen Point	396.8	MP4	47	-1.71	-9.78
Michelsen Point	397.8	MP4	48	-1.28	-9.57
Michelsen Point	398.8	MP4	49	-1.44	-12.11
Michelsen Point	399.8	MP4	50	0.43	-10.82
Michelsen Point	400.8	MP4	51	0.69	-12.45
Michelsen Point	401.8	MP4	52	-0.56	-11.16
Michelsen Point	402.8	MP4	53	-0.87	-9.95
Michelsen Point	403.8	MP4	54	-1.45	-10.83
Michelsen Point	404.8	MP4	55	-1.72	-11.28
Michelsen Point	405.8	MP4	56	-3.44	-9.58
Michelsen Point	406.8	MP4	57	-1.14	-10.67
Michelsen Point	407.8	MP4	58	-2.51	-10.11
Michelsen Point	408.8	MP4	59	-0.65	-9.92
Michelsen Point	409.8	MP4	60	-1.01	-10.44
Michelsen Point	410.8	MP4	61	-3.15	-11.02
Michelsen Point	411.8	MP4	62	-2.96	-11.87
Michelsen Point	412.8	MP4	63	-3.22	-11.77

Section	Section Height (m)	Subsection	Subsection Height (m)	d13C (carb)	d18O (carb)
Michelsen Point	413.8	MP4	64	-1.68	-9.96
Michelsen Point	414.8	MP4	65	-2.07	-10.01
Michelsen Point	415.8	MP4	66	-1.13	-10.60
Michelsen Point	417.8	MP4	68	-0.79	-12.04
Michelsen Point	418.8	MP4	69	-0.20	-12.10
Michelsen Point	419.8	MP4	70	-3.33	-11.79
Michelsen Point	420.8	MP4	71	-1.48	-10.28
Michelsen Point	421.8	MP4	72	-0.32	-10.94
Michelsen Point	422.8	MP4	73	-3.60	-9.05
Michelsen Point	423.8	MP4	74	-3.83	-14.17
Michelsen Point	424.8	MP4	75	-2.42	-9.45
Michelsen Point	425.8	MP4	76	-2.15	-9.03
Michelsen Point	426.8	MP4	77	-1.14	-10.25
Michelsen Point	427.8	MP4	78	-0.36	-12.16
Michelsen Point	428.8	MP4	79	-1.17	-11.75
Michelsen Point	429.8	MP4	80	-0.32	-10.72
Michelsen Point	430.8	MP4	81	-0.78	-10.98
Michelsen Point	431.8	MP4	82	-0.27	-11.86
Michelsen Point	432.8	MP4	83	-0.93	-11.15
Michelsen Point	433.8	MP4	84	-0.30	-13.42
Michelsen Point	434.8	MP4	85	-1.19	-9.67
Michelsen Point	435.8	MP4	86	-0.01	-11.55
Michelsen Point	436.8	MP4	87	-0.76	-10.16
Michelsen Point	437.8	MP4	88	1.07	-11.67
Michelsen Point	438.8	MP4	89	0.23	-12.91
Michelsen Point	439.8	MP4	90	0.72	-9.18
Michelsen Point	440.8	MP4	91	-0.75	-11.97
Michelsen Point	441.8	MP4	92	-0.15	-12.72
Michelsen Point	442.8	MP4	93	-0.94	-10.03
Michelsen Point	443.8	MP4	94	-0.92	-11.76
Michelsen Point	444.8	MP4	95	-0.55	-11.40
Michelsen Point	445.8	MP4	96	0.66	-11.03
Michelsen Point	446.8	MP4	97	0.57	-10.37
Michelsen Point	447.8	MP4	98	0.63	-11.68
Michelsen Point	448.8	MP4	99	-0.79	-13.94
Michelsen Point	449.8	MP4	100	-0.63	-9.18
Michelsen Point	450.8	MP4	101	0.36	-12.03
Michelsen Point	451.8	MP4	102	-0.67	-10.70
Michelsen Point	452.8	MP4	103	-1.21	-10.84
Michelsen Point	453.8	MP4	104	0.39	-11.19
Michelsen Point	454.8	MP4	105	-0.24	-11.08

Section	Section Height (m)	Subsection	Subsection Height (m)	d13C (carb)	d18O (carb)
Michelsen Point	456.8	MP4	107	-1.50	-11.16
Michelsen Point	457.8	MP4	108	-1.53	-9.59
Michelsen Point	460.7	MP4	110.9	-2.70	-10.52
Michelsen Point	461.8	MP4	112	-1.86	-11.46
Michelsen Point	462.3	MP4	112.5	-2.00	-10.83

Appendix C5: Kyuquot Sound geochemical data.

Section	Section Height (m)	Subsection	Subsection Height (m)	d13C (carb)	d18O (carb)
Mushroom Point North	0.3	MUP1	0.3	-3.05	-16.14
Mushroom Point North	0.9	MUP1	0.9	-3.90	-16.01
Mushroom Point North	2	MUP1	2	-4.71	-14.78
Mushroom Point North	2.9	MUP1	2.9	-3.24	-16.60
Mushroom Point North	4	MUP1	4	-5.59	-15.67
Mushroom Point North	5	MUP1	5	-2.51	-15.44
Mushroom Point North	6.4	MUP1	6.4	-3.64	-14.64
Mushroom Point North	7.6	MUP1	7.6	-2.96	-16.17
Mushroom Point North	8.1	MUP1	8.1	-3.43	-13.20
Mushroom Point North	9.9	MUP1	9.9	-3.60	-15.18
Mushroom Point North	11.5	MUP1	11.5	-3.03	-14.90
Mushroom Point North	14.3	MUP1	14.3	-2.77	-14.02
Mushroom Point North	15.3	MUP1	15.3	-2.76	-14.77
Mushroom Point North	15.9	MUP1	15.9	-0.59	-12.85
Mushroom Point North	16.3	MUP1	16.3	-4.97	-13.61
Mushroom Point North	17.6	MUP1	17.6	-3.00	-14.80
Mushroom Point North	19	MUP1	19	-3.05	-13.39
Mushroom Point North	20.9	MUP1	20.9	-2.19	-14.86
Mushroom Point North	30.9	MUP1	30.9	-2.33	-14.98
Mushroom Point North	32	MUP1	32	-2.51	-13.97
Mushroom Point North	33.2	MUP1	33.2	-3.10	-13.36
Mushroom Point North	34	MUP1	34	-2.40	-14.49
Mushroom Point North	36	MUP1	36	-1.43	-13.70
Mushroom Point North	37	MUP1	37	-2.42	-13.93
Mushroom Point North	38.8	MUP1	38.8	-2.08	-14.29
Mushroom Point North	39.3	MUP1	39.3	-0.89	-12.64
Mushroom Point North	40.3	MUP1	40.3	-0.13	-12.76

Section	Section Height (m)	Subsection	Subsection Height (m)	d13C (carb)	d18O (carb)
Mushroom Point North	41	MUP1	41	-0.54	-13.49
Mushroom Point North	42	MUP1	42	-1.47	-14.29
Mushroom Point North	42.6	MUP1	42.6	-0.92	-13.64
Mushroom Point North	44.1	MUP1	44.1	-0.07	-12.54
Mushroom Point North	45	MUP1	45	1.26	-11.57
Mushroom Point North	46.1	MUP1	46.1	-0.80	-14.03
Mushroom Point North	46.9	MUP1	46.9	-2.08	-14.53
Mushroom Point North	48	MUP1	48	-1.18	-13.83
Mushroom Point North	49	MUP1	49	-0.89	-14.42
Mushroom Point North	50	MUP1	50	0.06	-11.59
Mushroom Point North	51.2	MUP1	51.2	-0.73	-13.31
Mushroom Point North	52	MUP1	52	-0.43	-14.12
Mushroom Point North	53	MUP1	53	-0.52	-13.96
Mushroom Point North	54	MUP1	54	-1.48	-14.09
Mushroom Point North	55	MUP1	55	-1.33	-12.95
Mushroom Point North	56	MUP1	56	-1.19	-13.33
Mushroom Point North	57	MUP1	57	-0.72	-12.78
Mushroom Point North	57.6	MUP1	57.6	-0.24	-12.45
Mushroom Point North	58.2	MUP1	58.2	-0.46	-12.28
Mushroom Point North	59	MUP1	59	0.34	-13.06
Mushroom Point North	60	MUP1	60	-0.77	-12.20
Mushroom Point North	61	MUP1	61	-0.24	-12.41
Mushroom Point North	62	MUP1	62	-0.96	-12.91
Mushroom Point North	63	MUP1	63	-0.56	-13.72
Mushroom Point North	64	MUP1	64	-0.12	-14.06
Mushroom Point North	66	MUP1	66	-0.38	-13.62
Mushroom Point North	67	MUP1	67	-2.16	-12.38
Mushroom Point North	68	MUP1	68	-1.76	-14.17
Mushroom Point North	69	MUP1	69	-0.98	-13.25
Mushroom Point North	70.1	MUP1	70.1	-1.53	-11.90
Mushroom Point North	71	MUP1	71	-1.44	-12.84
Mushroom Point North	72	MUP1	72	-2.38	-12.40
Mushroom Point North	72.6	MUP1	72.6	-1.95	-9.94
Mushroom Point North	73.6	MUP1	73.6	-1.72	-12.24
Mushroom Point North	75	MUP1	75	-1.39	-12.52
Mushroom Point North	76	MUP1	76	-1.28	-10.63
Mushroom Point North	76.1	MUP1	76.1	-1.43	-11.71
Mushroom Point North	77.9	MUP1	77.9	-1.16	-11.52

Section	Section Height (m)	Subsection	Subsection Height (m)	d13C (carb)	d18O (carb)
Mushroom Point North	79	MUP1	79	-1.84	-12.68
Mushroom Point North	80	MUP1	80	-1.19	-12.19
Mushroom Point North	81	MUP1	81	-1.33	-11.52
Mushroom Point North	82	MUP1	82	-1.17	-11.07
Mushroom Point North	83	MUP1	83	-1.92	-11.97
Mushroom Point North	84	MUP1	84	-0.79	-10.58
Mushroom Point North	85	MUP1	85	-0.55	-11.23
Mushroom Point North	86	MUP1	86	-1.23	-13.23
Mushroom Point North	87	MUP1	87	-0.84	-11.15
Mushroom Point North	88.4	MUP1	88.4	-1.71	-12.76
Mushroom Point North	91.1	MUP1	91.1	-0.36	-10.67
Mushroom Point North	134	MUP1	134	-1.13	-13.23
Mushroom Point North	134.7	MUP1	134.7	-0.96	-10.22
Mushroom Point North	139	MUP1	139	-0.30	-12.62
Mushroom Point North	139.9	MUP1	139.9	-1.28	-8.17
Mushroom Point North	141	MUP1	141	-0.36	-9.79
Mushroom Point North	142	MUP1	142	-0.58	-11.18
Mushroom Point North	143	MUP1	143	-1.21	-11.43
Mushroom Point North	144	MUP1	144	-0.18	-12.22
Mushroom Point North	145	MUP1	145	-0.79	-12.33
Mushroom Point North	146	MUP1	146	-1.58	-9.55
Mushroom Point North	147	MUP1	147	-3.39	-9.02
Mushroom Point North	148.1	MUP1	148.1	-2.01	-8.58
Mushroom Point North	149	MUP1	149	-2.24	-11.09
Mushroom Point North	149.6	MUP1	149.6	-1.51	-11.37
Mushroom Point North	150	MUP1	150	-1.38	-11.92
Mushroom Point North	151	MUP1	151	-1.00	-12.37
Mushroom Point North	152	MUP1	152	-0.60	-10.81
Mushroom Point North	155	MUP1	155	-0.42	-12.82
Mushroom Point North	156	MUP1	156	-0.19	-7.34
Mushroom Point North	157	MUP1	157	-1.10	-13.52
Mushroom Point North	158	MUP1	158	-1.55	-10.50
Mushroom Point North	159	MUP1	159	-1.62	-11.87
Mushroom Point North	160	MUP1	160	-1.82	-11.46
Mushroom Point North	161	MUP1	161	-0.71	-13.43
Mushroom Point North	162	MUP1	162	-0.55	-13.25
Mushroom Point North	164	MUP1	164	-0.38	-9.13
Mushroom Point North	165	MUP1	165	-0.78	-9.35
Mushroom Point North	166	MUP1	166	-0.61	-11.21
Mushroom Point North	167	MUP1	167	-1.26	-10.23
Mushroom Point North	168	MUP1	168	-0.73	-12.32

Section	Section Height (m)	Subsection	Subsection Height (m)	d13C (carb)	d18O (carb)
Mushroom Point North	169	MUP1	169	1.27	-6.56
Mushroom Point North	170	MUP1	170	-0.84	-11.66
Mushroom Point North	171	MUP1	171	-0.20	-8.42
Mushroom Point North	172	MUP1	172	-0.51	-12.75
Mushroom Point North	173	MUP1	173	-0.51	-10.17
Mushroom Point North	174	MUP1	174	-0.24	-9.78
Mushroom Point North	180	MUP1	180	0.30	-9.26
Mushroom Point North	181	MUP1	181	-0.75	-10.73
Mushroom Point North	182	MUP1	182	-0.40	-12.36
Mushroom Point North	183	MUP1	183	-1.51	-10.65
Mushroom Point North	184	MUP1	184	0.17	-9.88
Mushroom Point North	185	MUP1	185	-0.56	-12.57
Mushroom Point North	203	MUP1	203	0.18	-10.58
Mushroom Point North	204	MUP1	204	-1.11	-11.66
Mushroom Point North	205	MUP1	205	0.04	-12.20
Mushroom Point North	206	MUP1	206	0.34	-12.56
Mushroom Point North	207	MUP1	207	-0.02	-13.52
Mushroom Point North	208	MUP1	208	-0.41	-13.44
Mushroom Point North	209	MUP1	209	-3.29	-12.66
Mushroom Point North	210	MUP1	210	-1.55	-11.69
Mushroom Point North	211	MUP1	211	-2.77	-13.65
Mushroom Point North	212	MUP1	212	-3.45	-13.20
Mushroom Point North	212.7	MUP1	212.7	-1.89	-12.80
Mushroom Point North	214	MUP1	214	-3.16	-13.24
Mushroom Point North	215	MUP1	215	-2.84	-11.16
Mushroom Point North	216	MUP1	216	-2.46	-10.81
Mushroom Point North	217	MUP1	217	-3.90	-12.05
Mushroom Point North	218	MUP1	218	-5.00	-12.61
Mushroom Point North	219	MUP1	219	-3.85	-12.92
Mushroom Point North	220	MUP1	220	-3.76	-12.22
Mushroom Point North	221	MUP1	221	-2.46	-12.85
Mushroom Point North	222	MUP1	222	-2.67	-11.28
Mushroom Point North	222.5	MUP1	222.5	-2.50	-11.07
Mushroom Point North	223	MUP1	223	-3.72	-11.24
Mushroom Point North	224	MUP1	224	-4.52	-12.72
Mushroom Point North	225	MUP1	225	-2.44	-11.42
Mushroom Point North	226	MUP1	226	-3.71	-11.49
Mushroom Point North	227	MUP1	227	-2.73	-11.51

Section	Section Height (m)	Subsection	Subsection Height (m)	d13C (carb)	d18O (carb)
Mushroom Point North	279.4	MUP1	279.4	-12.18	-8.85
Mushroom Point North	280.3	MUP1	280.3	-10.36	-10.84
Mushroom Point South	7	MUP2	7	-0.63	-12.78
Mushroom Point South	8.1	MUP2	8.1	-1.44	-11.73
Mushroom Point South	9.5	MUP2	9.5	-1.03	-9.93
Mushroom Point South	10	MUP2	10	-0.94	-12.70
Mushroom Point South	10.4	MUP2	10.4	-5.70	-13.75
Mushroom Point South	11	MUP2	11	-0.51	-12.78
Mushroom Point South	11.9	MUP2	11.9	-0.67	-12.64
Mushroom Point South	14.5	MUP2	14.5	-0.31	-13.32
Mushroom Point South	16	MUP2	16	-0.49	-13.04
Mushroom Point South	18	MUP2	18	-1.43	-8.59
Mushroom Point South	19	MUP2	19	-0.76	-13.11
Mushroom Point South	23	MUP2	23	-0.81	-13.13
Mushroom Point South	24	MUP2	24	0.23	-13.73
Mushroom Point South	25	MUP2	25	-0.51	-13.52
Mushroom Point South	25.6	MUP2	25.6	-1.52	-9.55
Mushroom Point South	26	MUP2	26	-1.28	-12.27
Mushroom Point South	27	MUP2	27	-0.70	-13.26
Mushroom Point South	28.2	MUP2	28.2	0.09	-10.08
Mushroom Point South	29	MUP2	29	0.14	-13.98
Mushroom Point South	29.9	MUP2	29.9	0.86	-9.48
Mushroom Point South	31	MUP2	31	0.07	-7.52
Mushroom Point South	34	MUP2	34	-1.72	-11.86
Mushroom Point South	34.9	MUP2	34.9	-1.04	-10.43
Mushroom Point South	37	MUP2	37	-1.36	-12.73
Mushroom Point South	38	MUP2	38	0.07	-9.95
Mushroom Point South	39	MUP2	39	-4.11	-12.69
Mushroom Point South	39.5	MUP2	39.5	-0.88	-10.29
Mushroom Point South	39.9	MUP2	39.9	-2.21	-9.86
Mushroom Point South	41	MUP2	41	-0.98	-10.08
Mushroom Point South	42.1	MUP2	42.1	-1.38	-10.91
Mushroom Point South	43.1	MUP2	43.1	-2.08	-12.51
Mushroom Point South	45	MUP2	45	-0.80	-13.01
Mushroom Point South	48	MUP2	48	0.94	-10.11
Mushroom Point South	49	MUP2	49	1.22	-9.29
Mushroom Point South	50	MUP2	50	0.52	-8.82
Mushroom Point South	57.1	MUP2	57.1	0.26	-13.62
Mushroom Point South	58.4	MUP2	58.4	-0.51	-10.97
Mushroom Point South	59	MUP2	59	-0.89	-14.20
Mushroom Point South	60	MUP2	60	-1.33	-13.36

Section	Section Height (m)	Subsection	Subsection Height (m)	d13C (carb)	d18O (carb)
Mushroom Point South	61.1	MUP2	61.1	-0.63	-12.27
Mushroom Point South	62.5	MUP2	62.5	-1.59	-14.51
Mushroom Point South	83	MUP2	83	-1.62	-12.11
Mushroom Point South	84	MUP2	84	-1.52	-10.97
Mushroom Point South	85	MUP2	85	-3.74	-12.31
Mushroom Point South	86	MUP2	86	-2.74	-12.00
Mushroom Point South	87	MUP2	87	-3.87	-10.30
Mushroom Point South	88	MUP2	88	-2.27	-10.20
Mushroom Point South	88.4	MUP2	88.4	-1.47	-11.82
Mushroom Point South	89	MUP2	89	-1.57	-9.16
Mushroom Point South	89.1	MUP2	89.1	-1.83	-12.30
Mushroom Point South	90.4	MUP2	90.4	-2.26	-12.27
Mushroom Point South	93	MUP2	93	-3.93	-14.04
Mushroom Point South	94	MUP2	94	-3.69	-13.80
Mushroom Point South	95	MUP2	95	-3.91	-13.97
Mushroom Point South	95.8	MUP2	95.8	-3.62	-14.37
Mushroom Point South	97	MUP2	97	-3.95	-14.37
Mushroom Point South	98	MUP2	98	-5.49	-12.54
Mushroom Point South	99	MUP2	99	-5.16	-14.60
Mushroom Point South	99.6	MUP2	99.6	-4.55	-13.44
Mushroom Point South	99.8	MUP2	99.8	-4.43	-13.79
Mushroom Point South	100.4	MUP2	100.4	-4.28	-14.23
Mushroom Point South	101.2	MUP2	101.2	-3.29	-13.01
Mushroom Point South	102.5	MUP2	102.5	-3.61	-13.89
Mushroom Point South	103.2	MUP2	103.2	-3.75	-13.42
Mushroom Point South	104	MUP2	104	-5.63	-14.19
Mushroom Point South	105.8	MUP2	105.8	-6.95	-14.50
Mushroom Point South	107.2	MUP2	107.2	-4.30	-15.16
Mushroom Point South	108.4	MUP2	108.4	-5.78	-14.67
Mushroom Point South	117.2	MUP2	117.2	-6.17	-11.19
Mushroom Point South	118.2	MUP2	118.2	-7.45	-15.33
Mushroom Point South	119	MUP2	119	-5.17	-14.22
Mushroom Point South	120	MUP2	120	-3.10	-11.32
Mushroom Point South	121	MUP2	121	-2.70	-12.98
Mushroom Point South	122	MUP2	122	-3.19	-11.51
Mushroom Point South	123	MUP2	123	-3.98	-12.59
Mushroom Point South	124	MUP2	124	-2.26	-13.61
Mushroom Point South	125.1	MUP2	125.1	-2.91	-10.98

Section	Section Height (m)	Subsection	Subsection Height (m)	d13C (carb)	d18O (carb)
Mushroom Point South	126	MUP2	126	-4.98	-11.98
Mushroom Point South	126.8	MUP2	126.8	-4.64	-12.38
Mushroom Point South	128	MUP2	128	-5.14	-10.88
Mushroom Point South	129	MUP2	129	-4.60	-12.10
Mushroom Point South	130	MUP2	130	-6.02	-14.36
Mushroom Point South	131	MUP2	131	-5.50	-13.99
Mushroom Point South	131.7	MUP2	131.7	-5.74	-15.06
Mushroom Point South	135.3	MUP2	135.3	-8.59	-15.25
Mushroom Point South	136.8	MUP2	136.8	-6.97	-14.20
Mushroom Point South	138.6	MUP2	138.6	-3.52	-13.99
Mushroom Point South	139.3	MUP2	139.3	-4.44	-14.38
Mushroom Point South	140.3	MUP2	140.3	-5.28	-12.76
Mushroom Point South	141	MUP2	141	-5.21	-13.70
Mushroom Point South	142	MUP2	142	-5.18	-13.51
Mushroom Point South	143	MUP2	143	-6.05	-14.24
Mushroom Point South	144	MUP2	144	-5.96	-13.29
Mushroom Point South	144.7	MUP2	144.7	-4.42	-14.26
Mushroom Point South	145.4	MUP2	145.4	-7.57	-13.91
Mushroom Point South	146	MUP2	146	-5.80	-14.72
Mushroom Point South	161.2	MUP2	161.2	-11.91	-10.34
Mushroom Point South	162.3	MUP2	162.3	-8.79	-15.06
Mushroom Point South	164.4	MUP2	164.4	-11.68	-14.71
Mushroom Point South	164.8	MUP2	164.8	-12.63	-14.76
Mushroom Point South	166.2	MUP2	166.2	-15.26	-10.93
Mushroom Point South	167	MUP2	167	-14.17	-11.00
Mushroom Point South	168	MUP2	168	-7.31	-5.70
Mushroom Point South	169.1	MUP2	169.1	-3.66	-9.99
Mushroom Point South	170	MUP2	170	-5.47	-8.53
Mushroom Point South	171	MUP2	171	-0.44	-8.01
Mushroom Point South	172	MUP2	172	1.48	-11.01
Mushroom Point South	173	MUP2	173	-0.34	-7.45
Mushroom Point South	174	MUP2	174	-0.61	-7.43
Mushroom Point South	175	MUP2	175	0.62	-7.76
Mushroom Point South	176	MUP2	176	1.03	-7.10
Mushroom Point South	177	MUP2	177	0.82	-6.20
Mushroom Point South	178	MUP2	178	0.45	-7.12
Mushroom Point South	178.4	MUP2	178.4	-0.12	-7.02
Walters Island East	0	WIE	0	-0.21	-13.98
Walters Island East	1	WIE	1	0.15	-13.31
Walters Island East	2	WIE	2	0.58	-13.45
Walters Island East	2.6	WIE	2.6	1.07	-13.60

Section	Section Height (m)	Subsection	Subsection Height (m)	d13C (carb)	d18O (carb)
Walters Island East	3.5	WIE	3.5	0.65	-12.65
Walters Island East	4	WIE	4	0.81	-13.43
Walters Island East	5	WIE	5	-0.15	-13.64
Walters Island East	6	WIE	6	0.49	-14.07
Walters Island East	6.4	WIE	6.4	0.27	-12.78
Walters Island East	7	WIE	7	0.23	-12.66
Walters Island East	7.3	WIE	7.3	-0.03	-12.73
Walters Island East	9	WIE	9	-1.04	-13.06
Walters Island East	10	WIE	10	-0.40	-12.08
Walters Island East	11	WIE	11	-0.14	-12.62
Walters Island East	12	WIE	12	-0.07	-12.73
Walters Island East	13	WIE	13	-0.83	-12.74
Walters Island East	14	WIE	14	-0.64	-12.49
Walters Island East	15	WIE	15	-0.92	-12.62
Walters Island East	15.9	WIE	15.9	-0.92	-12.61
Walters Island East	21.3	WIE	21.3	-2.17	-12.07
Walters Island East	22	WIE	22	-0.71	-12.44
Walters Island East	23	WIE	23	-1.30	-12.37
Walters Island East	24	WIE	24	-1.03	-12.86
Walters Island East	25	WIE	25	-1.94	-12.59
Walters Island East	26.1	WIE	26.1	-2.68	-12.88
Walters Island East	27	WIE	27	-1.77	-13.39
Walters Island East	28	WIE	28	-2.13	-13.03
Walters Island East	31	WIE	31	-1.26	-13.71
Walters Island East	32	WIE	32	-1.66	-12.16
Walters Island East	33	WIE	33	-1.58	-13.13
Walters Island East	48.5	WIE	48.5	-1.35	-14.11
Walters Island East	49.7	WIE	49.7	-1.28	-12.05